LEABHARLANN CHOLÁISTE NA TRÍONÓIDE, BAILE ÁTHA CLIATH
Ollscoil Átha Cliath

TRINITY COLLEGE LIBRARY DUBLIN
The University of Dublin

Terms and Conditions of Use of Digitised Theses from Trinity College Library Dublin

Copyright statement

All material supplied by Trinity College Library is protected by copyright (under the Copyright and Related Rights Act, 2000 as amended) and other relevant Intellectual Property Rights. By accessing and using a Digitised Thesis from Trinity College Library you acknowledge that all Intellectual Property Rights in any Works supplied are the sole and exclusive property of the copyright and/or other IPR holder. Specific copyright holders may not be explicitly identified. Use of materials from other sources within a thesis should not be construed as a claim over them.

A non-exclusive, non-transferable licence is hereby granted to those using or reproducing, in whole or in part, the material for valid purposes, providing the copyright owners are acknowledged using the normal conventions. Where specific permission to use material is required, this is identified and such permission must be sought from the copyright holder or agency cited.

Liability statement

By using a Digitised Thesis, I accept that Trinity College Dublin bears no legal responsibility for the accuracy, legality or comprehensiveness of materials contained within the thesis, and that Trinity College Dublin accepts no liability for indirect, consequential, or incidental, damages or losses arising from use of the thesis for whatever reason. Information located in a thesis may be subject to specific use constraints, details of which may not be explicitly described. It is the responsibility of potential and actual users to be aware of such constraints and to abide by them. By making use of material from a digitised thesis, you accept these copyright and disclaimer provisions. Where it is brought to the attention of Trinity College Library that there may be a breach of copyright or other restraint, it is the policy to withdraw or take down access to a thesis while the issue is being resolved.

Access Agreement

By using a Digitised Thesis from Trinity College Library you are bound by the following Terms & Conditions. Please read them carefully.

I have read and I understand the following statement: All material supplied via a Digitised Thesis from Trinity College Library is protected by copyright and other intellectual property rights, and duplication or sale of all or part of any of a thesis is not permitted, except that material may be duplicated by you for your research use or for educational purposes in electronic or print form providing the copyright owners are acknowledged using the normal conventions. You must obtain permission for any other use. Electronic or print copies may not be offered, whether for sale or otherwise to anyone. This copy has been supplied on the understanding that it is copyright material and that no quotation from the thesis may be published without proper acknowledgement.

Resonant Soft X-ray Spectroscopic Studies of Certain Transition Metal Oxides

A thesis submitted for the degree of

Doctor of Philosophy

University of Dublin

Brian Kennedy

School of Physics, Trinity College Dublin

February 2011

This written volume is dedicated to my friends Thomas Russell and Laura Greer on the occasion of their wedding.

13 Westland Row, Dublin 01/29/11

To Borrow a phrase from a political memoir I once opened: getting a PhD was an experience absolutely not to be missed - and absolutely not to be repeated. Ever.

Contained in the following paragraphs is an expression of gratitude to the people who played a role in the process, and if it is lengthy then so be it, there are many people to thank. Even - you might say *particularly* - a success as humble and contingent as my own is a bride with many husbands. And even at that, I am cleaving rigidly to my "public life", so if you are a sainted mother, father, older sister, younger sister, beloved cousin, uncle, or aunt of mine you can skip this section. The order of the list reflects the degree to which I would be minced meat without the person named.

First, in any order of precedence is Dr Cormac McGuinness. He is as close as I have known personally to a polymath, with such an abundant store of knowledge, embracing everything that you might expect it to embrace, as well as things you wouldn't, necessarily. His brilliant mind is a source of great pride to those of us who have worked for him. And I daresay he is famous for it far and wide. I particularly mention his many pains taken over the calculations we present in this thesis, and the rigour and dedication he applied in making funding and beamtime applications, which stands as a sterling example to his students for the future in this vital activity. His contributions are so valuable that if I could do my PhD all over again, I would badger him a great deal more about this report or that result. But I'll badger him *from now on* even though I'm finished. Now we'll call it collaboration. I hope that, beginning in the near future we will put our large store of results to good use. All of our data is potentially useful, and a good asset to have. The trained eye sees very quickly! And for future reference, readers, Cormac is also a very generous support-figure in the many walks of his students' lives, should you ever need him. And the way he handled my eleventh-hour crises was in its own distinctive way exemplary. I sympathize profusely for the many cares I have brought down on his brow, and I hope we have a long future of crossed paths.

Dr Franz Hennies, onetime beamline scientist at Maxlab I511, my new boss and a great friend. I had the extremely good fortune to meet him towards the end of my research and I think joining him at Maxlab will prove to be one of the best things I ever did, for the opportunities he has made available to me, and the unique generosity he has extended by allowing me the space and time to finish my thesis. I hope I can work hard to repay his trust and kindness. Here's to our (near) future together in liquid RIXS!

Dr Satheesh Krishnamurthy was another brilliant admixture of scientist and great friend. Our conversations range between almost armwrestling over the interpretation of a spectrum to great laughter at the "news of the day" in our respective departments. Inclining more towards the latter, if the truth be stated plainly.

I would like to include at this point a special word for Cormac, Franz and Satheesh's families. Cormac's especially. I'm glad to say that, thanks to a meeting that Cormac had to attend, I did baby-sit on one occasion for my supervisor! It isn't every graduate student who has had that honour bestowed on them. It is the least I could do considering the amount of time he devotes to me, when his young family is in their most precious years. Visiting Franz's family and the many visits I have made with Satheesh and Bhavna have brought a healthy balance to my hectic twenty-something (mostly) bachelor's Dublin lifestyle. Not least it provides me with a reminder of the family life I love so well, often at a some distance from my old homestead.

A warm word for the beamline scientists: Dr Jinghua Guo, who provided very generous and always cheerful and welcome suggestions, and kindly hosted me during my Short Term Travelling Fellowship in Summer 2009. Per-Anders Glans who continues to help me in times of crisis with important tips on x-ray spectrometers. Tim Learmonth for never leaving me at sea when I travelled to the ALS on my own. Dr Tanel Käämbre, Dr Franz Hennies (again) and Dr Annette Pietzch for giving me a free hand at Maxlab over the years. I also mention Dr Thorsten Schmitt of PSI, Switzerland. Though the spectroscopy I did at his beamline doesn't appear here, he has been something of an unwitting role model over the years. An inspiration to take pride in your work.

To the people who provided samples for our spectroscopic study. The renowned Erasmus Smith's Professor of Natural and Experimental Philosophy Prof. Mike Coey FRS, and his associates Venky, Lucio, Karsten and Johnathan. Though in the cosmos of those who have come within the orbit of the Coey group, I am but a sub-atomic particle, and this is reminiscent of an altarboy sending his thanks to the Pope, my trajectory has been influenced by the interaction nonetheless. Prof. Russ Egdell, Oxon., was very generous with his samples and contact. I hope to send him some "articles in press" in the near future based on the results presented in this thesis. Prof Yuri Gun'ko and Dr Anna Zukova generously lent me many interesting samples.

Dr Peter Blaha (WIEN2k) has given very generously of his time and interest in our project. His detailed communications have provided an excellent support to me in writing sections of this thesis, and I hope the work that has come about during this PhD is the start of something useful. Dr Charles Patterson provided strong advice in a field where bearings were difficult to find, and often shifted.

A special word for Prof. Iggy McGovern for all the vacuum supplies we acquired on long term loan over the years. And for the gems of wit and lyric he dispensed with judicious thrift - the more to accord them their true value. In the same breath I mention Prof. John McGilp, to whom I always felt I could turn for help - not that I did in the end, but I formed the opinion that if I needed a chat I could always turn to John. And that was an important sense of security that I acknowledge.

And now, from the appreciative to the valedictorial. In years to come, I intend this part of the thesis to serve as a reminder, pleasant or unpleasent as the case may be, of the high spirits that coloured everything as the last grains of sand from my time at Trinity College fell through the glass - and with it the final flush of youth. With good riddance, you may agree, gentle reader!

Where would I be without the Irish education system? Not an entirely rhetorical question! But it is really better not to wonder. I have a complex relationship with the memories of my various *alma maters*, but as they say in Sligo *by hook or by crook* I won a unique version of an education out of it in the long run. Also, as ancient wisdom states: it taketh two to tango, and I share the blame for being a profligate youth. As they would also tellingly pronounce in Sligo: Trinity College *put smácht on him*! IRCSET and Intel combined via the Embark initiative, and Science Foundation Ireland helped to fund my studentship, on what in the years to come will be seen as gilt-edged terms. I was well kept, and couldn't complain. I hope they see an economically tangible return on their investment eventually.

A word for my peers from the realm of the McGuinness Group, and its allies:

Nikos - the older brother I never had, complete with a healthy chip on his shoulder for the spoiled younger feckless eejit of a brother that makes me. Brendan Holland for his reliable South Pacific humour, impressive stature (he was the tallest, and I daresay most *gainly* of us), and for poking more or less gentle fun at my laziness. Brendan Arnold for being the affable English gentleman to bear the brunt of my post-colonial conversational pranks and for being such an all-round brick in indulging my inclinations for impromptu celebrations of obscure Saints' days (Saint David the Apostle of Wales's feast day being particularly looked forward to for its special and rather intricate dinner...Saint Molaise the Unpronounceable of Inishmurray, rather less so) and for being history's most easygoing housemate at 17 Lombard Street East. Declan, on the one hand for lending a responsive ear to my interminable blather, and at other times for leavening my brooding temperament and natural tendency for a poisonous cynicism towards anything not from Sligo; also for everything from singsongs to speaking *as gaeilge* that kept my spirits up at synchrotrons, and for correcting my bibliography when I couldn't face it. Daniel my cultured friend, who's wedding at harvest time in Manhattan is one of the ultimate (loose leaf) Barry's tea *Golden Moments* and who shared with me the enjoyment of fine things, and sampling the best, and, perhaps less reputably, a bed in a hostel in San Francisco on one occasion (When in Rome...). Summer students Eleanor Nolan (XPS of Co:ZnO) and Al Grogan (Calculated polarization dependent O K-edge RXES of TiO_2) also have a well-earned place within these pages. Finally the larger surface group of Karsten, Chris, John C, Niall, Lena *et al.* deserve humourous mention for their *banterful* ways and the workaday give and take that we all chipped into.

My eternal gratitude to the Guinness Brewery for the indescribably ambrosian incense with which it sanctifies the grey granite doorsteps of Dublin. Manys and manys the time it has wafted me to a reverie, carried thither and yon on the quickening zephyrs with which Trinity College exhales the soft airs of its centuries of youth. A spouse and midwife to scholarship and fluency, long may it stand at St. James's Gate. Also, BBC world service was a comfort to me during the darkest hours. Literally. One of the results of my PhD is that I can recite the points of reference from the 1am shipping forecast from memory.

A word for the School:

Prof James Lunney: his tenure as head of school coincided with most of my PhD and he was always great fun, approachable and talkative. Dr Colm Stephens for sharing my political leanings and helping to create a continuity in the uniquely understatedly positive atmosphere of the school. Prof Stefano Sanvito and Dr Mauro Ferreira who were the directors of graduate studies during my time and were very gracious and kind when I felt like a meddle or was in a muddle. John Kelly, our Chief, as everyone knows is a brilliant character. I would like to acknowledge his friendly slagging as absolutely top drawer and just the tonic, now much missed in my daily life. When I needed a firm hand, he provided that too. And I suppose if I am remembered at all within the School of Physics, it will be for that incident. Jeanette Cummins, Rebecca Owens and Robbie Gallagher were infinitely tolerant and accommodating when it came to the bureaucratic necessities that I invariably put off til past the day of reckoning. The School of Physics in general during my time there was so clearly brimming at a flood-tide line of expectation and brilliance, and the quality of the hospitality that was afforded to us all honoured the lofty and liberal standards of its ancient foundation. I hope that in years to come, when the humour is on us we will look back and say

> "Happy are We who made hay when the sun shone"

and

> "Bliss was it in that dawn to be alive, But to be young was very heaven!"

though, perhaps there would want to be more than the humour on us to carry on like that.

A word for my science friends: ("nothing is ever lost, or can be lost, my science friends") Dr Friedrich Wetterling (P'doc. Mannheim, Germany), and Dr Luiz Felipe Periera (P'doc. Mainz, Germany) who were great and high-spirited friends to me, and who leave very precious memories, especially of weekends spent in Sligo; cycling home from a party in the late, regretted Bolton Hall at daybreak in the high summer; and feasting on oysters in Howth. (See above re. generous terms).

Finally, and closest to home, no one who knows me would take umbridge when I name my friends of longest standing. The men in my life who have been my real teachers: Dr. Patrick Egan (Sligo and Gaithersburg, MD), and his brother Dr. Brendan Egan (Sligo and University College, Dublin) for the glorious ease and natural affinity we enjoy between us now in our adult lives was worth the turmoil of youth and young manhood; Dr. Neil T. Clancy (Waterford and Imperial College, London) my stalwart lab-mate, erstwhile house-mate, sometime play-mate and alltime best-mate; and Thomas Russell (Tipperary and Sandymount, Dublin), a gentleman of whom, more anon. How dully different life would have been had I not chanced upon such rare characters. Yeats said it more succinctly than I have wanted to:

> "Think where man's glory most begins and ends,
> And say my glory was I had such friends."

Rutile-type transition-metal oxides are extremely fertile areas of study both for fundamental and technological reasons due to the range of physical properties they present, such as insulating TiO_2, semiconducting SnO_2 and metallic RuO_2. The chemical bonding of such rutile-type oxides is assumed to have an essentially ionic character despite differences in the outer electronic structures of the cations, from empty outer shell (Ti^{4+}), to partially filled (Ru^{4+}) to filled (Sn^{4+}), but has been shown to become progressively more covalent, and details of their electronic structure are still under intense experimental study and theoretical consideration. To this end, resonant x-ray absorption and emission spectroscopy (RXES) provides a sensitive element-specific and symmetry-selective probe of the unoccupied and occupied electronic bandstructure of these materials.

In this study, a combination of the natural linear dichroism of the rutile crystal structure, and the symmetry-selectivity of the resonant soft x-ray absorption and emission spectroscopies at the O K-edge were exploited to probe the O $2p$ partial density of states projections on the crystalline a and c axes, and hence to observe varations in the π- and σ-like metal-oxygen bonding in three chosen bulk crystal rutile-type oxides: SnO_2, RuO_2 and TiO_2. The character of the O sp^2 $2p_y$ orbital oriented perpendicular to the plane containing the three metal cations that coordinate each oxygen anion in the rutile structure (referred to as a M_3O plane) is a matter of particular interest. It can be used to corroborate the molecular-orbital scheme of bonding in rutile oxides that has been suggested, by comparing symmetry-selectrd experimental spectra with calculated projected O $2p$ partial densities of states and simulated RXES. It is in this fashion that we show the symmetry-selective, polarization-dependent RXES can be modelled completely through density functional theory methods, and is done so here specifically through the WIEN2K code, and the bonding arrangements of the O $2p_y$ orbital in particular can be studied for different rutile species.

The bonding implications for the same structural motif of M_3O planes in a different crystal structure, namely anatase TiO_2 are investigated via experimental and simulated RXES based on calculated electronic structures. O K-edge RXES is also applied to a nanostructured anatase TiO_2 system, and the results are interpreted with reference to the results of the polarization-dependent study of bulk single crystal anatase TiO_2.

Some of the most promising host candidate materials for dilute magnetic semiconductors are also rutile oxides, TiO_2 and SnO_2 being prominent among them. We report on the results of our O K-edge and Co L-edge RXES study of dilute magnetic semiconducting Co-doped ZnO epitaxial films produced by pulsed laser deposition from a solid target and metallo-organic chemical vapour deposition. We indentify possible spectroscopic fingerprints of metallic Co and oxygen vacancy defects in the films.

I, the undersigned, make the following declarations regarding this thesis:

1. that this thesis has not been submitted as an exercise for a degree to Trinity College Dublin or any other university
2. that this thesis is entirely my own work, with the exception of the assistance noted in the acknowledgements
3. that the library of Trinity College Dublin may lend or copy this thesis on request

signed: Brian Kennedy 14 February 2011

Contents

List of Figures

Chapter 1

Introduction

The spectroscopic investigation described in this thesis arose from an original objective to study the electronic structure of dilute magnetic semiconductor materials. Initially Co doped ZnO, and SnO_2 doped with Co, Fe and Mn were selected for study in an element specific and symmetry selective fashion using soft x-ray emission, absorption and photoelectron spectroscopy at the O K and metal L edges. Among the most promising host oxides for dilute magnetic semiconductors, it so happens that TiO_2 and SnO_2 form rutile-type crystal structures where each metal cation is octahedrally coordinated by oxygen ligands and a trigonal planar arrangement of metal cations forms around each ligand. Aside from their use in dilute magnetic semiconductors, rutile-type oxides posses a range of electronic properties and their rôle in technological applications continues to evolve.

In each case above, it was necessary to study the undoped host oxides ZnO and SnO_2 in order to contrast the influence of the dopants on the electronic structure. Also, in relation to the field of dilute magnetic semiconducting materials there are strong suggestions that additional states introduced to the electronic structure by the presence of defect impurities in the dilute magnetic semiconducting hosts play important roles in the mediation of the spin order reported in such systems. Spectroscopic measurements of the electronic structure of such doped oxides are also required, and new approaches to the study of the electronic structure in rutile-like oxides are reported in the present thesis.

It was then established that the rutile-type oxides ought to be particularly amenable to polarization-dependent x-ray absorption and emission at the oxygen K-edge, due to the natural linear dichroism caused by the highly anisotropic charge distribution and ordered planes of metal-oxygen (M-O) bonds present in the system. This is caused by the combination of σ and π bonds between metal and oxygen atoms in the rutile structure, where the σ bonds are formed by metal d and oxygen sp^2 hybridized orbitals that overlap along the internuclear axes and the π bonds are formed by orbtials perpendicular to the internuclear axes. Of particular interest, and also of relevance to the present and future functionalities of these rutile oxides, is a clear understanding of the role played by the O $2p_y$ orbital that is oriented perpendicular to the M_3O trigonal plane in the rutile bonding. These orbitals are expected to be largely nonbonding in TiO_2 with its formal valence implying a d^0 occupancy. The filling and consequent lowering in energy of the d levels should lead to a greater tendency for these orbitals to hybridize and become occupied, as in the case of RuO_2, whereas the completely filled d levels expected in SnO_2 suggest a likely return to a TiO_2 - like isolated character of the O $2p_y$ orbitals. The hybridization between the O $2p_y$ and d orbitals is intimately linked to the variety of electronic structures presented by the rutile transition metal oxides, and a polarization dependent soft x-ray spectroscopic study at the O K - edge has unique strengths in characterizing the behaviour of these orbitals.

An apparatus was available at beamline I511-3 of the Max II synchrotron in MAXlab, Lund, Sweden that allowed the scattering axis to be rotated to measure an out-of-plane scattering geometry, and combined with the more conventional in-plane measurements that were possible there and at the other synchrotrons used, it was possible to attempt a complete polarization-dependent study in the fashion envisaged. To our knowledge the effects of this natural dichroism on the x-ray absorption and emission at the O K edge have not been reported until now.

Furthermore, the polarization-dependent features in the potential dilute magnetic semiconducting host materials, SnO_2 and TiO_2, requires a thorough presentation, lest the effects of the natural dichroism be overlooked in the interpretation of spectra in favour of impurities or other speculated sources of variation between experimental measurements. This baseline study will be helpful in this regard.

Thus over the course of this research, the spectroscopic study of the $3d$ transition metal doped dilute magnetic semiconductor systems at the O K and Co L edges took a lesser role to the polarization-dependent investigation of the O $2p$ partial density of states in the conduction and valence band of the undoped rutile oxides, where RuO_2 was also studied.

The scientific discourse on dilute magnetic semiconductors has been strongly influenced by a combination of theoretically modelled mechanisms for the alignment of dilute spins in semiconducting materials at room temperatures, and the electronic structure calculations that have been interpreted with respect to one or other of such proposed models. Experimental measurements of the electronic structure of these systems is also much called for as a mechanism to probe the calculated electronic structures and verify their consistency with the experimental materials. In this thesis the results of resonant x-ray spectroscopy at metal L-edges and oxygen K-edges in Co doped ZnO (as an exemplary dilute magnetic semiconducting material), are presented and interpreted.

The aims of the experiments described in this thesis are summarized under the following six headings:

1. To use a combination of symmetry selectivity and polarization dependence in core level x-ray absorption and particularly resonant x-ray emission spectroscopies (RXES) at the oxygen anion K-edge to explore the electronic structure of transition metal oxides.

2. To observe the natural linear dichroism found at the oxygen anion K edge in rutile transition metal oxides and exploit this through RXES in order to gain an effective experimental measure of the state-specific anion partial density of states associated with the oxygen $2p$ component of the various metal-oxygen σ-like and π-like molecular orbitals.

3. To investigate whether these experimental RXES measurements can be effectively simulated by appropriate k-selective, spatially-selective and energy-selective calculations of the RXES spectra from these compounds within a DFT approach.

4. To explore the variation in electronic structure and spectra between a number of single crystal rutile transition metal oxides with various d shell fillings. This is the first step towards a more comprehensive and systematic exploration of the electronic structure of rutile transition metal oxides with regard to the progressive filling of their d shells.

5. To apply these techniques to similar transition metal oxides, in particular those with the same structural motif, *i.e.* Ti_3O planes. To this end, anatase TiO_2 was studied, where the local configuration is much changed not simply due to the bond-lengths and bond-angles in the Ti_3O plane.

6. To utilize the knowledge gained by the means outlined above, to study the electronic structure of selected transition metal oxides when they are adapted to provide important applications. The electronic structure of nanostructured

aggregates of anatase TiO_2, which have shown high rates of photocatalytic activity and were available through a collaboration were included in the study for this reason. As described previously, the electronic structure of a dilute transition metal doped semiconductor oxide, Co doped ZnO, was extensively studied to locate spectral features attributable to the metal dopant and other impurities on the electronic structure of the system.

From this point, the thesis is arranged into six chapters, set out by material studied rather than chronological order of precedence.

Chapter 2 contains a description of the forms of x-ray spectroscopy used in these experiments, the methods and apparatus employed in the spectroscopy and a discussion of the particular characteristics of soft x-ray scattering that govern the polarization dependent study of dichroic materials.

Chapter 3 introduces the details of the rutile crystal structure, which is common to the three examples investigated in the present study (TiO_2, RuO_2 and SnO_2), as well as the density functional theory calculations of the element, symmetry and spatially selected density of states and simulated resonant x-ray emission spectra presented in the thesis for these rutile materials.

Chapter 4 is the first chapter that presents and discusses results of the spectroscopic study, concerning the experiments that were performed on bulk single crystal SnO_2.

Chapters 5 and 6 continue the presentation of results from the undoped rutile oxides with the polarization dependent studies of RuO_2 and TiO_2 respectively. Chapter 6 includes the polarization dependent study of bulk rutile and anatase TiO_2 and the O K edge absorption and emission spectroscopy performed on anatase TiO_2 nanosheets.

Chapter 7 is assigned to the discussion of Co doped ZnO as a dilute magnetic semiconductor, and the results of our x-ray absorption, emission and photoelectron spectroscopic studies of its electronic structure at the O K and Co L edges.

The final chapter contains a summary of the results of the investigations undertaken and the conclusions the author has formed from them. There is also a discussion of the work that is continuing to exploit the polarization dependent soft x-ray spectroscopy techniques in rutile-type oxides and fluorides. Some supplementary information is contained in an appendix.

Chapter 2

Soft X-ray Emission Techniques and Synchrotron Radiation

Soft x-ray spectroscopy refers to a family of techniques that includes the core level x-ray absorption spectroscopy (XAS) and x-ray emission spectroscopy (XES) and the x-ray photoelectron spectroscopy (XPS) used in this thesis. All of these techniques exploit the interaction of soft x-rays and bound electrons, and are used here to study the electronic structure of selected transition metal oxide systems. This chapter describes these three forms of x-ray spectroscopy, two of which XAS, and XES, typically use synchrotron sources. The general principles of the synchrotron and its components are also described as well as the particular beamlines where the experiments reported here were conducted. To begin with, the various spectroscopic techniques used can be distinguished from each other in terms of their *modus operandi* and the information that they provide.

Both XAS and XPS are techniques that create a hole in an occupied level, usually a core level in the former, both core and valence levels in the latter. X-ray and Auger emission spectroscopy arise from the decay of the core or valence hole excited state. As described further below, x-ray absorption is a technique that like inverse photoelectron spectroscopy and electron energy loss spectroscopy ultimately yields information about the unoccupied states in the conduction band of the system. X-ray and ultraviolet photoelectron spectroscopy and x-ray emission spectroscopy are used to study the occupied states, including those composing the valence band.

The well-defined and separated energies of the core levels in different elements usually allows the core level spectroscopies to probe the electronic structure of materials element by element. The elemental selectivity of the contributions to the valence levels encourages the use of core level spectroscopy to identify changes in the electronic structure of a material by doping or structural effects.

The fact that a core level electron is used in all the spectroscopies mentioned in this chapter makes each technique a local probe of the electronic structure due to the localized nature of the core electrons. To to a greater or lesser extent the valence and conduction band states will have a non-localized character, but the excitation and decay of core holes yields a projection of those unoccupied and occupied states respectively onto a localized site. The information yielded will thus be specific to the location of the core hole, and the nature of the spectroscopy.

2.1 X-ray Absorption Spectroscopy

The binding energy of the K- shell and L- shell electrons in these oxygen and the transition metals relevant to the present study fall within the region of the spectrum designated as soft x-rays. For example this region of the spectrum between100 and 1000 eV contains K- shell absorption edges between carbon at $\sim$ 284 eV and oxygen at $\sim$ 530 eV, and L-shell absorption edges between silicon at $\sim$ 100 eV and copper at $\sim$ 930 eV. Where a tunable source of soft x-rays is available a core level electron from such an atomic-like orbital can be used to probe the unoccupied states above the highest occupied molecular orbital in a molecular system or the Fermi level in a crystalline solid. The absorption of an x-ray photon of sufficient energy will promote the core level electron into one of these unoccupied states.

The transition rate at which a core electron is excited by a photon of a particular energy into an unoccupied state within the solid is governed essentially by Fermi's Golden Rule (defined in equation 2.3) and thus by the electric dipole interaction, the radial and spatial overlap between the core electron and unoccupied state, the relative orientation of the polarization of the incoming light and the unoccupied states and of course on the final density of states. Thus controlling the excitation energy and polarization and measuring the relative transition rate yields information about the electronic structure of the interrogated system. This provides a basic description of the process of soft x-ray absorption spectroscopy around a core level transition.

Figure 2.1 shows a sketch of this process with some additional detail regarding the regions of the conduction band that will be used to describe some of the other selection rules governing the transition rate which vary in the type of information they provide on the unoccupied density of states in a system. While X-ray absorption spectroscopy refers to the general process described, different titles have gained currency as the field developed, such as NEXAFS which is used interchangeably with XAS throughout this thesis. NEXAFS stands for Near Edge X-ray Absorption Fine Structure, which as the title indicates, probes states within $\sim 50\,\mathrm{eV}$ of the absorption threshold. Another distinguishing acronym used in XAS is XANES which also refers to near edge structure but typically is used by the hard x-ray community.

For the K absorption edge in light elements such as oxygen, it is the unoccupied density of states that contributes the most dominant component to the shape of the transition rate as a function of the incident photon energy (otherwise the *absorption cross section*) that is referred to in the most general sense as an X-ray Absorption Spectrum. For L- and other absorption edges, the spectrum has a more complicated relationship with the partial density of states in the conduction band, particularly with the presence of crystal field multiplet effects and the spin orbit interaction on the core level electron leading to a superposition of features on the partial density of states.

There are comprehensive introductions to x-ray absorption spectroscopy contained in Stöhr's *NEXAFS* [12] and Kotani and de Groot's *Core Level Spectroscopies* [13], to both of which the description included in this chapter owes much.

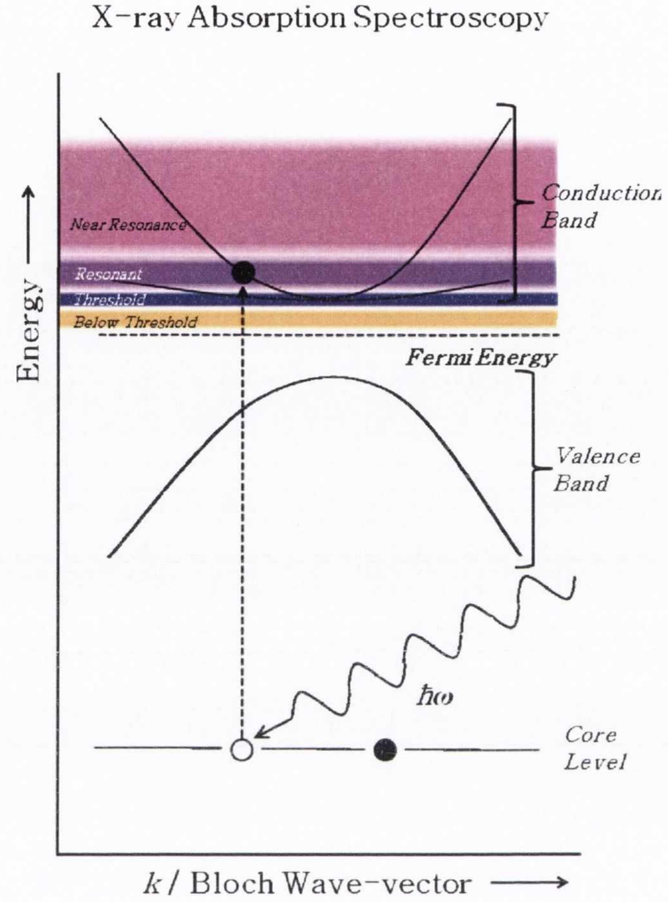

Figure 2.1: X-ray Absorption: A diagram showing the transition by a core level electron to a state in the conduction band, withing the bandstructure of a crystalline semiconductor upon absorption of an x-ray photon, $\hbar\omega$.

2.1.1 The absorption cross section and the golden rule

Further to the element and site specific nature of x-ray absorption spectroscopy qualitatively described in the previous section, the two remaining parameters that characterize the absorption process require a lengthier justification.

The first of these is the dipole approximation that is employed in soft x-ray absorption spectroscopy. The result of this approximation is the dipole selection rule for the change in orbital angular momentum quantum number, stated as $\triangle l = \pm 1$ in a given single-electron transition. This adds a further symmetry-selective dimension to the local and site specific nature of the soft x-ray absorption or emission process, as a dipole transition will select an unoccupied p orbital for the excitation of an electron from an s orbital. As well as the symmetry selectivity introduced by the dipole selection rule, the absorption cross section is also polarization dependent.

Where the valence states are formed by combinations of orbitals resulting in a non-spherically symmetric spatial orientation, the absorption cross section for excitation into a certain valence state is proportional to the angle between the bond axis and the polarization vector of the incident electromagnetic radiation. Ranging from zero at a 90° orientation to maximum absorption for a mutually parallel orientation, this dependence will also be justified by considering the theory of x-ray absorption in more detail.

The description of the absorption process begins by considering the effect an electromagnetic field has on the behaviour of a bound electron. The vector potential of the electromagnetic field may be written in terms of creation creation and annihilation operators $a^{\dagger}_{\mathrm{k}\alpha}$ and $a_{\mathrm{k}\alpha}$ as

$$\mathbf{A}(\vec{\mathbf{r}}) = \hat{\mathbf{q}}\frac{A_0}{2}\left(a_{\mathrm{k}\alpha}\mathrm{e}^{\mathrm{i}(\tilde{\mathbf{k}}\cdot\tilde{\mathbf{r}})} + a^{\dagger}_{\mathrm{k}\alpha}\mathrm{e}^{-\mathrm{i}(\tilde{\mathbf{k}}\cdot\tilde{\mathbf{r}})}\right) \tag{2.1}$$

where $\hat{\mathbf{q}}$ is a unit vector in the direction of the electric field of the wave. The creation operator $a^{\dagger}_{\mathrm{k}\alpha}$ adds a photon of wavevector k and polarization α to the radiation field, and the annihilation operator $a_{\mathrm{k}\alpha}$ removes one.

The excitation of a bound electron by a photon is treated theoretically by considering that the transition is induced by the vector potential of the electromagnetic wave $\mathbf{A}$ operating on the momentum of the electron $\mathbf{p}$ via the interaction Hamiltonian H_{int}. The interaction Hamiltonian between the electromagnetic wave and the bound electron is written as

$$H_{int} = \frac{e}{2m_e c}\sum_i\left(2\mathbf{A}(\vec{\mathbf{r}})\cdot\mathbf{p}_i + \frac{e}{c}\mathbf{A}(\tilde{\mathbf{r}})\cdot\mathbf{A}(\vec{\mathbf{r}})\right) \tag{2.2}$$

For a single absorption event, where the number of photons decreases by one, only the $\mathbf{p}\cdot\mathbf{A}$ terms contribute to the interaction Hamiltonian, giving

$$H_{int} = \frac{e}{m_e c}\mathbf{A}(\vec{\mathbf{r}})\cdot\mathbf{p}$$

where $\sum_i \mathbf{p}_i$ has been replaced by $\mathbf{p}$.

Using this form of the interaction Hamiltonian, the transition probability between initial state $|\psi_i\rangle$ and final state $|\psi_f\rangle$ by the absorption (annihilation) of a photon -

Fermi's Golden Rule - can be written in the following form

$$\begin{aligned} w_{i\to f} &= \frac{2\pi}{\hbar}\left|\langle\psi_f\left|H_{int}\right|\psi_i\rangle\right|^2 \rho(E)\delta\left(E_f - E_i - \hbar\omega\right) \\ &= \frac{2\pi}{\hbar}\left|\left\langle\psi_f\left|\frac{eA_0}{2m_e c}\mathrm{e}^{\mathrm{i}(\tilde{\mathbf{k}}\cdot\tilde{\mathbf{r}})}\mathbf{q}\cdot\mathbf{p}\right|\psi_i\right\rangle\right|^2 \rho(E)\delta\left(\ldots\right) \\ &= \frac{\pi e^2 A_0^2}{2\hbar m_e^2 c^2}\left|\langle\psi_f\left|(1+\mathrm{i}(\mathbf{k}\cdot\mathbf{r})+\cdots)(\mathbf{q}\cdot\mathbf{p})\right|\psi_i\rangle\right|^2 \rho(E)\delta\left(\ldots\right) \end{aligned} \tag{2.3}$$

where $\rho(E)$ denotes the density of final states and the delta function in the first equation applies conservation of energy to the absorption process. The delta function is abbreviated in the subsequent iterations for convenience. The Golden Rule in its final form illustrates the origins of both the dipole approximation and the polarization dependence of the absorption transition, as explained in the following paragraphs.

Firstly, the dipole approximation arises from the expansion of the relevant terms in the Taylor expansion of exponential factor $\mathrm{e}^{\mathrm{i}(\tilde{\mathbf{k}}\cdot\tilde{\mathbf{r}})}$ in the interaction Hamiltonian matrix element in equation 2.3. As the wavelength of the soft x-rays is $20-30$ times greater than the extent of the core level electron's orbital, $\mathrm{e}^{\mathrm{i}(\tilde{\mathbf{k}}\cdot\tilde{\mathbf{r}})} \to 1$, and only the first term of the expansion in the squared matrix element is retained. The next term in the expansion is the electric quadrupole operator, the effects of which are not included in the present consideration.

As the amplitude of a dipole transition is given by $\langle\psi_f|\,\mathbf{q}\cdot\mathbf{p}\,|\psi_i\rangle = \int \psi_f(\mathbf{q}\cdot\mathbf{p})\psi_i dr^3$, the integrand must be symmetric for the integral to have a non-zero result. The dipole operator $\mathbf{q}\cdot\mathbf{p}$ is antisymmetric, so by the symmetry product rules ψ_f and ψ_i must be of opposite symmetry for the transition to have a non-zero amplitude. Therefore transitions between orbitals of the same symmetry *i.e.* $s \to s$ or $s \to d$ are dipole forbidden while $s \to p$ and $p \to s$ or d are dipole allowed. This selection rule can also be expressed in terms of the orbital angular momentum quantum number $\Delta l = \pm 1$ for dipole transitions.

The polarization dependence of the absorption transition is introduced by the $\mathbf{q}\cdot\mathbf{p}$ form of the interaction matrix element that obviously, as an inner product, will oscillate with the angle between the direction of the electric field vector $\mathbf{q}$ and the momentum vector of the state involved in the transition $\mathbf{p}$. This quality or linear dichroism in soft x-ray absorption spectroscopy is very useful for determining the orientation of ordered molecules and the spatial properties of adsorbates at surfaces [12]. For the spectroscopy of rutile oxides this property can be exploited by rotating the direction of the electric field vector with respect to the crystalline axes to determine which projected components of the density of states differ along each of the crystalline axes individually. In other words, any non spherical charge distribution gives rise to a measured anisotropy in the x-ray absorption process. If the origin of the charge anisotropy is due to bonding alone, rather than a combination of bonding and a magnetic interaction we speak of "natural" linear dichroism, following the convention described by Stöhr and Siegmann in reference [14].

2.1.2 The modes of measuring an absorption spectrum

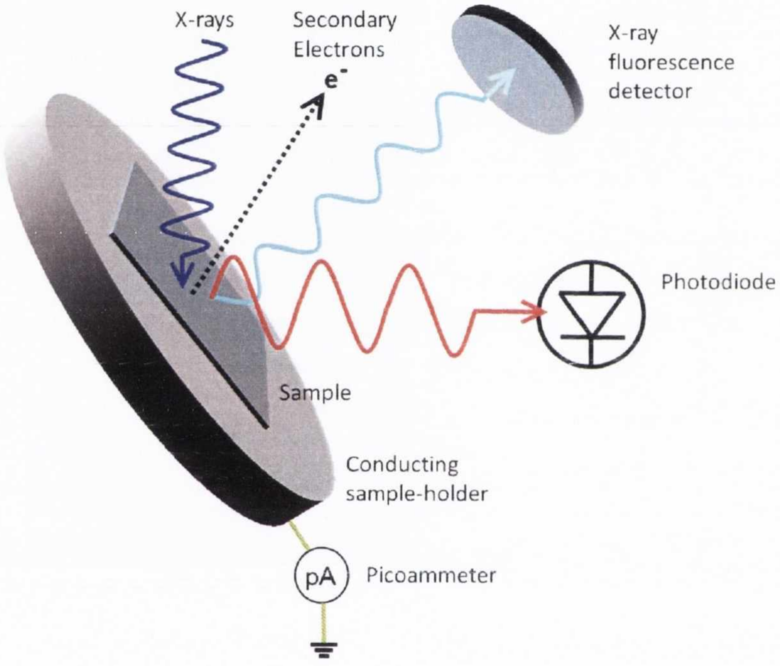

Figure 2.2: Modes of measuring the absorption cross section as a function of incoming photon energy

A NEXAFS spectrum essentially depicts the absorption cross section as a function of the energy of the incident photons. The relaxation pathways within the core excited system can be harnessed to provide various modes of measuring the absorption cross section. Non radiative relaxation of the core hole is the most likely process for soft x-ray excitation in a light element, and this process results in the ejection of an Auger electron which in turn leads to a current of secondary electrons in the material. This can be measured as the drain current of electrons from ground that replace any electrons scattered from the illuminated sample that exit its surface. This mode is referred to as the Total Electron Yield (TEY), and it is a convenient method for measuring the absorption cross section in conducting samples as the magnitude of the secondary electron induced drain current is directly proportional to the number of core holes created, which in turn is directly proportional to the absorption cross section. The shallow escape depth for an electron in a solid makes the Total Electron Yield mode sensitive to the surface region of the sample. The drain current is weaker and more susceptible to noise when a sample is insulating.

The Partial Electron Yield (PEY) measures the electrons emitted in a narrow kinetic energy range, selected with respect to the absorption edge in question such as the kinetic energy of the O KLL Auger electrons in which case it may be termed the Auger yield. The integrated number of Auger electrons reflects the number of core holes created for a particular excitation energy. An electron detector can alternately integrate the current of O $1s$ core level photoelectrons ejected for each excitation energy, though this is not possible near or on resonance as this is below the ionization potential. Unlike the Auger electrons the photoelectron will also change kinetic energy with excitation energy. These methods are very surface sensitive

Radiative relaxation, with cross sections that are as little as $\lesssim 0.7\%$ of those of the non radiative channels for the C, N and O K hole [15] provide a bulk-dominated mode of measuring a NEXAFS spectrum. The optical photoluminescence of the relaxing system can be recorded as a function of the energy of the incident radiation using a photodiode to collect emitted photons. An x-ray emission detector can also be used to record the intensity of x-rays emitted during core hole relaxation, and this is referred to as the Partial Fluorescence Yield (PFY) mode. If the photodiode or channeltron in photomultiplier mode were also responsive to ultraviolet and x-ray emission as well as optical emission, then the signal recorded is termed the total fluorescence yield (TFY).

The radiative modes are most suitable for measuring NEXAFS from insulating samples, due to the difficulty in grounding the surface of the insulator. The observed effects of the core hole in the final state on the electrostatics of the excited atom can vary depending on the states in the conduction band that are populated by the absorption. The detectors must have a clear line of sight to the sample under investigation in order to gather a useful signal, and in practice this can limit the angles of incidence at which NEXAFS spectra can be measured in the radiative modes depending on the other instruments used. In practice, it is desirable to record NEXAFS using all of the modes described.

The variable intensity of the flux of photons across an energy range selected for a NEXAFS experiment as well as the beam instability due to current drops and decay demands that the absorption cross sections recorded are normalized to the incident photon intensity. The major sources of the variable intensity are the characteristic undulator spectrum and the absorption of photons at certain resonances by contaminated beamline optics, mostly by hydrocarbons leading to sinks in intensity within carbon and oxygen energy windows. The method employed for measuring the incident photon intensity throughout the experiments performed for this thesis was to place a highly transmitting Au plated mesh in the path of the beam between the undulator and the sample, and to normalize the absorption cross section measured by each of the relevant modes to this intensity, which itself was typically measured by TEY in a drain current mode.

Although in the present thesis the O K - edge NEXAFS spectra are compared directly with calculated partial densities of states, in practice the dynamic interaction of the core hole and the valence electrons can form a core-hole exciton which depends on the character of the states populated in the conduction band [16]. The modified crystal potential surrounding the core hole causes a shift to lower energy of features in the NEXAFS spectra when compared to the total density of states measured in bremsstrahlung isochromatic spectroscopy for example. Changes in the relative amplitude of the features in experimental spectra compared to simulated spectra which do not include the core hole exactly, or at all, are also caused by the core hole potential. These effects depend on the degree of screening of the core hole by the valence electrons, which is somewhere between the static limits used to approximate soft x-ray absorption namely the "initial state approximation" or "frozen orbital approximation" where the effects of the core hole are neglected and the "final state rule" where the interaction with the core-hole is specifically dealt with. As stated by von Barth and Grossmann "The [final state] rule states that, disregarding the singular Fermi edges, accurate x-ray emission and absorption spectra of simple metals may be obtained from ordinary one-electron theory provided the relevant dipole matrix elements are calculated from valence wave functions obtained in the potential of the final state of the x-ray process, i.e. a potential reflecting the fully screened core hole in absorption but not in emission" [16].

2.2 X-ray Photoelectron Spectroscopy

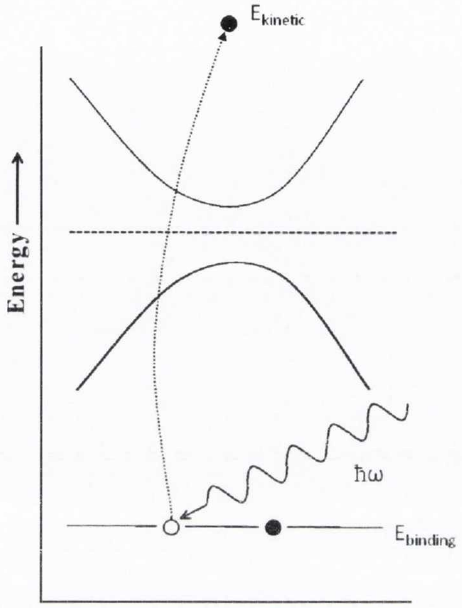

Figure 2.3: A simplified picture of core level x-ray photoelectron spectroscopy in a solid, showing a core electron ionized with a remaining kinetic energy from the incoming photon $\hbar\omega$.

X-ray photoelectron spectroscopy is a complementary spectroscopic technique that also functions by the creation of holes in occupied electronic energy levels. Where it is performed with varying excitation energies selected to enhance the absorption of certain occupied states at or near core level absorption thresholds it is referred to as resonant photoelectron spectroscopy. The photon energy may also be varied in order to enhance the surface sensitivity of the photoemission due to the varying inelastic mean free path, or the response from differing atomic orbitals due to varying photoionization cross sections.

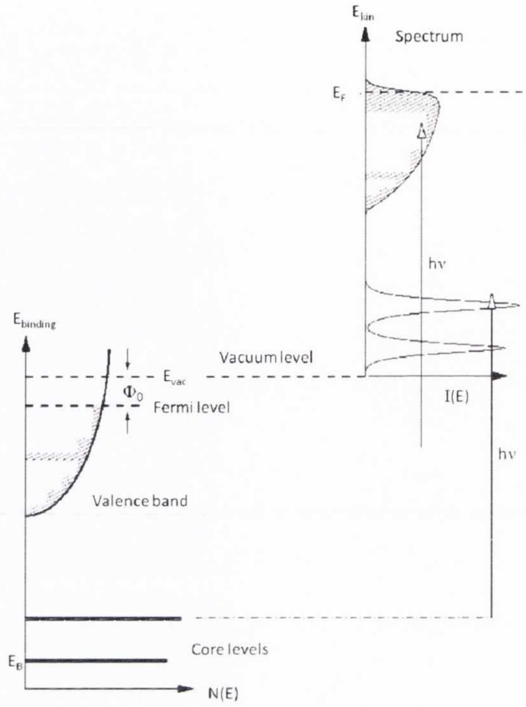

Figure 2.4: A more detailed schematic view of the photoemission process from Hüfner's textbook [1] with the binding energies of the occupied levels labeled E_B, the energy of the exciting photon $h\nu$, the kinetic energy of the ionized electron E_{kin} and the work function of the material's surface Φ_0.

The core-level and valence band XPS reported in this thesis were recorded using a monochromated conventional rotating anode source, and a hemispherical analyzer. X-ray photoelectron spectroscopy using conventional target sources became the dominant technique for measuring the electronic structure of solids in the era before the continuously tunable synchrotron sources of x-rays. Einstein's familiar equation for the photoelectric effect is the starting point for considering the process of x-ray photoelectron spectroscopy. This may be written as

$$E_{kinetic} = \hbar\omega_{incident} - (E_{binding} + \phi)$$

where the energy of the incident photon $\hbar\omega_{incident}$ ionizes an electron from a core or valence level and leaves it in the vacuum with a kinetic energy $E_{kinetic}$ given by subtracting its binding energy and the term ϕ referred to as the work-function which is a constant energy barrier characteristic of the surface of the material. An electron spectrometer placed in the proximity of the excited sample collects the emitted electrons and disperses them by their kinetic energy (and k-vector) allowing a reconstruction of the binding energies of the levels from which the electrons have originated. This is a self-evidently powerful technique for measuring the energy and density of the occupied states of a system, which is why valence band XPS was referred to as a complementary technique to NEXAFS that probes the unoccupied states.

2.2.1 Features of X-ray Photoelectron Spectra

As the final state of the excited electron in XPS is above the ionization threshold, and represented by a plane wave, the dipole approximation does not constrain the transitions to those allowed by the orbital angular momentum of the final state as is the case for bound states. Therefore, without accounting for the fine structure of the spectra, XPS yields a non symmetry selected map of the total density of the occupied density of states as opposed to the partial density of states in the regime of the dipole approximation. Thus valence band XPS (or UPS) gives the density of states in the valence band which can be compared to the results of other x-ray or optical spectroscopies or indeed with electronic structure calculations. Angle resolved photoelectron spectroscopy is neglected in this discussion.

In practice electrons ionized from equivalent core levels in a sample can give rise to shifted peaks in the spectrum of measured kinetic energies, which may be termed apparent core level shifts. This is because their origin is not necessarily caused by actual shifts in the binding energy of the core level, but by differing degrees of core hole screening depending on the valence of the parent atom, which is sensitive to its chemical and physical environment through its outer shell electrons. Apparent shifts in core level binding energies are often registered as an asymmetry in a peak once a function fitting the photoelectron background has been subtracted from the data. Surface preparation is important to differentiate between contamination and more inherent effects. Such asymmetries are often associated with a low energy excitation such as a plasmon, reducing the kinetic energy of the outgoing photoelectron. Alternatively, charge transfer satellites or also different screening of the core hole can give rise to multiple sets of peaks for the same site and are not necessarily indicative of different chemical sites. It is also important to note that, particularly for elemental semiconductors, there is likely to be observed a surface core-level shift especially where surface reconstructions occur.

The shape of the total density of states in the valence band is the most important result related to the bandstructure that can be derived from unpolarized photoelectron spectroscopy. Valence states with low binding energies typically have a low ionization cross section for soft x-ray photons, so ultraviolet radiation from a conventional source which is commonly a helium lamp providing $\sim$ 21 eV photons is most often used to study this region. UPS at differing photon energies can be very useful, particularly in exploiting delayed maxima in subshell photoionization cross sections for the transition metal $3d$ subshells where at several tens of eV above the ionization threshold the $3d$ states in the valence band will be much more prominent than with He I photon energies. Equally, resonant photoemission at the $2p-3d$ threshold can also give useful information about the distribution of $3d$ states in the valence band of a transition metal oxide.

Of particular interest to the current study are valence band widths and peak positions with which to compare the results of x-ray emission measurements, and the presence of additional densities of states in the band gap of semiconductors that may be associated with doping and impurities. Quantitative information regarding the relative concentrations of elements is also present in an x-ray photoelectron spectrum, and within a certain peak it is convenient to estimate the ratio of each of the peak's components by area when investigating the origins of an asymmetry. As with all spectroscopic measurements comparison with the results of electronic structure calculations is informative.

As well as the apparent core level shifts another important secondary feature in XPS spectra are satellite peaks caused by the scattering of the ionized electron exciting resonant transitions among the valence electrons before reaching the free state. These characteristic features are termed shake-up (or shake-off) peaks.

Insulating samples represent a difficulty for XPS and UPS as the sample can not readily compensate for the charge lost through electron ionization through a drain current from the ground. A flux of thermionically emitted electrons from a filament can be accelerated to a given low kinetic energy and directed towards the surface of the sample to provide this charge neutralization. The operating parameters of the electron source in this regard need to be determined for different samples based on the mitigation of artifacts in the photoelectron spectra caused by the sample charging. However, the relatively low kinetic energy of the electrons ionized from the valence band when an ultraviolet source is used disqualify the use of such a charge neutralization technique, as the electrons from the thermionic source in the charge neutralizer can enter the analyzer.

2.2.2 XPS experimental layout

The electrons ionized by the x-ray or ultra violet photons are collected and dispersed by a combination of electrostatic lens and an analyzer, as depicted in figure 2.5.

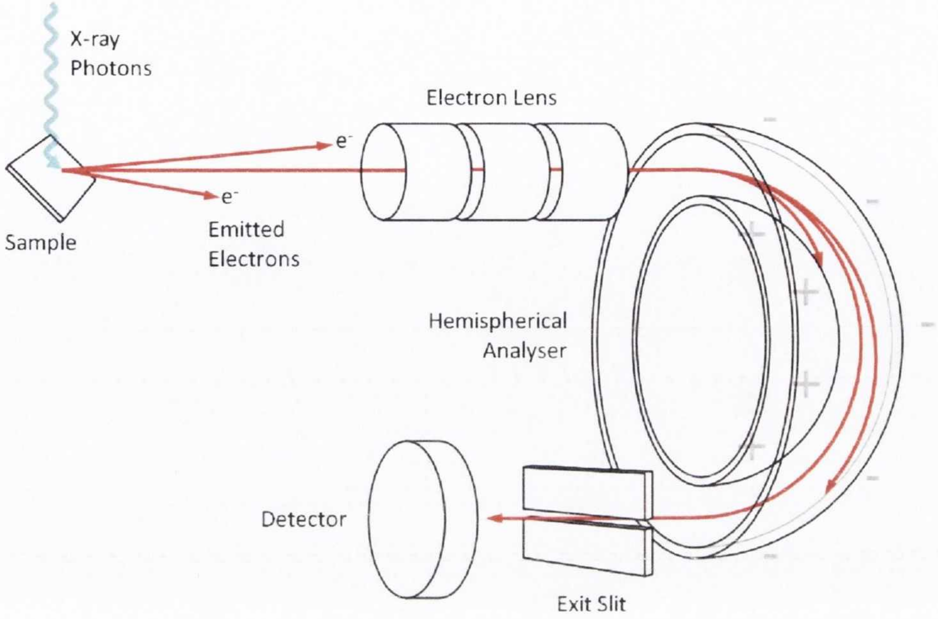

Figure 2.5: A schematic diagram of an XPS experiment showing the components of the spectrometer

The array of components referred to as the electron lens in figure 2.5 collect the emitted electrons and also provide a varying retardation or acceleration such that the electrons with a specified kinetic energy enter the hemispherical analyzer with the same terminal 'pass energy'. This is a variable property of the analyzer which is selected in a trade-off between the energy resolution and transmission of the spectrometer. The hemispherical analyzer consists of two nested concentric hemispheres with an electric field maintained between the two such that electrons entering with the set pass energy are focused to a point on the equator of the hemisphere 180° from the entrance. The electric field of the analyzer will cause electrons outside the pass energy window to collide with the inner or outer hemisphere. The spectrometer usually has an exit slit to provide further energy resolution in the measured spectrum, and the detector commonly consists of a high voltage "channeltron" electron multiplier tube.

The XPS system used to record the spectra included in this thesis, unless otherwise stated, was the Scienta ESCA300 located in the National Centre for Electron Spectroscopy and Surface Analysis at Daresbury Laboratory in Cheshire, United Kingdom. The excitation source is a monochromated rotating anode target that produces Al K_α 1486.7 eV x-rays. This hemispherical analyzer has a radius of 300 mm contributing to an overall resolution of the source and spectrometer combined of 0.3 eV , where the FWHM of the monochromated Al source is 0.26 eV.

2.3 X-ray Emission Spectroscopy

The relaxation of a core hole excited state by the emission of an x-ray photon and the simultaneous filling of the core hole forms the basis of x-ray emission spectroscopy. The radiative decay of a core hole created by soft x-ray absorption also results in the emission of a soft x-ray of similar energy if there is only one fluorescence channel available. Where a variety of initial states from which the core hole can be filled are available and a valence band electron fills the hole, then an emission spectrum is obtained through the coupling of the core hole and the valence states through that fluorescence channel. The dipole approximation also governs soft x-ray emission transitions between the valence levels and the core hole. Therefore the creation of an oxygen $1s$ core hole may lead to a radiative transition involving either an occupied state with oxygen $2p$ character, and a transition metal $2p$ hole will decay by a transition involving an occupied state of either $3d$ or $4s$ character. States of $3s$ character can also fill the $2p$ core hole in the case of a core-core transition. In fact all of the properties stated previously for soft x-ray absorption spectroscopy are present in soft x-ray emission spectroscopy *i.e.* it is "an element and symmetry selective, polarization dependent, probe of the local partial density of states", where the final state rule also applies.

As shown in figure 2.6 for low Z elements at soft x-ray energies the lifetime of the radiative relaxation is $\sim$ 1000 times longer than the non-radiative channel, as the fluorescence yield is as little as $\sim$ 0.7% [15]. A core hole excited state on an oxygen $1s$ or metal $2p$ state is most likely to decay with the emission of an Auger electron. Soft x-ray emission spectroscopy is therefore only practical at ultra-bright synchrotron sources of x-rays, with the use of efficient detectors.

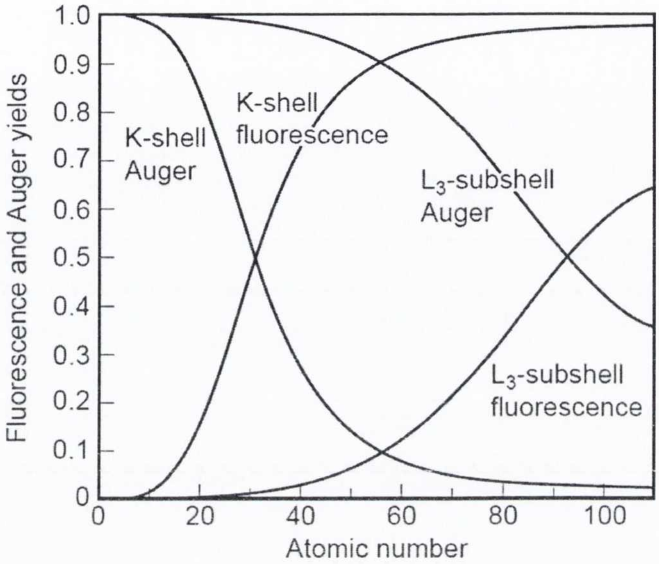

Figure 2.6: Non radiative and radiative transition rates as a function of atomic number Z from Attwood's textbook [2].

Within the umbrella of x-ray emission spectroscopy, different types of spectra exist, largely characterized by the proximity of the exciting photon energy to a 'resonance' or an absorption threshold. X-ray absorption is the first step (or first half-step) involved in the overall x-ray emission process. This is foreseen in figure 2.1 where the x-ray absorption step is sketched, and the energy regions that correspond to states at the bottom of the conduction band are given the labels used in this thesis "threshold", "resonant" and "above resonance" respectively.

It would be misleading to include a general energy scale that clearly defined the various regions, which depends on the properties of the material in question, *i.e.* whether it is a molecular system, a wide band Coulombic solid or a strongly correlated electron system. However the first 5 eV above the absorption threshold can usually be expected to fall into the "resonant" category, and the term used to describe the process of radiative excitation and de-excitation is scattering.

At excitation energies close to the absorption threshold, the presence of the excited core electron in a conduction band state can modify the band structure of the valence states. With this in mind, it is to be expected that the emission spectra close to threshold will have an element of excitation energy dependence. The situation that occurs for energies further above resonance can be described more justifiably as two step process. Such a process comprises a core hole excitation with subsequent emission by transitions between occupied valence levels and the core hole. Due to the large dispersion of the states above resonance a wider range of crystal momenta in the valence band can contribute to the emission, and the resulting spectrum integrates over all possible contributing k states. The reviews of Gel'mukhanov and Ågren [5] and Kotani and Shin [17] form the basis of the discussion of resonant soft x-ray scattering considered in this chapter. The form of the diagrams are amended from the cartoons used in the thesis of Thorsten Schmitt [18] .

2.3.1 Theoretical background of x-ray scattering

Theoretically, the process of x-ray emission is described by a transition probability that uses the interaction Hamiltonian between an electromagnetic wave and an electron, introduced in equation 2.2 as its starting point [18]. The resulting description of the scattering process follows the Kramers-Heisenberg relation, a familiar result from the quantum theory of the interaction of light and atoms. The scattering process is modeled as a differential cross section for scattering into a solid angle Ω

$$\begin{aligned}\left[\frac{d\sigma}{d\Omega d\omega_2}\right] = \sum_f \Bigg| & \frac{e^2}{2m_e c^2}\left\langle f\left|\mathbf{A_1}\cdot\mathbf{A_2}\right|i\right\rangle \\ & + \frac{e}{m_e c}\sum_{c,v}\left[\frac{\left\langle i\left|\mathbf{p_1}\cdot\mathbf{A_1}\right|m\right\rangle\left\langle m\left|\mathbf{p_2}\cdot\mathbf{A_2}\right|f\right\rangle}{E_m - E_i - \hbar\omega_1 - \frac{i\Gamma_m}{2}} + \frac{\left\langle i\left|\mathbf{p_1}\cdot\mathbf{A_1}\right|m\right\rangle\left\langle m\left|\mathbf{p_2}\cdot\mathbf{A_2}\right|f\right\rangle}{E_i - E_m + \hbar\omega_2}\right]\Bigg|^2 \\ & \times\delta\left(E_i + \hbar\omega_1 - E_f - \hbar\omega_2\right) \qquad (2.4)\end{aligned}$$

where $\mathbf{p_n}$ is the momentum vector of electron n , and $\mathbf{A_n}$ is the vector potential at electron n of the electromagnetic radiation field, with $\mathbf{p_1}\cdot\mathbf{A_1}$ acting on the core level electron exciting it to the valence state, and $\mathbf{p_2}\cdot\mathbf{A_2}$ acting on the valence electron that fills the core hole. E_i , E_m and E_f denote the energy of the initial , intermediate and final states i, m and f respectively [19, 13]. $\hbar\omega_1$ and $\hbar\omega_2$ denote the energy of the absorbed and emitted photons respectively and Γ_m denotes the lifetime of the intermediate state. The indices c and v label an initial and final state in the conduction and valence bands respectively. As previously noted, this core hole lifetime is defined by the sum of the transition rates for the radiative and non radiative decay channel.

The first term in the RHS of the equation, with the $\mathbf{A}\cdot\mathbf{A}$ matrix element, does not contribute to single photon processes and is not included in the present analysis. It describes the amplitude of the Thomson scattering of incident x-rays which is responsible for x-ray diffraction. The second and third terms summed over all intermediate levels m describe resonant and non-resonant single photon scattering processes. It can be seen that the second term dominates the scattering amplitude as $\hbar\omega_1 \rightarrow (E_m - E_i)$, which indicates the condition of resonance. The delta function represents the energy conservation of the scattering process.

The physical interpretation of the resonant and non-resonant scattering process in the Kramers Heisenberg scattering cross section, which are described by the two leftmost terms in equation 2.4 is sketched in figure 2.7. The process depicted in figure 2.7 part (i), where the core hole decays by a recombination with the excited core level electron is referred to as participator decay, and is responsible for the elastic features present in the emission spectra presented. Participator decay is greatly enhanced at threshold, especially when the conduction electron is localized to the vicinity of the intermediate core hole. The central diagram in the sketch describes the resonant inelastic scattering process, and is labeled spectator decay in the diagram. This refers to the fact that the transition between valence and core level takes place in the presence of a core level electron in a proximate conduction band state, and the relevant term in the Kramers-Heisenberg formula accounts for the dependence on the incident photon energy $\hbar\omega_1$ which represents a coupling through a variety of accessible intermediate states. The third term, which describes the non-resonant scattering process, indicates that the scattered intensities will be independent of the exciting photon energy. This term describes the scattering that dominates for excitation energies further from the absorption threshold.

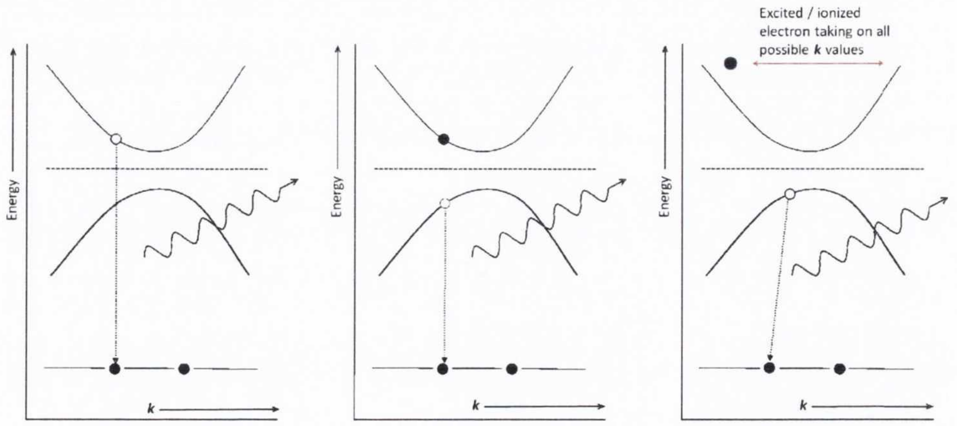

(i) Participator Decay (ii) Spectator Decay (iii) Normal X-ray Emission

Figure 2.7: Three sketches representing relevant final states in the Kramers Heisenberg single-photon scattering terms in equation 2.4 in terms of a solid bandstructure of a crystalline semiconductor

Because of the mechanisms described by equation 2.4 and figure 2.7, the interpretation of an x-ray emission spectrum must take account of the fact that these three scattering terms give rise to a number of components that can be present alongside each other. Thus an x-ray emission spectrum may include features due to elastic scattering, energy dependent features due to the resonant inelastic scattering process RIXS or also RXES, and a component that is independent of the energy of the incident photon that is referred to as non-resonant, fluorescent or normal x-ray emission (NXES) [17]. The description of the interaction of electromagnetic radiation and atoms in this chapter owes it form and arguments to the excellent discussions of the topic in Sakurai's Advanced Quantum Mechanics [20] and Corney's Atomic and Laser Spectroscopy [21].

2.3.2 The soft x-ray emission spectrometers

Two of the three soft x-ray spectrometers used to measure the emission spectra in this thesis were manufactured by Gammadata, based on designs by the Nordgren group at Uppsala University [3]. They are located at ALS Beamline 7.0.1 and Maxlab Beamline I511-3. The second type of spectrometer was the one used at ALS Beamline 8.0.1 for measuring XAS and RXES at the O K and Co L edges of Co doped ZnO. This section begins by describing the focusing principle common to both, namely the Rowland circle geometry of entrance slit, spherical gratings and detector. Most attention is given to the Nordgren-type spectrometer as it accounts for the bulk of the measurements.

2.3.2.1 Rowland circle grazing incidence soft x-ray emission spectrometers

Grazing incidence reflective optics are required to focus soft x-ray wavelengths due to the non existent normal incidence reflectivity of materials in this spectral region. The focusing of the x-rays is achieved with a Rowland circle geometry, shown in figure 2.8 where the spectrometer slit, grazing incidence spherical concave grating, and two-dimensional x-ray detector are located on a circle with a diameter equal to the radius of the spherical grating which is shown as a dashed circumference in the sketch. Along the Rowland circle the focusing condition of the slit-grating combination is satisfied [22]. The diffraction equation is then given by $m\lambda = d(\sin\alpha + \sin\beta)$.

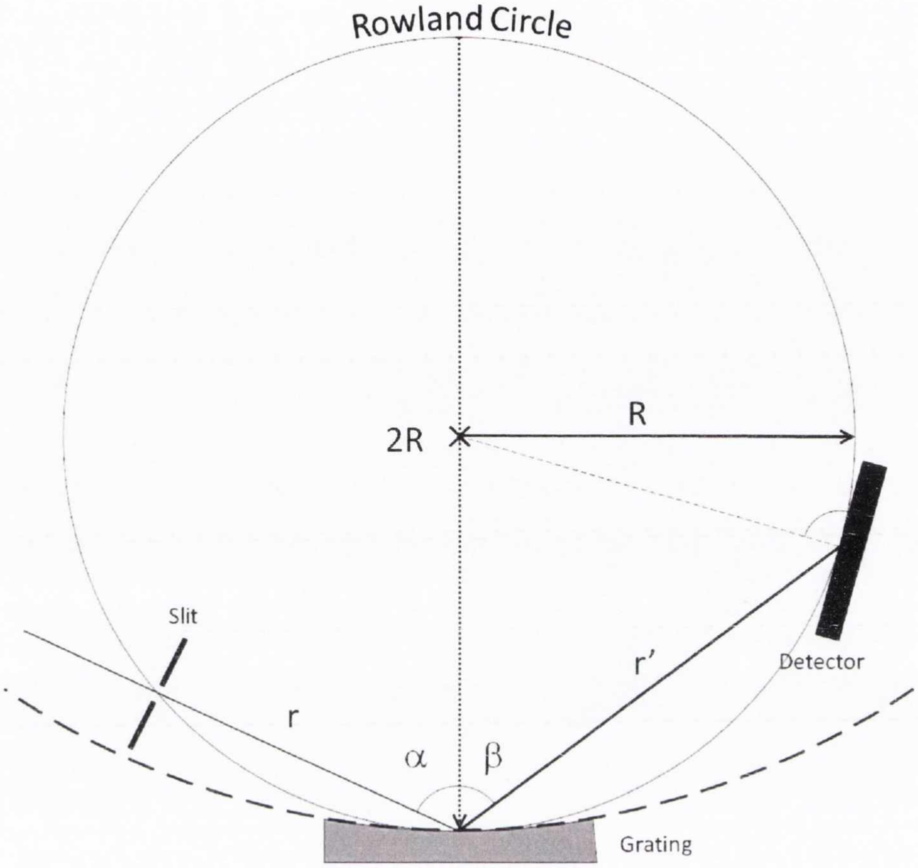

Figure 2.8: Grazing incidence rowland circle focusing geometry for a concave spherical reflection grating.

2.3.2.2 The Nordgren-type spectrometer at ALS 7.0.1 and Maxlab $I511-3$

Figure 2.9 reproduces a detailed diagram of the Nordgren-type spectrometer. Part (A) shows that there are three gratings present in the spectrometer with fixed orientations all with a groove density and blaze angle for a particular energy region. Each grating can be selected in turn by physically translating a grating selector to form an aperture that allows illumination of a single grating only.

The three gratings are oriented such that they can be illuminated independently by use of a grating selector composed of two horizontal baffles or flags. The combination of each grating and the entrance slit defines its own Rowland circle. Further, the combination of slit and grating also defines a solid angle for acceptance of emission from the sample. Where the synchrotron light intersects the surface of the sample ultimately defines the "sourcepoint" for the emission. Assuming the synchrotron beam remains fixed, as the sample moves the sourcepoint will also change its position within the chamber, with the execution of a translation of the surface plane of the sample by a displacement vector within that plane. A feature of the Nordgren design is that the optical axis of the x-ray emission spectrometer may be rotated about an axis parallel to the rulings on the gratings and typically is also parallel to the beam direction. The optical axis is defined by the path between the centre of the selected grating and the centre of the entrance slit. These optical axes are indicated for each of the three gratings in part (C) of figure 2.9. The rotation about this axis allows for the acceptance angle to be directed towards the source point where this action is referred to as "tuning", or optimizing the optical axis of the spectrometer.

The construction of the spectrometer entrance slit is of the form of two off-set knife edges, which is shown in enlarged detail in Part (C) of figure 2.9. The slit has a variable width based on its rotation in the sense indicated by the rocking arrow. This rotation gives a range of effective slit widths between closed and 120 μm, though the effective slit width differs for a particular setting due to the differing optical axes.

Each point on the spherical gratings focuses x-rays of the same wavelength to a conic section or crescent shaped profile on the planar surface of the two-dimensional detector. This is an aberration that may be corrected or straightened by offsetting adjacent slices of the detector with respect to each other in the dispersive detector direction during the processing stage. This allows the two dimensional spectrum across the detector to be converted to a normal one dimensional spectrum by summation along the non-dispersing detector direction.

On occasion for a tightly focused synchrotron beam on the sample, the size of the source point dominates over the slit size in determining the angular spread of the emission reaching the selected grating. Where the grating is underfilled, i.e. not all of the ruled surface is illuminated due to the source point not being fully within the acceptance angle of the slit, then the average angle of incidence of the emission onto the grating, α, may differ from the design value or vary with different "tunings" of the spectrometer. This can lead to an unintended shift of the emission spectrum on a stationary detector according to the diffraction equation $m\lambda = d(\sin\alpha' + \sin\beta')$ and calibration of the emission spectrum can become more difficult.

Part (A) of figure 2.9 shows the degrees of motion of the x-ray detector. It can be translated by a stepper motor or by hand in the directions X and Y to follow the Rowland circles of each of the gratings. The sense in which the detector can tilt is also indicated on the Z axis of the coordinate system. This alters the tangentiality of the detector to the Rowland circle. As the detector is flat and has a diameter of 40 mm its entire surface area cannot be in focus simultaneously. In practice it is desirable to position the detector such that its centre coincides with the centre of the energy range of interest, using well established emission lines to calibrate the detector position.

Part (B) of figure 2.9 shows a detailed cross section of the detector which is constructed from two stacks of micro-channel plate (MCP) electron multipliers in a chevron or zig-zag arrangement behind a deflector plate that is maintained at a negative potential of $\sim 1\,\mathrm{kV}$ with respect to the MCP array. The uppermost MCP in each stack is coated with a $0.3\,\mu\mathrm{m}$ layer of CsI to create a seed-shower of secondary electrons when a soft x-ray photon is incident, that is then amplified by a factor of approximately 10^8 as it cascades through the MCP stacks [23]. The deflector suppresses any secondary electrons that take off vertically from the top of the CsI layer and force them back to contribute to the electron shower associated with the arrival of a photon. The electron shower arriving at the resistive anode encoder (RAE) has its position addressed by measuring the difference in the resulting current registered for a given event at each of the corners of the RAE using a position analyzer.

The energy scale of the x-ray emission spectrometer was calibrated in either one of two ways depending on convenience. The tabulated values of the characteristic energies for the Zn $L_\alpha$and L_β x-ray emission lines were recorded from a pure Zn foil in 2^{nd} order diffraction. It was also possible to calibrate the monochromator energy using the well characterized position of the π^* absorption peak in the rutile TiO_2 O K XAS, and where sufficiently strong elastic peaks were present in the measured emission spectra the position of these were used to calibrate the energy dispersion of the spectrometer. The angle of the detector was verified by obtaining a value for the distance in channels between the Zn $L_{\alpha,\beta}$ lines from software and angling the detector until the expected dispersion is obtained at a tangent to the Rowland circle. The focus position of the detector, where it intersects the Rowland circle is obtained by moving the detector closer in or further away along the ray joining the detector and the diffraction grating, until for a given emission line the narrowest width or best focus is obtained.

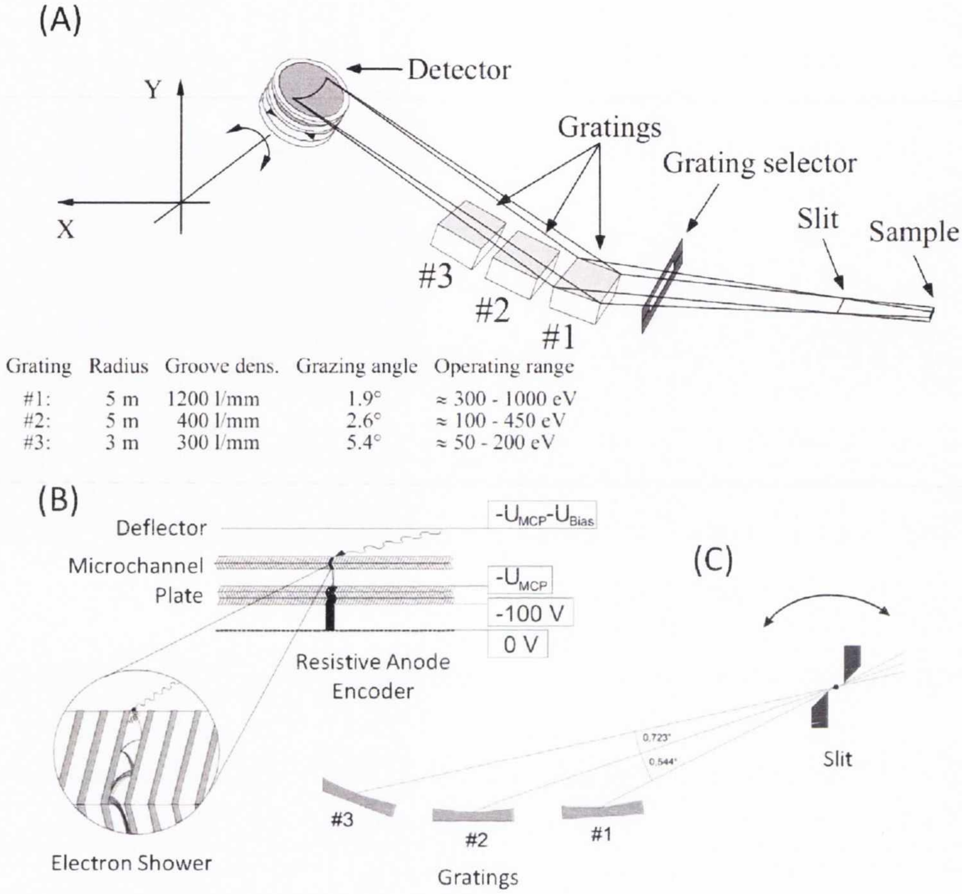

Grating	Radius	Groove dens.	Grazing angle	Operating range
#1:	5 m	1200 l/mm	1.9°	≈ 300 - 1000 eV
#2:	5 m	400 l/mm	2.6°	≈ 100 - 450 eV
#3:	3 m	300 l/mm	5.4°	≈ 50 - 200 eV

Figure 2.9: The Gammadata XES300/350 spectrometer (A) sample - slit - grating selector - gratings - detector layout (B) detail of the detector: the Deflector, MCP and Resistive Anode Encoder high voltages (C) detail of the relative orientations of the spherical gratings with respect to the slit. Diagram by Nordgren *et al.* [3].

2.3.2.3 ALS beamline 8.0.1 XES Spectrometer

The spectrometer at ALS beamline 8.0.1 is shown in figure 2.10. The plane containing the Rowland circle(s) of its spherical diffraction gratings is rotated by 90° compared to the XES300 and lies in the horizontal plane of polarization of the x-rays.

The position of the entrance slit is fixed, and is between $2 - 10$ mm of the sample depending on its thickness. The width of the entrance slit is adjusted by varying the voltage applied to a piezoelectric crystal in the slit mechanism. There is a choice of 4 spherical diffraction gratings in the spectrometer, covering an energy range from $40 - 1000$ eV. The grating used for the soft x-ray emission results presented in this thesis was the 1500 $lines/\text{mm}$ grating of 10 m radius. Similar to the XES300 the detector is a stack of MCPs 40 mm in diameter, with the first plate coated with a layer of CsI. As there is no physically relevant information relating to the sample in the vertical variation of the spectra, rows of channels in this direction are binned for more convenient handling of the data.

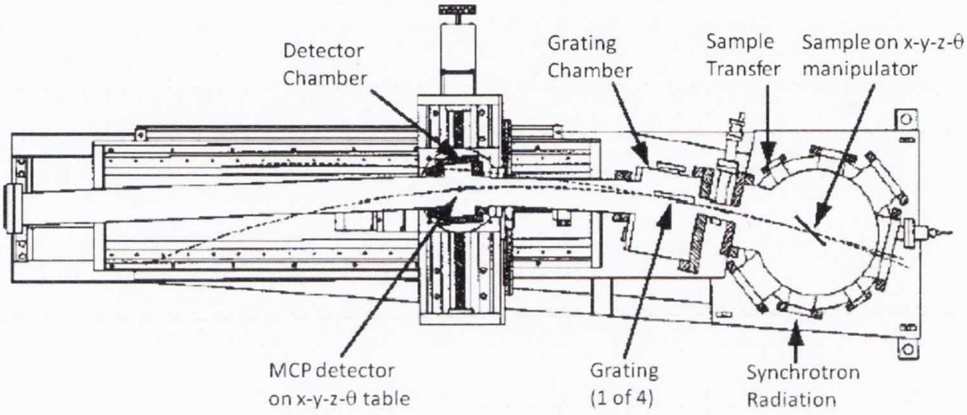

Figure 2.10: The Soft X-ray Fluorescence Spectrometer at ALS Beamline 8.0.1 [4]

2.3.3 Anisotropy of resonant x-ray scattering

The Kramers-Heisenberg equation 2.4 given earlier presents the total transition rate for RIXS but with no discussion of the angular dependence or of the detailed energy dependence in the context of solids. We introduce these topics the present section.

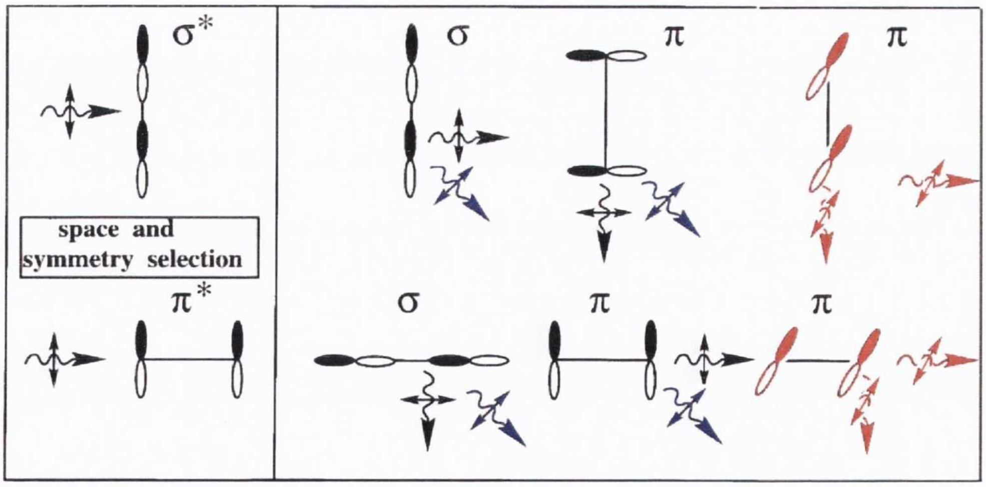

Figure 2.11: Symmetry selectivity in x-ray emission spectra due to varying spectrometer position with respect the polarization of the exciting photons. Adapted from Gel'mukhanov and Ågren, (figure 32) [5].

2.3.3.1 State selectivity in Resonant Scattering by scattering geometry

The diagram in figure 2.11 is from page 134 of Gel'mukhanov and Agren, and is intended to illustrate the state selectivity that is inherent in the x-ray scattering process involving a polarized source of x-rays and an anisotropic bonding arrangement within a molecule or solid subject to the excitation. It shows a view from above of an incident photon with a polarization vector in the plane of the page. This diagram is most appropriate when considering simple molecular orbitals formed in homogeneous or heterogeneous (homonuclear or heteronuclear) diatomic molecules which is the context in which the argument and this specific picture is developed. There are two types of bond shown in the molecule depicted in figure 2.11. The p orbitals oriented along the internuclear axis form σ bonds with the orbitals oriented perpendicular to this axis both in the plane of the page, which are black in the diagram and perpendicular to the plane of the page, which are coloured red in the diagram forming π bonds.

As mentioned in section 2.1.1 due to the inner product form of the dipole transition matrix element, the angle between the polarization vector of the electric field and the projection of the orbital angular momentum determines the strength of the absorption, with maximum cross section when the two are parallel, and minimum when they are perpendicular in a $\cos^2$ dependence due to the squared matrix element. Thus the incident photon shown in the upper half of figure 2.11 with its electric field vector aligned parallel to the internuclear axis excites a core electron into a σ^* bonded unoccupied state as shown. When the spectrometer is located in the plane of scattering and oriented such that its axis is looking along the internuclear axis, only transitions from states involved in π bonds will generate any intensity in the direction of the spectrometer. In the lower half of figure 2.11 the orientation of the internuclear axis with respect to the electric field vector of the x-rays excites an electron into the unoccupied π^* unoccupied states in the plane of the page. When the spectrometer is also in the plane of the page with its axis aligned along the electric field vector of the x-rays it will detect emission from the σ states along the internuclear axis as shown and the π bonded states perpendicular to the plane of the page as shown.

Although figure 2.11 is developed in the context of in-plane scattering only, it can be adopted for out of plane scattering geometries where the intermediate states selected give rise to different selections in the recorded emission. For example for σ^* absorption, a 90° out of plane geometry will have σ as well as π emission. Thus for the same intermediate state selected in-plane versus out-of-plane scattering differ in their contributions to the emission.

A more complex picture of anisotropic scattering due to chemical bond selectivity emerges in the case of sp^2 hybridization and particularly in rutile transition metal oxides which unlike graphite, have mutually orthogonal sets of sp^2 planes within the crystal structure. This will be discussed further in the following chapter. For the time being, it is useful to take the particular instance of graphite to explain the k-selectivity of RIXS.

2.3.3.2 Anisotropy of the elastic scattering

Though currently undulators such as UE44 at the Swiss Light Source allow the polarization of the x-ray beam to be selected between vertical, horizontal or circular, the emission spectra presented in this thesis were obtained using undulators with a fixed horizontal polarization. In this case, to observe out-of-plane scattering the emission spectrometer must be moved either by placing it on a different port on the analysis chamber, or by rotating the entire analysis chamber. Both approaches to the observation of out-of-plane scattering have been attempted, but the out-of-plane emission presented here was obtained solely at MAXlab beamline I511 which has a rotatable analysis chamber and is described in a following section. The most prominent difference between the observed scattering of the in-plane and the out-of-plane geometry is the enhanced presence of elastically scattered photons in the out-of-plane geometry. This is due to the fact that the elastic scattering results from participator decay (see figure 2.7) and the shape of the radiation field caused by this transition is similar to the $\cos^2\theta$ "donut" of the dipole oscillator, where the intensity is zero along the axis of the oscillation and maximum in the plane perpendicular to this direction. Hence the elastic scattering observed for in-plane scattering is almost entirely suppressed.

2.3.3.3 The k- selectivity of RIXS

Figure 2.12 is an adapted form of the results presented by Carlisle *et al* in a study of graphite [6]. That study demonstrated that graphite is an ideal system in which to observe the symmetry and crystal momentum selectivity of RIXS. Graphite, as a planar sp^2 hybridized system also serves as an excellent example of different states probed by altering the scattering geometry for the rutile oxides studied in this thesis.

Firstly, in panel (A) of figure 2.12 the three coloured bars from left to right highlight the regions of the electronic structure probed by the scattering of photons with energies tuned to excite core level transitions into states (i) (ii) and (iii) above the Fermi energy. The scattering resulting from these excitation energies along with a photon energy far above threshold are shown in panel (B). The geometry of the scattering is also varied, with angles of 25° and 70° between the spectrometer axis and the surface of the graphite for each incident photon energy as sketched in the upper left hand corner of panel (B). Panel (C) contains calculated emission spectra from graphite for the same incident photon energies and spectrometer axis orientations selected in the experimental measurement. The results demonstrate that RIXS is both a symmetry and crystal momentum selective technique.

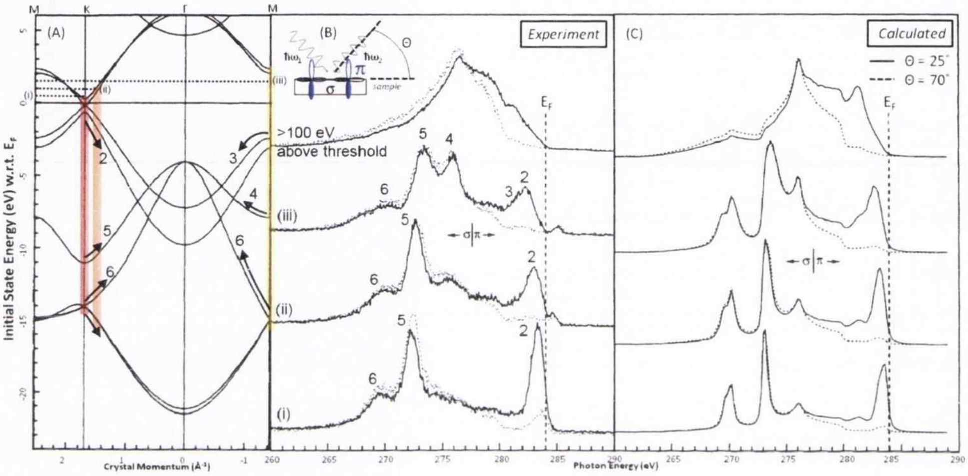

Figure 2.12: Symmetry and k - selectivity of RIXS, adapted from Carlisle's *et al* study of graphite at the C K edge [6]. Panel (A) shows depicts the calculated band structure diagram for graphite along high symmetry directions in the Brillouin zone. Panel (B) shows the emission spectra for incident photon energies associated with excitations into states (i) (ii) and (iii) as well as an incident photon energy far above threshold. The emission spectra were measured at two different spectrometer orientations with respect to the surface of the graphite sample as the sketch in panel (B) depicts. Panel (C) shows calculated emission spectra for the energies and orientations used in the experiment.

It is the features labeled 2 and 3 in the emission spectra between photon energies of 280 eV and the Fermi energy E_F that show most variation as the angle of the outgoing emission from the planar surface of the (0001) graphite sample is varied. For the grazing exit angle of 25°, states of π symmetry will be predominantly excited into as they lie perpendicular to the planes parallel to the (0001) surface. As the spectrometer axis is approaching alignment with the surface normal for this sample orientation, the emission is dominated by σ bonded occupied states. For the same reason, with a near normal angle of incidence of 75° the states excited into are σ^* in the conduction band and the emission is from π bonded states. This allows a clear distinction to be drawn spectroscopically between densities of states composed of σ and π bonding, which verifies the symmetry of the bands in the calculated electronic structure. The calculated emission spectra also show this clear suppression and enhancement of emission from the π density of states, located in the vicinity of the valence band in this planar sp^2 hybridized solid.

In resonant soft x-ray scattering the total momentum of system: the crystal momentum ($\mathbf{k}$) and that of the photons is conserved for the excitation and decay in the RIXS process. This may be formulated in the following equation

$$\mathbf{k}_{\mathbf{in}}^{\text{photon}} - \mathbf{k}_{\mathbf{out}}^{\text{photon}} = \Delta\mathbf{k}_{\mathbf{crystal}} \tag{2.5}$$

where the wave vectors of the absorbed and emitted photon are labeled $\mathbf{k}_{\mathbf{in}}$ and $\mathbf{k}_{\mathbf{out}}$, and $\Delta\mathbf{k}_{\mathbf{crystal}}$ denotes the change in the crystal momentum of the system before the excitation and after the filling of the core hole with a valence band electron. For a scattering angle of 90° at the O K-edge the necessary change in crystal momentum will be given by

$$\left|\Delta\mathbf{k}^{\text{photon}}\right| = \left|\mathbf{k}_{\mathbf{in}}^{\text{photon}} - \mathbf{k}_{\mathbf{out}}^{\text{photon}}\right| = 2\mathrm{k}\sin\theta$$

for a photon in and photon out of 530eV, the wavelength $\lambda = 23.39\text{Å}$ and therefore $\mathrm{k}^{\text{photon}} = 0.042\,\text{Å}^{-1}$

$$\left|\Delta\mathbf{k}^{\text{photon}}\right| = 0.059\,\text{Å}^{-1}$$

In a rutile oxide the smallest span of the Brillouin Zone in reciprocal space gives $\mathrm{k}_{\max} = {}^{\pi}/_{a}$; $a \approx 4.5$ Å giving

$$\mathrm{k}_{\max} = 0.698\,\text{Å}^{-1}$$

Thus the scattering of crystal momentum amounts to $\sim 8.5\%$ of the smallest span of the Brillouin zone, and the core hole is filled by an electron from the valence band from a state of essentially identical crystal momentum. For most of the relatively slowly dispersing bands in the rutile oxides the energy bandwidth of the monochromator used would select a much greater proportion of the Brillouin zone.

The obvious effect of $\mathbf{k}$ conservation on the emission spectra is the dispersion of peaks with changing incident photon energy as the electrons from the valence band contributing to the emission are selected from states with the same crystal momentum as the excited occupied state in the conduction band. In figure 2.12 the three on-resonant spectra in experiment and calculation show this dispersion in their features. The peaks in the density of states are associated with flat regions of the electronic structure. In spectrum (*i*) the excitation energy excites the core level electron into the lowest energy unoccupied state, located at the high symmetry Γ point in $\mathbf{k}$ space which is located at the centre of the Brillouin zone. The regions of the electronic structure where the density of states are located that contribute to the emission are those that intersect with the red shaded slice through the diagram, the width of which indicates the finite bandwidth of the incident photons. The strongest example of the effect of **k** conservation on the spectra is observed between spectra *(ii)* and *(iii)* where peak 4 arises. This is because the excitation energy for spectrum *(iii)* is sufficient to excite the core electron into a state at the **M** symmetry point in the Brillouin zone, and this in turn selects the states approximately falling within the yellow shaded slice of the band structure diagram to contribute to the emission. The different sense of the dispersion of different peaks in the emission spectra is also evident. Peak 2 and peak 5 move in opposite directions as the excitation energy is increased, essentially moving towards each other in accordance with the direction of the dispersion in the electronic band structure. Broadening is also apparent with increasing excitation energy, as the states contributing to the emission move away from the flat regions around the high symmetry points, giving rise to a broader density of states.

While the agreement between the dispersion of the peaks and the dispersion of the states in the electronic structure diagram is clear, allowing peaks $2-6$ to be attributed to particular regions, in practice the dispersion of the electronic structure is three dimensional and the diagram plots the dispersion along one dimensional paths through the Brillouin zone. The dispersion of the peaks in the spectra would therefore not be expected to be identical to the calculated band structure diagram, but a qualitative comparison is feasible, particularly for the graphite planar sp^2 bonded system.

2.4 Synchrotrons and Beamlines

Although throughout the middle decades of the 20^{th} century x-ray emission was carried out using both conventional x-ray targets and accelerated electrons as the excitation source, resonant x-ray emission and x-ray absorption are only feasible with far brighter sources of x-rays continuously tunable in energy. Third generation synchrotron sources have answered both of these requirements, and their development led to a revival of these techniques from the late 1980s to the present day, as outlined in the review of Kotani and Shin [24].

2.4.1 Synchrotrons, Undulators and Monochromators

Previously, the inefficiency of the x-ray emission process was discussed for lighter elements and softer x-rays. However, the combination of ultra-bright sources of x-rays and optimally efficient grazing incident spectrometers mitigates this impediment sufficiently to make such experiments feasible. A synchrotron will have at least 10^{10} times higher photon flux than a compact laboratory source of x-rays [2], with the operating range of radiation produced varying between the far infrared to the hard x-ray region of the electromagnetic spectrum. Figure 2.13 shows a schematic diagram of a synchrotron indicating the major components which consist of a storage ring, which is the polygonal structure delineated by the bending magnets, and an undulator inserted into one of the straight sections between bending magnets. The beamline in the diagram is shown in a position to collect the x-rays emitted at a bending magnet. Generally, thermally generated electrons are accelerated to relativistic velocities and injected into a storage ring where they orbit continuously. The acceleration experienced by the electrons due to the bending magnets in the storage ring causes them to emit radiation. As the acceleration the electrons experience in the bending magnets is towards the centre of the ring, the familiar "donut" profiled radiation pattern is emitted with the maximum intensity in the plane perpendicular to the acceleration. Due to the relativistic energies of the electrons, the radiation pattern is Lorentz contracted in the laboratory frame of reference, and the radiation field is encountered as a narrow cone emitted tangentially to the electrons' bending path.

In previous generations of charged particle accelerators, synchrotron radiation was considered parasitic, as it results in the loss of energy to the charged particles. The accelerator replaces this energy by using radio frequency cavities, which the electrons pass through on their circuit of the ring. Third generation dedicated synchrotron facilities with higher brightness have been available since 1996 in the case of the ALS and the research presented here is from beamlines at the ALS and MAXlab.

Beamlines must be constructed to collect the x-rays emitted at a bending magnet in the storage ring and direct it towards the experiment. They may also gather the radiation emitted by the electrons on their path through an insertion device called an undulator which consists of a periodic magnetic structure below and above the electrons' path that causes them to undergo a sinusoidal path deflection in the laboratory frame of reference. The intensity of the resulting radiation emitted is proportional to the number of magnetic periods in the structure and inversely proportional to the gap, and while the spectrum of an undulator is not monochromatic, interference between the radiation emitted at all points along the path through the undulator produces intense peaks at a certain fundamental energy, and odd higher harmonics. This undulator spectrum may be shifted in energy by altering the strength of the magnetic field of the undulator by bringing its upper and lower halves closer together or increasing the vertical distance between them. A suitable monochromator, *i.e.* a diffraction grating and slit can select a chosen window of energy from the undulator output, while the peak intensity of the chosen undulator harmonic is varied to maximize the flux at the desired energy.

A further characteristic of the undulator is the polarization of the radiation emitted. Its polarization is parallel to the direction of the sinusoidal oscillations the electrons undergo, and may be altered by offsetting the undulator periodic magnetic structures with respect to each other, thereby altering the electron path, to produce horizontal, vertical, circular or helically polarized light.

The x-ray absorption and emission results presented in this thesis were obtained at undulator beamlines 7.0.1 and 8.0.1 at the Advanced Light Source, Lawrence Berkeley National Laboratory, Berkeley, California, and beamline I511-3 at the MAX II storage ring at the MAX-lab National Laboratory at Lund University in Lund, Sweden.

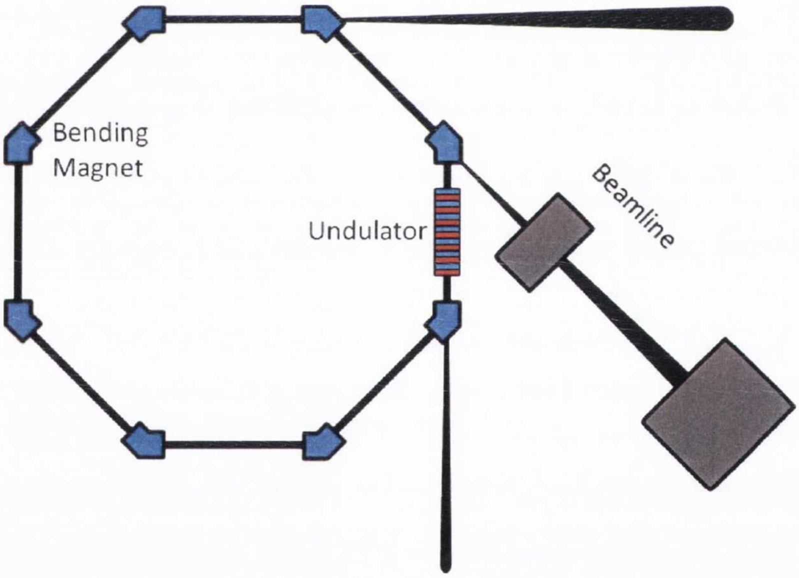

Figure 2.13: Sketch of a synchrotron storage ring and beamline, showing the bending magnets and the straight sections where insertion devices are located. The tangential-offshoot beamline construction is also indicated.

2.4.2 MAX-lab beamline I511-3

Detailed specifications of the beamline I511-3, where the entire body of work on the rutile oxides reported in this thesis was carried out, have been reported in [19]. The most relevant beamline parameters are abridged in this section. The source at

Beamline I511 is an undulator with 49 × 52 mm magnetic periods producing a flux of photons linearly polarized in the horizontal plane of the synchrotron. The light produced by the undulator is focused by a cylindrical mirror and directed onto a plane grating monochromator by a plane mirror. The high stability of the electron beam position in the ring allowed the monochromator to be designed without an entrance slit. The monochromator contains one plane diffraction grating ruled with 1200 lines/mm, which provides an energy range between 100 and 1200 eV. For the oxygen K edge absorption presented in this thesis where the energy range was centred around 525 eV, the 3^{rd} harmonic of the undulator was used with a resolution of between 200 meV and 400 meV.

The monochromated beam is directed to one of the three possible endstations by a translatable mirror. I511-3 is the beamline branch end station for bulk measurements. I511-3 is equipped with an x-ray emission spectrometer described in section 2.3.2 and also partial and total fluorescence yield detectors for NEXAFS. The entire analysis chamber containing the sample on its manipulator, the emission spectrometer and all other chamber accessories can be rotated mechanically by 90° to allow x-ray emission to be measured for in plane and out of plane geometries. This is indicated in figure 2.14 where the entire chamber is depicted rotating around the direction of the x-ray beam [25]. The optimum beam-spot size in the analysis chamber after refocusing by two Kirkpatrick-Baez bent elliptical mirrors is 10 μm × 30 μm in the vertical and horizontal respectively.

1

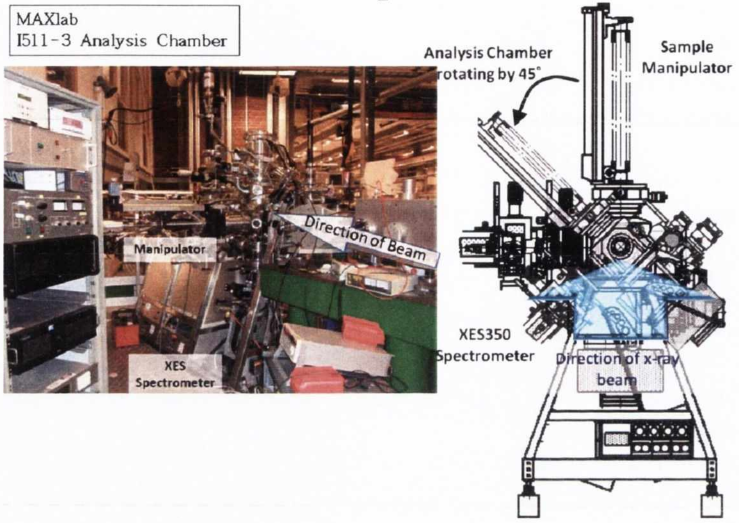

1

Figure 2.14: A sketch and photograph of the rotatable x-ray absorption and emission analysis chamber at the endstation of I511-3, MAXlab, Lund, Sweden. The analysis chamber is shown rotated to the out of plane scattering geometry.

2.4.3 ALS Beamline 7.0.1

This undulator beamline was used for the majority of x-ray emission and absorption from the dilute magnetic semiconductors and the anatase TiO_2 nanosheets. The beamline parameters included in this description are quoted from reference [26] and [18]. The undulator contains 89 × 50 mm magnetic periods. The horizontally polarized light produced by the undulator passes through a beam defining aperture that only allows the radiation in the central cone of the emission to propagate towards the condensing mirror that focuses light onto the monochromator. The monochromator consists of an entrance slit of variable width and fixed position that illuminates one of three selectable spherical gratings, depending on the energy range desired. The gratings are translatable under vacuum, and a combination of grating rotation and exit slit translation select a desired energy. The 380 $lines/\mathrm{mm}$ grating, and the 3^{rd} harmonic of the undulator was used for the O K edge with the high energy $925 lines/\mathrm{mm}$ grating and 5^{th} harmonic of the undulator used for the metal L edges. The resolution of the oxygen edge energies employed in the present thesis was approximately was between 200 meV and 400 meV as at beamline I511.

The beamline consists of a number of endstations that are selected by translating the endstation selecting mirror depicted in figure 2.15. Figure 2.15 also aims to give an indication of the beamline control system used to conduct the x-ray absorption and emission experiments for this thesis. The endstation computer collects the incident flux intensity via the gold plated mesh, in order to normalize the NEXAFS spectra as described in section 2.1.2. It also records the sample drain current, photodiode current for NEXAFS spectra and the positions and intensities for events on the emission detector. The endstation computer, in turn, controls the undulator gap, grating tilt and monochromator exit slit position in order to give the optimum intensity at a selected energy.

The focused spot size at the sample is $\sim 50 - 100\mu$m, where the focus is adjustable for the different endstation sample distances by the vertical refocusing mirror.

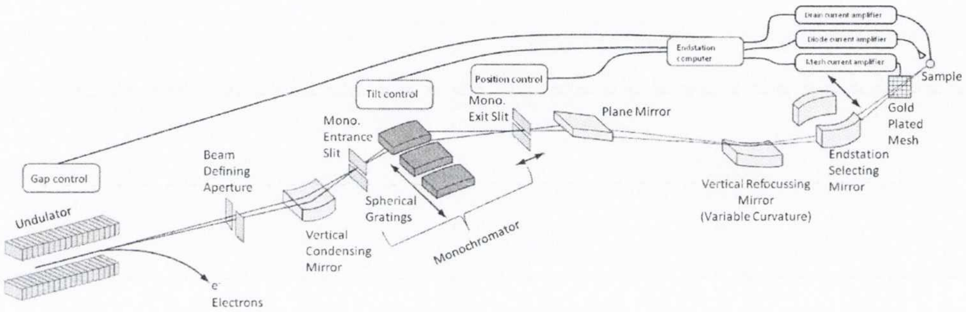

Figure 2.15: Overview of ALS Beamline 7.0.1, Lawrence Berkeley National Laboratory, from undulator to sample, adapted from beamline manual.

2.4.4 ALS Beamline 8.0.1

Both O K edge and and Co L edge NEXAFS and RXES on Co doped ZnO DMS films grown by MOCVD was carried out at Tulane University and the University of Tennessee at Knoxville's soft x-ray fluorescence endstation at beamline 8.0.1 [4]. The undulator contains 89×5.0 cm periods covering an energy range of $70 - 1200$ eV . The details of the monochromator at beamline 8.0.1 are essentially identical to those of beamline 7.0.1, and the similarity of the layout between these two beamlines did not require a schematic diagram of the layout to be included for both. The medium energy 380 lines/mm grating was used with the 3^{rd} undulator harmonic for the O K edge and the high energy 925 lines/mm grating was used with the 5^{th} harmonic of the undulator for the Co L edges.

The study of the band structure of graphite along high symmetry directions reported by Carlisle *et al.* [6] and discussed in section 2.3.3.3 was also performed at this beamline. NEXAFS is measured at this beamline in both TEY via the drain current to the sample and PFY mode using a channeltron in photon mode. The analysis chamber contains a soft x-ray emission spectrometer as described in section 2.3.2.3.

Refocusing of the beam in the horizontal direction produces a spot size on the sample in the analysis chamber of 500 μm × 100 μm spot size with a vertical oblong cross section.

2.5 Summary / Conclusions

The present chapter has outlined and described the principal features of the three spectroscopic techniques x-ray photoelectron, absorption and emission spectroscopy, employed in the study, alongside the physical apparatus used. Some particular characteristics of the spectra have been described, with particular attention to the geometry of scattering from σ and π bonded orbitals. We have shown that with the appropriate x-ray sources, instrumentation and knowledge of x-ray spectroscopic methods we can extract enhanced information about the electronic structure of solids. The following chapter will review rutile transition metal oxides and electronic structure calculation methods.

Chapter 3

Rutile Transition Metal Oxides: Structure and Calculations

Rutile is a common polymorph or structure of transition metal oxides with the MX_2 formula unit. The prototype of the structure is TiO_2 which has the mineralogical name rutile. The current chapter describes the physical structure of rutile, and the bonding relationships that form which determines the electronic structure of the systems that adopt this structure. The electronic structure of rutile systems is described in particular in terms of the O $2p$ partial density of states in those materials and how that relates to the O K-edge XAS and RXES measurements.

The electronic structures of some rutile-type oxides were calculated using the specific formulation of Density Functional Theory contained in the WIEN2k code. WIEN2k uses a full potential linear augmented plane wave formulation together with local orbitals, which are described in section 3.4. In particular, the calculated electronic structure yielded a partial density of states, projected along the crystal axes which were used to simulate the O K- edge Resonant X-ray Emission Spectra obtained experimentally.

3.1 Details of the Rutile Structure

The rutile structure is characterized by metal cations that are octahedrally coordinated by 6 anion ligands, the cations lining up into chains by edge sharing in the waist plane of each octahedron. The chains of octahedra that form by waist edge sharing stack in layers where the major axes of the octahedra are rotated by 90° from one layer to another as shown in figure 3.1. In MX_2 solids where the metal cation is coordinated by six ligand anions and the anions in turn are coordinated by

3 metal cations, rutile or the $P4_2/mnm$ space group is the most commonly resulting structural type [27].

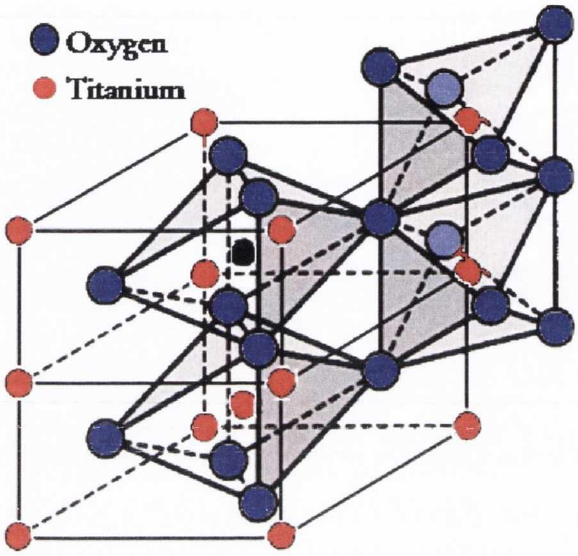

Figure 3.1: Adjacent octahedra in a typical rutile structure from [7]

While the metal cations are coordinated octahedrally by their ligands, the ligand anions are coordinated by 3 metal cations in flat triangular or trigonal planes. Each oxygen in the system is included in a triangular coordination of metal cations, and that demands a sp^2 hybridization of the s and p orbitals of the anion. These sp^2 orbitals can then form 3 σ metal-oxygen (M-O) bonds between their in-plane components and the cation d e_g orbitals whose lobes point directly towards the anion from the corners of the plane defined by the three metal cations surrounding the oxygen (the M_3O plane). There is one remaining p orbital left over that is not hybridized and is oriented perpendicular to the trigonal plane. This orbital forms can form weak π M-O bonds with the d t_{2g} orbitals of the surrounding metal cations, and is non-bonding to a greater or lesser extent in certain examples of rutile oxides. As they contain the principal axis of the octahedron, the M_3O planes repeat throughout the bulk crystal in families of planes at 90° to each other, but always parallel to the c axis of the structure containing the chains of octahedra. The M-O distances vary between the four distances around the waist of the octahedron, compared to the two M-O distances to the corner-sharing apices of the octahedron, thus defining the principal axis of the octahedron at right angles to the direction of the edge sharing chain (or c axis).

The foregoing description of the spatial arrangement of the bonds in the structure in is a general feature of rutile systems. However, the details of the M-O distances and octahedral distortions involved for different metal cations with different radii and *d* shell occupancies gives rise to the variety of electronic structures encountered in rutile transition metal oxides. From insulating and semiconducting in the case of TiO_2 and SnO_2 to half-metallic in the case of CrO_2 and metallic in the case of RuO_2.

The spatial separation of the M-O σ and π bonds, due to the location of the M-O σ bonds in the plane at 90° to the π / non-bonding orbitals will give rise to an anisotropy in the absorption of polarized electromagnetic radiation, depending on the angle of the polarization to the M_3O plane. When the polarization is parallel to the plane, the bonds oriented along this axis may absorb the radiation, but not the bonds perpendicular to it and vice-versa. This allows the M-O σ^* and π^* O $2p$ unoccupied partial density of states created by the σ and π bonds to be probed separately in X-ray Absorption Spectroscopy at the O K- edge by rotating the crystal axes with respect to a plane polarized source of x-rays.

Selecting the energy of the incoming photon and the geometry of the measurement of the outgoing photon in an X-ray Emission Spectroscopy experiment also allows the O $2p$ occupied partial density of states belonging to the M-O σ and M-O π bonds to be probed largely independently of each other, exploiting the linear dichroism described in the previous paragraph. The emission of radiation by dipole transitions between the O $2p$ part of density of states due to the σ and π M-O bonds in the M_3O plane and the O $1s$ core hole essentially gives rise to a σ^*absorption $\rightarrow$ π emission and π^* absorption $\rightarrow$ σ emission selectivity in a simple two-dimensional picture introduced first in the previous chapter. This takes account of the fact that the emitted x-ray photon is measured by a spectrometer fixed at an angle of 90° to the propagation vector of the incident photon [5].

3.2 The Formation of the Rutile Structure

In a MX_2 compound formed between two elements of differing electro-negativities such as metal dioxides, dihalides and disulphides, an ionic bonding model provides an approximate prediction and practical explanation of the crystal structure of the resulting solid where each metal cation is surrounded by a regular octahedral formation of anions, and each anion is surrounded by a triangular arrangement of metal cations. The crystal structure of many transition metal dioxides are closely related to this model structure. As rutile is a common structure for electronegative oxides and fluorides, its formation has previously been treated using ionic models [28, 29]. A simple ionic model, however does not give agreement with the observed parameters of rutile solids which requires some degree of covalent bonding in the solid [30]. For instance a degree of covalent bonding in the compound must be included to account for the cation-anion bond distances are observed in real solids where the purely ionic model predicts a constant cation-anion bond distance [27]. The somewhat shorter bond distances observed than those predicted by the ionic model also indicate a degree of covalent bonding in the system.

A more predictive qualitative model of the bonding and energetics of the rutile structure was developed based on a molecular orbital approach that takes account of the degree of covalent bonding in the system and leads to a rationale for the stability of the rutile structure that changes with the energetics of increased d shell occupation leading to a variety of structural modifications [7].

The mechanism that offers the most satisfactory explanation for the formation or adoption of the rutile-like structure by transition metal dioxides, in preference to the related orthorhombic $CaCl_2$ or the hexagonal close packed CdI_2 structures, is the competition between the formation of the metal-favoured octahedra and the oxygen-favoured trigonal planes. The rutile structure is a tetragonal modification of the orthorhombic $CaCl_2$ structure which is composed of 2 Ca atoms at $(0,0,0;\frac{1}{2},\frac{1}{2},\frac{1}{2})$ and 4 Cl atoms at $(\pm u,\pm v,0)$ and $(\frac{1}{2}\pm u,\frac{1}{2}\mp v,0)$ giving rise to 3 unequal axes in the crystal. Tetragonal rutile structures are formed where $u=v$ giving rise to the position of 2 metal cations at $(0,0,0;\frac{1}{2},\frac{1}{2},\frac{1}{2})$ and 4 oxygen anions at $(\pm u,\pm u,\frac{1}{2})$ and $(\frac{1}{2}\pm u,\frac{1}{2}\mp u,\frac{1}{2})$ and hence a tetragonal crystal with 2 axes of equal length and a third of unequal length. The metal cations are coordinated in octahedra formed by the anions, identical but rotated by 90° about the c-axis of the unit cell and translated by $(\frac{1}{2},\frac{1}{2},\frac{1}{2})$ as shown in figure 3.1. The primitive quarter rotation and translation of $(\frac{1}{2},\frac{1}{2},\frac{1}{2})$is summarized in rutile's $P4_2/mnm$ space group designation.

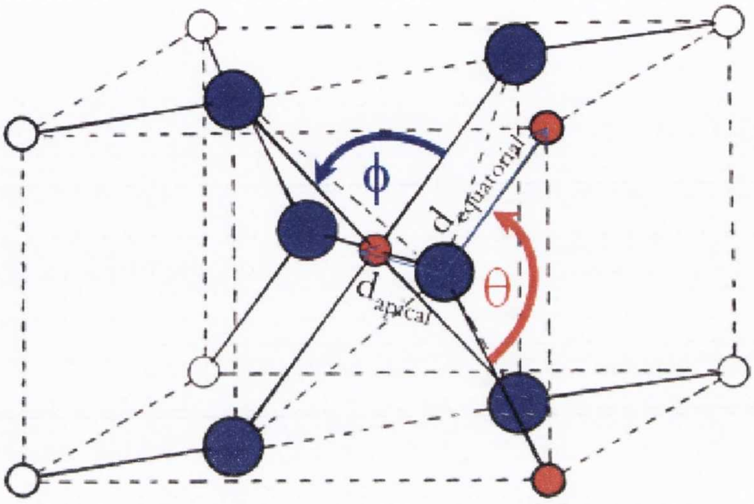

Figure 3.2: Metal-Oxygen distances d_{apical} and $d_{equatorial}$; bond angles θ within the M_3O trigonal plane, and ϕ in the equatorial plane of the MO_6 octahedron.

The apical and equatorial metal-oxygen distances are shown along with the metal-oxygen-metal bond angle θ in figure 3.2. The apical distance d_{apical} is defined as the distance between the metal cation at $\left(\frac{1}{2}, \frac{1}{2}, \frac{1}{2}\right)$ and the anions at $\left(\frac{1}{2} \pm u, \frac{1}{2} \mp u, \frac{1}{2}\right)$, the equatorial distance $d_{equatorial}$ is the distance between the cation at the centre of the octahedron and the anions in the waist or equatorial plane of the octahedron. If all the metal-oxygen distances were equal, $d_{apical} = d_{octahedral}$ the volume of the crystal would be filled with regular octahedra. The distortion of the octahedra also means that the trigonal plane centred around the apical oxygen is not equilateral and the bond angle θ varies with the cation-anion distances. The parameters that describe the distortion of the rutile octahedra are the lattice constant a, the unit cell ratio $\frac{c}{a}$, and the internal coordinate u. As a result also the O-M-O angles in the equatorial plane are not 90° which creates a rectangular rather than a square cross section.

	TiO_2	RuO_2	SnO_2
$a(\text{Å})$	4.593	4.492	4.740
c/a	0.644	0.692	0.673
u	0.305	0.306	0.306
$d_{apical}(\text{Å})$	1.982	1.944	2.053
$d_{equatorial}(\text{Å})$	1.948	1.983	2.055
θ	126.29°	128.84°	127.84°
ϕ	81.21°	76.78°	78.18°
Reference	[31]	[32]	[33]

Table 3.1: Rutile Structure Parameters for TiO_2, $RuO_2$and SnO_2

Table 3.2 outlines the lattice constants a, the $\frac{c}{a}$ ratio, the internal coordinate u, and the metal-oxygen bond distances for the series of transition metal oxides under consideration. By definition, the transition metals or rather their oxides have unfilled d shells and the properties of the transition metal oxides show altered properties at their number of d electrons while retaining the same distorted octahedral structure. CrO_2 even reverses the sense of the distortion in the rutile octahedron with $d_{apical} < d_{equatorial}$. Differing electronic structures are to be expected if, for instance, the metal-metal distance within the crystal structure decreases, permitting a greater degree of metal-metal bonding, or the d occupancy permits a Peierls distortion as in VO_2 upsetting the delicate balance outlined above.

TiO_2 with its d^0 configuration is a wide band gap insulator, at least in its stoichiometric form, and the aforementioned archetype of the rutile structure. As such, it offers the best model to study the electronic structure of other transition metal oxides by comparison as the filling of the d shell increases. In RuO_2 a $(4)d^4$ configuration results in a metallic system. Finally SnO_2 has a filled $4d$ shell, d^{10} in the rutile-like structure and is a transparent semiconductor.

3.3 The Bonding in a Rutile Structure

As mentioned previously, a molecular orbital approach provides a good qualitative basis to interpret the electronic structure of the rutile-like oxides, and has given accurate results in structural calculations [7]. The model presents a picture of the spatial orientation of the bonding and anti-bonding states and their position in relation to the Fermi energy as the valence band accommodates increasing numbers of electrons across the series. This section describes the molecular orbital approach to modelling the bonding in rutile, and how this is related to the approximate symmetry of the crystal structure. The most convenient point at which to begin is by definition of the coordinate axes that will be used to describe the alignment of the lobes of the metal and oxygen orbitals throughout this thesis.

3.3.1 The anion and cation coordinate system

To describe the distribution of charge within the rutile structure, and our results and calculations, it is useful to describe the system from the point of view of two differing coordinate systems for the oxygen $2p$ orthogonal components of the partial density of states.

The metal atoms in rutile dioxides form a body centred tetragonal lattice and it is convenient to follow Kunes *et al* [34] in defining a local coordinate system for both the metal and oxygen ions, according to their bonding axes within the oxygen octahedra that surround the metal atoms as shown in figure 3.3.1.

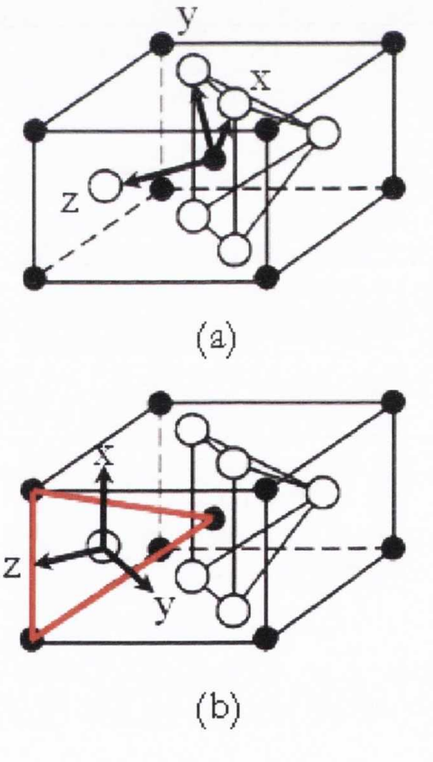

Figure 3.3: Demarcating the natural coordinate systems in a rutile geometry for (a) the cation and (b) the anion, adapted from [7]

The octahedra that surround corner and body-centred metal anions have their apical axes rotated by 90° with respect to each other along the crystal c axis, to which they are mutually perpendicular.

The local coordinate system for the metal anion is defined as follows: the Z_M axis is collinear with the metal-oxygen direction along the apical axes of the octahedra, and the X_M and Y_M axes point towards the oxygen atoms located at the corners of the equatorial plane or waist of the octahedra. In fact the direction of the metal local x and y axes is only approximately along the metal-oxygen equatorial directions, as the equatorial 'base' of the octahedra are generally distorted in rutile-type compounds by shortening or lengthening along the crystal c axis, giving a rectangular shape.

The Z_O axis of the apical and equatorial oxygen atom local coordinate system is collinear with the metal Z_M axis. The oxygen local Y_O axes are perpendicular to the M_3O planes that they are located in, and hence both the Z_O and Y_O are oriented at 45° to the crystalline a axis. The oxygen X_O axis is collinear with the crystalline c axis.

3.3.2 σ and π bonding between hybridized orbitals

In an octahedral ligand crystal field the energy degeneracy of the orbitals in the d shell is lifted, and they split into doubly degenerate e_g and triply degenerate t_{2g} orbitals. The higher energy e_g orbitals are those oriented directly towards the apical and equatorial anions while the lower energy t_{2g} orbitals are combinations of d orbitals that project through the faces of the octahedra.

Since there is a tetragonal distortion of the octahedral crystal field the degeneracy of the crystal field split d orbitals is lifted. When $d_{apical} = d_{equatorial}$ these orbitals are internally degenerate in energy. In octahedra where $d_{apical} \neq d_{equatorial}$ the internal degeneracy is lifted, and the orbitals split in energy as represented in figure 3.3.2.

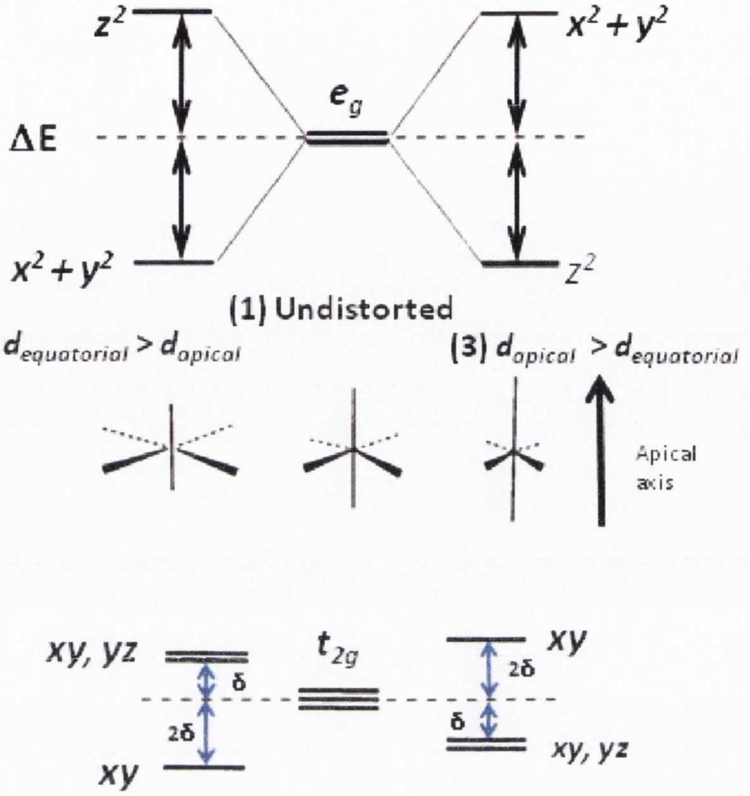

Figure 3.4: Rutile octahedral distortion - energy splitting in e_g and t_{2g} states, rearranged from [8]

The trigonal coordination of the anions creates the sp^2 combination of the $2s$ and $2p$ orbitals which form hybrid orbitals contained in the anion x-z plane, denoted $p_{x,z}$. The remaining p orbital oriented perpendicular to the plane is denoted p_y. The cation e_g states overlap with the anion p_x and p_z orbitals while the t_{2g} states are oriented such that they can form a π-type interaction with the p_y anion states.

It is the cation d_{z^2} and $d_{x^2-y^2}$ orbitals that form the e_g orbitals under octahedral crystal symmetry. The octahedral geometry of these orbitals leads them to combine with the $4s$ and $4p$ sp^3 hybridized states of the metal cation at their sites to form $e_g^2\,sp^3$ orbitals oriented towards the ligand anions. The sp^2 hybridized orbitals of the trigonally coordinated ligand anions form M-O σ bonds with the cation $e_g^2\,sp^3$ orbitals all lying oriented in the trigonal plane itself. The bonding and anti bonding states formed by these M-O σ bonds are located in the molecular orbital approach depicted in figure 3.5 as the two lowest energy shaded bonding bands, and the two highest energy unshaded antibonding bands. Of the two bonding-antibonding pairs of bands the outermost bonding-antibonding pair of bands, with the larger proportion of anion

$2s$ orbital character are formed by the M-O σ bond along the octahedral apical axis, between the cation d_{z^2} e_g sp^3 orbitals and the anion p_x and p_z sp^2 orbitals. The inner pair of σ bonding-antibonding bands is formed by the bonds along the octahedral equatorial axis between the cation $d_{x^2-y^2}$ e_g sp^3 orbitals and the p_x and p_z anion sp^2 orbitals. These M-O σ symmetry bands contain proportionally more anion $2p$ orbital character.

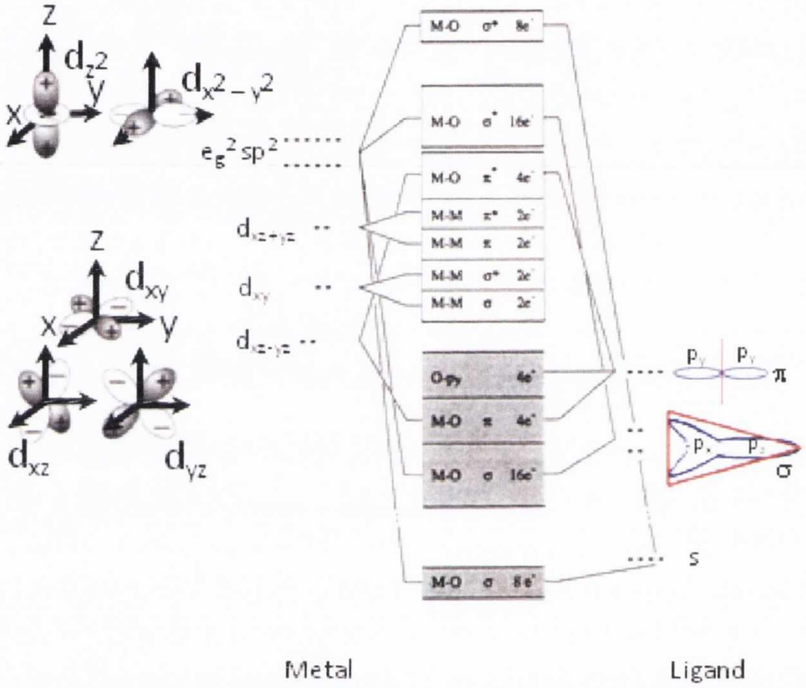

Figure 3.5: Molecular-Orbital picture of the bonding in rutile TiO_2 adapted from [7]

The remaining anion p_y orbital that is oriented along an axis perpendicular to the trigonal plane containing the anion, can participate in a M-O π bonding interaction with the combination of the cation t_{2g} states that results in the same orientation. This refers to the d_{xz-yz} combination within the plane containing the metal cation perpendicular to the c-axis. In figure 3.5 the bands created by the bonding-antibonding pairs of these states are the only cation-anion π bonding pairs represented on the diagram. As will be seen later, the sharp peak in the density of states at the top of the valence band in TiO_2 indicates that the oxygen p_y orbital is also partially non-bonding, as in TiO_2 the formal occupancy of these t_{2g} derived d bands is zero as they are far away in energy.

Of the remaining t_{2g} states the d_{xz+yz} combination oriented parallel to the $(\bar{1}10)$ plane and the d_{xy} orbitals oriented parallel to the (110) plane can only form weak M-M π and M-M σ bonds respectively with other cations a distance c away. In d^1 systems, such as VO_2 this M-M bonding becomes more important. In the molecular orbital picture, the bands created by these metal-metal σ and π bonding-antibonding pairs are the two innermost unshaded pairs of bands that form the bottom of the conduction band. The bonding overlap between these orbitals should increase with decreased metal-metal distance for instance in a more distorted rutile structure. For instance, the distortion due to the Jahn-Teller dimer pairing of metal cations along the edge-sharing chains of the octahedra with increased d shell occupation leading to layers of paired octahedra.

3.4 Details of the Electronic Structure Calculations

In the present section, the theory on which the band structures, partial densities of states and simulated RXES we present is discussed. There follows a general description of the calculation of electronic structures of periodic crystalline bulk materials, and an outline of how we adapted the calculated band structure diagrams and densities of states to produce simulated spectra.

The calculations use a formulation of density functional theory, which treats all properties of a material as functionals of its ground state charge density in order to circumvent the complexity of the many body system of electrons and nuclei. Related earlier density-oriented approximations such as the Thomas-Fermi model were essentially heuristic approaches to calculating the properties of materials. The starting point of density functional theory is the proof of the Kohn-Sham theorems described in section 3.4.2, and the prescription of the form of the equations that a charge density will need to satisfy in order to solve exactly the ground state energy of the system. The following sections outline the steps involved in constructing density functional theory and its implementation in the WIEN2K formulation, which is also well summarized in [35].

All of the WIEN2K calculations carried out for the purposes of comparison with or modelling of the experimental results were carried out by Cormac McGuinness in close consultation with the author of this thesis.

3.4.1 The Born-Oppenheimer Approximation

In a solid the many-particle Hamiltonian for a system of mutually interacting electrons and nuclei is given by

$$\begin{aligned}\hat{H} = -\frac{\hbar^2}{2}\sum_i \frac{\nabla^2_{\vec{R_i}}}{M_i} - \frac{\hbar^2}{2}\sum_i \frac{\nabla^2_{\vec{r_i}}}{m_e} - \frac{1}{4\pi\epsilon_0}\sum_{i,j} \frac{e^2 Z_i}{\left|\vec{R_i} - \vec{r_j}\right|} + \\ \frac{1}{8\pi\epsilon_0}\sum_{i\neq j} \frac{e^2}{\left|\vec{r_i} - \vec{r_j}\right|} + \frac{1}{8\pi\epsilon_0}\sum_{i\neq j} \frac{e Z_i Z_j}{\left|\vec{R_i} - \vec{R_j}\right|} \qquad (3.1)\end{aligned}$$

the five terms from left to right describing the kinetic energy of the nuclei, the kinetic energy of the electrons, the potential energy due to the electron-nuclei Coulombic interaction, the potential energy due to the electron-electron Coulombic interaction, and the potential energy due to the Coulombic interaction between the nuclei.

The most fundamental approximation to reduce the many body Hamiltonian is to consider the relative momenta of the electrons and nuclei. This gives rise to the approximation where the nuclei are considered to be stationary as they move so much more slowly than the electrons in the system, namely the Born-Oppenheimer approximation. This reduces the many-body Hamiltonian by removing the nuclei kinetic energy term and the term describing the Coulombic interaction between the nuclei becomes a constant. In principle the problem is now dealing with NZ mobile electrons subject to the potential of their interactions with each other and the external potential of the stationary nuclei. Thus the many body Hamiltonian may be written as

$$\hat{H} = \hat{T} + \hat{V} + \hat{V}_{ext}$$

This equation consists of a pair of "universal" terms that do not include the effects of the nuclei in the system, and hence are not dependent on the particular details of the many electron system in question. The contribution from the nuclei, that gives rise to the particular electronic behaviour due to the type of environment the electrons are contained in, is described by the $\hat{V}_{ext}$ term, usually just the Coulombic field of the nuclei.

The Born-Oppenheimer approximation pre-dates Density Functional Theory by about 40 years and has provided the foundation for other methods for electronic structure calculations such as the Hartree-Fock method. The Thomas-Fermi method is a direct fore-bearer of the Density Functional Theory as it began the search for the ground state energy of a system in terms of its charge density.

3.4.2 The Hohenberg-Kohn Theorems

Density Functional Theory is founded on two theorems of Hohenberg and Kohn [36]. The first theorem states that there is a unique correspondence between the ground state charge density $\rho(\overrightarrow{r})$ of a many electron system and the ground state external potential V_{ext}. The ground state external potential defines the many-body wave function of the ground state system. All ground state observables of the system can then be reclaimed by operating on this many body wave-function, including, of course, the ground state charge density itself. In general, the ground state charge density therefore contains as much information about the ground state system as the many body wave function itself. Any observable quantity represented by the operator $\hat{O}$ can therefore be described as a functional of the ground state charge density, ρ

$$\langle\psi|\,\hat{O}\,|\psi\rangle = O(\rho)$$

This converts the intractable many body problem into one which is formulated with a macroscopic quantity, without sacrificing any of the information contained in the many body wave-function.

The second founding theorem outlines the form that the ground state total energy functional $E(\rho)$ takes with respect to the ground state charge density ρ

$$\begin{aligned} E(\rho) &= \langle\psi|\,\hat{T}+\hat{V}\,|\psi\rangle + \langle\psi|\,\hat{V}_{ext}\,|\psi\rangle \\ &= F_{HK}(\rho) + \int \rho(\overrightarrow{r})V_{ext}(\overrightarrow{r})dr \end{aligned}$$

where the universal component of the total energy functional, that is independent of the details of the many electron system is separated into the Hohenberg Kohn universal functional term, denoted $F_{HK}(\rho)$. This separation of universal and particular functionals of the ground state density is similar to the grouping of terms obtained after applying the Born-Oppenheimer approximation to the many-body Hamiltonian.

Finally, for a given external potential $V_{ext}(\overrightarrow{r})$ the ground state charge density is the one for which the total energy of the system will be minimized. This indicates the variational principle by which an initial estimation of the ground state charge density can be iterated until the total energy of the ground state converges in a self consistent field, yielding a solution for the ground state charge density and hence any ground state observable.

DFT was founded with the proof that the ground state charge density of a system is a quantity as fundamental as the many-body wave function of the system in the ground state. Therefore all information the external potential of the system, the

Hartree and exchange-correlation energy is contained fully in the ground state charge density, and Hohenberg and Kohn formulated a conceptually exact equation for the ground state energy of a system with a given external potential as a functional of the charge density.

To approach a solution for the density functional, a system in which electrons do not interact with each other is imagined in order to suspend the complexity of the mutual interaction of the electrons due to exchange and correlation. Such imaginary or Kohn-Sham electrons interact only with an external potential and will satisfy a Schrodinger-like equation that is much simpler as it does not contain the electron-electron interaction. The external potential that is constructed for these non interacting electrons to feel is such that their ground state charge density is identical to the ground state charge density of the real system of the interacting electrons of interest.

This is a great simplification as it is straightforward to find an exact solution to a Schrodinger equation in which the electrons do not interact. The non-interacting problem extracts the largest terms from the density functional that are known exactly, namely the kinetic energy and the coulomb-like electrostatic energy. A numerical solution is then found for the remaining small terms which comprise the energy of exchange and correlation that must be approximated. The physical advantage of doing this it that the first two terms capture most of the physics of the system and the third term is small. In order to make DFT into a practical algorithm, what remains is to find an approximation for the exchange correlation term. This has been done by using a local density approximation and it is the success of this approach that has led to DFT becoming a practical theory.

3.4.3 The Kohn-Sham System

The problem outlined by the Hohenberg-Kohn theorems still contains all the complexity of a charge density subject to electron-electron interactions, and the solution of the regular Schrodinger equation in such a system would involve all of the coupled differential equations of the mutually interacting electrons yielding an essentially still intractable problem.

The Kohn-Sham approach is based on the fundamental equivalence of the ground state charge density between a real-world system of interacting electrons subject to an external potential and the fiction of non-interacting electrons subject to a potential accounting for the external potential of the lattice as well as the potential containing the contribution from the exchange and correlation effects in the electron cloud. The real world electron-electron interaction is reduced to a potential field, like the external potential of the post Born-Oppenheimer Hamiltonian, in the fictitious world of the non interacting electrons. The ground state charge density in both the interacting and non-interacting systems are identical. Rather than treating the real system of electrons and their complex interactions, the problem is reformulated in terms of a radically simplified system of imaginary particles that allows the interaction of the electrons to be treated as a potential, which in turn can be approximated.

These imaginary particles may be referred to as the Kohn-Sham electrons for future reference and and the potential that they are subject to is the Kohn-Sham potential. The Kohn-Sham potential includes three components: the potential due to the electrostatic interaction between individual volumes of the charge density denoted V_{HF} as it is essentially the Hartree-Fock potential, the potential due to the exchange-correlation interaction between individual volumes of the charge density denoted V_{XC}, and the external potential due to the atomic nuclei, V_{ext}. Finally, the kinetic energy of the Kohn-Sham electrons, T_0, is well defined. This gives the formulation of the Kohn-Sham Hamiltonian

$$\hat{H}_{KS} = \hat{T}_0 + \hat{V}_{HF} + \hat{V}_{XC} + \hat{V}_{ext} \tag{3.2}$$

This Hamiltonian acts on the Kohn-Sham electron wave-function yielding its energy

$$\hat{H}_{KS}\psi^i_{KS} = E^i_{KS}\psi^i_{KS} \tag{3.3}$$

and the ground state charge density of an N-electron system is given by the sum of the N lowest energy Kohn-Sham electron wave-functions

$$\rho(\overrightarrow{r}) = \sum_{i=1}^{N} \psi^{i*}_{KS}\psi^i_{KS}$$

The remaining caveats are

1. the exchange-correlation potential in the Kohn-Sham Hamiltonian is still not a defined quantity and its approximation must be attempted. The Local Density Approximation that is also employed in the Thomas-Fermi approach to calculating the quantum kinetic energy of an inhomogeneous electron gas serves this purpose and is described below.

2. a practical mechanism for solving the Kohn-Sham equations must be found, once the mathematical form of the Kohn-Sham wave-functions is defined. For the purposes of the work described in this thesis in modeling the electronic structure of the rutile oxides a specific type of plane wave expansion with modifications is used for the Kohn-Sham orbitals.

3.4.4 Solving the Kohn-Sham Equation

Beginning with an initial guess or ansatz for the ground state charge density $\rho(\overrightarrow{r})$, the various elements of the Kohn-Sham Hamiltonian which are themselves functionals of this charge density are constructed and assembled in the following equation, from 3.2 and 3.3

$$\left(\frac{-\hbar^2}{2m_e}\overrightarrow{\nabla}^2 + \frac{e^2}{4\pi\epsilon_0}\int \frac{\rho(\overrightarrow{r}')}{|\overrightarrow{r} - \overrightarrow{r}'|}dr' + V_{XC} + V_{EXT}\right)\psi^i_{KS}(\overrightarrow{r}) = \epsilon^i_{KS}\psi^i_{KS}(\overrightarrow{r})$$

where the first term is the kinetic energy, the second term is the Hartree energy and the fourth term is the external potential. The exchange correlation potential in the Hamiltonian is the remaining unknown and it is approximated by using the Local Density Approximation.

In the local density approximation the large non-homogeneous charge density is divided into infinitesimal volumes within which the charge density can be approximated as homogeneous. The contribution coming from this infinitesimal volume to the overall exchange-correlation energy will be given by its volume times the exchange-correlation energy density of the homogeneous electron gas at that density.

The simplification arises because the total ground state energy of a homogeneous electron gas can be calculated numerically for an interacting electron gas, for instance by using quantum Monte Carlo methods. Given that the total ground state energy of a homogeneous electron gas, and the kinetic and electrostatic energies can be calculated for various densities, the exchange-correlation energy density of a homogeneous electron gas can therefore also be obtained by subtraction. The overall exchange-correlation energy of the non-homogeneous gas is the integral of the contributions from all the infinitesimal volumes. Evaluating this numerical solution for the exchange correlation energy at many different densities gives the exchange correlation energy as a function of the charge density.

Having expanded all the terms in the Kohn-Sham Hamiltonian, a method for solving the quasi-particle Schrodinger equation for the individual wave functions must be specified. In principle this requires choosing a basis set or the general form of the wave-functions that will add to form the solutions and the number of members of this basis set that are to be used to define the solution. Then the coefficients of each member of the basis set may be solved by matrix diagonalization to yield the set number of coefficients. The speed or cost of the computation and accuracy of the result is critically determined by the form of the basis set chosen and the number of members of the basis set employed. The closer the form of the chosen basis set to the form of the quasi-particle wave-function, the fewer members required to give a relatively unbiased result. The quasi particle wave function solution is written as

$$\psi^{i}_{KS} = \sum_{p=1}^{P} c^{p}_{KS}\psi^{p}_{b}$$

where P, p denote the number of basis set functions to be used to construct the solution, and the label for each member respectively; ψ^{p}_{b} denotes the pth member of the basis set and c^{p}_{KS} its coefficient.

3.4.5 WIEN2K and the Full Potential Linearized Augmented Plane Wave Basis Set

The general features of a WIEN2K calculation are summarized in this section. Comprehensive introductions are available such as that of Cottenier [37].

As mentioned previously the components of the basis set employed by the WIEN2K code are referred to as Full-potential Linear Augmented Plane waves. "Augmented" refers to the fact that the single particle wave functions are separated between those regions close to the atomic nuclei and an interstitial region between the nucleus-proximity region. In practice this results in a spherical volume defined around the nuclei where the quasi particle wave-functions are expanded as atomic-like orbitals in form, and the quasi particle wave-function in the interstitial region is expanded by a plane wave like basis set. "Linear" refers to the fact that the energy dependence of the atomic-like radial functions is linearized subject to a chosen linearization energy where an energy derivative of the radial wave-function is included to improve the accuracy of its application to radial functions of differing orbital symmetry.

The size of the volume defining the atomic-like region from the interstitial region is a variable that must be decided upon judiciously to yield an accurate ground state charge density. A further modification of the nuclear region basis set includes local orbitals to simulate the effects of tightly bound atomic levels that are localized around the nuclei and do not permeate the interstitial region. This local orbital amendment is applied to the valence orbitals involved in bonding. The Full-Potential treatment of the basis set refers to the fact that whereas the potential in a muffin-tin approximation is considered to be spherically symmetric around the atomic nuclei, a more general approach expands both the potential and charge density in spherical harmonics inside the nuclear sphere, and as a Fourier sum in the interstitial region. While the muffin-tin approximation is sufficient for describing close-packed systems such as face centred cubic crystals, the full-potential expansion can be used in covalently bonded systems, and other lower-dimensional solids. A complete description of the Wien2k implementation of the LDA-FLAPW technique in DFT can be found elsewhere in the literature [38].

3.4.6 Simulating X-ray spectroscopic measurements

The calculated unoccupied bandstructure, more specifically the unoccupied oxygen $2p$ partial density of states is often compared directly to the oxygen K-edge XAS spectra although proper account should be taken of the "final state rule" [16] and the existence of excitonic behaviour. Nonetheless such a comparison is useful in the first instance, and the oxygen $2p$ partial density of states projected along orthogonal axes can be compared directly to the measured O K-edge XAS with the linearly polarized light aligned along these axes. A more meaningful comparison would simulate the XAS by taking into account the $1s - 2p$ transition matrix elements, the core-hole lifetime broadening, the excited state lifetime broadening and the instrumental resolution. The PDOS projected $||a$ and $||c$ will be compared to the XAS obtained with $\mathbf{E}||a$ and $\mathbf{E}||c$.

The calculated occupied bandstructure is converted into simulated resonant x-ray emission spectra for comparison with the experimental resonant x-ray emission spectra as follows:

1. For a given experimental excitation energy, an excitation bandwidth is defined within the unoccupied bandstructure which serves to determine the possible k-points that will contribute to the subsequent emission. Recall that the momentum transferred to the crystal by absorption or emission of a soft x-ray photon, even in a 90° scattering geometry, is relatively small compared to the crystal momentum spanned by the dispersion of states along any of the principal high symmetry directions in the reciprocal space Brillouin zone. Thus the k-points selected in the unoccupied band structure in the absorption process determine the k-points from within the occupied states directly below them which contribute to the resonant soft x-ray emission.

2. In addition the linear polarization of the incoming light, and the projection of this light onto the real-space crystal axes effectively determines the weighting that will arise from any individual k-point selected in the unoccupied states. That is, the proportion of the polarization selected orbital character of the band will determine a weighting for the energy-selected k-point. Thus, k-points in the occupied band structure that contribute to the emission are both selected

and are weigthed in this process. See the discussion of the Kramers-Heisenberg relation for the scattering cross section and the origin of RIXS in chapter 2.

Further to this, we must consider the orientation of the x-ray emission spectrometer with respect to the crystal axes. The dipole emission arising from the filling of a 1s core hole that propagates in a specific direction (*i.e.* towards the spectrometer) must be the real space projection of the 2p PDOS in the plane perpendicular to the direction of propagation. The normal x-ray emission recorded in this geometry would reflect an equal contribution from all possible bands within the occupied bandstructure, and as the spectrometer is not polarization selective this will reflect the sum of two orthogonal projections or components of the 2p PDOS (but not the total 2p DOS which is spherically averaged).

However, in the resonant case described above, not all k-points are selected to contribute to the emission nor are they equally weigthed. Thus for a given emission geometry (of which there are four distinct geometries in the case of a tetragonal crystal such as rutile) that determines the two axes on which the 2p PDOS is projected, the weights assigned to the selected k-points are then used to weight these two orthogonal projections and these weigthed partial densities of states are then used in simulating the resonant x-ray emission spectrum.

In principle this is different for each (i) excitation energy, (ii) orientation of the incoming linear polarization with respect to the crystal axes, (iii) orientation of the outgoing emitted photons, or axis of the x-ray emission spectrometer with respect to the crystal axes. Combining these gives a polarization dependent, symmetry selective and state selective probe of the occupied 2p PDOS. All of this is contained within the formalism if the Kramers-Heisenberg formula for resonant x-ray scattering [39, 24] as discussed in chapter 2, but on occasion it is overlooked that the measurement process involves the real space projection of two orthogonal components of the 2p PDOS contributing to the measured emission spectrum.

The final step in simulating the resonant x-ray emission spectrum is calculating the transition matrix elements between the 2p states and the 1s hole, accounting for core hole lifetime broadening, valence hole lifetime broadening and instrumental broadening. The variation in the weights of the spectral components, arising from specific metal-oxygen molecular orbitals, should correspond between the simulated spectra and the energy dependent changes observed in the experimental measurements.

3.5 Summary

The adoption of the rutile structure strikes a balance between the ionic transfer of electrons to the ligand ions in MX_2 compounds and covalent bonding σ and π interactions between the metal and ligand orbitals, giving rise to the natural linear dichroism. The spatial arrangement of the M-O σ and π states, combined with the other selection rules of the x-ray scattering process allow the weigthed occupied O $2p$ partial density of states projections along individual crystal axes to be probed independently, in a k-selective, symmetry and geometry dependent manner.

The WIEN2K formulation of DFT yields a realistic treatment of the electronic structure in covalently bonded systems. It provides a projected partial density of states from which RXES spectra can be simulated, allowing further interpretation of the experimental results.

Chapter 4

Resonant x-ray emission and absorption spectroscopy of rutile SnO_2

4.1 Introduction

Stannic oxide or cassiterite both refer to the rutile polymorph of SnO_2, which it adopts at ambient temperatures and pressures. As with most materials, the rate of development in applications for SnO_2 has overtaken the establishment of a detailed understanding of its electronic structure. The present study addresses part of that deficit by making in-depth measurements which are compared to appropriate electronic structure calculations of the valence and conduction band densities of states. This is the first time that an account of the natural linear dichroism in the O K -edge x-ray absorption and in the subsequent x-ray scattering of bulk single crystal SnO_2 due to its rutile structure has been given. Section 4.2 briefly discusses some important applications of SnO_2. Section 4.3 describes the experimental measurements that were performed. Section 4.4 presents the results of the calculated electronic structure, partial densities of states and simulated spectra, and section 4.6 discusses the results and calculations in the context of other experimental results and calculations available in the literature.

4.2 Applications of SnO_2 and motivations for study

Several of the bulk and surface properties of SnO_2 make it very suitable for a variety of electronic and chemical uses, and have led to its wide study. Three of the foremost examples of SnO_2 in such materials applications are

1. as one of a number of transparent conducting oxides (TCOs) that also includes Sn-doped In_2O_3 (indium tin oxide or ITO) and ZnO
2. as a catalyst material for gaseous reactions and as a medium for gas sensing which is its most widespread application
3. as a dielectric material in electronics that also encompasses its use as a host oxide for dilute magnetic semiconducting applications.

Each of these applications is founded on the electronic properties of SnO_2. Batzill and Diebold's review examines the development of SnO_2 materials up to the present decade [40]. The first two topics are briefly discussed in the present section, while the third topic is discussed more extensively towards the end of chapter 6.

4.2.1 Transparent Conducting Oxides

The first application listed above, transparent conducting oxides combine the ability to transmit light at optical wavelengths and conduct charge through its lattice [40]. The transparency of the material is defined by a transmission window where the short wavelength/high energy limit corresponds to the optical band gap. Above this energy absorption due to interband excitations is energetically possible. The long wavelength/low energy limit is defined by the energy of plasma excitations of the bound electrons within the system.

In an intrinsic TCO such as undoped SnO_2, defect states give rise to a donated population of electrons in the conduction band. If in turn the conduction states form a broad band with relatively high electron mobility then the factors are present for transparent conductivity [41]. Good metallic conductors tend also to be good reflectors at visible wavelengths, and TCOs are an unusual species of electronic conductor. They find uses as coatings in applications where visible light is to be transmitted, and infra-red wavelengths reflected to decrease heat loss through window glazing for instance. They also find application as transparent contacts to the active layers of optoelectronic elements such as solar-powered photovoltaic cells, or as transparent electrodes incorporated into display arrays.

Of particular importance to the TCO application is the alteration of the conduction properties of pure SnO_2 when defects are present that alter its stoichiometry. This is the case with oxygen vacancies and tin interstitials which are found to have an energy of formation low enough to expect an abundant concentration in the SnO_2 lattice (see *e.g.* [42]). Though pure SnO_2 is an insulator with a wide band-gap of

3.62 eV [43], the defects states caused by oxygen vacancies make a concentration of charge carriers available creating a higher conductivity.

4.2.2 Gas sensing and dielectric applications

In the case of redox catalytic reactions and gas sensing, the changes in the electronic structure brought about by the adsorption of gas molecules at SnO_2 surfaces provides the mechanism of action for both of these applications [40]. The results of the XPS study carried as part of the current study will contribute to the explanation of the differences between the bulk and surface electronic structure of SnO_2, though this has been explained previously [44, 9, 45].

4.2.3 Motivation

To refine the performance of SnO_2 as a dielectric medium, and to understand its role as a host oxide for charge-donating magnetic impurities (see e.g. [46]), detailed knowledge of the electronic structure is required (see *e.g.* [47]). When the electronic structure is probed by linearly-polarized x-ray spectroscopy, it is necessary to identify the changes in the valence and conduction band density of states in SnO_2 that are caused by the natural linear dichroic scattering of the rutile system from those additional features that may be associated with impurities and surface non stoichiometry.

Therefore the character and location of the states in the valence and conduction bands, associated with the various bonding and antibonding overlaps between orbitals, are questions of immediate relevance to explaining the behaviour of SnO_2 in both of the foregoing application groupings. The constituent states in the valence and conduction bands are estimated by considering the results of the spectroscopies with reference to the scattering geometry. The calculated electronic structure justifies the designations of the spectral features.

A further motivation is to study the electronic structure of SnO_2 as part of a broader study of the structurally similar rutile-type oxides, as mentioned previously, from TiO_2 a d^0 oxide, through RuO_2 a d^4 oxide and to SnO_2 a d^{10} oxide [29].

The rest of this chapter details the experiments carried out on an oriented single crystal of SnO_2 [48]. The details of its production are described in section 4.3.2. These include valence band and core level XPS of SnO_2 and the synchrotron radiation based measurements of the O K- edge x-ray absorption and O K- edge resonant x-ray emission spectra. These latter measurements employed linearly-polarized x-ray beams and the specific orientation of the crystal with respect to the beam is discussed. The interpretation of these measurements is supported, in particular, by electronic structure calculations which also simulate the resonant x-ray emission spectra obtained here.

4.3 Experimental Measurements

The present section provides details of the oriented crystal sample used during the study, and the polarization-dependent spectroscopic measurements that were carried out, as well as the x-ray photoelectron spectroscopy. The details of the sample mounting, to access the geometries necessary in the polarization-dependent study are also provided.

4.3.1 Non polarization-dependent results in the study

As we present results of x-ray photoelectron spectroscopy in the present chapter it is important to distinguish clearly between the polarization-dependent XAS and XES and the XPS results, to which the natural linear dichroism is essentially irrelevant. To begin with, the rotating anode, or any laboratory source of x-rays for that matter, is unpolarized.

Secondly, where $h\nu \gg$O 1*s* binding energy, then the photoelectron is excited into the photoionization continuum and no dichroism will be observed to exist, the 1*s* core electronic wavefunction being spherically symmetric.

For valence band XPS (VB XPS), with $h\nu \gg$ VB states binding energy, again the photoelectron is promoted to the photoionization continuum and for ionization of O 2*p* states there should be essentially no distinction even if one had a linearly-polarized source of x-rays.

Only for ultraviolet photoelectron spectroscopy (UPS) where $h\nu >$VB states binding energy will the vector product $(\overrightarrow{A} \cdot \overrightarrow{p})$ of the electromagnetic potential and the non-spherical distribution of 2*p* electrons and other symmetry elements arising from band structure will come into play, entering the domain of angle resolved photoelectron spectroscopy (ARPES). However, where the source is not polarized, the then this is averaged over all possible angles.

4.3.2 Sample Preparation

The undoped bulk single crystal SnO_2 used in the study was provided by the Egdell group of the Inorganic Chemistry Laboratory in Oxford. The crystal was grown by dissociative sublimation of polycrystalline SnO_2 powder to produce a partial pressure of SnO within a furnace. This SnO vapour was then carried to the growth area of the furnace by a flow of an inert carrier gas (N_2). In the Al_2O_3 growth crucible the SnO reoxidized to form a pillar-shaped single crystal of SnO_2 with a square cross section. Details of the growth method have been detailed elsewhere in the literature [48]. It or a similar crystal have been used in a number of studies over the years [44, 9, 49, 45, 50]. The size of the crystal is $\sim 12\,\mathrm{mm} \times 4\,\mathrm{mm} \times 3\,\mathrm{mm}$.

The largest surface is the (110) plane of the crystal. XRD was performed as described elsewhere in the present thesis to confirm the rutile c axis lay in the large surface plane, parallel to the long edge of the crystal with the two a axes both protruding from the surface at 45°.

Prior to being mounted in vacuum for x-ray spectroscopy, the SnO_2 crystal was hand polished with a diamond slurry to remove a surface layer that was deposited during the sputtering of an adjacent sample during previous experiments. It was then cleaned and degreased in the usual manner by ultrasonication in acetone, followed by isopropyl alcohol and then blow dried in N_2. The crystal is almost entirely transparent, with a slight gray shading.

To recapitulate the structural details of SnO_2: it is a rutile type compound of the $P4_2/mnm$ space group with a tetragonal unit cell [29]. The coordination of the Sn is in an octahedral SnO_6 which edge shares in a direction parallel to the c axis. The local planar coordination of oxygen atoms is in Sn_3O planes and in the rutile unit cell these planes are all vertical containing the c axis. The unit cell is defined by three mutually perpendicular crystal axes of which two are of equal length, the a axes, and a third unequal c axis. The axes have length $a = 4.7397$ Å, $c = 3.1877$ Å and the internal parameter $u = 0.3058$.

4.3.3 Sample mounting for polarization-dependent study

The SnO_2 single crystal was mounted on a sample plate with the (110) face parallel to the plane of the plate. This was transferred through the load lock system at I511-3 and mounted on a 6-axis manipulator (x, y, z polar θ about x, azimuthal rotation about the sample normal ($\pm 90°$) and a tilt of about $-10° \rightarrow 45°$).

The long axis of the crystal was oriented in the horizontal plane. The XAS spectrum obtained at normal incidence of the photon beam onto the (110) surface of the SnO_2 crystal has the linearly-polarized light in the horizontal plane parallel to the [001] direction which is collinear with the c-axis. This is designated $\mathbf{E}||c$. To obtain a spectrum corresponding to $\mathbf{E}||a$, the crystal is rotated by 90° about the normal to the plane, and then a polar rotation of θ by 45°. The photon beam is then incident at 45° to the (110) surface, proceeding along [010] (or [100]) directions. The electric field vector of the linearly-polarized light is thus along [100] (or [100]), the a-axis and thus $\mathbf{E}||a$, the c- axis being oriented vertically.

In some instances an exact scattering geometry would require the photon exit angle to be at zero degrees from the surface with the beam normally incident onto the sample, where the emission spectrometer is at 90° to the beam direction. To allow photons from the illuminated area of the sample surface to reach the emission spectrometer, a "grazing-exit" geometry is necessary with an exit angle to the surface of about 15° – 20°. The incident angle onto the surface is then about 75° – 70° respectively. Thus for the in-plane $\mathbf{E}||c$ RXES measurement geometry an additional polar rotation of about 15° away from the exact normal incidence geometry used to obtain the O K- edge $\mathbf{E}||c$ XAS is required. The XAS is repeated in this approximate $\mathbf{E}||c$ geometry to guide the choice of resonant excitation energies.

4.3.4 Valence Band and Core level XPS of SnO_2

The XPS studies were carried out at the UK National Centre for Electron Spectroscopy and Surfaces (NCESS) at Daresbury Laboratory, UK. using a monochromated Al K_α rotating anode source. A detailed description of the apparatus and sample preparation for this experiment is given elsewhere in this thesis. It is the total density of states in the valence band that is probed in the spectra rather than the element specific orbital resolved partial density of states accessible in XES. The energy scale of the spectrometer is calibrated by imposing a solid shift with respect to a reference value of the adventitious carbon $1s$ binding energy.

4.3.5 O K-edge XAS of SnO_2

The O K edge x-ray absorption experiments reported in this chapter were carried out at soft x-ray undulator beamline I511-3 at MAX II synchrotron at MAXlab in Lund, Sweden. A detailed description of the experimental setup is located elsewhere in this thesis (see chapter 2). The resolution of the beamline monochromator was set to ~ 0.1 eV for the XAS spectra. The spectra were recorded in both TEY and PFY mode, using the sample drain current and a MCP respectively. The energy scale of the monochromator was calibrated with respect to the first π^* peak in the O K-edge of TiO_2 [51].

4.3.6 O K-edge XES of SnO_2

Taking into account the dipole, space and symmetry selection rules described in elsewhere, the RXES spectra give a direct measure of the occupied oxygen $2p$ PDOS of specific bonding orbitals that form the valence band of SnO_2, and also the hybridized contribution of the metal cation orbitals to these states. It is only in single-crystal rutile type oxides that the symmetry selectivity of the scattering can be completely decoupled from the photon energy dependence, as described in section 4.5. The RXES measurements were also made at MAXlab beamline I511-3, using a Nordgren-type grazing-incidence spherical grating spectrometer. The monochromator resolution was set to $\sim 0.5\,\mathrm{eV}$, which combined with the spectrometer resolution of $0.4\,\mathrm{eV}$ yields an overall approximate resolution of $\sim 0.7\,\mathrm{eV}$ in the O K edge spectra.

To access the four separate scattering geometries the spectra were recorded for both in-plane and out-of-plane spectrometer orientations. The energy window of the emission detector was calibrated with reference to a Zn $L_{\alpha,\beta}$ emission line in second order, and further with reference to the elastic peaks in the spectra where they were available for some of the scattering geometries.

4.4 Experimental Results

The results of the x-ray spectroscopy are included partly in the present section, where the individual features of the spectra are described. The rest of the results are located in section 4.5, where they are presented alongside the O and Sn partial density of states and the simulated RXES spectra.

4.4.1 Valence Band XPS

The VB XPS spectrum is shown alongside a non-resonant XES spectrum in figure 4.1, and it consists of three main peaks, and discussed at length in earlier XPS studies of SnO_2 surfaces [9, 44, 45, 52]. The first peak at a binding energy of 5 eV has been attributed to O $2p$ π bonding or non-bonding states, while the two peaks at 7.5 eV and 11 eV binding energy have likewise been assigned to O $2p$ - Sn $5p$ σ and O $2p$ - Sn $5s$ hybridized states respectively. McGuinness *et al.* were the first to directly compare the VB XPS spectra of SnO_2 with the non-resonant XES spectrum of, in the earlier case of McGuinness *et al.*, an emission spectrum from SnO_2 powder [10]. The non-resonant XES spectrum from this work shown in the lower panel of figure 4.1 has been obtained at MAXlab in the E$||c$, XES $||c$ geometry from the single crystal as described.

At the top of the VB density of states there is a ledge of occupied states tailing off into the bandgap. This density of states within the band gap has been noted before in polycrystalline doped SnO_2 samples and was associated with the surface composition of the sample. Its origin was attributed to a Sn $5s$-$5p$ hybrid state formed under the influence of the electric field gradient between the 50% of surface Sn atoms that have been reduced to Sn (II) and the Sn (IV) in the bulk [9].

4.4.2 O K-edge XAS of SnO_2

The spectra recorded for the two orthogonal orientations of the SnO_2 single crystal with respect to the linearly-polarized photon beam, in brief the two polarizations, are shown in figure 4.2 and exhibit the large degree of linear natural dichroism present in rutile SnO_2. The O K-edge XAS spectrum of SnO_2 has been reported previously by McGuinness *et al.* [10] for powdered SnO_2 , by Figuereido *et al.* [53] for a sample of natural cassiterite among others. None to date have observed the natural linear dichroism reported here. The O K-edge XAS from the SnO_2 powder represents the averaged polarization over all possible orientations of a crystal.

The O K-edge spectra shown in figure 4.2 are normalized to unit area. The O $2p$ - Sn $5sp^2\sigma^*$ states in the conduction band at 533.9 eV are strongly selected when the polarization vector of the x-rays is oriented parallel to the crystalline c axis. The declining weights of the conduction band peaks with increasing energy in the E$||c$ orientation is reversed when the polarization is switched to be parallel to one of the a axes, $\mathbf{E}\perp c$. Then the highest energy peak at $\sim$ 541 eV is dominant. Where the only possible excitation in the E$||\,c$ polarization is into σ^* anti-bonded states, the E$||\,a$ polarization permits both σ^* and π^* to be excited. This shifts the majority of the spectral weight in the E$||\,a$ orientation to the peaks higher in the conduction band as the π^* states become accessible. In both orientations the onset of absorption into the O $2p$-Sn $5s$ hybridized states in the conduction band occurs at the same energy.

4.4.3 O K-edge XES of SnO_2

From the example included in figure 4.1 it is clear that the XES spectra at the O K-edge are composed of three main features, corresponding to those observed in the

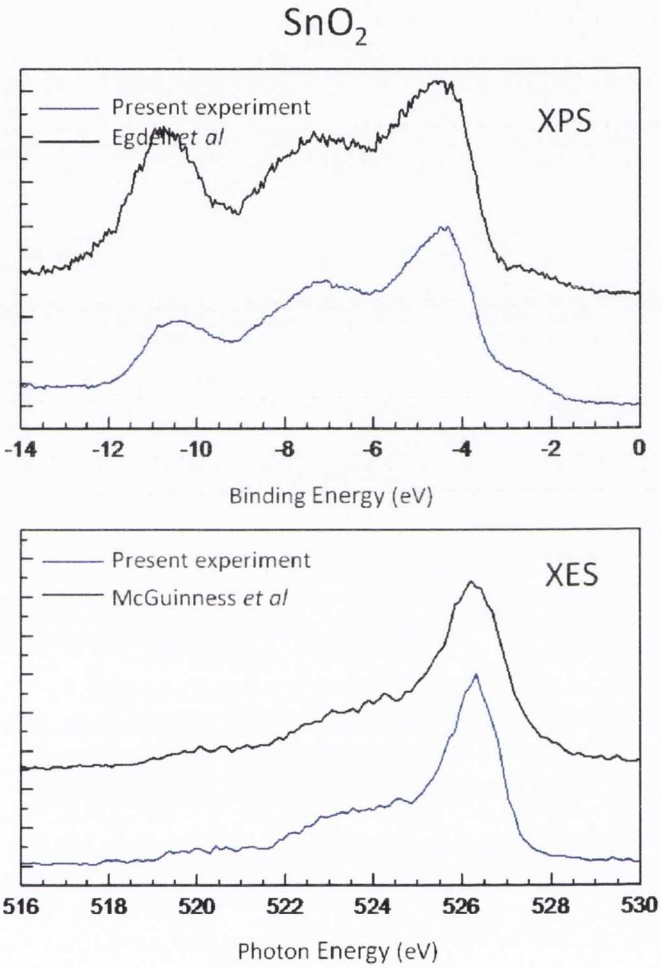

Figure 4.1: Valence band XPS compared to the results from bulk single crystal rutile SnO_2 by Egdell *et al.* [9], and O K-edge non-resonant XES from bulk rutile SnO_2 $\mathbf{E}||c$, XES along c, compared to the results by McGuinness *et al.* from a powdered SnO_2 sample [10].

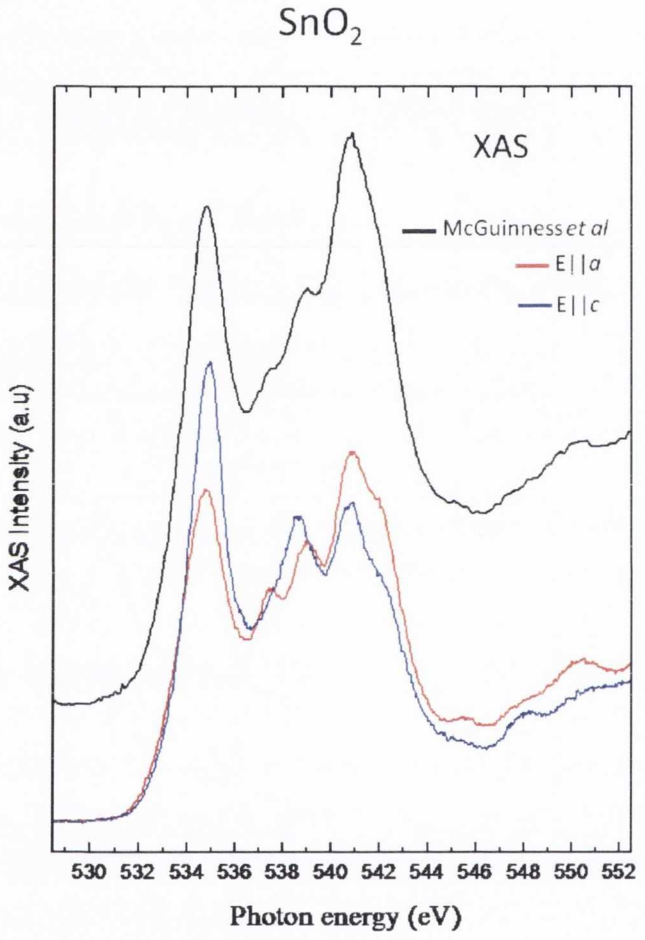

Figure 4.2: Rutile SnO$_2$ O K-edge XAS with **E**$||a$ and **E**$||c$, and O K-edge of unoriented powdered SnO$_2$ from McGuinness *et al.* [10].

VB XPS spectra. As XES provides an element-specific orbital-selected measure of the valence band partial density of states, in this case the O $2p$ character of the regions of the valence band identified in the XPS spectrum is uncovered, through our excitation-dependent measurements.

The highest energy emission peak is rather sharp and is due to the O $2p$ π-like non-bonding states at the top of the valence band that are relatively non-interacting and non-dispersing. The subsequent shoulder and third feature represent the O $2p$ hybridized orbitals which make σ bonds with the Sn $5p$ and $5s$ orbitals respectively. The weakness of the third feature in the XES spectrum indicates the relatively low degree of hybridization between the O $2p$ and Sn $5s$ states at the bottom of the valence band.

No evidence of the additional density of states that extends into the bandgap that was observed in the VB XPS spectra was seen in the XES, which argues against an oxygen character, as has already been explained in section 4.4.1. However, it should also be noted that the XAS is a bulk measure of the density of sates and since the photon attenuation below the O K-edge absorption onset is ~ 200 nm the average depth of the emission can be calculated to be $\sim 25\,\text{nm}$ in a 45° in - 45° out geometry.

Figure 4.3 gives an overview of the RXES spectra that were recorded in the present study. The excitation energies are indicated in the first panel with the associated states in the valence band. Elastic peaks are visible in the out of plane geometries. The relative intensity of the feature at 523.5 eV varies most between different orientations. The origins of this variation are clear when comparison is made to the calculated densities of states and difference spectra are computed to isolate the O $2p$ partial density of states projected on the crystalline c axis.

4.5 Electronic Structure Calculations

Density functional theory in the WIEN2k formulation has been used to calculate the electronic band structure of bulk SnO_2.

As with any electronic structure calculation, not only is the total density of states available but so are the various partial densities of states, as well as the individual projections of these partial densities of states along either (approximately) particular Sn-O bonding axes or along the real-space crystalline axes.

A number of previous electronic structure calculations of SnO_2 have been summarized by McGuinness *et al.* [54]. These range from Robertson [55], Sherwood [56],

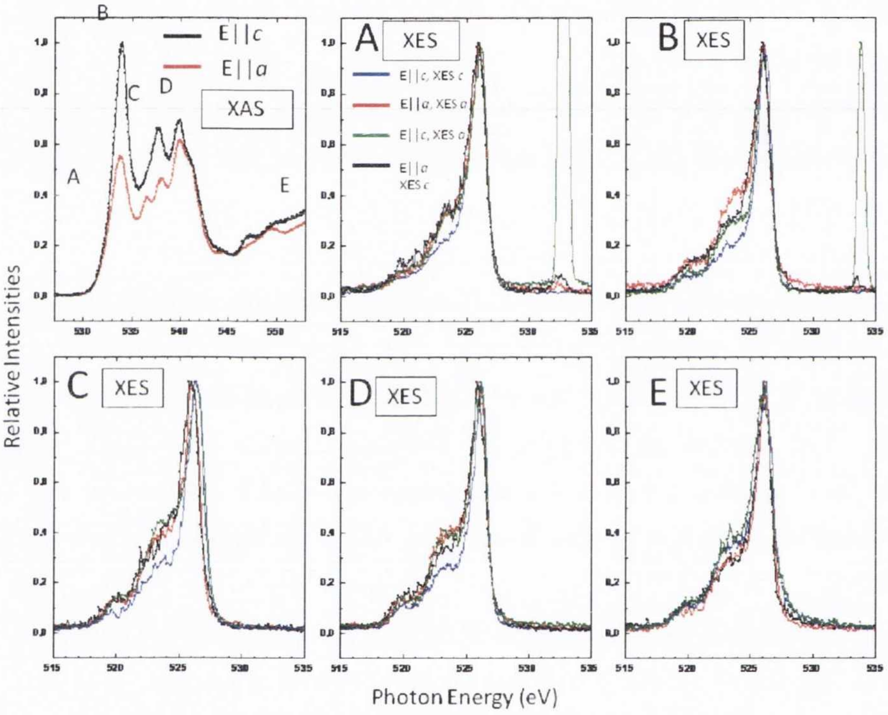

Figure 4.3: O K-edge XAS and RXES from bulk single crystal SnO_2. The four unique combinations of absorption and emission alignments of electric field vector, crystal axis and emission spectrometer are listed in the legend for RXES excitation energy A.

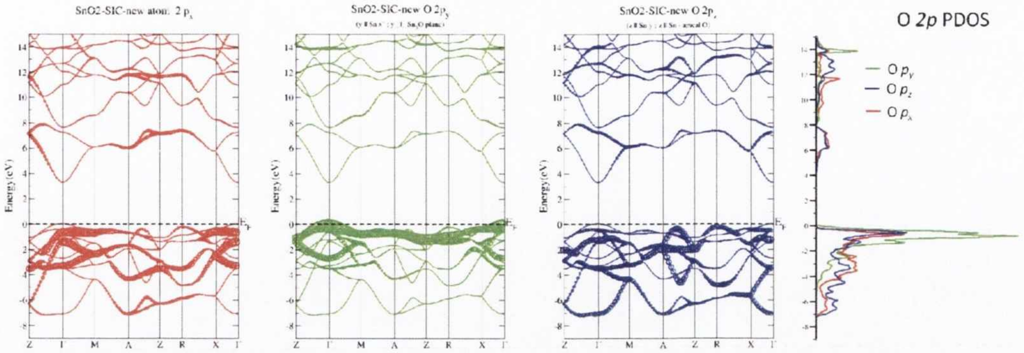

Figure 4.4: Band structure diagram and O $2p$ band character plots and PDOS projected on the natural basis set of axes of the LDA+U^{SIC} calculation for SnO_2

Medvedeva *et al.* [57] and Munnix *et al.* [58]. More recently these should include Godin [43], Reimann [59], Godinho [42], Liu [60], Hamad [61], Mi [62], and Persson [63] [64] among others.

The majority of these are LDA calculations, usually with the augmented plane wave framework. The most useful from the point of view of comparison with experiment are those of Persson [65, 66] albeit with an emphasis in these papers on optical excitation. When any calculation of electronic structure has satisfactorily converged, one of the first outputs to consider is the band structure diagram showing dispersion of bands along high symmetry directions in the reduced Brillouin zone. A particular partial component of the DOS, the contribution of that to a particular band is displayed by the weight of the line representing that band, as shown in figures 4.4 and 4.5.

4.5.1 Application of the self interaction correction (LDA+U^{SIC})

The details of the WIEN2k formulation of DFT using full-potential augmented linearized plane waves are laid out in chapter 2. Within this framework the electronic structure, and the total and partial density of states of SnO_2 was calculated using both a standard WIEN2K density functional theory calculation with experimental lattice constants and optimised u, and a non-standard modification of the local density approximation (LDA). The two approaches were attempted as in some circumstances standard DFT fails to calculate the correct bandgaps. The non-standard calculation was performed using a LDA+U^{SIC} type potential which effectively incorporates a spatial delocalization of the p states in the system while localizing the d states via

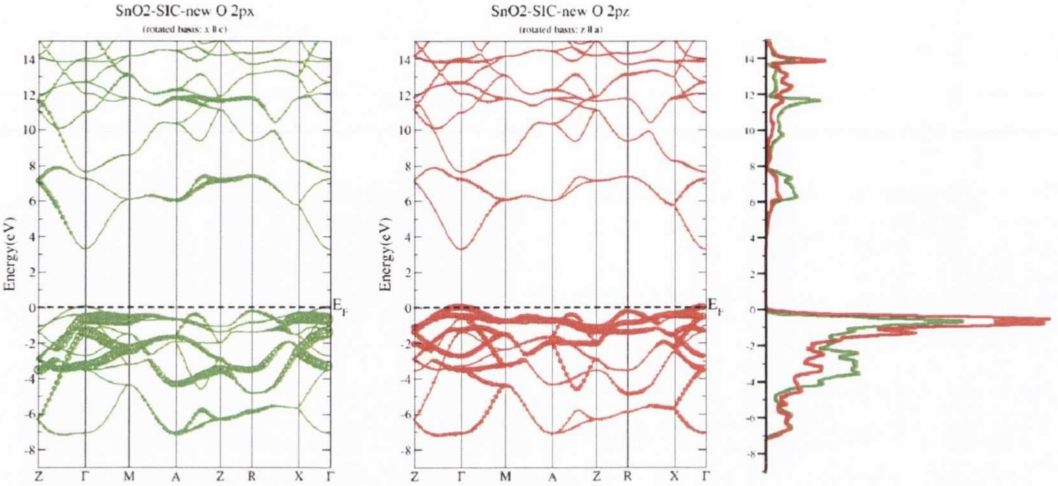

Figure 4.5: Band structure diagram and O $2p$ band character plots and PDOS projected on the rotated basis set of axes corresponding to the crystalline a and c axes of the LDA+$\mathrm{U}^{\mathrm{SIC}}$ calculation for $\mathrm{SnO_2}$

a Coulombic self-interaction-like correction (SIC) optimized to reproduce the correct optical band gap for $\mathrm{SnO_2}$. Details of the SIC approach are to be found in the reports of Persson *et al.* [66, 67, 65] using approaches outlined earlier [68, 64].

From this result the total density of states, and the partial density of states resolved by ion and quantum number l are obtained. Furthermore, the projections of the density of states onto a natural system of orthogonal axes for Sn and O, and a rotated basis set in which this natural set is transformed onto the crystalline axes is deduced from the electronic structure plot. The RXES spectra are in turn simulated from these projected densities of states, incorporating a combination of the crystal momentum conservation and space selectivity of the scattering geometry.

RXES spectra were simulated for a number of excitation energies by producing linear combinations of the crystal momentum weighted partial density of states projected onto the real space crystalline axes (rotated basis set), depending on the relative orientation of the x-ray spectrometer, single crystal and linear polarization.

4.5.2 Comparison of SIC and standard calculation

The principal difference between two methods, the LDA and the LDA+$\mathrm{U}^{\mathrm{SIC}}$ (the results of both calculations are shown in figure 4.6) is the more accurate (adjusted) bandgap energy of ~ 3.5 eV. The LDA approach gives a bandgap of ≤ 2.0 eV . Further, there is an improved representation of the bottom of the conduction band

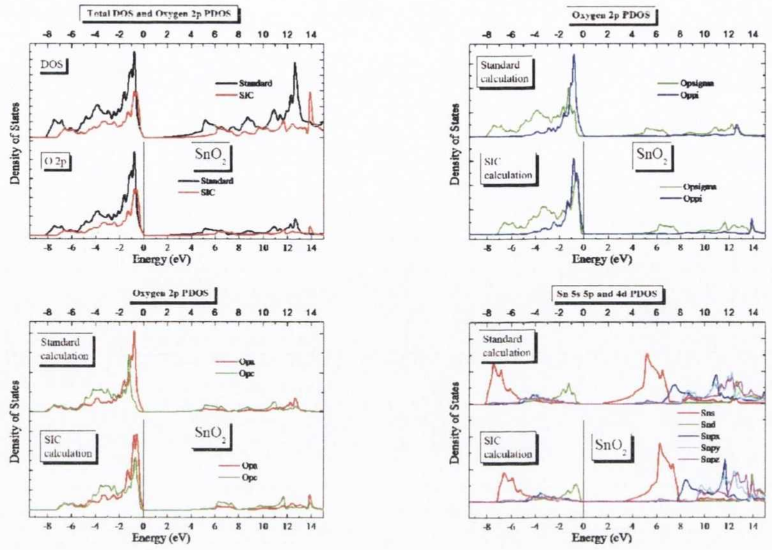

Figure 4.6: A comparison between the standard LDA and LDA+U^{SIC} calculated O 2p PDOS and Sn s, p, and d PDOS for SnO$_2$

by narrowing the dispersion of the Sn 5s states. Optical excitations are better modeled where, in particular, the dispersion or effective heavy hole mass in the non-bonding orbital is more accurately represented [65]. The LDA+U^{SIC} calculation results in a narrower valence band than the standard calculation, with an overall width of 7 eV compared to 8eV. The conduction band density of states are shifted to higher energies and the relative weights are somewhat redistributed, thought the overall width of the O 2p component of the conduction band is very similar for both calculations. The O 2p PDOS at the top of the valence band shows a striking difference between the LDA+U^{SIC} and standard calculation. This is evident in both the rotated basis set projected and the σ, π-resolved PDOS in figure 4.6. The PDOS projected onto the crystalline c axis has its centre of gravity shifted closer to the Fermi energy in the LDA+U^{SIC} calculation. This is because the O 2p σ states hybridized with the Sn 4d PDOS is shifted higher in the valence band for the non-standard calculation.

Figure 4.7 overlays the calculated O and Sn partial density of states (PDOS) for SnO$_2$ calculated via the LDA+U^{SIC} scheme. The top panel shows the combined O 2p PDOS and the Sn 5s, 5p and 4d PDOS. The main 4d peak is not shown, but appears at a binding energy of ~ -22 eV with respect to the Fermi level in good agreement with shallow core level XPS [54, 52].

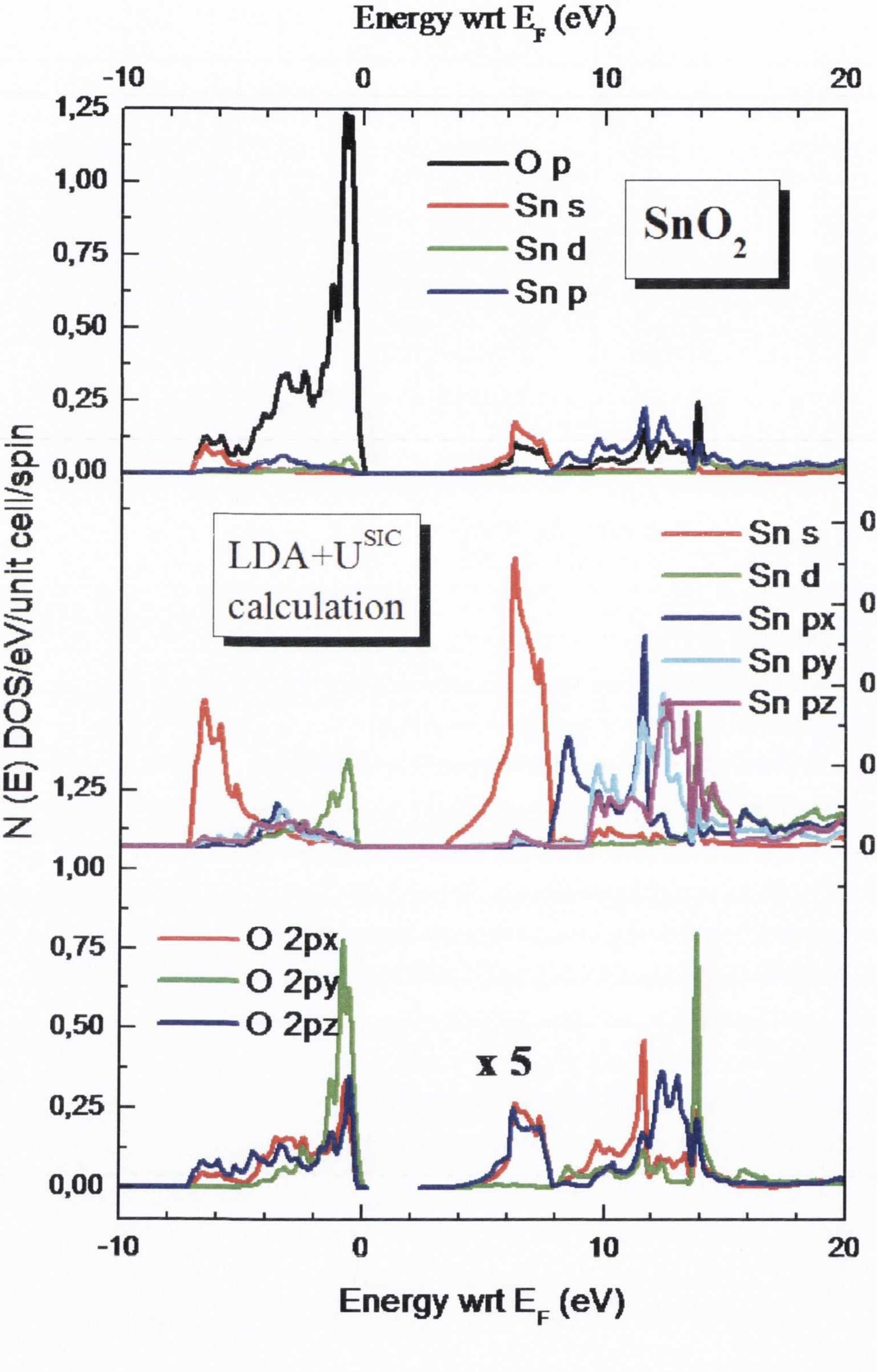

Figure 4.7: Combined LDA+U$^{\mathrm{SIC}}$ calculation of the O $2p$ and Sn s, p and d PDOS for SnO_2 (upper panel), the Sn s, d, and p_x, p_y, p_z PDOS (middle panel) and the O $2p_x$ $2p_y$ and $2p_z$ PDOS (lower panel). The orthogonal projections are in the natural basis set with $y \perp SnO_3$, $x || c$ and $z \perp c$ but within Sn_3O plane and parallel to Sn-O apical bond direction.

The middle panel shows the Sn PDOS with a more magnified vertical scale than the top panel and the Sn $5p$ states split in the three components along the x, y and z axes defined within the calculation. This orthogonal xyz basis has its z axis along the Sn-O apical direction for both the Sn and O atom. This corresponds to the [110] direction in the rutile unit cell which defines the central axis of the SnO_6 octahedron passing through the central Sn and apical O atoms. The z direction also lies within the Sn_3O plane, as does the x axis, which is parallel to the crystallographic c axis. The y axis is oriented perpendicular to the Sn_3O plane.

The bottom panel shows the three orthogonal projections of the oxygen $2p$ PDOS. The states projected on the x and z axes are within the Sn_3O plane and are derived from the sp^2 hybridized Sn-O σ bonds which lie within the Sn_3O plane. The y axis projected density of states reflects the Sn-O π-like bonds which are perpendicular to the Sn_3O plane. The vertical scale of the conduction band density of states is expanded by a factor of five to allow for more ready comparison.

4.5.3 O $2p$ PDOS projected onto a rotated basis set

In figure 4.8 the lower panel shows the O $2p$ PDOS of SnO_2 which are divided between those states which are sp^2 derived Sn-O σbonds within the Sn_3O plane ($p_x + p_z$) or Sn-O π -like bonds that are perpendicular to the Sn_3O plane (p_y). This designation of the xyz axes is the natural coordinate frame from which to consider O bonding.

A useful alternative way of viewing the O $2p$ PDOS is to consider the PDOS as projected onto the three orthogonal crystal axes within the tetragonal rutile unit cell. This coordinate system is referred to as the rotated basis set. Only two crystal projections are shown as the rotated basis set mixes the p_y and p_z components of the natural basis set and projects them along the $\{100\}$ and $\{010\}$ crystallographic axes, which are equivalent to each other, this being denoted the projection along the rutile a axis. The projection along the rutile c axis is identically equal to the earlier p_x component in figure 4.7.

4.5.4 Conduction band: O K-edge XAS vs. O $2p$ PDOS in rotated basis set

Figure 4.9 compares the O K-edge XAS of SnO_2 and the O $2p$ PDOS. The upper panel shows the XAS obtained with a 0.1eV resolution at MAX-lab beamline I511-3 in March 2006. The spectra were obtained in TFY mode with the crystal oriented such

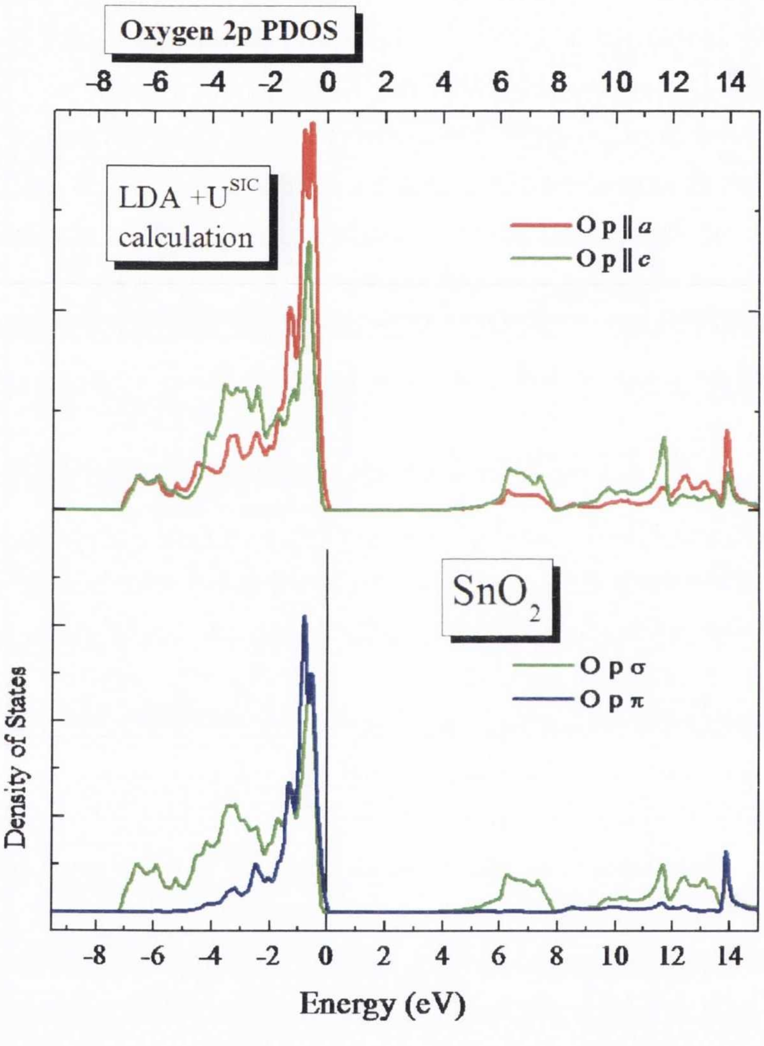

Figure 4.8: The σ,π (lower panel) and crystalline-axis projection (upper panel) of the calculated O $2p$ PDOS in the valence and conduction band for rutile SnO_2.

that the linearly-polarized x-rays were either exactly parallel to the rutile c-axis or to the rutile a-axis. For the (110) face of the single crystal in question this corresponds to the c-axis in the horizontal plane and with normal angle of incidence, or the c-axis in the vertical plane of the laboratory frame of reference and an angle of incidence of 45°.

The lowest panel shows the unoccupied O $2p$ PDOS as either sp^2 derived Sn-O σ bonds in the Sn_3O plane (the $(p_x + p_z)$ projection), or as π-like bonds perpendicular to the Sn_3O plane (the p_y projection). The middle panel shows the O $2p$ PDOS projected along the rutile a - and c - axes respectively and can be usefully compared to both the natural basis in the lower part which show the origin of the features and the XAS spectra obtained with linearly-polarized light in the upper panel.

The unoccupied PDOS shown here is unbroadened. Broadening to match the experiment would take into account the Gaussian instrumental resolution (0.1eV) and the Lorentzian core-hole lifetime broadening (0.3 eV) as well as excitonic effects and final state rules which are not taken into account in this straightforward comparison with the calculated O $2p$ PDOS.

4.5.5 Simulated RXES spectra

The simulation of the RXES spectra at the O K-edge using the calculated rotated-basis O $2p$ PDOS will been described in detail for the example of the RuO_2 calculations. RXES were calculated for the ten different excitation energies indicated by the arrows in the calculated unoccupied $2p$ PDOS given in Rydberg energies in figure 4.10. In addition a non-resonant XES spectrum for the emission geometries is calculated.

The following figures 4.11 to 4.14 present a sample of the calculated RXES spectra compared to the corresponding experimental spectra for excitation energies 1) at the threshold of absorption, 2) at the first peak in the absorption spectrum formed by the Sn-O σ bonds in the Sn_3O plane, 3) at the third peak in the absorption spectrum $\sim$ 4 eV above threshold, 4) at the fourth peak in the absorption spectrum which is $\sim$ 6 eV above threshold and 5) a non-resonant excitation energy $\sim$ 20 eV above the onset of absorption. These excitations are labeled A, B, C and D in figure 4.3 . Their energies are 533.2 eV, 534.0 eV, 537.4 eV and 539.4 eV respectively.

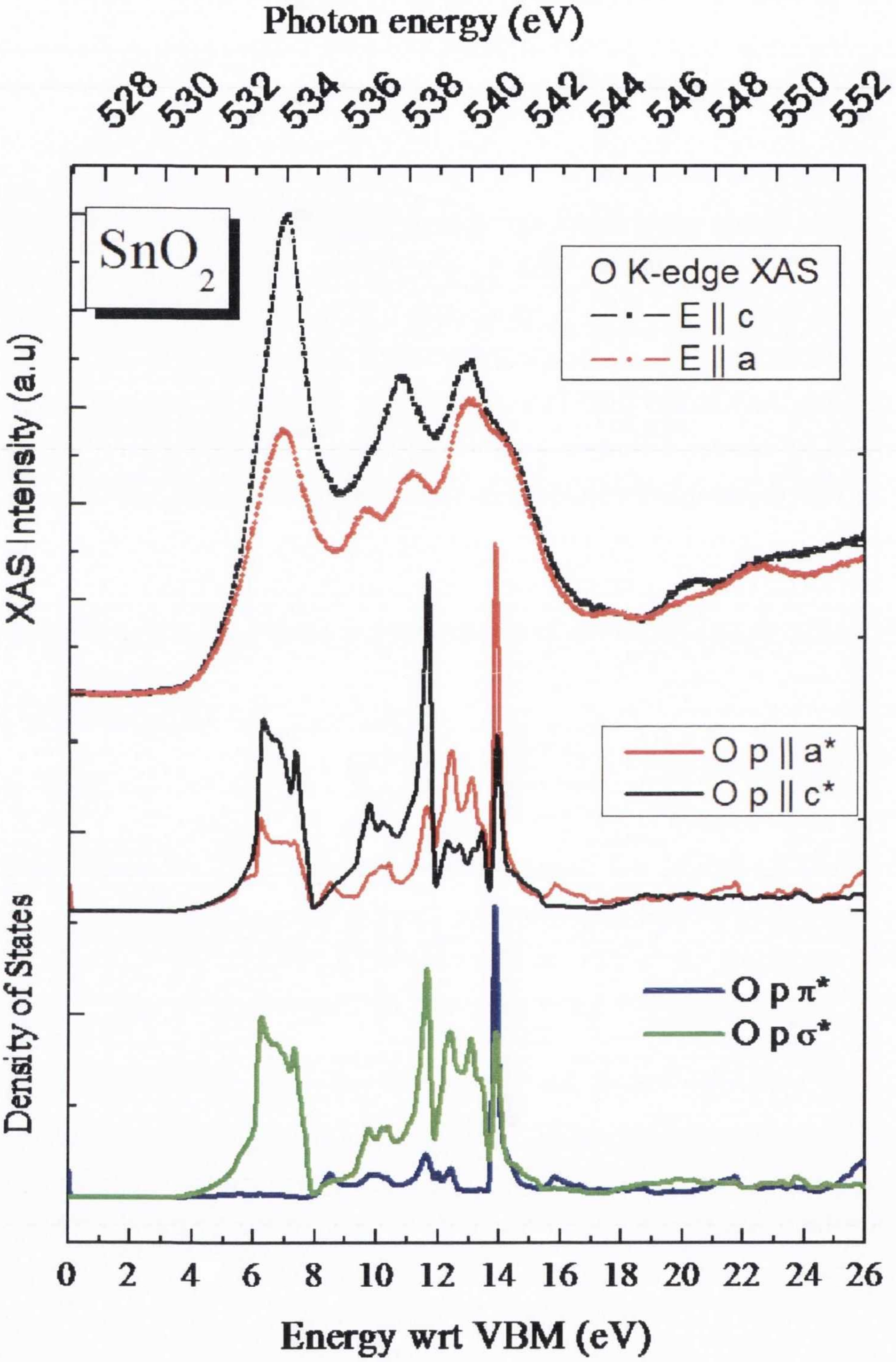

Figure 4.9: O *K*-edge XAS compared to the symmetry and crystalline axis projected O 2*p* PDOS in the conduction band of rutile SnO_2

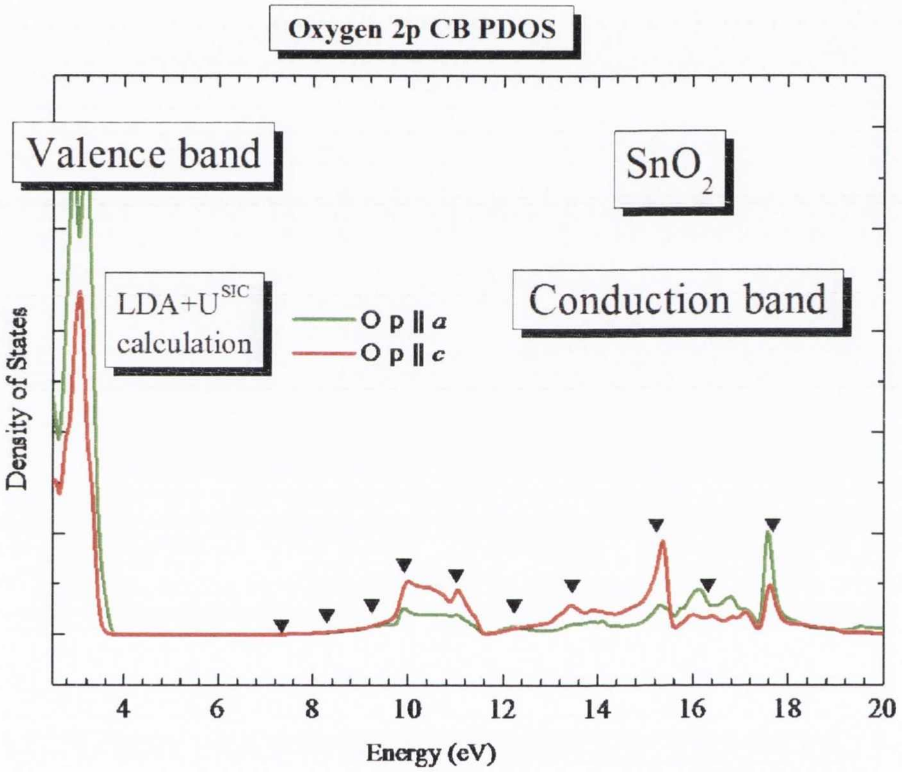

Figure 4.10: Excitation energies selected for the simulated RXES spectra. The energy scale internal to the calculations is in Rydbergs with the energy calculated on an absolute basis.

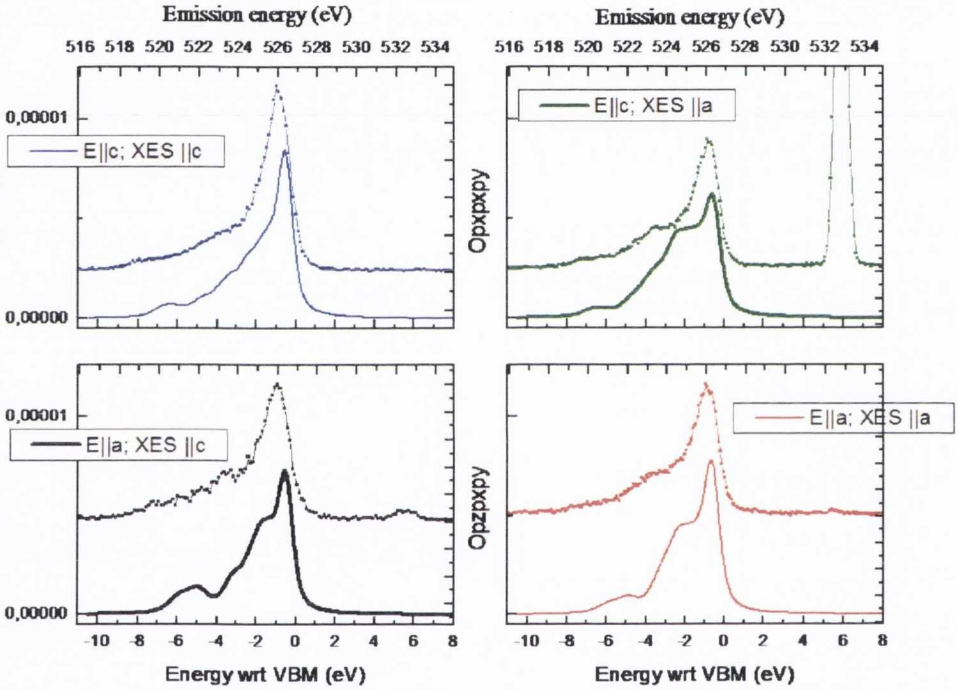

Figure 4.11: Rutile SnO_2: simulated and measured RXES for a threshold excitation of 533.2 eV corresponding to excitation A in figure 4.3, and the third marker in figure 4.10

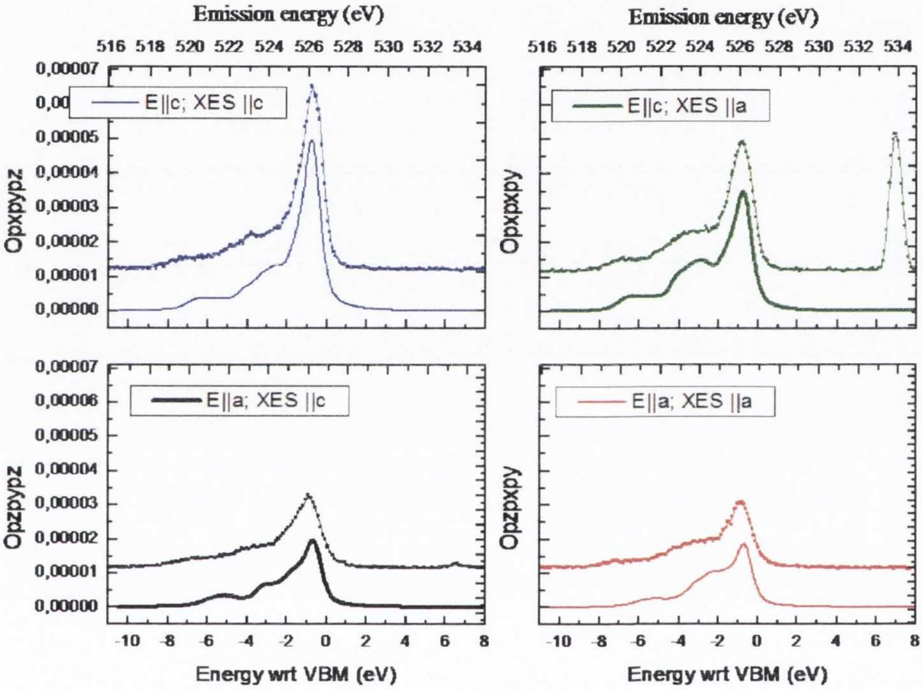

Figure 4.12: Rutile SnO_2: simulated and measured RXES for a threshold excitation of 534.0eV corresponding to excitation B in figure 4.3, and the fourth marker in figure 4.10

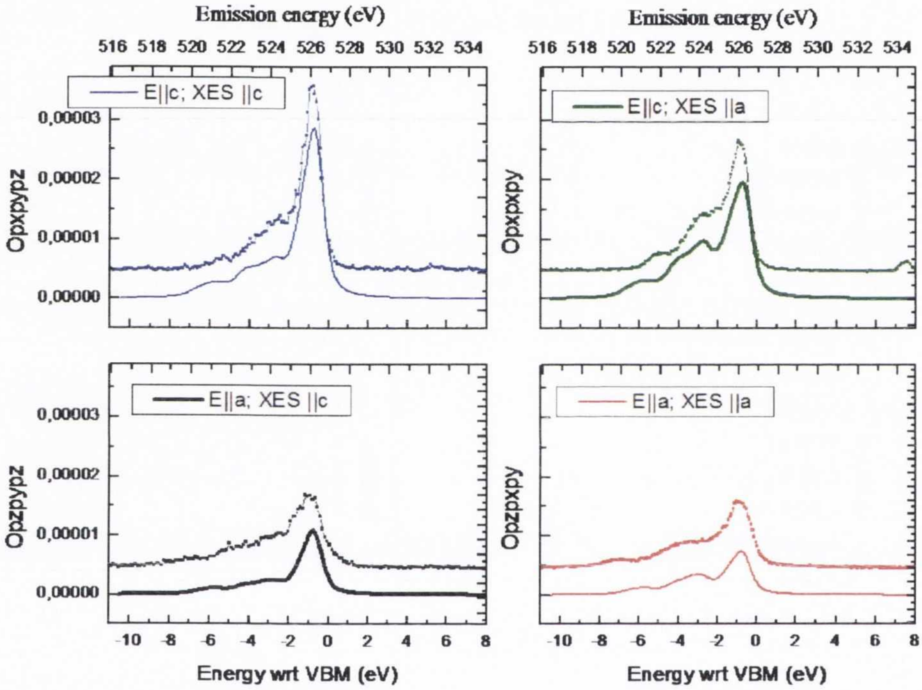

Figure 4.13: Rutile SnO_2: simulated and measured RXES for a threshold excitation of 537.4 eV corresponding to excitation C in figure 4.3, and the seventh marker in figure 4.10

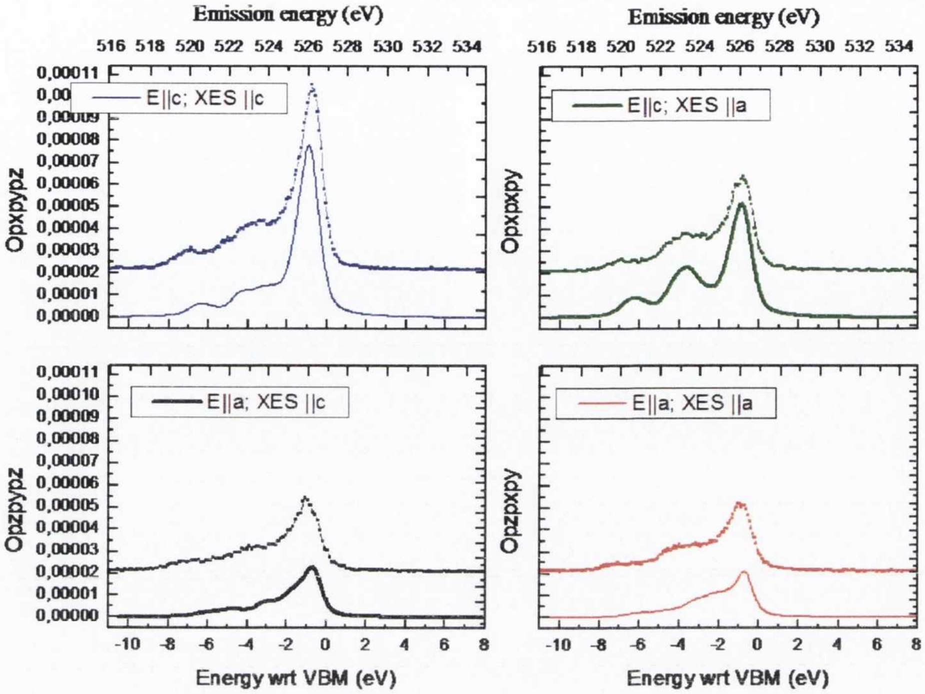

Figure 4.14: Rutile SnO_2: simulated and measured RXES for a threshold excitation of 539.4eV corresponding to excitation D in figure 4.3, and the eighth marker in figure 4.10

When the experimental spectra in the different orientations are scaled to the same relative intensities as the calculated emission spectra, their correspondence with the calculated spectra is clearly apparent. The decrease in the signal to noise ratio with decreasing photon energy and the offset in the alignment of the crystal axes and the polarization vector necessitated by the experimental setup represent sources of disparity in the comparison. However the relative intensities and widths of the features in the emission spectra show remarkable agreement.

In particular, the width of the main peak and the relative intensity of the lower energy shoulder and tail compared to the main peak follows the trend predicted by the calculations. In the E$||c$, XES along c geometry for instance, the main peak in the spectrum at the highest photon energy that corresponds to the O $2p$ π bonded states is at its most intense. The low energy shoulder of this main peak represents a greater fraction of the spectral weight in the spectra recorded with the XES along one of the a axes.

4.5.6 Difference spectra for non-resonant energies and the first peak

The qualitative agreement between the simulated and experimental spectra is emphasised even more strongly by producing difference spectra using both the non-resonant and resonant experimental spectra for the same excitation geometry with the emission spectrometer aligned along an a-and c-axis. Where resonant spectra with a single axis projection, either along a or c are trivial to produce from the calculations, experimentally the actual non-resonant XES reflect the sum of two orthogonal polarizations, *i.e.* the projected partial densities of states in the plane defined by the two axes orthogonal to the direction of emission.

The calculated non-resonant spectra (NXES) projected along single axes are shown in figures 4.15 and 4.16. While the same single axes projections are not directly accessible experimentally, they can be extracted from the experimental spectra by appropriate normalization, and subtraction after applying multiplicative factors derived from the spectral weight ratio for the calculated projections along the c and a axes respectively. The results of this spectral subtraction correspond well with the spectra predicted by the single axis projected calculations for the non-resonant excitation energies for both E$||a$ and E$||c$ orientations. This result is the strongest evidence we can provide of the reasonableness of the LDA+$\mathrm{U}^{\mathrm{SIC}}$ calculation, and the crystal axis-projected density of states.

The same subtractions carried out for the excitation energy corresponding to the first peak in the absorption spectrum showed a similar qualitative agreement. The resonant energy difference spectra also indicate that for the same selected k-points there is a significant difference between the XES spectrum projected along the c axis for E$||a$ and E$||c$. This can be contrasted where a differing set of intermediate k-points are selected, *i.e.* with **E**$||c$ in XAS versus **E**$||a$ in XAS, as for instance in figures 4.17 and 4.18, where the spectra shown in the respective figures differ only by the intermediate state selected by the absorption and hence a differing weighting of k-points contributing to emission.

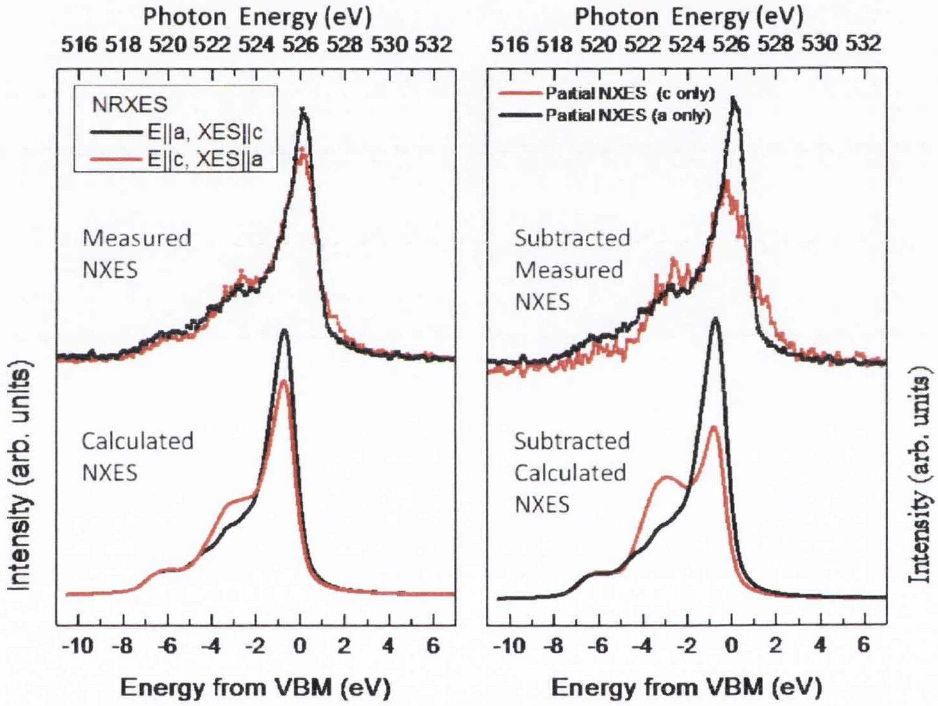

Figure 4.15: Difference Spectrum between E$||a$ XES $||c$, and E$||a$ XES $||a$ for resonant energy B in figure 4.3, fourth excitation energy in figure 4.10

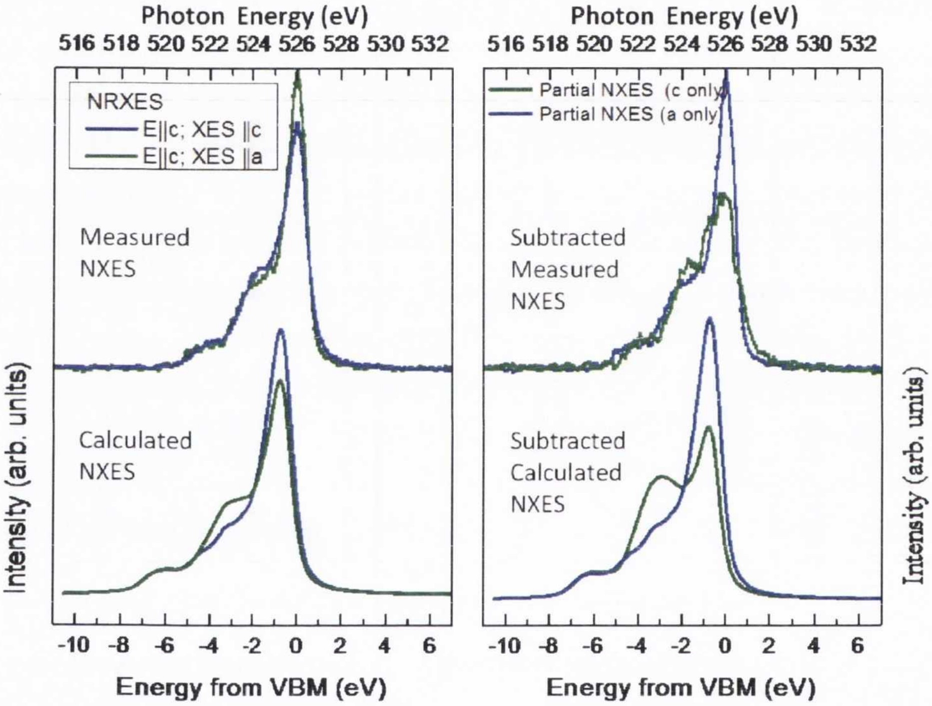

Figure 4.16: Difference Spectrum between E$||c$ XES $||a$, and E$||c$ XES $||c$ for resonant energy B in figure 4.3, fourth excitation energy in figure 4.10

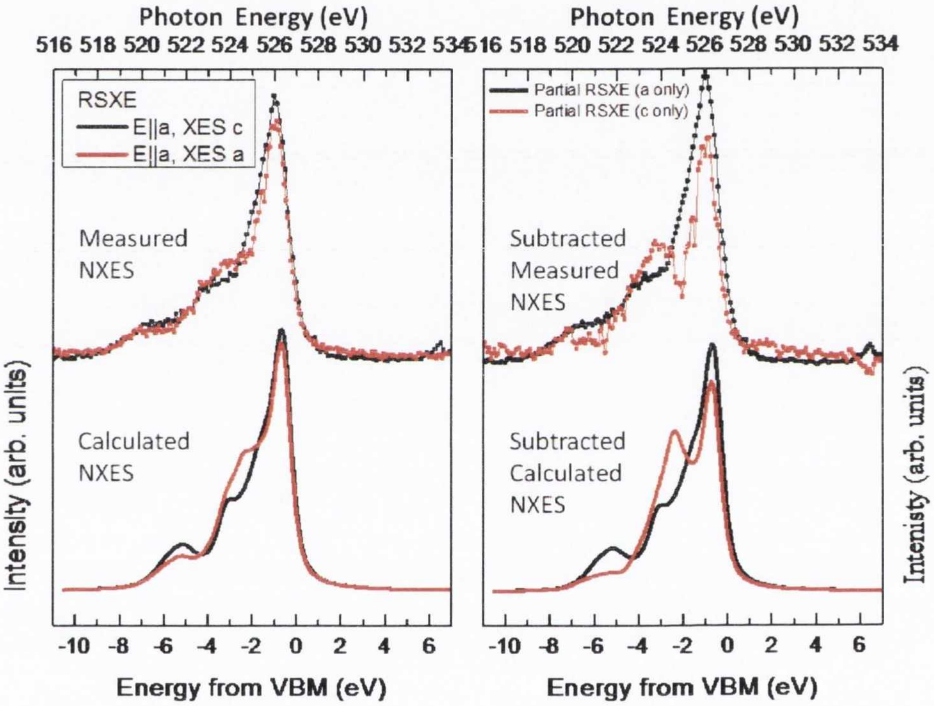

Figure 4.17: Difference Spectrum between E$||a$ XES $||c$, and E$||a$ XES $||a$ for resonant energy E in figure 4.3, tenth excitation energy in figure 4.10

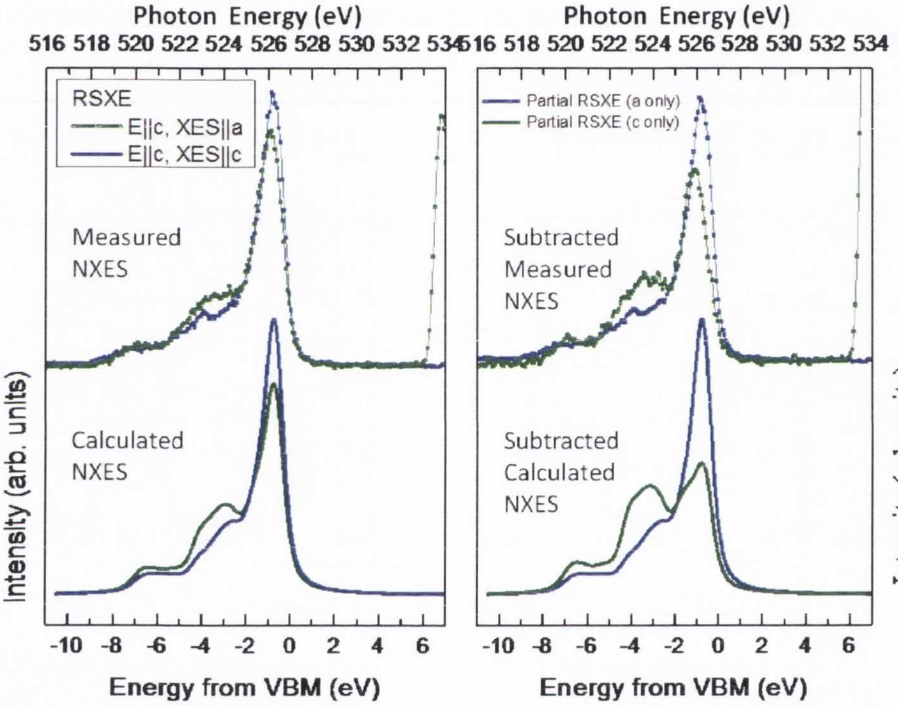

Figure 4.18: Difference Spectrum between E$||a$ XES $||c$, and E$||a$ XES $||a$ for resonant energy E in figure 4.3, tenth excitation energy in figure 4.10

4.6 Discussion

In the molecular orbital scheme for a rutile-type transition metal oxide, the filling of the valence band states in the M_2O_4 energy level diagram results in the top of the valence band being composed of states derived from Sn-O σ bonds, overlapping with a band derived from Sn-O π-type bonds [7]. The bottom of the conduction band is formed by Sn 5s states followed by unfilled Sn-O σ^* antibonding states. The partial filling of the σ band gives rise to the presence of states of both σ and π symmetry at the top of the valence band in SnO_2.

4.6.1 O K-edge XAS

Figure 4.9 contains the O K-edge XAS presented alongside the O 2p PDOS projected onto the rotated crystallographic basis set and the symmetry-resolved O 2p PDOS. In the O K-edge absorption spectrum the peaks at 534eV and 540eV are visible in both orientations, but with inverted intensity ratios. The peak in the absorption spectrum in both orientations, located at 534eV is clearly attributed to σ^* antibonding states by reference to the calculated symmetry-resolved density of states centred at 7 eV above the Fermi level. In both experimental geometries, E$||a$ and E$||c$ the σ^* states in the Sn_3O trigonal plane are accessible. The E$||c$ orientation has a stronger cross section for absorption into these sp^2 hybridized states than for the E$||a$ orientation. This is due to the $\sim$ 100% greater projection of sp^2 p_x states onto the the crystallographic c axis. This is understandable as within the trigonal plane two of the three sp^2 orbitals have projections along the c axis, while the third is orthogonal. It is this orthogonal sp^2 orbital in the p_z orientation that accounts for the σ^* projection onto the a axis at the bottom of the conduction band.

The presence of a faint high energy shoulder in the first peak of the absorption spectrum in the E$||c$ orientation at about 534.5 eV is reproduced in the calculated PDOS projected onto the c axis. The two peaks in the absorption spectrum for the E$||a$ orientation at 536 eV and 538 eV are also attributed to the sp^2 hybridized σ^* states in the Sn_3O trigonal plane. Likewise, the broad peak at 537.5 eV in the E$||c$ spectrum is attributed to sp^2 hybridized σ^* states in the Sn_3O plane. The calculated PDOS indicate that in this 5 eV portion of the spectrum between the two peaks common to both orientations at 9 and 18 eV above the valence band maximum, there is a separation in energy between the sp^2 hybridized density of states projected onto the a and c axes. The σ^* states with a projection onto the c axis congregate in the lower half of the energy range ending in the sharp, intense spike in the PDOS at

12 eV above the valence band maximum. The states above this energy have a greater projection onto the crystallographic *a* axis. While this splitting is not as clear-cut in the experimental spectrum, the locations in energy of the spectral weight this region follows the trend predicted in the calculation. The figure containing the calculated PDOS, resolved for the three axes of the natural basis set, identifies the states with the predominant projected density of states along the *c* axis as O $2p_x$ states, and those with a predominant projection along the *a* axis are due to the bonds oriented along the p_z axis.

The relative intensities of the experimental peaks are reversed between the two orientations, with the largest density of states projected along the *c* axis located at the very bottom of the conduction band, and decreasing with increasing photon energy. The density of states projected along the *c* axis are entirely composed of σ^* states, while the states projected along the *a* axis are a combination of σ^* and π^* states. Thus, the intensity of the absorption increases from threshold with increasing photon energy in the $E||a$ orientation, culminating in the most intense π^* - composed peak at 540 eV. This peak coincides with a sharp density of states with σ^* symmetry, which is visible in the $E||c$ orientation. Overall, the calculations predict that the Sn 5*s* orbitals make the largest contribution to the conduction band compared to the *p* and *d* orbitals which is largely supported by the intensity of the first hybridized peak in the O *K*-edge XAS.

4.6.2 VB XPS and RXES at the O *K*-edge: theory and experiment

The density of states observed in the valence band XPS extending into the bandgap is not present in the calculated density of states, which leaves unaltered their previous attribution to states created by a surface configuration in SnO_2 producing a Sn 5*s* - 5*p* hybridization in the Sn ions of lower coordination on the surface. The peak located at a binding energy of -11 eV is relatively stronger than the peak observed previously in undoped SnO_2 where the valence band was measured using an equivalent instrument and monochromated source [9]. This difference may be explained by the combination of the suppression of Sn 5*s* intensity at the bottom of the valence band in a substitutionially doped system, and the difference in the valence band density of states observed between a polycrystalline and single crystal sample. In another study, a density of states above the valence band maximum is observed after argon ion bombardment of the (110) surface, and is associated with the an oxygen deficient, non-stoichiometric surface [44].

The relative positions of Sn s p and d derived densities of states within the valence band in the present calculations correspond with some previously calculated electronic structures of SnO_2 in the literature. In another calculation where the axially projected O $2p$ PDOS was calculated, the results reflected closer agreement with the standard DFT calculation without the SIC, in the sense that there was an offset between the peaks at the top of the valence band associated with the in plane and out of plane O sp^2 orbitals. However, that is not readily observed in our experimental spectra.

As mentioned in section 4.4.3 the RXES spectra shown in figure 4.3 have a feature at 523.5 eV that is suppressed in the XES along c geometries (blue traces), which represent a PDOS projection onto the a axis. Thus from the experimental results alone this region of the valence band can be associated with a density of states projected on the rutile c axis. This association is borne out by the calculations, where the O $2p$ σ states in the natural p_x direction are located at this position in the valence band. The position of this peak in the E$||c$XES along a spectra tends to move to lower energies away from the main peak at 526 eV as states with greater Sn p character in the conduction band are populated with increasing excitation energy. This drift is reproduced in the simulated RXES spectra. The dispersion of the states in the valence band is very apparent when by comparing the spectrum taken at the threshold excitation energy to the higher energy excitations. The main peak at 526 eV is broader on threshold as the density of states contributing to the emission become very close in energy and merge somewhat.

4.6.3 Difference Spectra

The difference spectra produced for resonant and non-resonant energies allowed the comparison between the O K-edge XES projected onto the a and c axes and the simulated projected XES spectra. The calculated O $2p$ PDOS is also clearly comparable to the experimentally derived individual axes projections. The comparison is somewhat more revealing at the resonant energy, corresponding to the peak in the conduction band at 533.9 eV, most probably due to the smaller subset of non-equally weighted k-points in the RXES spectrum as opposed to the emission from all k-points in the Brillouin zone selected and weighted equally by a non-resonant excitation.

The relative intensity of the features in the difference spectra closely resemble the ratios predicted by the calculated spectra, with the exception of the non-resonant energy spectrum for E$||c$, where the suppressed intensity towards the top of the valence band in the XES spectrum projected along the c axis is not observed to the same extent experimentally, possibly due either to the significant geometrical offset, or to the increased spectral density near the valence band maximum edge arising as one approaches ~ 20 eV above threshold due to double valence hole emission.

4.7 Conclusions

In this chapter the detailed treatment which the valence band of SnO_2 has received via XPS and O K-edge XES and DFT electronic structure calculations under the auspices of this thesis has been outlined and discussed. As is the case with the following chapters on TiO_2 and RuO_2, this is the first report of polarization-dependent RXES at the O K-edge in SnO_2, showing the clear effects of the natural linear dichroism created by the rutile crystal structure.

The valence band XPS of single crystal rutile SnO2 obtained and presented in this thesis shows a density of states trailing into the band-gap, which, with reference to a previous study of Egdell *et al.* [69] we attribute to a surface reconstruction related additional density of states. In the analysis of our valence band XPS of doped samples the presence of a surface-related additional density of states extending into the band-gap must be borne in mind.

The polarization dependent XAS at the O K-edge clearly demonstrated the predicted effects on the PDOS in the conduction band of the natural linear dichroism in rutile. RXES at the O K-edge also showed quite clear effects, with due account taken of the energy resolution achieved, of the natural linear dichroism on the PDOS in the valence band of SnO_2.

The RXES spectra simulated from the calculated density of states showed detailed agreement with the experimentally observed XES projected along the crystalline a and c axes took the form predicted by the spectra . This agreement is a firm illustration of the power of polarization dependent RXES, particularly in as offering a further insight into bonding.

In the extended analysis of the experimental results, a weighted subtraction was found to yield a good reconstruction of the XES originating from states oriented along the crystalline a and c axes individually for a given excitation-geometry selection of intermediate states, via their agreement with the subtractions derived from the simulated spectra.

Chapter 5

Polarization dependent resonant x-ray absorption and emission spectroscopy study of rutile RuO_2

5.1 Introduction

This chapter treats the resonant x-ray emission spectroscopic study of RuO_2 in the following five sections. Section 5.2 explains the structural properties of RuO_2 and how these relate to the resulting electronic structure of the bulk crystal, as well as outlining some of the applications for which RuO_2 is well suited. Section 5.3 describes the details of an electronic structure calculation, and outlines the parameters selected within the Full Potential Linearized Augmented Plane Wave (FLAPW) Density Functional Theory (DFT) framework. This section also considers the attributes of previous electronic structure calculations performed for RuO_2. Section 5.4 reviews the experimental setup and how the polarization selectivity of the material is exploited using linearly polarized X-rays. This section also includes the details of how RuO_2 single crystals can be synthesized. The fifth section outlines and discusses the results of both the calculations and the x-ray spectroscopic experiment, before the final section gives some conclusions regarding RuO_2.

5.2 The structural properties of RuO_2

At ambient conditions rutile is the most stable phase of RuO_2 where the ruthenium assumes a tetravalent state, as its single $5s$ electron and three of its seven $4d$ electrons form bonds with the oxygen anions. As RuO_2 is an electrical conductor there is clearly not a completely ionic bond between the oxygen and ruthenium atoms, and bearing this in mind some mixture of covalent and ionic bonding is to be expected. But the valence designations arising within the limits of the ionic model may still be used to consider the ruthenium of RuO_2 as a d^4 cation, with an almost half filled $4d$ shell. The Ru cation is octahedrally coordinated by the surrounding six oxygen anions and so there is the usual lifting of the degeneracy of the atomic d orbitals giving rise to the lower t_{2g} states and the higher e_g states. As it is a d^4 cation, and the spin orbit splitting of the $4d$ shell is small, there is little (if any) difference between the spin channels. As a result the d^4 occupation results in a partially filled t_{2g} band and hence the metallic conductivity of RuO_2. In general the d shell occupation is one of the quantities that combine to determine the geometric and electronic structure of transition metal oxides.

Also in the ionic limit the oxygen $2p$ orbitals are completely filled and thus will be compressed in energy while the Fermi level will be composed of the ruthenium $4d$ t_{2g} states as noted above. The behaviour of transition metal oxides that undergo metal to insulator transitions as their temperature decreases is understandable in terms of the density of states at the Fermi level. Where the Fermi level occurs at a spike in the density of states the system is unstable. It seeks to minimize the density of states at the Fermi level by acquiring an alternative geometry as the thermal energy that maintains the system in the unstable configuration decreases with the temperature [70]. There are a rich array of transition metal oxides that exhibit a metal to insulating transition over a given temperature range via structural transitions. This group includes VO, VO_2, V_2O_3, NbO_2, and Ti_3O_5. Or in the case of CrO_2 it can reduce its energy becoming a half metallic ferromagnet with a density of states at the Fermi level in one spin channel only [71]. It has been calculated that RuO_2 is energetically on the verge of such a magnetic instability itself due to the high density of states at its Fermi level [72].

5.2.1 Structural studies of RuO_2

Early crystallographic data from RuO_2 indicated that it shared the same crystal structure as TiO_2 and SnO_2 which has since been accurately confirmed [32]. Within the oxygen coordination octahedron, however, the waist Ru-O distances are found to be greater than the apical distances by about 2% where the TiO_2 octahedron is distorted in the opposite fashion, with the apical distances larger than the waist Ti-O distances. This reversal of the sense of the octahedral distortion should affect the bonding arrangements of RuO_2 compared to other rutile oxides such as TiO_2. For instance this tetragonal distortion of the RuO_2 octahedron lifts the degeneracy of the

t_{2g} levels and splits them in an opposite sense to the tetragonal distortion splitting in TiO_2. That a distortion in the octahedra would lift the degeneracy of the t_{2g} levels in a way that depends on the sense of the distortion is to be expected when the increased and decreased proximity of the Ru 4*d* t_{2g} orbitals to the negative oxygen ions is considered. There is also a contraction of the O-O distances along the shared edges of the octahedra, accompanied by an expansion of the O-O distances parallel to the crystalline *c* axis. This rectangular distortion in the waist of the octahedron is attributable to the electrostatic repulsion between the oxygen anions not involved in edge sharing. The variation in the degree of this particular distortion appears to be caused by the variation in electron density on the oxygen groups due the different filling of the *d* orbital on the metal cation [28].

The differing bond lengths indicated by the octahedral distortion combined with the increased *d* shell filling results in a trend towards a greater degree of co-valence in the bonding throughout the valence band, not only in RuO_2 but as a general trend in rutile oxides [28]. This is a direct consequence of the greater degree of overlap between the metal and oxygen orbitals that is obtained by increasing *d* shell filling. As shells fill they are drawn lower in energy. The more filled the shell, the more stable it is, which is to say that its energy is lowered in the process. But why does this necessarily lead to a greater degree of overlap? this is suggestive of an increase in the physical overlap of the orbitals, the geometry must change, *i.e.* the octahedron must shrink as the bands fill. Baur notes that "In developing a model to fully explain the precise structural trends in the rutile type dioxides, it appears that at least four effects need to be considered, namely electrostatic interactions [non-bonded O-O repulsions], cell volume, *d*-orbital occupancy, and metal-metal interactions"[28]. The same must be said of the trend in the larger family of transition metal oxide properties across the series. The structure of RuO_2 both physical and electronic lies along these trends and serves as a contrast to TiO_2, the d^0 starting point just as SnO_2 represents the d^{10} endpoint.

5.2.2 Applications of RuO_2

Of the approximately 12 tonnes of ruthenium produced globally annually, roughly 50% is destined for applications in the electronics industry as electrical contacts and chip resistors, and 40% for the chemical industry, primarily for use in dimensionally stable anodes for chlorine production in electrochemical cells [73]. RuO_2 is the most environmentally stable of the transition metal dioxides with a high enthalpy of formation and resistance to corrosion, whose electrical conductive properties have led to its use as an electrical contact material. This is in addition to other uses such as an electrode conductor material in integrated circuits, as well as its use as a selective catalyst in the oxidation process of methane in the synthesis of gases [74]. RuO_2 has been used as a catalyst in the oxidation of methane [75]. A major technical application of RuO_2 is in the chlor-alkali industry as a catalyst in the evolution of Cl_2 [74]. RuO_2 has also been used successfully as a corrosion-resistant low overpotential electrode for the evolution of chlorine and oxygen gas and as a catalyst in the photodissociation of H_2O [76]. RuO_2 has long been used as a practical infrared bolometer, further to its intended use as a precision resistor material. Another potential use for RuO_2 is in field emission applications [77, 78] since their successful synthesis in nanorod structures [79]. Another potential application of ruthenium based metal oxides that has been investigated is their use as rechargeable battery cathode materials. A previous spectroscopic study has compared layered Li_2RuO_3 and rutile RuO_2 in terms of their electrochemical performance [80].

5.3 Electronic structure calculations of RuO_2

This section provides a detailed outline of how the electronic structure of RuO_2 was calculated and how oxygen K-edge emission spectra were obtained from the results. The first section reviews some previous electronic structure calculations of rutile RuO_2 and assesses their relative success. The final section details the local coordinate system adopted for the purpose of the calculation.

5.3.1 Introduction

The first computation of an electronic structure for $RuO_2$was reported by Mattheiss [81] in which a linear combination of atomic orbitals (LCAO) interpolation method was used to fit the results of a non-relativistic augmented plane wave calculation, which resulted in a good representation of the RuO_2 bands but did not result in the correct splitting between the O $2p$ and Ru $4d$ states in the valence band, which was subsequently borne out by UPS data [82]. In most of the theoretical studies of RuO_2 that followed, the crystal potential was approximated in some fashion [83, 84, 85] which is a possible source of error in calculated binding energies and bandwidths [86].

The calculations of de Almeida *et al* [86] and Benyahia *et al* [87] used a full potential linearized augmented plane waves (FP-LAPW) and found strong correspondence between the resulting valence charge density contour plots and those of Sorantin and Schwarz [7]. Subsequently the full potential studies of Demazeau [72] and Hamad [61] established that the generalized gradient approximation to the exchange and correlation potential was the most suitable treatment of the $4d$ electrons in RuO_2. The results of Almeida's [86] full-potential calculation shows improved agreement with valence band widths as measured in XPS [70] compared to some non-full-potential calculations [88].

5.3.2 Details of the present RuO_2 Calculations

The present calculation takes as its starting point that of de Almeida [86], and was performed within the framework of DFT, using WIEN2k as described in chapter 3. The exchange and correlation potential was approximated using the generalized gradient approximation (GGA) of Perdew and Wang [89]. The lattice parameters used were those of Bolzan [29]. The muffin tin radii of the atomic spheres used were $1.85\,au$ for Ru and $1.75\,au$ for O. The calculation was performed using $R_{mt}K_{max} = 9.0$ which yields $\sim$ 1500 plane waves to describe the valence and semi-core states. The charge density and potentials were expanded up to $l = 10$ inside the atomic spheres. An energy difference of $\Delta E \leq 10^{-3}\,eV$ was used as the convergence criterion between successive iterations. The charge difference ΔQ between successive iterations in the self consistent convergence cycle was $0.001e$. There were 2900 k points contained in the reduced Brillouin Zone.

5.3.3 Results of the calculations

We present here a variety of bandstructure diagrams for rutile RuO_2 arising from the electronic structure calculations. These are all of the form of band-character plots where the proportion of a particular band or portion of a band that has a particular site and orbital character is given by the size of the circle located at that k-point. For the differing axes X_O, Y_O and Z_O discussed previously, this gives us a useful insight into the bonding and character of the PDOS and of the experimental spectra.

The electronic structure band diagrams shown in figure 5.1 depict the dispersion of the crystal momentum states within the first Brillouin zone. The three band structure diagrams show the states of predominant O $2p$ character, with the various marker sizes in diagrams a-c denoting the projection of the crystal momentum states along the oxygen local coordinate system axes X, Y and Z respectively. The integrated density of states projected along these respective axes, which is calculated from the three preceding electronic structure diagrams is contained in panel (d) of figure 5.1. The band structure diagrams shown are band-character plots with the weights of the lines barying according to the proportion of the selected character of the (a) O $2p_x$ (b) $2p_y$ (c) $2p_z$ and (d) shows the integrated PDOS of these components.

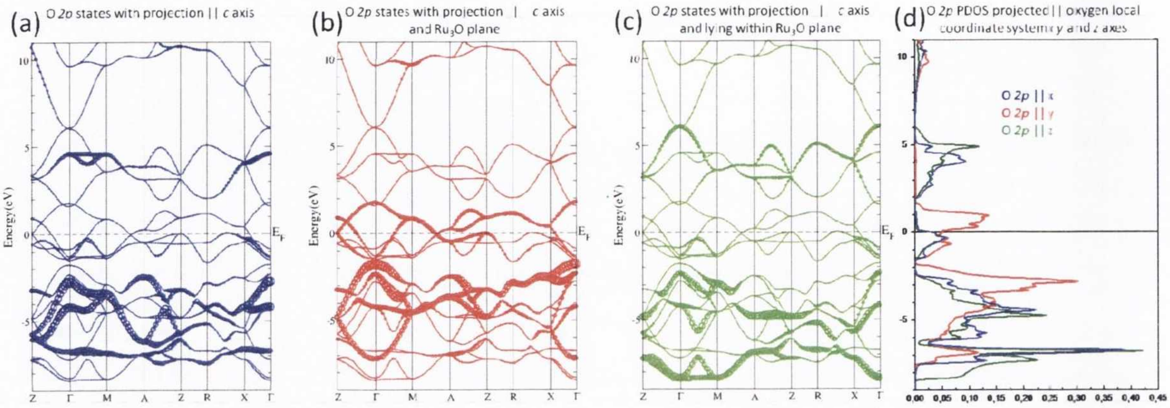

Figure 5.1: Electronic structure diagrams following a natural basis set projection, and the resulting axis-projected density of states.

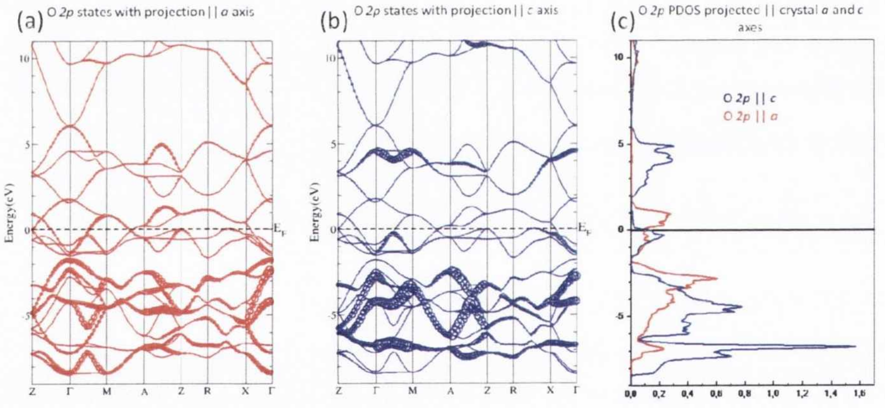

Figure 5.2: Electronic structure diagrams, highlighting the band-character of each component and following a rotated basis set projection along the crystalline a and c axes, and the resulting axis projected density of states.

Panel (a) and (b) of Fig. 5.2 again depict the bandstructure within the first Brillouin zone of RuO_2, where again the size of the markers used in the band-character diagrams identifies the degree to which the crystal states have a projection along the crystalline a and c axes. The integrated projected PDOS are shown in panel (c). It is ultimately the O $2p$ PDOS $||a$ and $||c$ that the polarization dependent x-ray spectroscopy can probe.

The density of states in the valence band is formed from states created by σ and π molecular orbital bonding character between the O and Ru ions. The valence band with predominant O $2p$ character begins at $-8.5\,eV$ and extends up to $-1.8\,eV$ with respect to the Fermi level. The remaining narrow part of the valence band that reaches to the Fermi level is composed of Ru $4d$ t_{2g} that can participate in π bonds with O $2p$ states. This Ru $4d$ t_{2g} band contains some non-dispersing sections, for instance between A-Z-R, which will create a spike in the density of states just below the Fermi level. The gap between the top of the O $2p$ band and the bottom of the Ru $4d$ band is open all throughout the Brillouin Zone and has its minimum value at the Γ point where it is about $0.25\,eV$ wide.

The $^2/_3$ filled Ru t_{2g} states continue across the Fermi level into the conduction band, where the crystal field splitting between the e_g and t_{2g} states and its effect on the electronic structure is clearly evident. Between points A and Z in the Brillouin Zone the states created by a σ-like antibonding combination of e_g Ru $4d$ and O $2p$ orbitals extend between $2\,eV$ and $5\,eV$ above the Fermi energy. The band formed by the π-like bonding combination of the six Ru t_{2g} orbitals (of which four are occupied) and the O $2p$ orbitals starts just below this.

The gap between the e_g and t_{2g} states extends throughout the Brillouin Zone for the most part. There are some dispersing states that overlap around the Γ point, but their dispersion indicates that they will give rise to a very small density of states between the split d levels, compared to the flatter bands inside the e_g manifold. In general the more compressed the electronic structure is, the higher the degree of covalency between ions. In this context the overlap between the e_g and t_{2g} states in the conduction band seems small. Typically DFT underestimates the bandgap around the Fermi level, but in this instance correctly predicts the metallic nature of RuO_2.

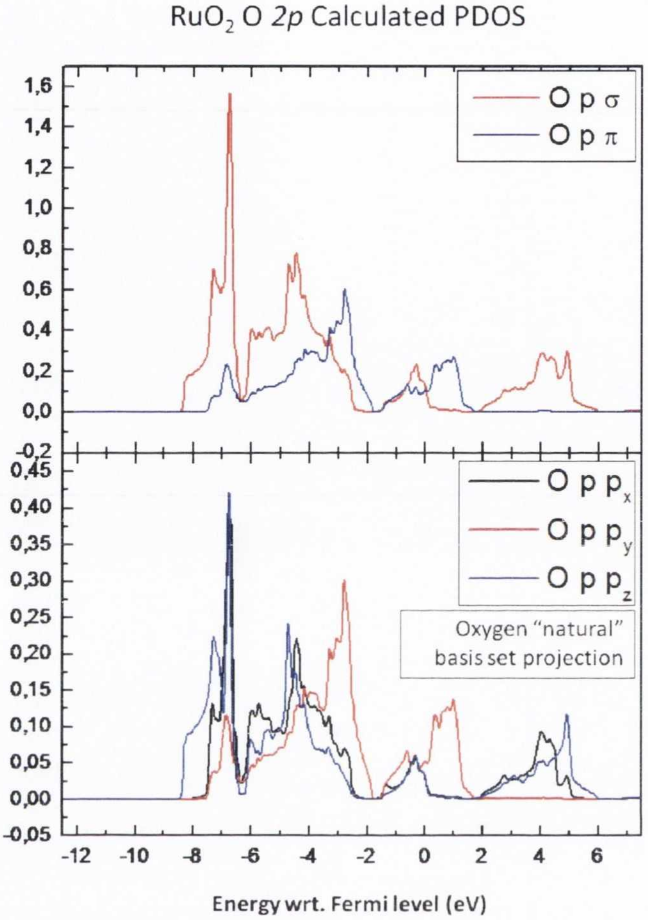

Figure 5.3: Calculated O $2p$ PDOS in the valence and conduction band of rutile RuO$_2$. The lower panel shows the PDOS projected along the axes of the oxygen natural coordinate system as defined in chapter 3. The upper panel shows the σ-like and π-like projections of the PDOS.

Figure 5.3 combines panels (d) and (c) from figures 5.1 and 5.2 respectively, and shows the calculated the O $2p$ PDOS in the valence and conduction band, indicating the projections of the PDOS both by bonding character (σ or π) or the natural coordinate axis defined for the oxygen ion (xyz). The calculated O $2p$ PDOS in the conduction band is compared to the polarization dependent O K-edge XAS in figure 5.7.

5.4 Experimental Measurements

A brief review of previous experimental measurements of RuO_2 is given here followed by a discussion of our single crystal sample and the specific details of the measurements that we have completed.

5.4.1 Previous experimental studies of the electronic structure of RuO_2

While the identification of the different sources of the density of states in the valence band based on polarization dependent x-ray absorption and emission has not been presented before, previous experimental studies of the band structure of RuO_2 have measured their magneto-resistance [90], magneto-thermal oscillation [91], magnetic susceptibility [92], electrical transport [93, 94], specific heat [95] , ultraviolet and x-ray photoelectron spectroscopy [96, 97, 98, 99], optical reflectivity [100, 86], and electron energy loss spectroscopy [70].

A mechanism for metallic conduction in rutile oxides was proposed by Rogers *et al* [101]. That study attempted a systematic correlation of the crystal chemistries of the transition metal dioxides with rutile-related structures based on the formation of an empty to partially and fully filled metal-oxygen π^* band. The scheme as outlined demands careful study of the valence band of the rutile dioxides. Riga *et al.* performed XPS on the valence band of different d shell fillings in TiO_2, RuO_2 and IrO_2 [97], in order to investigate the qualitative molecular orbital model proposed by Rogers. In the Riga study the evolving asymmetry noted in the core level peaks was attributed to the differing number of conduction electrons in the outer shells and consequent effect on the screening of the core hole.

Goel *et al.* [100] reported reflectivity measurements of RuO_2 and IrO_2 for $E \| c$ and $E \perp c$, and derived real and imaginary parts of the complex dielectric constant and refractive index for RuO_2 and IrO_2 from the reflectivity measurements, which in turn were compared by de Almeida *et al* [86] with the results of their calculations and found to agree well.

Cox *et al.*'s studies of ternary ruthenium oxides used UPS and XPS and High Resolution Electron Energy Loss Spectroscopy (HREELS) performed on pyrochlore ruthenium(IV) oxides $Pb_2Ru_2O_{7-v}$, $Bi_2Ru_2O_7$ and $Y_2Ru_2O_7$; the perovskites $SrRuO_3$ and $CaRuO_3$; and the ruthenate $Bi_{2-x}Gd_xRu_2O_7$, x :$0 \rightarrow 2$[70]. In the case of the listed oxides, the transition to non-metallic behaviour in the sequence of materials is associated with correlation-induced electron localization. The decrease in the screening of the Ru $3d$ hole by conduction electrons, and the decreasing density of states at the Fermi energy tracks the progress towards non-metallic behaviour. In the case of the ruthenate $Bi_{2-x}Gd_xRu_2O_7$, x is increased in increments from 0 to 2 , spanning from metallic to semiconducting behaviour associated with the t_{2g}^4 $4d$ electron configuration becoming increasingly more localized.

In order to distinguish between the p and d partial density of states in the valence band, Daniels previously used resonant photoemission spectroscopy where a synchrotron source was employed to obtain several different photon energies between $70 - 130\, eV$ [82]. The same study investigated mixed RuO_2-IrO_2 crystals to enable the identification of spectral features by monitoring their energy shift as a function of chemical composition. According to the calculations of Mattheiss [81] the metal d states contribute to the density of states predominantly just below the Fermi level, with a weaker contribution at deeper energies between $4\,eV$ and $8\,eV$ below the Fermi level. The photoemission experiments of Daniels *et al* [82] agree with Mattheiss's large $p - d$ separation, with which our calculations modeled after de Almeida [86] do not concur.

5.4.2 Synthesis of single crystal RuO_2 samples

The RuO_2 single crystal samples studied here were supplied by Russel G Egdell. They were produced by a method similar to that described by Huang *et al* [102] involving chemical vapour transport in an open flow gradient quartz tube furnace. The precursor selected for optimal single crystal growth and growth rate was a mixture of polycrystalline RuO_2 and pure Ru metal powder. XRD was used to determine the orientation of the surface plane, and the position of the crystalline a and c axes. The largest natural face of the single crystal as grown was (110), with the c axis [001] oriented parallel to the shorter edges of the face. The a axes were contained in a plane perpendicular to the (110) face, and were both oriented at 45° to the surface.

The surface of the crystal is a (110) surface. Thus the c-axis lies in the surface plane of the crystal with the two equivalent a-axes at 90° to the c-axis but at 45° to the plane of the surface. XRD was used to clearly reveal the (001) direction.

5.4.3 Orientation for X-ray Spectroscopic Measurements

The orientation of the crystal with respect to the linearly polarized light of the synchrotron is described. At both ALS BL8.0 and $I511 - 3$ the linear polarization is fixed within the horizontal plane of the orbit of the synchrotron. In addition the orientation of the XES spectrometer - wholly in the horizontal plane at ALS BL8.0 but rotatable about the beam direction in $I511-3$ is also specified. When the intermediate selection criteria is specified as $E||c$, then in a horizontal in-plane scattering geometry the light is normally incident onto the surface of the sample with the c-axis direction in the horizontal. In such a 90° scattering geometry in the horizontal plane (in-plane), then the emission propagates out along the c-axis. Of course for the actual measurement the grazing exit photons actually propagate out at $\sim 10-15°$ from the surface as the sample must be rotated at least this much for a sizable emission signal to be recorded.

However for an intermediate selection criterion of $E||c$ but in a vertical (out-of-plane) scattering geometry the incoming light is not along the [110] direction as before, but is kept so that it is along a [100] direction (or a axis) in order that the exiting emission is also along an a-axis. In this case the c-axis is horizontal and parallel to the linearly polarized light, but the surface is inclined at 45°to the incoming beam direction, and at 45° to the exiting emission, or spectrometer axis. Such is the situation at $I511-3$ where the sample manipulator rotates together with the XES spectrometer as described in detail in chapter 2, and a simple polar rotation of the sample manipulator allows for this. This is denoted $E||c$, $XES||a$, (out-of-plane) and the previous measurement geometry denoted $E||c$, $XES||c$, (in-plane).

5.5 Results and Discussion

5.5.1 General points

In the RXES spectra the excitation energies chosen are generally very close to the absorption threshold, and in this case also the Fermi level. The elastically scattered peak, subject to lifetime and instrumental broadening, that is visible primarily in the out of plane geometry overlaps with the features at the top of the valence band. The overlapping of the elastic peak with the features at the top of the valence band is not to be mistaken for a shift of the Fermi level.

Unless otherwise stated the emission spectra are subject to a resolution of $\triangle E = 0.7eV$ due to the bandwidth of the monochromator, and a further $\triangle E = 0.7eV$ due to the instrumental resolution of the X-ray Emission Spectrometer as determined by the entrance slit effective width. In the figures showing a stacked collection of resonant spectra recorded in the same geometry, the very threshold spectrum is repeated with a dotted trace to enable convenient comparison to allow the energy dependence to be clearly identified. It would be instructive to compare the non-resonant or "normal" x-ray emission spectra (NXES) and the calculated O $2p$ PDOS with the valence band UPS from RuO_2 measured by Cox *et al.* [96]. It is only feasible to make a qualitative comparison between the energy dependence of the emission spectra in each orientation rather than cleaving to an exact comparison between any single pair of calculated and measured spectra as the emission spectra are relative and not absolute in scale.

5.5.2 X-ray Absorption

The absence of multiplet effects at the O $K-$absorption edge make a qualitative comparison between the x-ray absorption spectra and the O $2p$ PDOS possible. The axis-projected density of states is probed by alternating between orienting the a and c axes of the crystal parallel to the electric field vector of the x-rays.

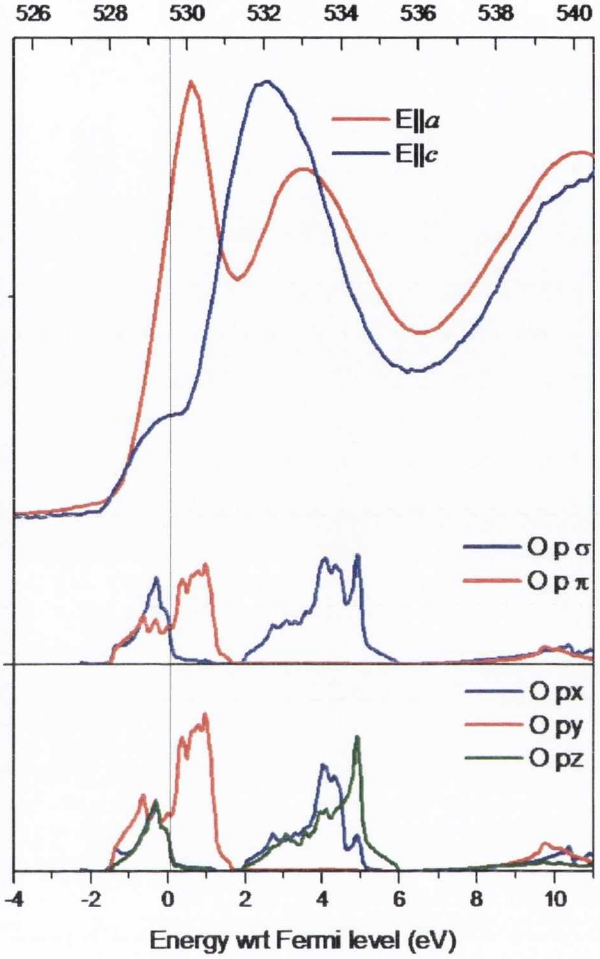

Figure 5.4: XAS at the O K edge for both $E\|a$ and $E\|c$ orientations with respect to the RuO_2 crystal axes. Also shown in the lower and middle panel respectively are the calculated natural coordinate axes projection of the O $2p$ PDOS, and the O $2p$ σ-like and π-like PDOS

For the $E\|a$ orientation, the O $2p$ partial density of states projected onto the a axis contains components from both the π^* antibonding states formed by π overlap between the $2p_y$ orbitals perpendicular to the M_3O plane and the Ru $4d$ t_{2g} orbitals, as well as the σ^* antibonding states formed by the Ru $4d$ e_g orbitals. The projected density of states on each of the a axes is equivalent.

For the $E\|c$ orientation, the c axis of the crystal contains no projection of the π bonded states perpendicular to the RuO_3 trigonal plane. In this geometry the peak associated with the population of these states is absent. Neither is the projection of σ states onto the c axis identical to the a axis. There is also an absence of O $2p$ p_z states projecting onto the c axis.

These spectra can be directly compared to that observed from the half-metallic rutile CrO_2 [103] which shows a very similar natural linear dichroism at the O K-edge. This is not unexpected as the Ru d^4 configuration gives rise to $2/3$ filled t_{2g} levels. In CrO_2 the d^2configuration give a $2/3$ filled majority spin t_{2g} levels which are spin-orbit split from the minority spin t_{2g} levels by several eV.

The π^* 4d t_{2g} derived peak is isolated at 530.1 eV, some $\sim$ 3 eV above threshold in the $\mathbf{E}||a$ geometry. The maximum at 532.0 eV in the O K-edge XAS for the$\mathbf{E}||c$ geometry corresponds to the Ru 4d e_g - O 2p σ^* derived orbitals. The states at higher energies are Ru 5p-5s derived states. The noticeable shoulder between 528 eV and 530 eV is most likely due to core-hole effects in the XAS and it is not reflected in the ground state O 2p PDOS projected along the c-axis. Alternatively, perhaps when considering Daniels *et al.*'s results [82] a more complex LDA + U calculation for RuO_2 is warranted with a greater on-site localization of the 4d orbitals.

5.5.3 NXES spectra

Figure 5.5 contains the O K-edge non-resonant NXES from all four possible excitation and spectrometer orientations. In the $E||a$, XES along a geometry the polarization of the incident beam is parallel to an a axis of the crystal. This geometry permits absorption into both the π^* and σ^* unoccupied density of states, as the electric field vector E is parallel to projected components of both the σ_z^* and the σ_{x+z}^* bonded states in the M_3O plane and the π^* states perpendicular to the plane. The XES spectrometer is aligned along the other a axis giving rise to emission from the projected density of states in the vertical plane containing the a and c axes. In the resulting spectrum, the σ PDOS at the bottom of the valence band are more prominent indicating that the projection of O σ_z states along the a and c axes is at a maximum in this geometry. The π bonded density of states is very much diminished by comparison.

Likewise, the scattering geometry allows a projection of both π and σ bonded states in the valence band to contribute to the emission, but the projection of the σ bonded states dominates over the π bonded states.

At the top of the valence band, the projected density of states arising from π bonding between O 2p - Ru 4d t_{2g} states contributes to the emission spectrum. The comparative weakness of this contribution is evident in the failure to resolve a distinct peak for this density of states in the emission spectrum in this geometry. Both the dominance of the σ bonded density of states at the bottom of the valence band and the relatively weak contribution of the t_{2g} states at the top are well reproduced in the calculated spectra as shown by comparing the experimental results in figure 5.5 with the simulated non-resonant O K-edge XES in figure 5.6.

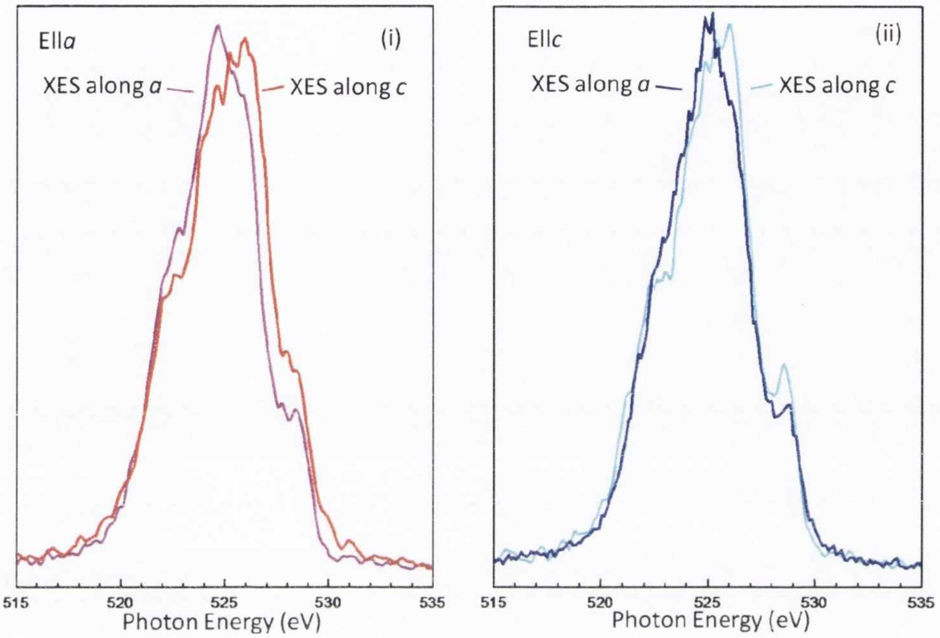

Figure 5.5: O K -edge NXES (i) $E\|a$, XES along a and XES along c (ii) $E\|c$, XES along a and XES along c.

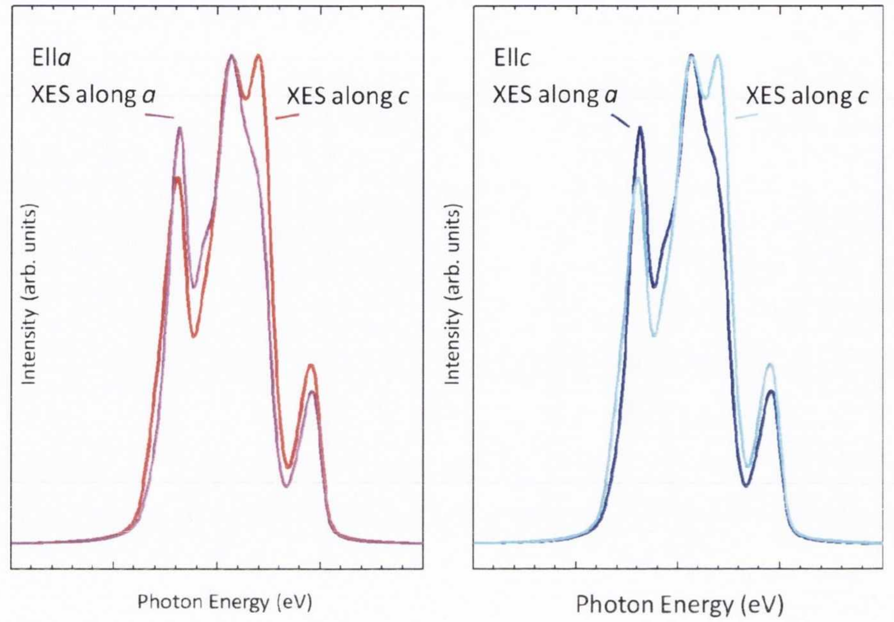

Figure 5.6: Simulated O K-edge NXES (i) $E||a$, XES along a and XES along c (ii) $E||c$, XES along a and XES along c

In the $E||c$, XES along c geometry the polarization of the incident beam is parallel to the c axis of the crystal. The σ bonded states in the M_3O plane have a projected density of states parallel to this axis, namely the σ_{x+z} states. The density of states formed by σ bonding along the apical axis of the octahedra are orthogonal to this axis and have no projected density of states along it. The density of states formed by π bonded O $2p_y$ orbitals are also orthogonal and do not have a projection along the c axis. In this, the second of the 'in plane' spectra, the balance of the spectral weight is shifted towards the top of the valence band, due to the dominance of the emission from the π bonded density of states projected onto the two a axes. The proportion of the spectrum originating from emission from the bottom of the valence band is greatly reduced, though it is possible to detect emission from the projection of the σ_z states in this orientation. The two narrow peaks in the O $2p$ occupied density of states corresponding to the projection of the narrow π bonded states at the top of the valence band and the σ bonded states 1 eV lower in energy are resolved in the emission spectrum. The sharp peak at the Fermi level created by the projection of the Ru $4d$ $t_{2g}\sigma$ bonded states is at its most prominent in this orientation. The dominance of projected π states over σ states in the emission, and the maximized contribution from the projected Ru $4d$ $t_{2g}\pi$ bonded states just below the Fermi level are both reproduced in the calculated Normal X-ray Emission Spectrum as seen in figure 5.6.

In the $E\|a$, XES along c, geometry the intermediate states into which excitation is possible are the same as those for spectrum 1. The orientation of the spectrometer along the c-axis in this geometry allows the a axes projected density of states to predominate the emission spectrum. This is the same situation encountered in spectrum 2 and involves the same π bonded states at the top of the valence band. While the experimental resolution was not sufficient to resolve the sharp peak created by the $a-$axis projected π bonded Ru $4d$ t_{2g} density of states, the increased spectral weight in this position is present, the narrow pinnacle of the projected O $2p_y$ density of states is visible in this spectrum.

The $E\|c$, XES along a spectrum is strongly similar to the $E\|a$, XES along a a similarity that is mirrored in the calculated spectra. The spectral weight proportions in the emission spectra shows the predominant contribution from σ bonded states at the bottom of the valence band, evident in the filling in of the shoulder present towards the bottom of the valence band in spectra 2 and 3. As is the case for spectrum 1 the contribution from the states at the top of the valence band, formed by the projection π bonded O $2p_y$ and Ru $4d$ t_{2g} orbitals is suppressed in this geometry.

5.5.3.1 Polarization dependent Resonant X-ray Emission Spectra from RuO_2

Figure 5.7 shows the excitation energies selected for the resonant x-ray emission experiment. The two dashed black arrows indicate energies that were selected for excitation in both $E\|a$ and $E\|c$ orientations, but were not selected in all spectrometer orientations. The blue arrows indicate excitation energies that were selected for excitation in the $E\|a$ orientation, involving features that were absent from the $E\|a$ orientation, whose specific features selected for excitation are indicated with red arrows. Finally the solid black arrows indicate the excitation energies that are common to both orientations.

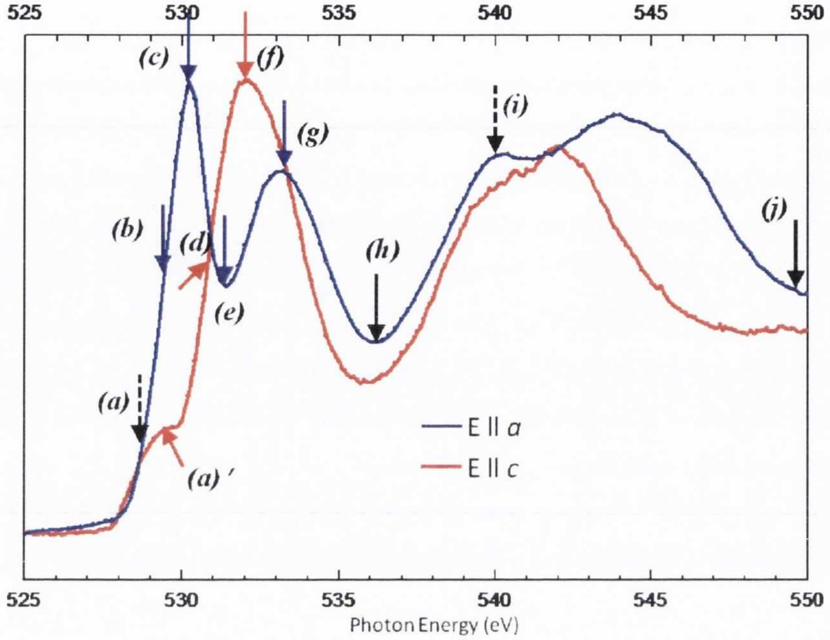

Figure 5.7: O K edge XAS spectra depicting the energies selected for resonant excitation

In figures 5.8, 5.9, 5.10 and 5.11 the experimental resonant emission spectra are displayed in the left hand panels with the calculated spectra in the right hand panels for comparison. The progression of the resonant spectra from the lowest to the highest within each panel follows the increasing excitation energy for each geometry. The experimental excitation energies selected are labeled in figure 5.7, and the RXES is simulated for excitation energies corresponding to the matching *feature* in the conduction band O $2p$ PDOS, rather than at the same exact energy as the experimental excitation. Also to aid comparison, the spectrum recorded at the lowest excitation energy is overlaid with each subsequent spectrum for both the experimental and calculated spectra.

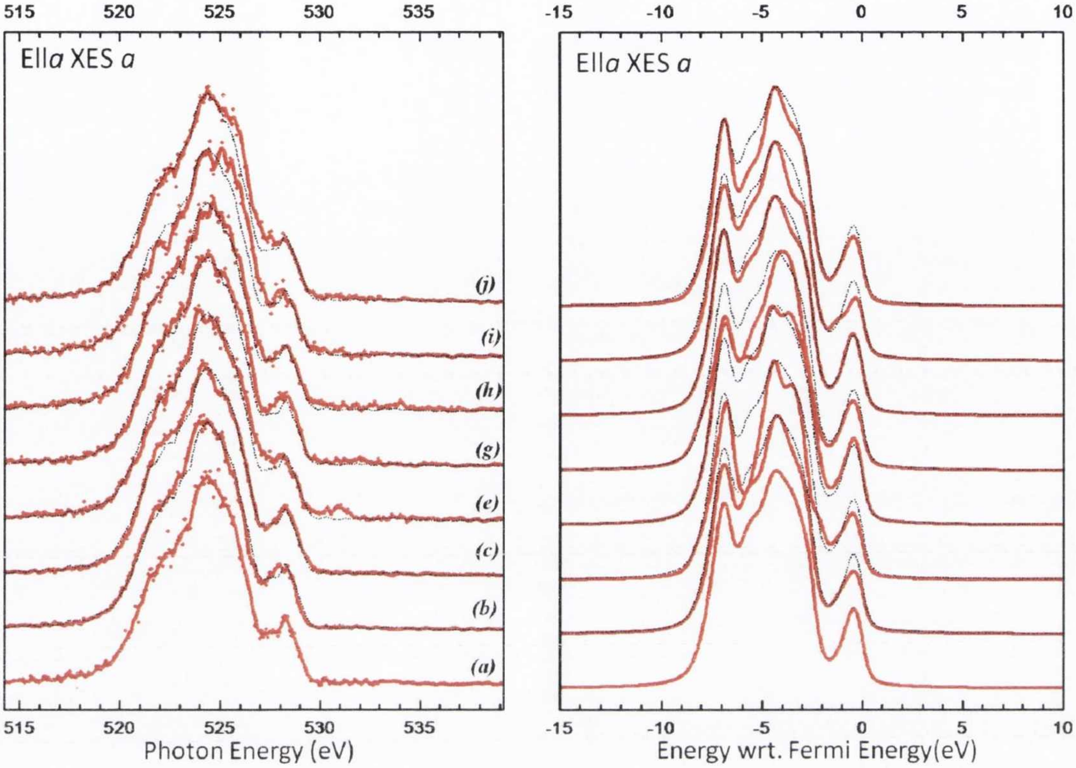

Figure 5.8: Resonant X-ray Emission Spectra with $E\|a$ and XES along a. This is an in-plane scattering geometry. The excitation energies are as labelled in figure 5.7

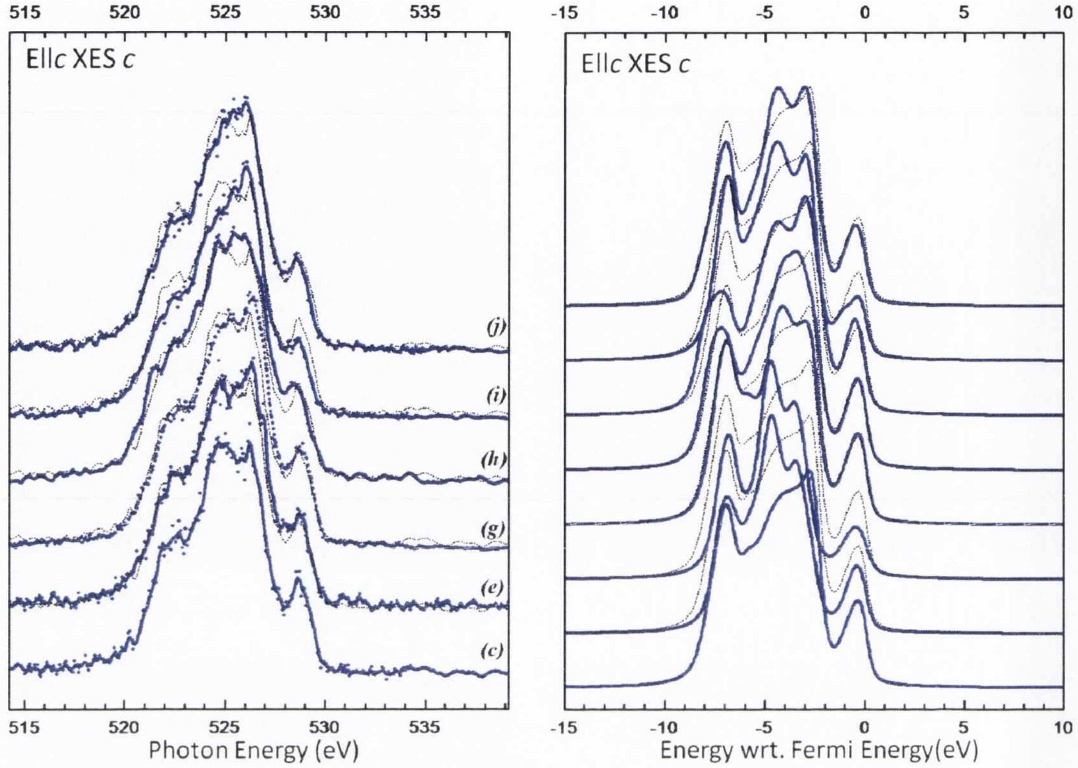

Figure 5.9: Resonant X-ray Emission Spectra with $E\|c$ and XES along c. This is an out-of-plane scattering geometry. The excitation energies are as labelled in figure 5.7

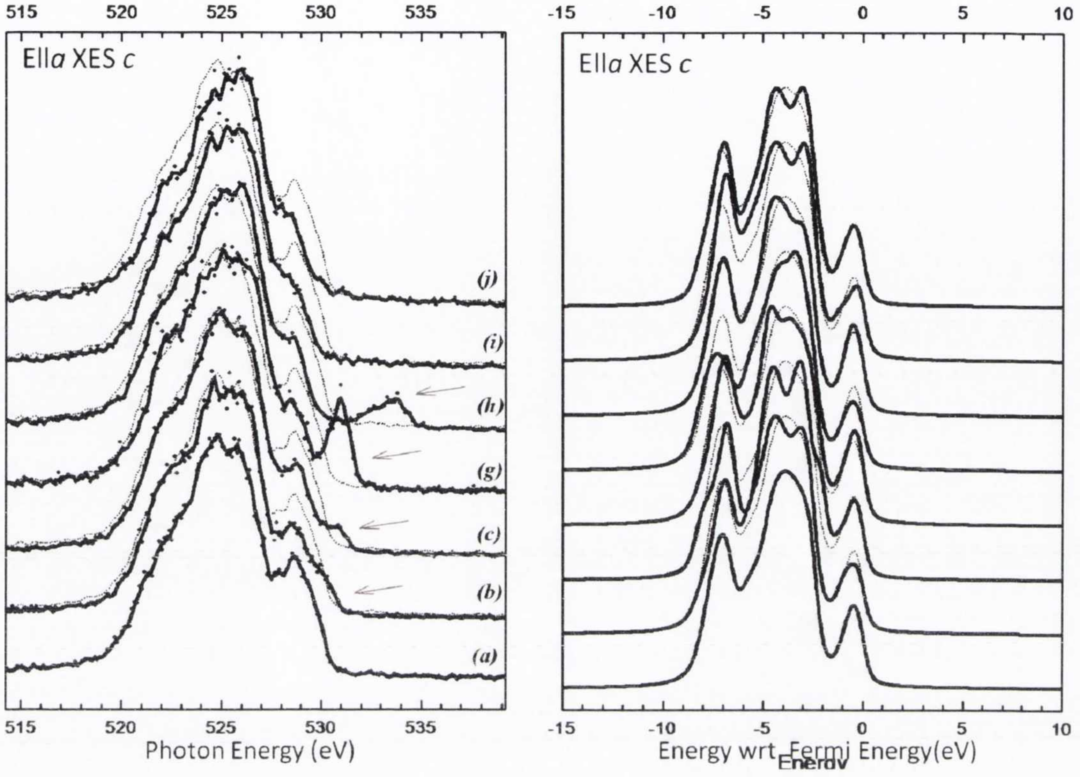

Figure 5.10: Resonant X-ray Emission Spectra with $E \| a$ and XES along c. This is an out-of-plane scattering geometry. The excitation energies are as labelled in figure 5.7

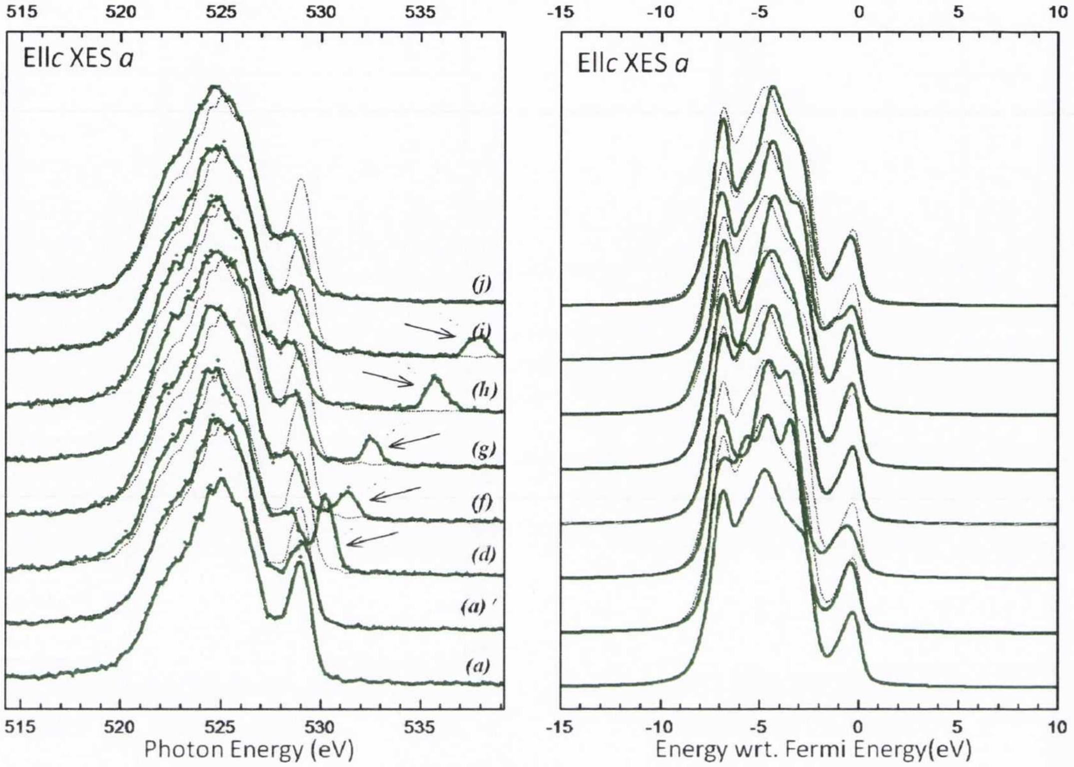

Figure 5.11: Resonant X-ray Emission Spectra with $E\|c$ and XES along a. This is an out-of-plane scattering geometry. The excitation energies are as labelled in figure 5.7

In the out-of-plane experimental RXES, the elastic peaks are indicated with arrows where they are within the energy window presented. The differences in the shape of the elastic feature recorded for the two different orientations is discussed in section 5.5.3.3.

For excitation energies within $\sim 8\,\text{eV}$ of the threshold of absorption the O $1s$ electron is excited into t_{2g} and e_g hybridized states that are more localized than the states formed by hybridization between the O $3p$ and Ru $5s$ orbitals. As has been described in chapter 2, this near-threshold energy region is the domain of RIXS/RXES where the presence of the O $1s$ photoelectron in a localized state in the conduction band causes the marked energy dependence of the resonant x-ray spectra. The change in shape of the calculated spectra displays this very clearly, with states at the top of the O $2p$ band contributing an additional feature to the spectra, while contributions from the states located in the centre of of the band rise and fall with increasing excitation energy. The measured spectra also show some of the increased weight towards the top of the O $2p$ band for the near threshold excitations. The variation in the emission from states towards the centre of the band is recorded as shifting proportions of spectral weight on the low energy slope of the spectra. The spectra from excitation energies further above threshold show little or no variation with excitation energy at the top of the O $2p$ band in both the calculations and the experimental results. The variation between spectra arises from states towards the centre of the band. The ratio of the intensity of the elastic peaks and main peaks of the emission spectra decreases with increasing excitation energy. The cross section for elastic decay is larger for more localized states lower in the conduction band. The recombination peak (participator decay) dominates the spectra for excitation energies close to threshold in the out-of-plane scattering spectra only where in additional specular reflection is enhanced.

As described in detail in chapter 3 the simulated RXES spectra are broadened by three factors. A Gaussian broadening to reflect the instrumental resolution of the XES instrument (0.7 eV), a Lorentzian core-hole lifetime broadening to reflect the O $1s$ core hole ($\sim 0.3\,\mathrm{eV}$) and a parameter that reflects the decreased valence hole lifetime, where the additional Lorentzian broadening increases from zero at the Fermi level to the bottom of the valence band. The parameter describing the valence hole lifetime broadening is the same as that chosen in the case of the SnO_2 and TiO_2 spectra but is perhaps not appropriate to the metallic RuO_2. The intense feature at $\sim 7\,\mathrm{eV}$ in the simulated RXES is not present in the experimental spectra, though there is clearly a feature at this energy. This could indicate that the valence hole broadening applied is not sufficient to account for that which is present in the experiment.

5.5.3.2 RuO_2 NXES difference spectra

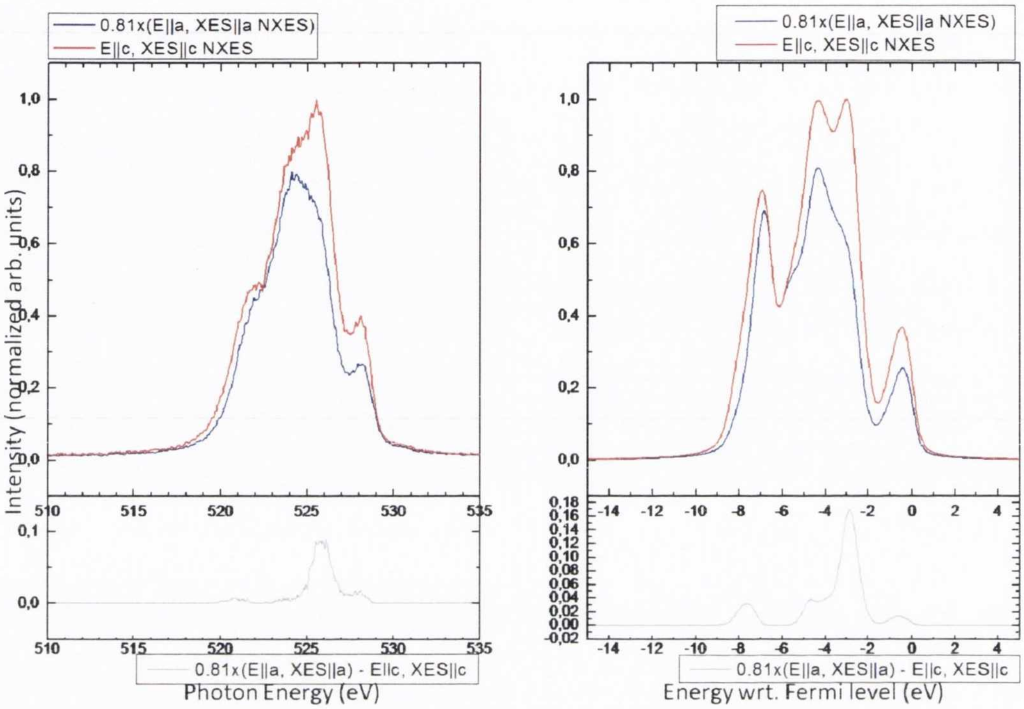

Figure 5.12: A subtraction of the **E**$||a$, XES$||a$ from the **E**$||c$, XES$||c$ NXES experimental spectrum in the left hand panel, with the subtraction of the equivalent non-resonant simulated spectra in the right hand panel.

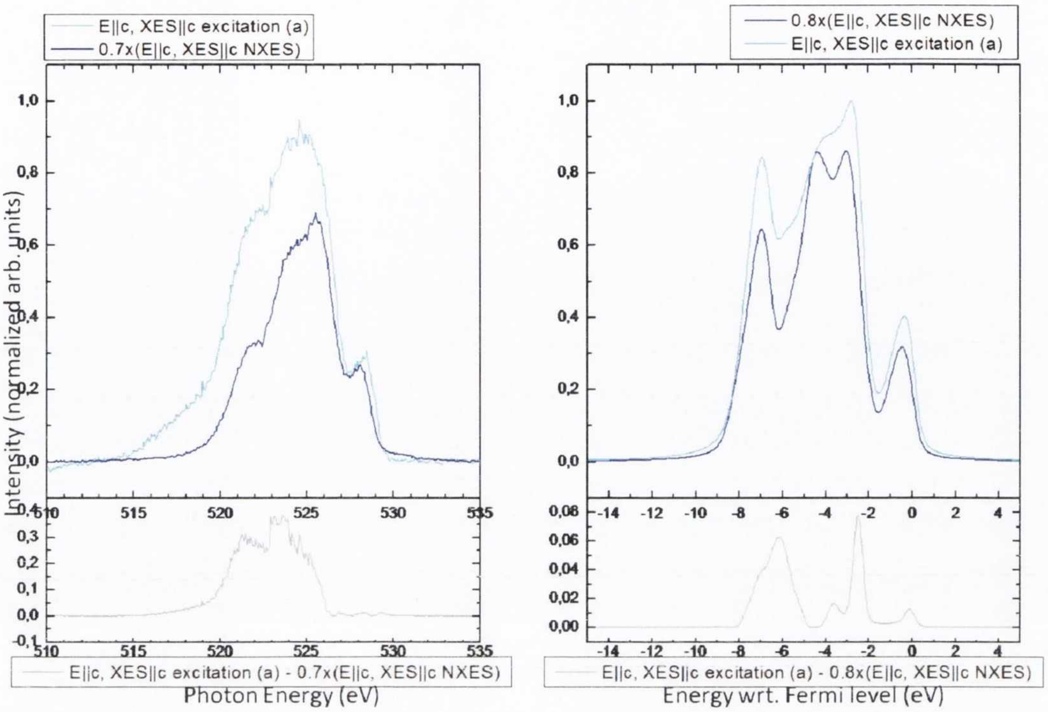

Figure 5.13: A subtraction of the NXES spectrum from the most threshold RXES excitation energy spectrum, labelled (a) in figure 5.7 for the **E**||c, XES||c scattering geometry in the left hand panel, with a subtraction of the simulated RXES for the equivalent energies in the right hand panel.

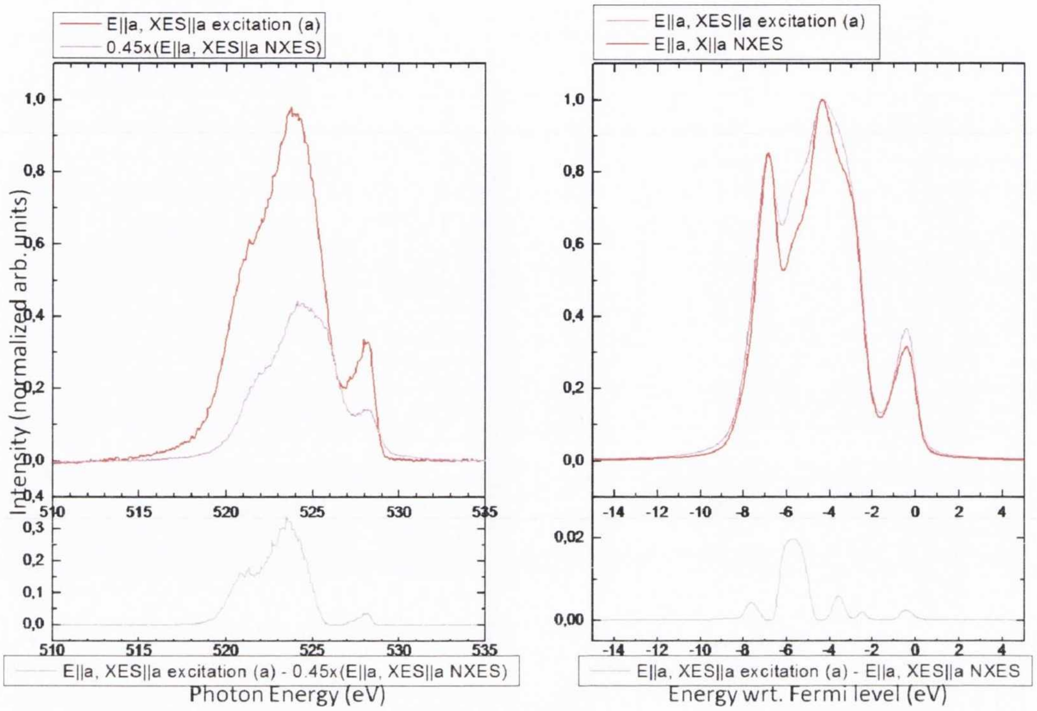

Figure 5.14: A subtraction of the NXES from the most threshold RSXE spectrum, excitation energy (a) in figure 5.7 for the $\mathbf{E}||a$, XES$||a$ scattering geometry in the left hand panel, with a subtraction of the equivalent simulated RXES in the right hand panel.

It was predicted by the molecular orbital bonding model that the density of states at the top of the valence band is composed of π- bonded Ru $4d$ t_{2g}-O $2p_y$ orbitals, which were non-bonding in the case of TiO_2, but bonding in this instance. Difference spectra were constructed by performing subtractions with certain pairs of the experimental and simulated RXES, after a suitable multiplicative factor had been applied. The selection of a multiplicative factor is a rather arbitrary decision, with the main selection criterion on our case being that the spectrum to be subtracted overlaps with the other spectrum to the greatest degree possible, such that all common density of states contributing to the emission in both orientations will be canceled out.

This was an application of the approach summarized in figures 5 and 6 of Eberhardt and Eisebitt [104], wheir their argument is that a k-selective RIXS spectrum can be obtained as opposed to the fraction of the RIXS spectrum that is k-unselective or equivalent to the non-resonant XES spectrum. This approach is intended to assess how much of our RXES spectra are k-selective. However, with the additional state selectivity (σ^* versus π^*) and its variation from threshold to non-renonant, those difference spectra may be more helpful in ascertaining the particular contribution of π or σ states from in-plane (or out-of-plane) scattering. It must be borne in mind that while the subtractions performed present the differences between spectra in "high relief", the subtractions shown in figures 5.12, 5.13 and 5.14 employ an *ad hoc* method in terms of the scaling applied to the spectra which are the arguments in the subtraction. The scaling was adjusted such that the negative remainders were minimized after the subtraction, and the result was squared, to remove the presence of a "negative" spectral weight difference in the result.

Figure 5.12 shows the RXES spectral weight remaining when normal emission spectra from different spectrometer orientations are subtracted from each other. In the left hand panel, the excitation geometry is $E||a$ and the right hand panel contains the NXES measured in the $E||c$ excitation geometry. The light gray-coloured trace in both panels depicts the remainder when the spectrum resulting from emission along the c axis is subtracted from emission along the a axis. This locates in energy the spectral contribution arising from the O $2p_y$ PDOS, which is solely projected in the plane defined by the two a axes. From the description of the M_3O trigonal planes this density of states has previously been assigned to π-like bonding by the O p_y orbitals. The black traces in both panels depict the intensity that remains when the NXES spectrum measured with XES$||a$ is subtracted from the NXES resulting from XES$||c$. This locates in energy the spectral contribution from the O $2p$ PDOS projected in the plane defined by one of the a axes and the c axis. The resulting spectral intensity has a far wider extent in energy than that obtained for the former subtraction covering most of the valence band.

Figures 5.13 and 5.14 show the difference spectra produced when the NXES spectrum is scaled to fit within the trace of the RXES spectrum produced by the lowest threshold absorption energy selected for both the $\mathbf{E}||a$, XES $||a$ and the $\mathbf{E}||c$, XES$||c$ scattering geometries respectively. As discussed by Eisebitt and Eberhardt [104] the NXES spectra are taken to represent the non-k-selected PDOS, due to the effective continuum of momenta readily accessible by the excited electron far above threshold in the conduction band. As described in chapter 2, the near-resonance RXES contains a combination of k-selected and non-k-selected components, and we attempt to identify the spectral features corresponding to the k-selected contribution by performing the subtraction described. Returning to figures 5.1, and 5.2 we suggest that at the threshold of absorption in the $\mathbf{E}||a$ orientation, the k-selected component extracted from the RXES would be expected to have maxima corresponding to the occupied O $2p$ PDOS close to the Z point (the density of states is further selected to those projected in the plane perpendicular to the a axis due to the XES$||a$ emission geometry). Likewise for the near threshold absorption in the $\mathbf{E}||c$ orientation, the k-selected component of the RXES should have maxima corresponding to the O $2p$ densities of states at the Γ point, with the XES$||c$ selecting the states at this point that have a projection in the plane defined by the two a axes.

5.5.3.3 The structure of the elastic peaks

Due to the dipole selection rule there are strong elastic peaks visible primarily in the out of plane scattering geometry. The form of these elastic peaks is also evidently polarization-dependent for reasons explained by the different densities of states projected on the crystalline a and c axes. The elastic peaks recorded in the $E||a$, XES along c geometry are asymmetric with a shoulder protruding from the low energy side. This asymmetry increases with excitation energy. The elastic peaks recorded in the $E||c$, XES along a geometry are relatively more symmetric by comparison, for all excitation energies chosen.

This phenomenon is due to the minimum in the density of states projected along the c axis just above the Fermi level. Emission taking place following the excitation of a valence electron into the unoccupied density of states is only available for the density of states projected along the a axes. The states projected along the c axis make a large contribution to the emission spectra in the $E||c$, XES along a geometry. On the contrary, the large density of states projected along the a axes just above the Fermi level give rise to $d-d^*$ transitions across the Fermi level from the valence band, that contribute inelastic structure to the elastic peak. These should correspond to reflectivity measurements such as those of Goel *et al.* [100] where very high reflectivity from 0.5 eV to 1.5 eV is recorded as being more prominent along the c-axis due to metal-metal bonding and t_{2g}-t_{2g}^* excitations.

5.6 Conclusions

The natural linear dichroism in rutile RuO_2 , the only metallic oxide studied in this thesis, was observed for both the conduction and valence band via polarization dependent XAS and XES at the O K edge respectively. As far as we are aware, no similar polarization-dependent XAS and RXES study of RuO_2 has been reported previously. We show clear evidence of the Ru $4d$ t_{2g} π^* PDOS in the O K-edge XAS in the E$||a$ geometry, and the contrasting prominence of the Ru $4d$ e_g σ^* PDOS for the E$||c$ geometry.

The experimental O K-edge RXES spectra show a strong energy dependence for excitationi energies within $\sim 8\,\mathrm{eV}$ of the threshold of absorption. The most contrast between the experimental spectra recorded in the various scattering geometries corresponded to the region at the top of the O $2p$ valence band PDOS in the valence band formed by π- bonding between the Ru $4d$ t_{2g} and O $2p_y$ orbital which was non-bonding in TiO_2.

The effects of the anisotropic PDOS spatial projections were most evident via the structure observed within the elastic peaks of the experimental RXES spectra. The minimum in the density of states projected on the c axis just above the Fermi level, and the large density of states projected along the a axes within the same energy region gives rise to a set of elastic peaks visible in the $E||a$, XES along c with a distinctly asymmetric profile. This is due to the to $d - d^*$ transitions across the Fermi level corresponding to the large a axis projected density of states contributing inelastic structure to the elastic peaks.

The difference spectra produced showed the location in energy of the spectral weight due to the O $2p_y$ density of states perpendicular to the M_3O planes. Although the approach was not as conclusive as that applied in the case of SnO_2 , the good agreement between the difference spectra in the $E||c$, XES along c geometry and the difference spectra for the corresponding simulated spectra indicates that the main parts of the σ versus π dependence is described correctly, certainly with respect to the NXES. Both the experimental RXES and difference spectra were well simulated by the calculated PDOS.

Chapter 6

Resonant x-ray emission and absorption spectroscopy of rutile and anatase TiO_2

6.1 Introduction

Rutile is a synonym for a particular crystal structure of TiO_2 which is also used as a label for the structure adopted by several other transition metal oxides and fluorides with a MA_2 formula unit. Rutile was originally the name given to a common ore of titanium on account of its red hue.

In all there are seven such polymorphs of TiO_2. The crystal structures TiO_2 adopts for ambient conditions are the tetragonal rutile and anatase phases, and the rhombohedral brookite [105]. The name anatase refers to the longer vertical axes noted in naturally occurring minerals with this structure compared to rutile.

It is to be expected that the different polymorphs of TiO_2 possess different electronic structures, surface configurations and optical properties [106]. And indeed, significant differences have been found between anatase and rutile in their electrical, magnetic and optical properties [107] and chemical properties, which are summarized elsewhere [108, 109, 107]. For instance anatase and rutile have different reported band gap values with rutile having a band gap close to 3.0 eV and anatase closer to 3.2 eV [108] in well-crystallized bulk single crystals. The brookite form of TiO_2 is not regarded as technologically useful, and it has not been widely studied. Both rutile and anatase in their stoichiometric forms are insulators, but readily generate concentrations of oxygen vacancies in their lattices by the reduction of their surfaces when heated to temperatures $\leq 1000\,^{\circ}\mathrm{C}$. In this state, they become n-type semiconductors.

The combination of high-resolution spectroscopy, x-ray diffraction and accurate electronic structure calculations, such as we are attempting here, has in the past led to corrections and reinterpretations of the bonding arrangements entered into by the ions in solids, and will only be summarized here as it applies to TiO_2 [30, 7].

TiO_2 is a material with many potential uses. As is the case with other transition metal oxides, surface processes, essentially the catalysis of redox reactions, constitute a large portion of their applications [108]. The search for a solar powered source of hydrogen has featured TiO_2 as one of its most important constituent materials [110]. This is particularly true of anatase TiO_2 [111].

In materials science the special properties of surfaces are of fundamental importance, and such alterations as the engineering of bandgaps promises to extend the usefulness of materials. While bandgap engineering by doping is well known, there are many opportunities to explore bandgap engineering by defect engineering and structuring. Alterations in the bandgap by applying the effects of quantum confinement is an active area of research [112]. Knowledge of the electronic structure of TiO_2 is important in it own right, and also as a means to understanding the electronic structure of a host of titanate systems such as $SrTiO_3$ and $BaTiO_3$.

This study takes as its starting point a molecular orbital picture of bonding in the rutile structure. From this model the polarization dependence of the x-ray absorption is used to resolve an axis-projected density of states in the conduction and valence band, using resonant x-ray emission, and varying the x-ray scattering geometry with respect to the linearly polarized x-rays.

This chapter presents the results of the study of the electronic structure of undoped TiO_2. A full polarization-dependent scattering study was completed on rutile TiO_2 to study the axes-projected O $2p$ PDOS. The valence and conduction band of nanostructured anatase TiO_2 was studied via XAS and XES at both the Ti $L_{2,3}$ and O K edge. XAS and XES was also performed on bulk single crystal anatase TiO_2 to investigate the possible effects of the nanostructures on the electronic structure. The electronic structure of rutile TiO_2 was calculated using the Wien2K formulation of DFT, yielding a calculated band structure, an ion and orbital-angular-momentum resolved PDOS in the valence and conduction bands and simulated polarization-dependent RXES. The electronic structure of anatase TiO_2 was also calculated to aid the interpretation of the valence and conduction band PDOS probed by XES and XES.

The chapter begins with a summary of the diverse role TiO_2 plays in technology, the emphasis primarily being on applications that the present study of the electronic structure may have some potential bearing on. It was considered most suitable to place a section outlining the structural parameters of rutile and anatase immediately preceding a brief description of a molecular-orbital interpretation of the bonding arrangements in the structures, leading into the presentation of the calculated bandstructure character plots, O $2p$ PDOS and rutile-anatase bandstructure comparison.

The subsequent sections describe the experimental details, and present the results of our polarization-dependent resonant emission and absorption study of the bulk crystals and the RXES simulated from the calculations presented in section 6.4. The O K-edge XAS and RXES from nano-anatase TiO_2 is also discussed.

6.2 Applications of rutile and anatase TiO_2

Selected applications of TiO_2, that particularly pertain to its electronic structure, reactivity and optical properties are arranged in this section under the appropriate technological fields that they belong to. Some of the most topical applications of TiO_2 include it's use as a a photocatalyst, a photovoltaic material, a photolytic medium for the evolution of hydrogen, and as an electronic material: a dielectric in logic devices or spintronic media, or as an electrochromic material and more recent memristive technologies.

To classify the family of applications of TiO_2 that are related to new directions in energy production, it can both be used to generate electricity from sunlight in a photovoltaic, or to generate hydrogen in a photolytic cell.

Due to its wide band-gap TiO_2 is suitable for use in photoinduced chemical reactions where irradiation of the TiO_2 with light creates an excited electron-hole pair that can be spatially separated before recombination. The absorption of light and creation of an electron - hole pair that migrate to the surface and interact with adsorbed species is the basis of the use of TiO_2 for photolytic production of hydrogen from water without external bias, photovoltaic generation of electricity from sunlight and the photocatalytic decomposition of organic molecules.

Many of the applications of TiO_2 rely on the properties of its surfaces rather than its bulk single crystal form, such as its role as a catalyst [113].

Finally, and foremost TiO_2 is widely used as a pigment, and as a constituent of sunscreen. As much as 98 % of the annual world production of TiO_2, exceeding 4 million tonnes, is used to make white pigments.

6.2.1 Photolysis and Photovoltaics

The first report of the photolytic evolution of hydrogen from water by photoexcited rutile TiO_2 by Fujishima and Honda [114], was the initial stimulus to many of the subsequent studies of the properties of the surfaces of TiO_2. The investigation of TiO_2 as a photolytic source of hydrogen has continued to the present day. The focus of much of the research is in achieving suitable band positions by doping the TiO_2 [115] or by synthesizing nanostructures. To this end a blue shift in the absorption edge of 0.2 eV for dimensions in the range of $5 - 10$ nm has been observed in nanostructured anatase TiO_2 [112]. Though the anatase polymorph has been shown to be the most efficient for photocatalysis, it is more difficult to synthesize single crystals [107].

Photovoltaic cells based on TiO_2 electrodes continue to be developed and refined in efficiency [116, 117]. To convert visible light to an electric current they rely on a dye-sensitization technique. In this approach an organic dye is adsorbed on the TiO_2 surface, and the absorption of light within the dye molecules promotes an electron to the LUMO, which then falls into the empty conduction band of the TiO_2 and can be collected by an external circuit. The dye must be regenerated after the absorption of the photon from the surrounding electrolyte in the cell. A review by Chen and Mao [111] and from Vaysierres [110] details these applications.

6.2.2 Catalysis

TiO_2 is widely used in the photocatalysis and photodegradation of organic molecules. The same mechanism of electron-hole generation, separation, migration and reduction/oxidation at TiO_2 surfaces is involved where adsorbed organic species are broken down at TiO_2 surfaces [108]. The applications of this reactivity include disinfection by the oxidation and destruction of organic pollutants in water, as well as the destruction of cells and other biological entities [118]. An extensive review of catalysis at TiO_2 surfaces has been reported in the literature [119].

6.2.3 Dielectric Applications

Dielectric applications of TiO_2 include its use as a host oxide for dilute magnetic semiconductors see *e.g.* [120] and its use as a gate oxide in MOSFETs and other logic devices, see *e.g.* [121].

Dilute magnetic semiconducting behaviour has been reported for ferromagnetically doped rutile and anatase TiO_2 [122, 123]. The role of oxygen vacancies that has been identified as critical to the process of catalysis at TiO_2 surfaces, is also expected to play a significant role in the ferromagnetic ordering of TiO_2 based dilute magnetic semiconductors.

Another dielectric-type application of TiO_2 is its doping and incorporation in DRAM capacitors [121], where it has displayed very low leakage currents for films as thin as 0.48nm. The manipulation of oxygen vacancies within TiO_2 by the application of an electric field, which is discussed in greater detail in the following section, has been demonstrated to provide a switchable current rectification behaviour in commercially procured rutile TiO_2 crystals [124].

6.2.4 Electrochromism

Another potential application of TiO_2 exploits the electrochromism of the material. Electrochromism describes the alteration in the colour of a solid by the application of an electric field. This change in colour, usually to a shade of dark blue from transparent, had previously been noted in bulk TiO_2 when it annealed in a vacuum, causing the stoichiometric TiO_2 to become reduced giving rise to a sufficient concentration of oxygen vacancy defects, $\mathrm{O}_\mathrm{V}^{2+}$ or Titanium interstitials. In fact, an early study linked the colour of the resulting TiO_2 with the percentage of all oxygen positions that were vacant [125]. In this study the samples varied between gray and yellow like tones, with blue-gray the darkest corresponding to an oxygen vacancy fraction of the total oxygen in the lattice of 0.85 %.

An interesting behaviour has since been reported in samples of single crystal rutile TiO_2 that have been reduced by annealing, when a constant electric field of several tens of V/cm was applied [126]. The application of a DC electric field, once it is of sufficient strength, causes the a region of deeper colouring to emerge in the reduced TiO_2. This alteration of the position of the coloured regions is caused, in one model, by oxygen vacancy defects present in the lattice, with their effective positive charge, which migrate towards the cathode (assuming that the temperature of the TiO_2 does not get high enough for a dominant current of Ti ions to flow in the lattice). The crystal visibly darkened in regions of high oxygen vacancy concentration due to the photon of visible light that is absorbed in the following transition

$$(\mathrm{O}_\mathrm{V}^{2+} \cdot \mathrm{Ti}^{3+}) \overset{\hbar\omega}{\rightarrow} \mathrm{O}_\mathrm{V}^{2+} + \mathrm{Ti}^{4+} + \mathrm{e}^-$$

that describes the transfer of charge out of the Ti-O_V pair. In the experiment the electric field was applied parallel to the rutile *c*-axis. The samples used had the same orientation as the samples used in the current thesis, the largest surface being the (110) surface and the *c* axis, or [001] direction oriented along the long edge of the crystal. The resistivity of the TiO_2 drops by some orders of magnitude upon reduction, and the application of an electric field of $\sim 100\,\mathrm{V/cm}$ results in a sufficient current density to cause the TiO_2 sample to glow by Joule heating [126].

Varying the transmittance of an optical material, and modulating its colour by electric signals has immediate importance to new approaches in surface coatings and display technology. Incorporation of Li^+ into the lattice of anatase nanocrystals of TiO_2 has been shown to result in a fast and high contrast switching in the visible and into the infrared, as summarized by Chen and Mao [111]. Another approach to the application of electrochromism also involves TiO_2 as a substrate for an electrochromic organic compound or dye that changes colour with oxidation state.

The interaction of the conduction band contours in TiO_2 with an external electric field facilitates the efficient and reversible transfer of electrons to adsorbed molecules at the TiO_2 surface. This has been acheived experimentally in TiO_2 nanostructures coated with different modular molecules with varying substituents depending on the suspending electrolyte and range of colours aimed for [127]. One electrochromic window that has been realized experimentally also employed a transparent counter-electrode of nanostructured SnO_2 to complete the redox circuit within the intervening electrolyte [128]. The efficiency of the electrochromism, and the response-time of the transmittance switching are related to the morphology of the crystalline TiO_2 samples.

6.2.5 Memristive Technology

The process described in the previous section whereby electromigration of either O_V or Ti_i causes resistivity changes is not favoured at room temperatures in bulk crystals but in nanostructured TiO_2 films the requisite dielectric fields can be achieved more easily [124]. This has in fact given rise to an implementation of the fourth missing circuit element "the memristor" as announced by the group of Williams [129]. This is implemented by a platinum electrode crossbar strategy sandwiching a rutile TiO_2 filling [130]. The state of the device after the application of the electric field is sensitive to the previously applied direction of the electric field and current flow and is thus a non-volatile memory element. Hewlett Packard have recently announced a new memory based on this $Pt/TiO_2/Pt$ memristor technology. The action of this memresitve technology has been recently studied by spatially selective NEXAFS or XAS at the Ti L-edge [131]. Future measurements at the O K-edge NEXAFS will perforce rely on some of the results presented in this thesis as otherwise they may misinterpret such variations as they observe.

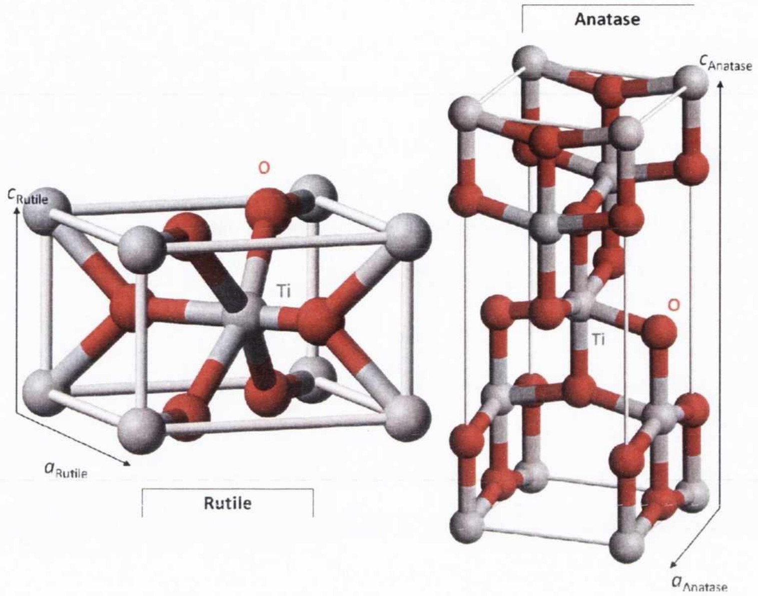

Figure 6.1: Rutile and anatase crystal lattice structures of TiO_2

6.3 The Rutile and Anatase Structures

While the crystal structure of both anatase and rutile TiO_2 is based on the coordination of a Ti ion by six O ions in distorted octahedra, Anatase is a larger and more complex unit cell than rutile, with greater volume: $34.1\,\text{Å}^3$ compared to $31.2\,\text{Å}^3$ per formula unit in rutile [132, 133] which is visible in figure 6.1. In both rutile and anatase the octahedra are distorted in the sense of having their apical bond distances longer than their equatorial bond distances. Adjacent TiO_6 octahedra in the rutile structure share edges and arrange in alternating layers with the major axis of the octahedra lying at 90° to each other. In the anatase TiO_6 octahedron the equatorial bonds are not aligned at 90° to the apical axis of the octahedron, with two of the opposing oxygens lying above the regular octahedral waist plane and the other two lying below the plane. Neighbouring octahedra share corner oxygens to form planes that pack by sharing edges with the planes of octahedra above and below. The distorted octahedra share four edges in anatase and two in rutile [134].

In addition, table 6.1 compares the bond lengths and other relevant crystal structure parameters of anatase and rutile TiO_2. Anatase TiO_2 belongs to the $I4_1/amd$ space group.

Structure	Rutile	Anatase
a (Å)	4.593 [135]	3.784 [136]
c (Å)	2.959 [135]	9.515 [136]
internal u parameter	0.305 [135]	0.208 [136]
Unit Cell Volume (Å^3)	62.5 [132]	136.3 [133]
nearest d_{M-M} (Å)	2.53	3.04
nearest d_{M-O} (Å)	1.949	1.934
Bandgap (eV)	3.0 [108]	3.2 [108]

Table 6.1: Rutile and anatase TiO_2 crystal structure parameters

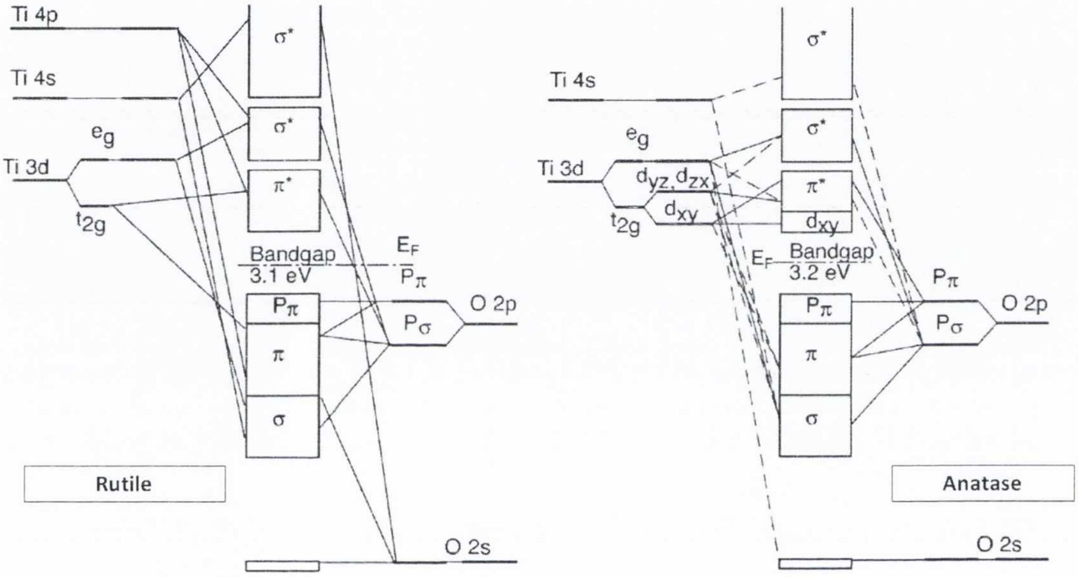

Figure 6.2: Molecular orbital diagram showing the σ and π bonding combinations in rutile and anatase TiO_2 from Thomas *et al.*. [11]

6.3.1 Molecular orbital scheme of bonding in rutile and anatase TiO_2

The approximately octahedral TiO_6 unit is common to all three polymorphs of TiO_2 listed in the the introduction to this chapter. A molecular orbital diagram is included to illustrate the expected differences in the electronic structure between anatase and rutile TiO_2.

While in the ionic model TiO_2 is regarded as a d^0 system, the rutile and anatase crystal structures create a partial occupancy of the d orbitals, which reduces the electrostatic energy implied in the purely ionic situation. In this fashion both ionic bonding, involving the transfer of charge from the Ti 3d orbitals to the O 2p orbitals, and covalent bonding involving the hybridization of the Ti 3d and O 2p orbitals play a role in the electronic structure of TiO_2. As summarized in table 6.1 the nearest metal-metal distance in anatase is larger than rutile. The Ti $3d$ t_{2g} orbitals are therefore more isolated in the anatase structure, where there is some interaction between neighbouring Ti ions in the rutile structure [107].

6.4 Electronic Bandstructure and PDOS calculations

In order to make a complete comparison to the results of the x-ray spectroscopic measurements, a set of DFT calculations for the electronic structure of TiO_2 were performed. These calculations employed the full potential linearized augmented plane wave basis set as implemented in the WIEN2K code. For the rutile structure the calculations were carried out using both the standard settings of the code as well as generalized gradient approximation of Perdew [89]. In particular for rutile TiO_2 Persson et al. [68, 137] similar to the instance of SnO_2 [65, 66] have used a LDA+U scheme to model the self-interaction correction Their motivation is to accurately model the effective mass of the heavy hole or the dispersion of the bands, particularly the band derived from the non-bonding p-orbital near the valence band maximum in order, in turn to accurately model the optical absorption near the band edge [68, 137]. We begin, as a starting point with their values of $U_d = 10.0$ eV for the Ti cation and $U_p = 0.0$ eV for the O anion to both enhance d localization and $p-d$ hybridization and to obtain an accurate value for the band gap. The electronic structure of rutile was calculated using the observed crystal structure and the experimentally determined lattice constants of $a = 4.953$ Å and $c = 2.957$ Å were used as the initial inputs. For rutile, the radius of the muffin tin spheres used to divide the volume of the cell into regions of atomic-like and plane-wave expansions of the Kohn-Sham wave functions was 1.95 au and 1.735 au for Ti and O respectively. The Brillouin zone was sampled with 1000 k points in order to obtain the DOS and PDOS results presented here.

The anatase TiO_2 calculation also employed the FP-LAPW approach implemented in WIEN2K. In this instance the calculation took as a starting point the calculation of Ryu *et al.* [138]. This employed the LDA approximation and did not implement the LDA+U approach described above for rutile TiO_2. As a result the calculated band gap for anatase TiO_2 is 2.5 eV. The anatase TiO_2 lattice paramaters of Horn were used in the calculation, namely $a = 3.784$ Å and $c = 9.515$ Å[136].

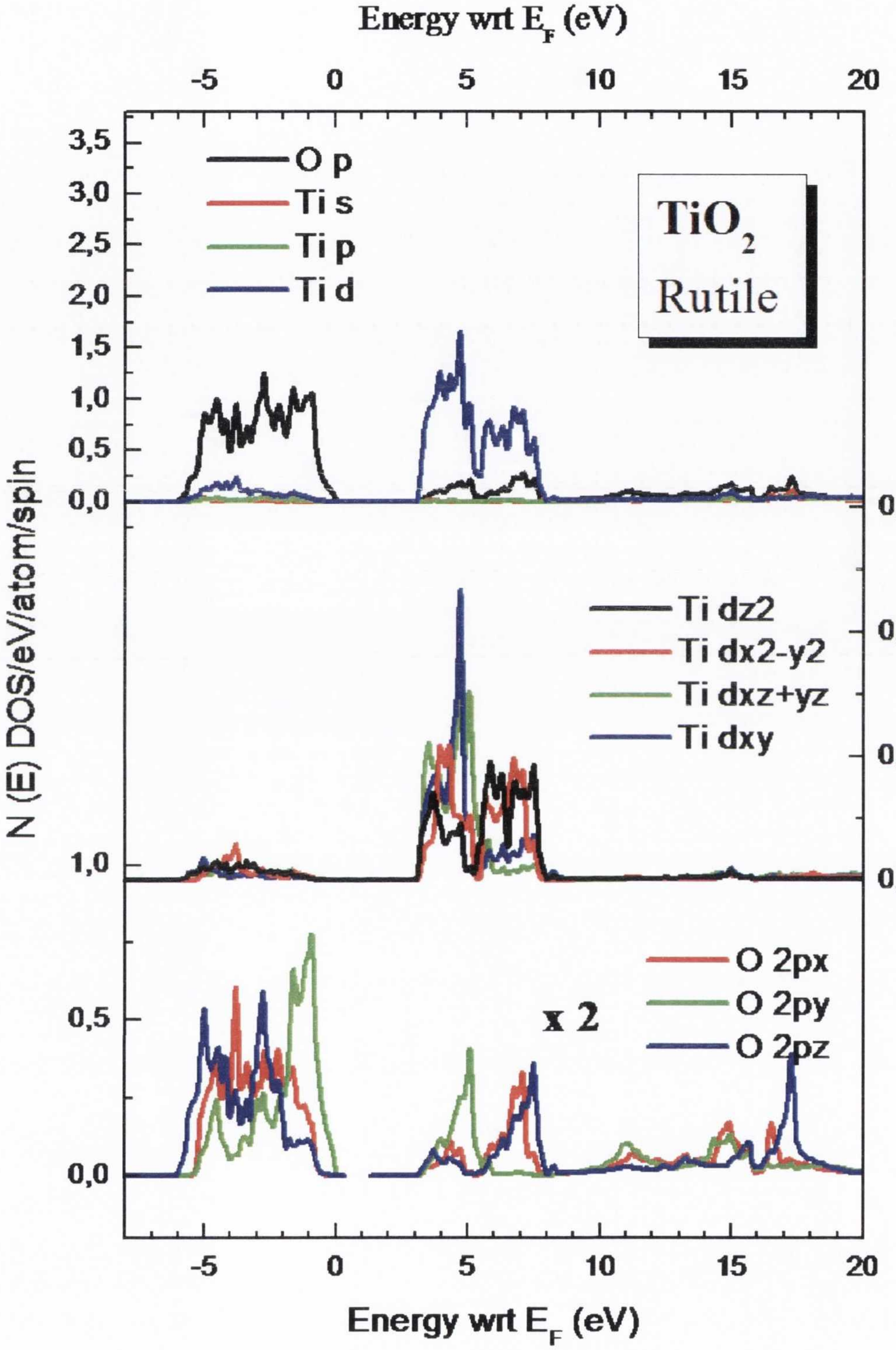

Figure 6.3: Calculated PDOS for rutile TiO_2 resolved by ion and axis projection. Top panel: O *p* and Ti *s*, *p* and *d* PDOS. Middle and Bottom panel: Ti *d* and O 2*p* PDOS projected onto the O natural coordinate axes respectively

6.4.1 Calculated bandstructures and projected densities of states for rutile and anatase TiO_2

Figure 6.3 shows the rutile TiO_2 PDOS for the Ti d, s and p components as well as the O $2p$ components. The d PDOS is further broken down into four components showing their e_g (d_{z^2} and $d_{x^2-y^2}$) and t_{2g} (d_{xy}, d_{xz+yz}) character. As the d_{xy} and d_{yz} orbitals yield an identical calculated projected PDOS, they are combined in the d_{xz+yz} PDOS. The O $2p$ PDOS is displayed according to the natural coordinate frame when O $2p_z$ is the projection along the z-axis which is along the apical direction of the TiO_6 octahedron and consequently reflects the O sp^2 hybridized orbitals which form M-O σ-bonds with the Ti cation e_g orbitals.

The O $2p_x$ projection is also within the Ti_3O plane and thus also reflects O sp^2 hybrid orbitals participating in M-O σ bonds with Ti d e_g orbitals, and their projection along the c-axis [001] direction which is parallel to x. Finally, the O $2p_y$ orbital is perpendicular to the Ti_3O plane and represents the non-bonding $2p$ orbital or O π which only barely takes on any Ti d-t_{2g} character. This non-bonding orbital dominates the valence band maximum.

The uppermost panel of figure 6.4 shows the anatase TiO_2 PDOS resolved by its O, Ti, and orbital angular momentum projections. The middle and lowermost panel show the Ti d PDOS, and the O $2p$ PDOS resolved by the individual axes projections for the O natural coordinate system respectively. The coordinate system for the Ti ions in the anatase crystal structure is that adopted by Asahi *et al.* [107] and also used by Thomas *et al.* [11] in the molecular orbital diagram reproduced in figure 6.2. In this local coordinate system the z axis is co-linear with the apical axis of the TiO_6 octahedra, and the x and y axes contained in the plane of the (distorted) octahedron's equator, and are each oriented approximately towards an equatorial oxygen. The local coordinate system of the O ion in anatase TiO_2 is the same as the rutile scheme, where the z axis is co-linear with the apical axis of the TiO_6 octahedron, the x axis is perpendicular to the z axis and lies in the M_3O plane, and the y axis is perpendicular to the M_3O plane. The distortion of the TiO_6 octahedra in the anatase crystal structure, resulting in the displacement of two opposite equatorial oxygen ions below the plane of the equator and two above the equatorial plane gives rise to the splitting of the t_{2g} levels depicted in figure 6.2 where the d_{xy} orbital is lower in energy than the two remaining t_{2g} orbitals, and is not involved significantly in any bonding-antibonding combinations, giving rise to a localized, non-dispersion non-bonding feature in the calculated projected PDOS.

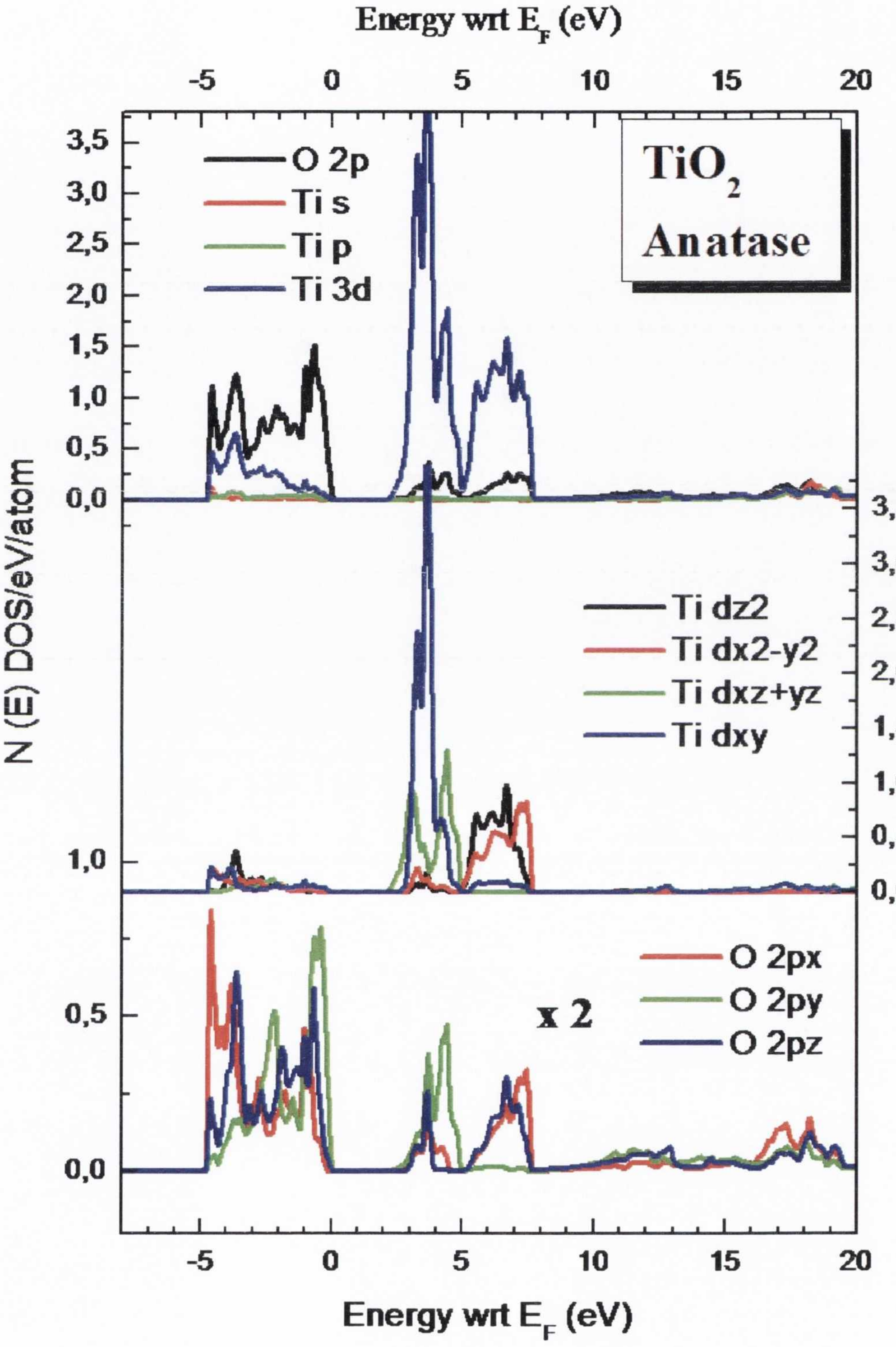

Figure 6.4: Calculated PDOS for anatase TiO_2 resolved by ion and axis projection. Top panel: O *p* and Ti *s*, *p* and *d* PDOS. Middle and Bottom panel: Ti *d* and O 2*p* PDOS projected onto the O natural coordinate axes respectively

This presentation of the calculated projected PDOS clearly identifies the σ bonding and antibonding states created by the Ti 3d e_g d_{z^2}, $d_{x^2+y^2}$ and O 2p_x , 2p_z orbitals which lie within the M_3O planes. As the d_{xy} and d_{yz} orbitals yield an identical calculated projected PDOS, in the anatase calculated projected Ti 3d PDOS shown in figure 6.4 the PDOS created by these orbitals is summarily represented by the Ti d_{xz+yz} PDOS in the figure. The most stable σ bonding combination, leading to the PDOS forming the bottom of the valence band is that between the Ti e_g 3d d_{xy}/d_{xz+yx} and 4s orbitals and the O 2p_x orbitals, which are somewhat lower in energy than the σ bonded states between the Ti 3d $d_{z^2}$and O 2p_z orbitals. In the molecular orbital diagram shown in figure 6.2, it can be seen that of the three Ti 3d t_{2g} orbitals, the d_{xy} orbital, as defined with respect to the local Ti coordinate system defined above is predicted not to form M-O or M-M π-bonds like the d_{yz} and d_{zx} orbitals forming a non-bonding Ti 3d PDOS at the conduction band minimum.

The top of the valence band is composed of the PDOS due to the O 2p_y orbitals, which are involved in π bonds with neighbouring Ti 3d $d_{x^2+y^2}$ orbitals which gives rise to a PDOS in the middle of the valence band, and have a large non-bonding character at the very top of the valence band. The non-bonding O 2p_y PDOS at the top of the valence band is answered by a PDOS created by the non-bonding Ti 3d d_{xz+yx} (designated d_{xy} in the molecular orbital scheme of Thomas *et al.* reproduced in figure 6.2) at the bottom of the conduction band, followed by the π^* states due to the small M-O π overlap between the O 2p_y and Ti 3d $d_{x^2+y^2}$ orbitals.

The antibonding counterpart of the σ-bonded states at the bottom of the valence band form the top half of the conduction band DOS, with a pronounced gap between this M-O σ^* DOS and the π^* DOS.

It is instructive to consider the rutile TiO_2 bandstructure diagram in the form of band character plots where the proportion of each band which takes on a particular orbital character is displayed. This is shown in figure 6.5 where the O 2p_x, 2p_y and 2p_z clearly illustrate for the different bands and regions of binding energy the bonding and partial density of states associated with each component.

Thus the non-bonding O 2p π-like band dominates the valence band maximum region while also participating in the π^* peak in the PDOS associated with emptying t_{2g} levels. The lowest binding energy part of the valence band is in turn due to the strong σ-bonding between the p_z projected sp^2 orbitals and the Ti e_g orbitals in particular along the Ti-O apical axis of the octahedra, or the common z projection of the Ti and O coordination frames. As every second Ti_3O plane is at 90° to each other, a more useful prescription for these tetragonal crystals is to see the projected density of states along the real crystal axes, as shown in figure 6.6. This inevitably mixes the sp^2 derived O $2p_z$ and non-bonding π-like $2p_y$ in obtaining a projection on the tetragonal rutile a-axis. The projection on the c-axis is directly that of the O $2p_x$ orbital.

Within the anatase crystal structure, the M_3O planes are also at 90° to each other, but the internal dimensions of the M_3O triangles vary between the structures, as well as their relationship with the crystallographic axes, where the c axis in the rutile crystal structure is co-linear with the base of the M_3O triangle, or the O $2p_x$ direction and in the anatase crystal structure is co-linear with perpendicular height of the M_3O triangle. Therefore, differences in the orbital character of the axes-projected PDOS are expected.

The Ti $3d$ e_g orbitals are clearly involved in a higher degree of M-M π bonding in rutile compared to anatase, comparing the middle panels of figures 6.3 and 6.4. The Ti $3d$ d_{z^2} and $d_{x^2-y^2}$ orbitals produce a significant calculated projected PDOS in the π-bonded region of the conduction band between an energy of 3 eV and 6 eV with respect to the Fermi energy. This is a direct effect of the 20% increase in the closest M-M distance in anatase compared to rutile TiO_2.

Figure 6.7 shows an enlarged re-oriented version of the top panel in figure 6.6, namely the σ- and π-projected O $2p$ PDOS for rutile TiO_2 in the upper half of the figure, overlaid with the σ- and π-like PDOS from anatase TiO_2 in the lower half of the figure. This comparison indicates a greater degree of M-O σ^*-antibonded states at the bottom of the conduction band, between both the O $2p_x$ and $2p_z$ and the Ti $3d$ d_{xy} orbitals in anatase than in rutile, which can be interpreted with reference to the anatase and rutile M_3O units, and the differences in the M-O distances and bonding angles between them.

6.4.2 Previous studies of anatase and rutile TiO_2 via electronic structure calculations

A previous study of O K-edge absorption from rutile TiO_2 in the form of a bulk natural mineral sample, identified two sharp peaks in at the bottom of the conduction band density of states with the ligand-field split Ti $3d$ states, but did not make a conclusion on the noted differences in the relative intensities of these peaks [139]. This study also related the form of the O $2p$ - Ti $4sp$ derived feature in the conduction band to the octahedral coordination of the Ti ion. The late transition meal oxides, d^5 and upwards show a diminished intensity in the "metal d" region of the conduction band due to the lesser degree of d hybridization as the shell fills and contracts. The lower

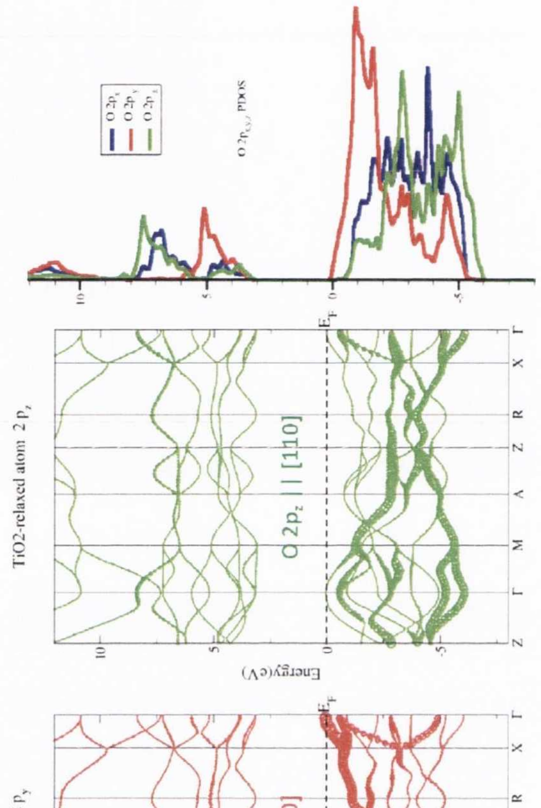

Figure 6.5: Calculated Bandstructure and PDOS of Rutile TiO_2 projected along the natural coordinate system xyz of the oxygen atom

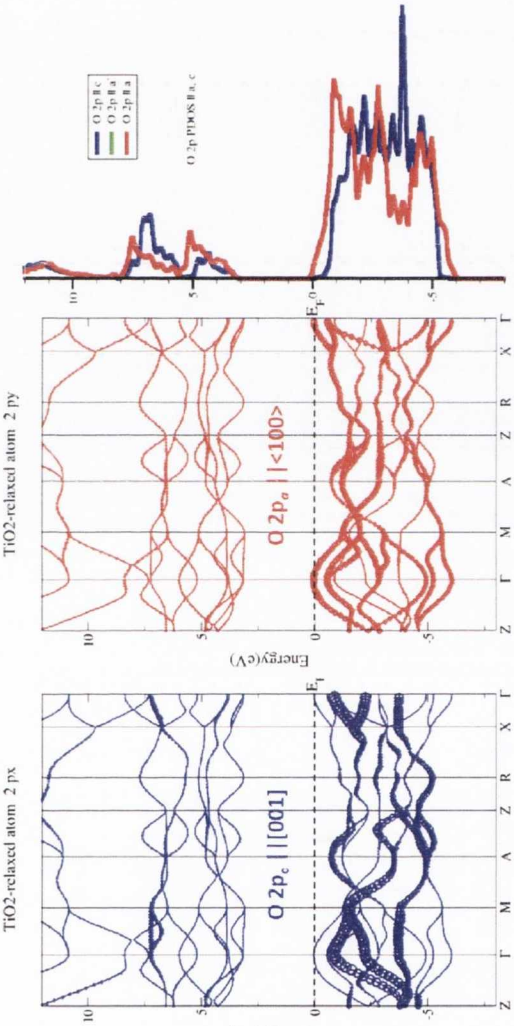

Figure 6.6: Calculated Bandstructure and PDOS of Rutile TiO_2 projected along the crystalline a and c crystalline axes

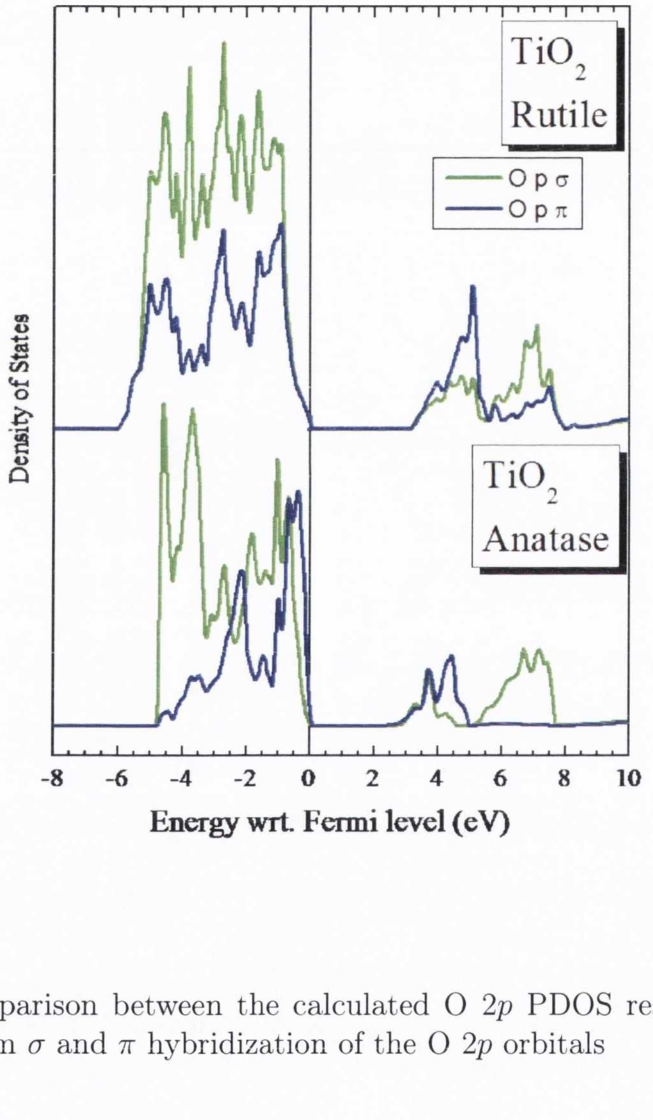

Figure 6.7: Comparison between the calculated O 2p PDOS resolved to show the contributions from σ and π hybridization of the O 2p orbitals

degree of hybridization corresponds to a lower degree of covalency in the bonding. The term ligand-field splitting is used to indicate the "bare" (ionic) crystal field splitting and the effects of hybridization with the coordinating ligands. De Groot's study [139] did not consider the origins of the intensity difference between the two peaks at the bottom of the conduction band in terms of the different spatial orientation of the σ and π bonds involving the e_g and t_{2g} orbitals respectively. The order of the e_g and t_{2g} derived states in the valence and conduction band is also reversed in the interpretation of the bonding in this study compared to the order obtained by the molecular bonding model. The authors subsequently revised their assignment of the bands [134].

A study of the Ti $L_{2,3}$-edge absorption spectrum of TiO_2 noted the different broadening in the spin-orbit split peaks [140]. A fraction of this broadening was attributed to the shorter lifetime of the L_2 hole due to the extra decay channel present in the Coster-Kronig Auger decay process. It is also noted that the larger hybridization of the e_g states gives rise to a wider bandwidth than the t_{2g} states. A multiplet calculation of the $L_{2,3}$ XAS spectrum of TiO_2 using reduced a D_{4h} symmetry rather than O_h also produces good agreement with the experimental spectrum. The origin of the two small peaks at the absorption threshold in the Ti $L_{2,3}$ absorption spectrum was shown to be part of the p^5d^1 multiplet.

A previous theoretical study of the electronic structure and optical properties of TiO_2 using a local-density approximation psuedopotential and plane wave approach calculated a valence band width of 5.7 eV [141]. O $2p$ states composed the top of the valence band, while the Ti $3d$ e_g and t_{2g} were spread throughout. The band gap calculated was direct-forbidden and occurred at Γ with an energy of 2.0 eV. The results of this calculation were similar to the results of the present calculation in terms of the band width and dispersion of the states in the band structure.

An earlier LDA calculation of de Groot was compared to previous calculations in terms of 1) the band gap 2) the width of the valence band 3) the width of the t_{2g} band 4) the width of the e_g band and 5) the crystal field splitting [134]. This study compared the calculated density of states with the O K-edge XAS for $SrTiO_3$, rutile TiO_2 and anatase TiO_2. It found the most notable difference between anatase and rutile in the energy region containing the Ti $4sp$ states, where the density of states derived from these orbitals in anatase is drawn lower in energy. This shift is interpreted with reference to the larger unit cell of the anatase structure, that leads to a smaller interaction between hybrid orbitals and lessens the bonding/antibonding energy difference.

A study of the rutile (110) surface made the point that the chemistry of the TiO_2 (110) surface may vary significantly for samples oxidized under different conditions, due to the consequent differences in surface morphology [142].

An earlier periodic psuedopotential Hartree-Fock calculation yielded non-spherical charge distributions around the ions and a rather flat band structure for rutile TiO_2 both of which corresponded with a large degree of ionicity [143]. It also found a hybridized partial density of states for Ti $3d$ and O $2s$ and $2p$ which supported the finding that the Ti $3d$ states were partially occupied, and were involved in the bonding, which had previously been deduced from experimental charge density maps [31].

A previous study of the valence and conduction band of nanocrystalline rutile TiO_2 by UPS and O K-edge XAS identified five features in the valence band density of states that were attributed to the Jahn-Teller lifting of the degeneracy in the Ti $3d$ levels [144]. A similar five features were extracted from the O K-edge XAS of TiO_2 by taking the second derative of the two O $2p$ - Ti $3d$ hybridized peaks at the bottom of the conduction band. The same study noted two defect related peaks above the valence band edge in the UPS spectra, and a peak at the top of the valence band was associated with the non-bonding O $2p$ states predicted in the molecular orbital bonding model.

A previous study the electronic structure of anatase TiO_2 found that the valence band was composed of three components. The bottom of the valence band was formed by an O $2p$ - Ti $3d$ e_g σ-bonded density of states. The middle of the valence band was composed of O $2p$ - Ti $3d$ $t_{2g}\pi$ bonded states and the top of the valence band was formed by O $2p$ π - oriented states that have a negligible degree of hybridization with the Ti $3d$ orbitals [107].

A previous study comparing the Ti $L_{2,3}$-edge XAS spectra of anatase and rutile TiO_2 noted a difference between the double peak in the L_3 region of the spectrum associated with the Ti $3d$ e_g states [105]. The differences in the e_g peak intensities were attributed to increasing strength of the crystal field related to the increasing delocalization of the $3d$ state. The same study reported differences in the O $2p$ - Ti $4sp$ derived peak in the O K-edge XAS.

The behaviour of the $3d$ orbitals in rutile TiO_2 bonding has been investigated experimentally using an electron diffraction technique to map the charge density of the single crystal [145]. The results of the study agree with the predictions of the molecular orbital model of the bonding in TiO_2, by finding the main concentration of charge in the $3d$ e_g orbitals hybridized with the O sp^2 orbitals of the equatorial oxygens in the TiO_6 octahedra, followed by the e_g orbitals that form σ bonds with the apical oxygens. The study also suggests a degree of π bonding between the $3d$ t_{2g} orbitals of nearest neighbour Ti atoms along the c axis, and the absence of σ bonding between the $3d$ orbitals of Ti atoms. The calculated Ti-atom orbital populations gave 2.62 electrons in the $3d$ band.

A subsequent study based on a periodic linear combination of atomic orbitals approach gave an occupancy of 2.8 electrons in the Ti $3d$ band [146].

Heiliger applied the technique of electron energy loss spectroscopy (EELS) and calculations based on DFT to rutile, anatase and brookite TiO_2 [147]. The study was also performed such as to analyze the orientation dependence of the spectra in the different polymorphs. This approach has a similar motivation to the work of the current thesis, where the existing calculations and experimental spectra had not exploited the spatial selectivity of the crystal structures to obtain orientation dependent electronic structure information, in our case the individual axis projections of the partial densities of states.

The O K-edge absorption spectrum as measured by EELS in Heiliger's changes significantly when the surface direction is changed between the crystalline a and c axes. The intensity of the O $2p$ sp^2 - Ti $3d$ e_g σ hybridized states at 534.0 eV is minimized in rutile when the surface direction is along the a axis. The Ti $L_{2,3}$ are not found to be orientation dependent. Their calculations agree in principle, though the relative intensity between the two peaks at 531.0 eV and 534.0 eV are not well reproduced by the theory.

On the other hand, the O K-edge absorption as measured by EELS shows closely identical spectra for anatase, rutile and brookite TiO_2 while the Ti $L_{2,3}$-edge shows a marked difference between the form and intensity of the peak associated with the σ - hybridized density of states at 460.0 eV and 465.5 eV in the L_2 and L_3 edges respectively.

The study of Thomas, Flavell *et al.* attempted to systematically compare the electronic structure of single crystal surfaces of rutile and anatase TiO_2 [11]. Using resonant photoemission and XAS at the O K and Ti L edges, the electronic structure of the anatase (001) and (101) and the rutile (110) surfaces was studied. The concentration of oxygen vacancies due to different preparation methods was confirmed as a source of variation in the photocatalytic activity of the various surfaces. Similar to previous valence band photoemission spectra from SnO_2 a feature at the low binding energy of $\sim$ 1 eV is found to be caused by states created by reduced Ti^{3+} ions at the surface. The constant initial state (CIS) analysis of the features in the valence band measured for the rutile (110) surface across the Ti $3p$ - $3d$ resonance confirmed the Ti $3d$ character present in the valence band. This analysis also identified the Ti $4sp$ character present at the bottom of the valence band where they form σ bonding molecular obitals. Ti $4p$ π-bonded character is assigned to a feature that resonates in the middle of the valence band by comparison with a calculated PDOS. The top of the valence band is found to be a mixture of π bonded and non-bonding O $2p$ orbitals. In contrast to rutile, the anatase valence band shows little or no Ti $4sp$ character.

The main difference between the the electronic structure of anatase and rutile TiO_2 is at the bottom of the conduction band, where in anatase TiO_2 this is composed of non bonding Ti $3d$ d_{xy} orbitals that are too far apart to form the same π hybridized orbitals with neighbouring Ti atoms as they do in rutile.

The CIS analysis of the valence band in anatase also indicates a higher level of O $2p$ non-bonding character at the top of the valence band than in rutile. The top of the valence band in rutile also contains a contribution from Ti $4p$ orbitals that is absent in anatase.

A previous study by Woicik *et al.* on the hybridized orbtials in the valence band of rutile TiO_2 combining site specific XPS and calculations employing psuedopotentials within the local density approximation and a plane-wave basis [148] determined the individual contributions of Ti and O to the valence band. The calculations gave a doubly lobed Ti PDOS in the valence band originating from Ti-O σ bonds between the Ti $3d$ e_g, $4s$ and $4p$ orbitals and the O sp^2 orbitals at the bottom of the valence band and the π bonded states between Ti $3d$ t_{2g} and $4p$ orbitals with O p_y orbitals at the top. The O $2p$ PDOS shows a triply lobed structure due to the additional non bonding O p_y orbitals at the top of the valence band.

A previous DFT study imposed a Hubbard U correction to the LDA-GGA calculated electronic structure of rutile and anatase TiO_2 to give an improved treatment of the modification created by oxygen vacancy defects [149]. This calculation located the electronic energy levels of the oxygen vacancy defect in rutile and anatase at 1 eV from the conduction band minimum. The calculation also identified a shallow state in the anatase conduction band 0.1 eV below the conduction band minimum in addition to the deep state 1 eV below the conduction band minimum. This additional state was explained by the delocalization of the defect electron due to the difference in the coordination and relaxation around the oxygen vacancy in anatase and rutile. It was suggested that such a state would facilitate increased catalytic activity.

6.5 Experimental Details

The following section outlines the details of the TiO_2 samples which are reported in the present section, and the experimental setup and parameters for the XAS and RXES. The anatase nanosheets, for which details of the growth are summarized in this section, were produced to study the different photocatalytic activities of nanosheets not only with differing proportions of a particular crystal surface, but having been subject to different cleaning solutions to remove the fluoride and other growth precursors from the surfaces.

6.5.1 Single crystal rutile and anatase samples

The single crystal rutile spectra were obtained from samples provided by the Egdell group, and from substrates provided by Dr. Simon O'Brien of CRANN, Trinity College Dublin and Pi-Kem, UK. The Egdell samples had a (110) main surface orientation, and were in the form of cuboids elongated along the c axis which was confirmed by XRD performed before the spectroscopic measurements. The O'Brien and Pi-Kem samples were 5 mm × 5 mm × 1 mm substrates with a (100) main surface orientation, which was confirmed by measuring the O K-edge XAS at intervals of rotation between 0° and 90°.

The single crystal anatase samples were cut and polished from a larger single crystal sample by SurfaceNet GmbH. The orientation of the largest surface was (001).

6.5.2 Anatase TiO_2 nanosheets

A systematic study of the size effects on the electronic structure by Ti $L_{2,3}$ XAS identified a clear trend in the electronic structure [150].

The electronic structure of TiO_2 has been observed by Ti $L_{2,3}$ edge XAS to change between bulk and nanocrystalline samples [151]. The crystal field splitting was observed to decrease in the TiO_2 nanocrystal.

A challenge to the practical application of TiO_2 as a photocatalyst is the fact that the most efficient surfaces for catalysis is also the surface with highest average energy, the (001) surface [152] [108]. TiO_2 nanostructures tend to form such that the lowest energy (101) face takes up most of the surface area, minimizing the surface energy.

Our collaborators produced samples of anatase TiO_2 nanosheets by employing a route to achieving an increased proportion of (001) surface area by terminating the surface with fluorine during growth. This has the effect of lowering the energy of the (001) surface compared to the (101) surface by introducing a Ti-F bond that alters the Ti-O bond lengths in the surface layer. Using a fluorinated surface growth route the nanostructures included in this thesis were synthesized such that up to 89% of their surface area is composed of the highly reactive (001) surface, and the resulting nanostructures perform well in cycled tests of their photocatalytic activity. The fluorination of the TiO_2 surfaces lowers the energy of the (001) surface and it was found that increasing the concentration of hydrofluoric acid in the solution both the size and the percentage of (001) surface area increased. It has been found that after growth the fluorinated surfaces can be cleaned by annealing to produce fluorine free surfaces without altering the crystal structure [152]. The nanosheets were grown using a hydrothermal growth mechanism involving the decomposition of tetrabutyl titanate in a hydrofluoric acid solution. XRD was used to identify the crystal plane forming the upper surfaces of the nanosheets that had been analyzed by SEM to provide an estimate of their dimensions. The results from the study presented here comprise two different (001) surface area proportions of TiO_2 nanosheets. The electronic structure of the resulting products was investigated by XAS and XES to determine if there was any difference that might be linked to the predominance of one surface plane over another.

In a previous experiment by the group that produced the samples the photocatalytic activity of the nanosheets was observed by placing them in a 1 mmol solution of methyl orange, an organic dye molecule and irradiating the container with UV light. Transmission of 465 nm light was used to monitor the rate of degradation of the methyl orange. The volume in the cell was replaced and the degradation cycle repeated seven times for samples of the nanosheets with differing percentages of (001) facets. The photocatalytic activity of the nanosheets increased strongly with (001) facet percentage.

For the O K-edge XAS and RXES, the samples of anatase nanosheets were prepared by using a mechanical vice to press the powder-like material into pieces of indium foil, which were then mounted on a sample-holder with adhesive copper tape and introduced to the analysis chamber via the loadlock, as with other conventional samples.

6.5.3 O K-edge XAS and RXES experimental parameters

All of the the in-plane and out-of-plane measurements on the bulk rutile TiO_2 presented here was undertaken at Maxlab beamline I511-3. The in-plane spectra were measured using a resistive anode encoder, while the out-of-plane spectra were measured using a combination of a phosphorescent screen behind the MCP detector, with a CCD camera capturing images of the screen as the electron showers created phosphorescence.

The in-plane measurements on the bulk anatase TiO_2 single crystal and the nanostructured anatase TiO_2 presented here took place at ALS beamline 7.0.1, and were measured with a resistive anode encoder type detector.

In general, the O K-edge XAS was measured in total electron yield mode with the monochromator resolution set to a calculated value of 0.2 eV for a photon energy of 530 eV. At Maxlab I511-3 this corresponded to an exit slit width of 20 μm. At ALS beamline 7.0.1, the monochromator entrance and exit slit were set to 30 μm and 50 μm respectively. The O K-edge RXES were measured with a calculated energy resolution of $\Delta E = 0.4$ eV for a photon energy of 530 eV, corresponding to an exit slit width of 50 μm at Maxlab I511-3 and an entrance and exit slit width of 70 μm at ALS beamline 7.0.1.

The anatase and rutile TiO_2 bulk single crystal samples were mounted in an identical fashion to that described for the SnO_2 bulk single crystals.

6.6 Results and Discussion

This section presents the results from the in-plane and out-of-plane RXES studies from bulk single-crystal rutile TiO_2, as well as the in-plane RXES from bulk single-crystal anatase TiO_2 , and the in-plane RXES from the anatase TiO_2 nanosheets. The experimental and simulated RXES spectra are discussed with reference to the molecular orbital diagram presented in figure 6.2 and the different dimensions of the anatase and rutile structures, particularly the different bonding angles between the anatase and rutile TiO_2 M_3O planes.

6.6.1 Rutile and Anatase TiO_2 O K-edge XAS and calculated O $2p$ unoccupied PDOS

Figures 6.8 and 6.9 show the O K-edge XAS with $E||c$ and $E||a$, and the calculated O $2p$ PDOS projected on the c and a for rutile and anatase TiO_2 bulk single crystals. The relative intensity of the spectral features are well reproduced in the calculated projected O $2p$ PDOS for both the rutile and anatase examples. The experimental spectra are normalized to unit area.

In the rutile O K-edge XAS the asymmetry in the π^* peak at 531.0 eV in the $E||c$ orientation, the offset between the centres of the σ^* peaks at ~ 534 eV between the $E||c$ and $E||a$ orientations, and the relative intensities of the features between 538 eV

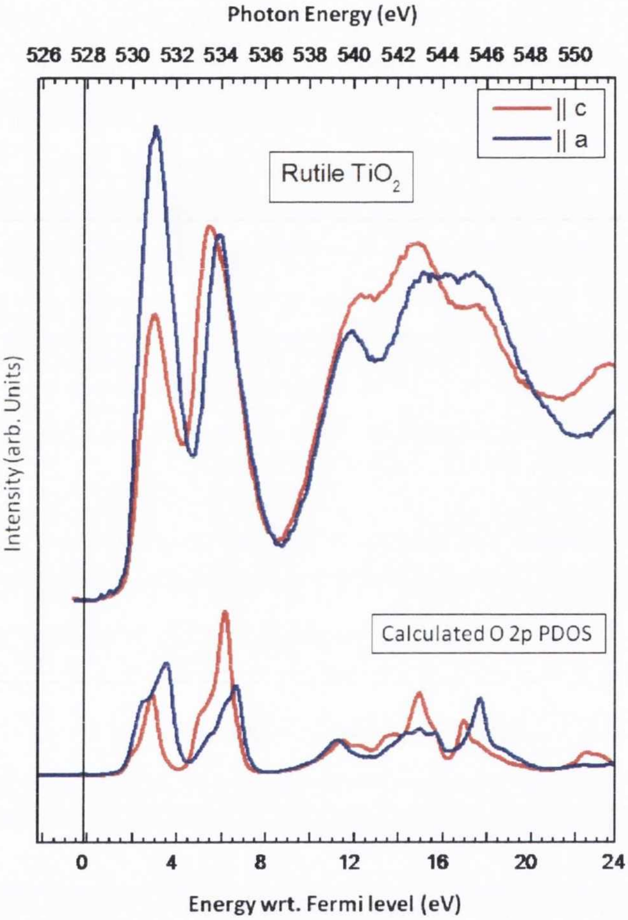

Figure 6.8: O *K*-edge XAS from bulk single crystal rutile TiO_2 compared with the calculated O $2p$ unoccupied PDOS projected along the crystalline *a* and *c* axes

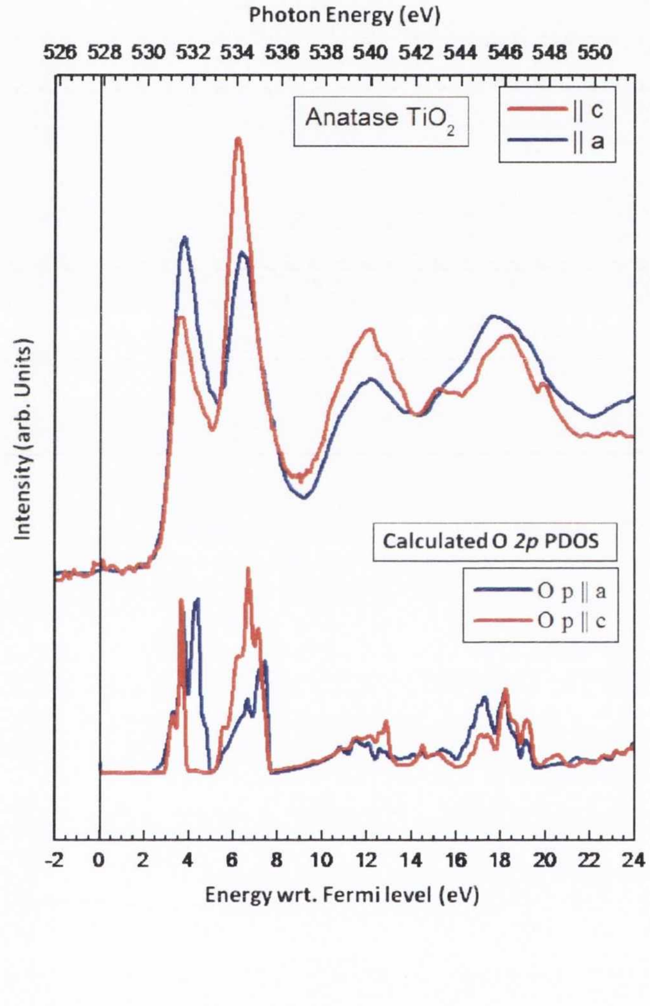

Figure 6.9: O K-edge TiO$_2$from bulk single crystal anatase TiO$_2$ compared with the calculated O 2p unoccupied PDOS projected along the crystalline a and c axes

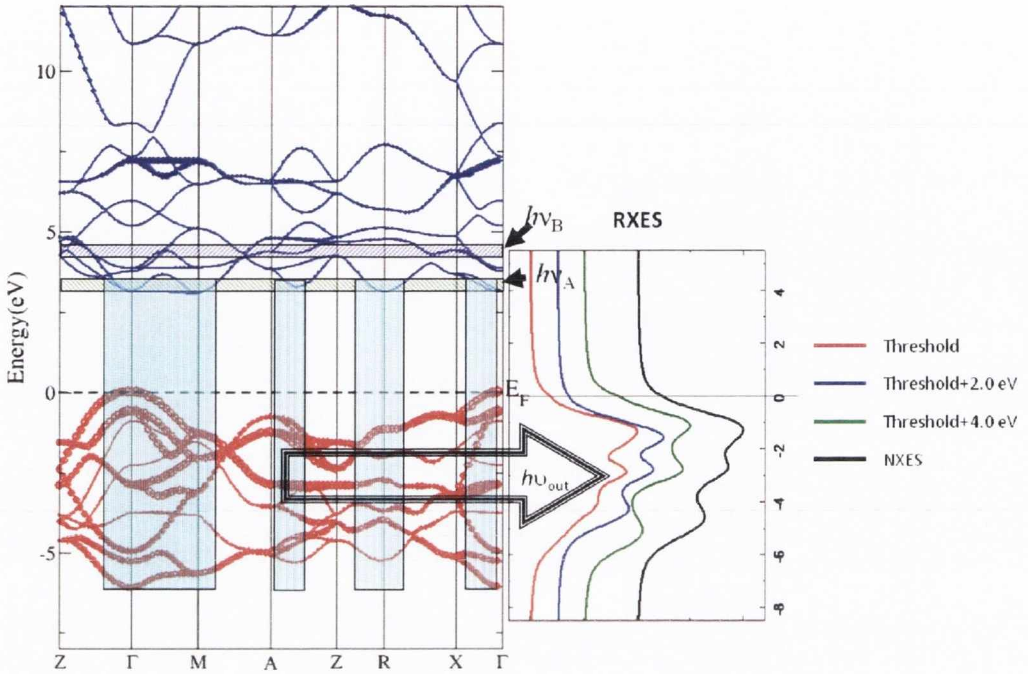

Figure 6.10: A diagram describing the simulation of RXES from rutile TiO_2 with respect to its calculated Band structure diagram, the horizontal cuts through the conduction band by the excitation energy $h\nu_i$ and the states within the same vertical "slice" of k-values in the valence band that are selected to contribute to the emission.

and 548 eV, are particularly noteworthy correspondences between the experimental spectra and the calculated PDOS.

For the anatase TiO_2 shown in figure 6.9 the increased width of the π^* peak in the $E||c$ orientation, the relative intensities of the σ^* peak and the features between 536 eV and 550 eV clearly agree between the experimental spectra and the calculated projected PDOS.

6.6.2 Bulk single crystal rutile polarization-dependent RXES study

At this point, some discussion of the mechanism employed in the simulation of the RXES in terms of the calculated band structure character plots is appropriate. Figure 6.10 combines the calculated band structure character diagrams selected to match the geometry of the excitation and scattering. In this example the geometry is $\mathbf{E}||c$, XES along c and therefore the states in the conduction band selected by the resonant excitation energies are represented by the c-axis projection of the O $2p$ PDOS band structure character plots. The horizontal slices through these states demonstrates the how the involved k-states are selected by the bandwidth of the exciting photons, and the character plots determine the weighting attributed to the selected states in the simulation. The vertical slices that are projected into the valence band from the intersections of these horizontal slices and the O $2p$ PDOS $||c$ band structure character states likewise determine the k-states selected to contribute to the emission. The valence band structure character plots for the XES along c geometry is composed by the O $2p$ PDOS projection onto the crystalline a-axes. The simulated RXES resulting from this combination of k-selection and weighting are shown adjacent to the valence band structure character plot for four different excitation energies: threshold, as indicated by the first horizontal slice through the conduction band followed by 2 eV and 4eV above threshold, and a NXES spectrum with an excitation energy of $\geq$ 15eV above threshold.

Figure 6.11 shows the O K-edge excitation energies selected for the experimental and simulated RXES. The upper panel shows the resonant features in the experimental O K-edge XAS spectrum, and the lower panel shows the corresponding energies selected for the simulated spectra and the features in the calculated O $2p$ PDOS that they are associated with. For both cases, the energy scale is not of sufficient extent to show the exact position of the NXES energy at 555 eV.

Figure 6.12 shows the experimental and simulated RXES for the four different excitation and emission geometries. The upper panel shows the spectra obtained for the threshold excitation energy, denoted a in figure 6.11 and the lower panel shows those obtained with an excitation energy denoted b in figure 6.11 and associated with the π^* peak at 531.0 eV in the O K-edge XAS.

Figure 6.13 shows the experimental and simulated RXES for the excitation energy corresponding to the σ^* peak in the upper panel and the peak at 539 eV in the lower panel for the four different excitation and scattering geometries.

Figure 6.14 shows the experimental and simulated RXES for excitation energies associated with the peak at $\sim$ 542eV which is most prominent in the E$||c$ orientation, in the upper panel and the NXES in the lower panel, for the four different experimental excitation and scattering geometries.

The experimental RXES presented have been scaled in intensity according to the relative intensities of the simulated spectra, and presenting the results in this fashion emphasizes the high degree of correspondence between the simulation and the experiment. For instance the three separate peaks in the simulated RXES arising from the M-O σ-bonded O $2p$ PDOS at the bottom of the valence band, the π-bonded

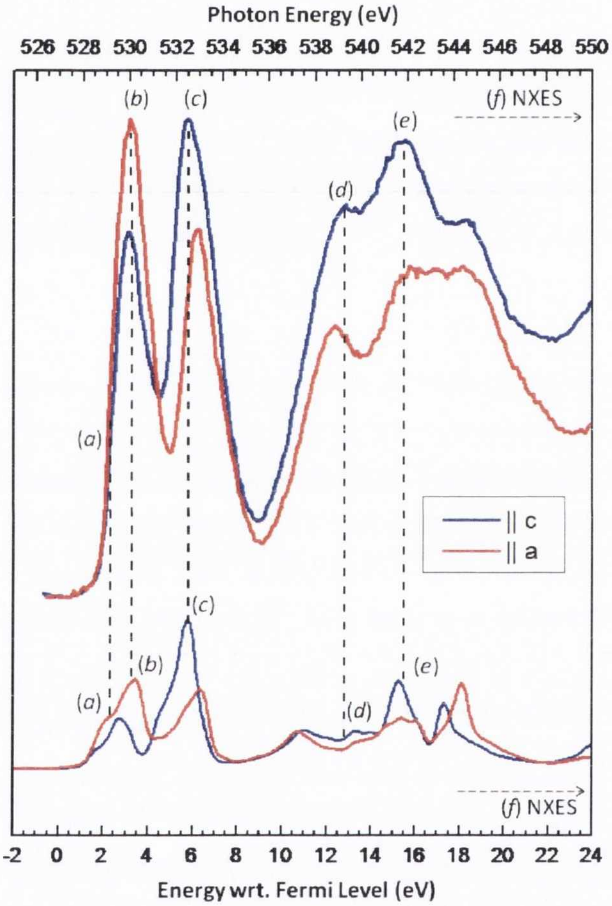

Figure 6.11: Rutile TiO_2 Experimental and simulated RXES excitation energies

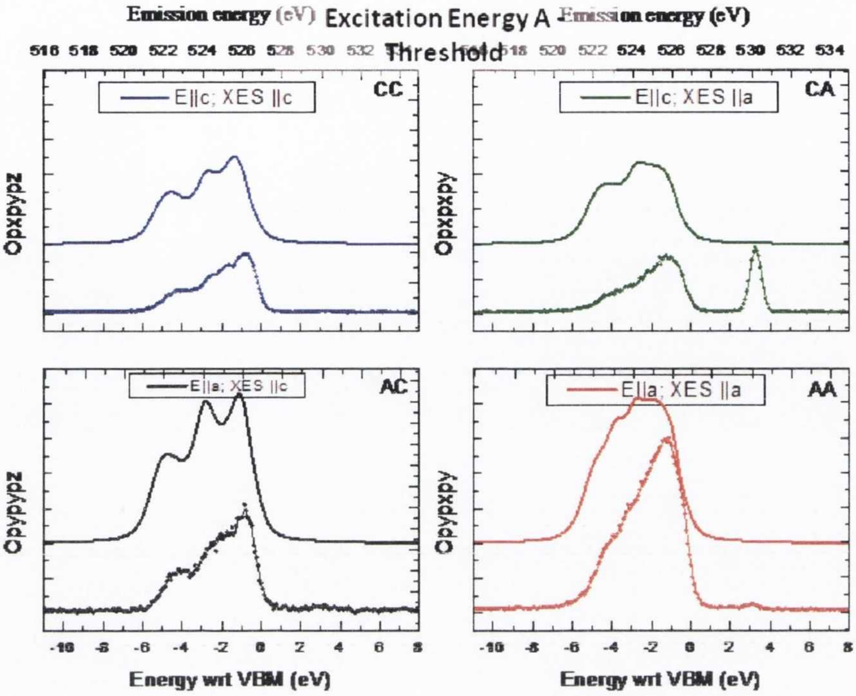

Excitation Energy A - Threshold

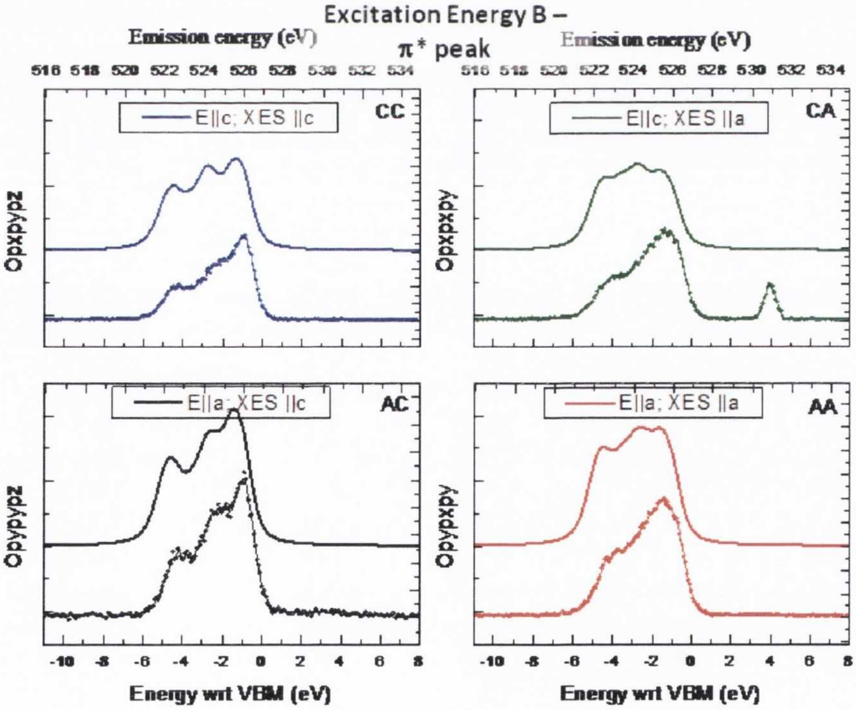

Excitation Energy B – π* peak

Figure 6.12: Simulated and experimental in-plane and out-of-plane O K-edge RXES from TiO_2 for excitation energies a (upper panel) and b (lower panel) in figure 6.11

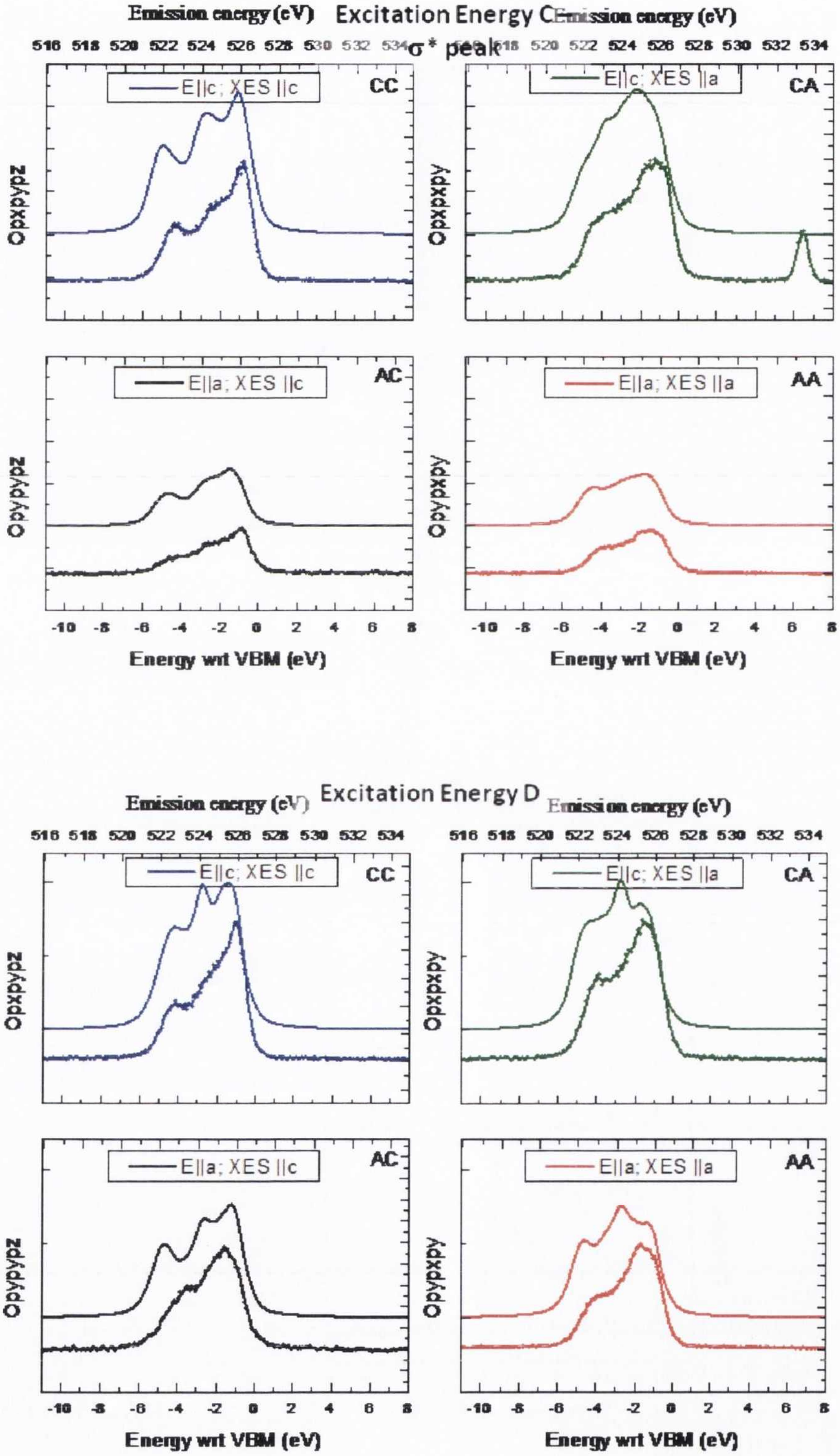

Figure 6.13: Simulated and experimental in-plane and out-of-plane O *K*-edge RXES from TiO_2 for excitation energies *c* (upper panel) and *d* (lower panel) in figure 6.11

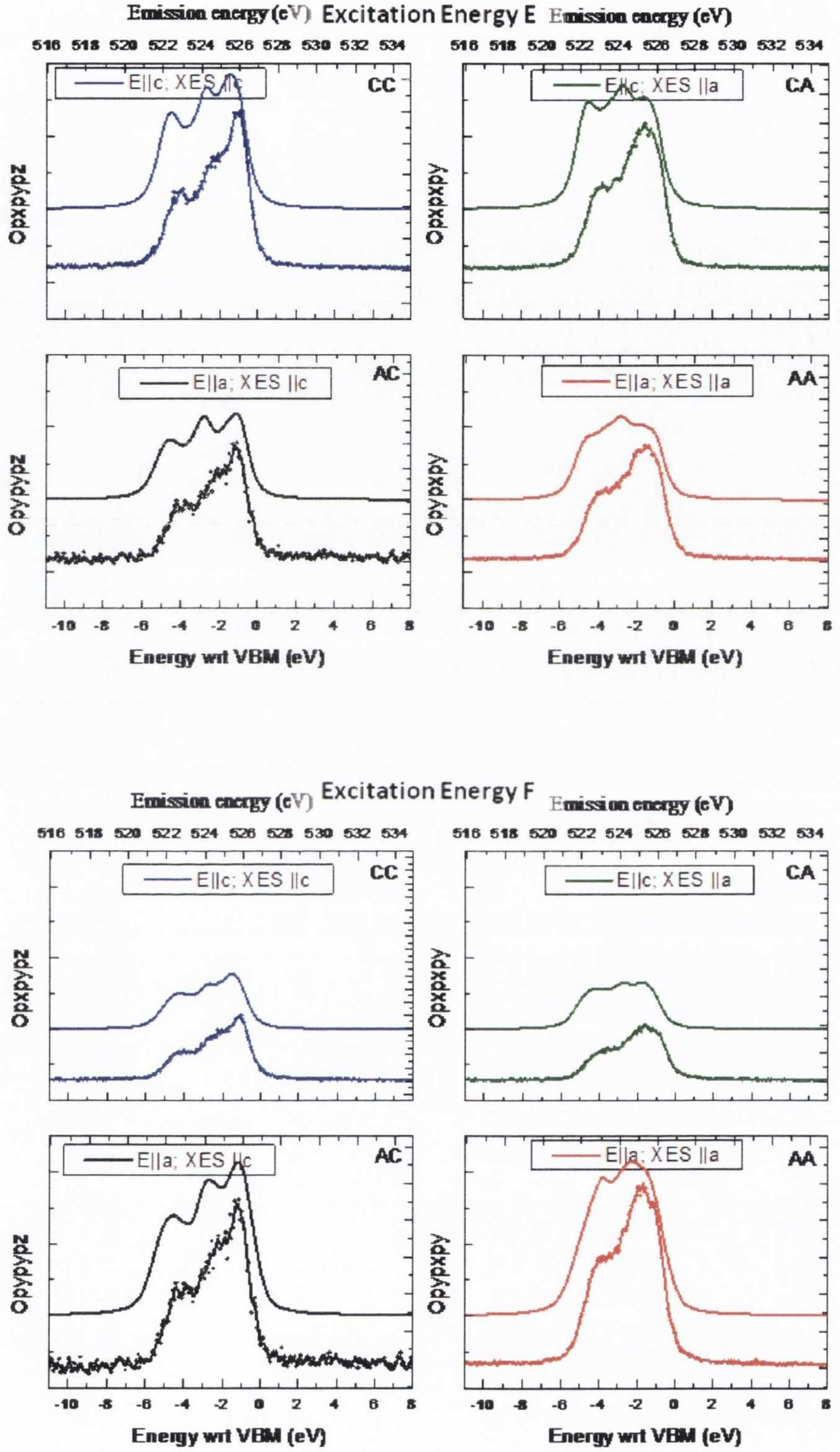

Figure 6.14: Simulated and experimental in-plane and out-of-plane O K-edge RXES from TiO_2 for excitation energies e (upper panel) and f (lower panel) in figure 6.11

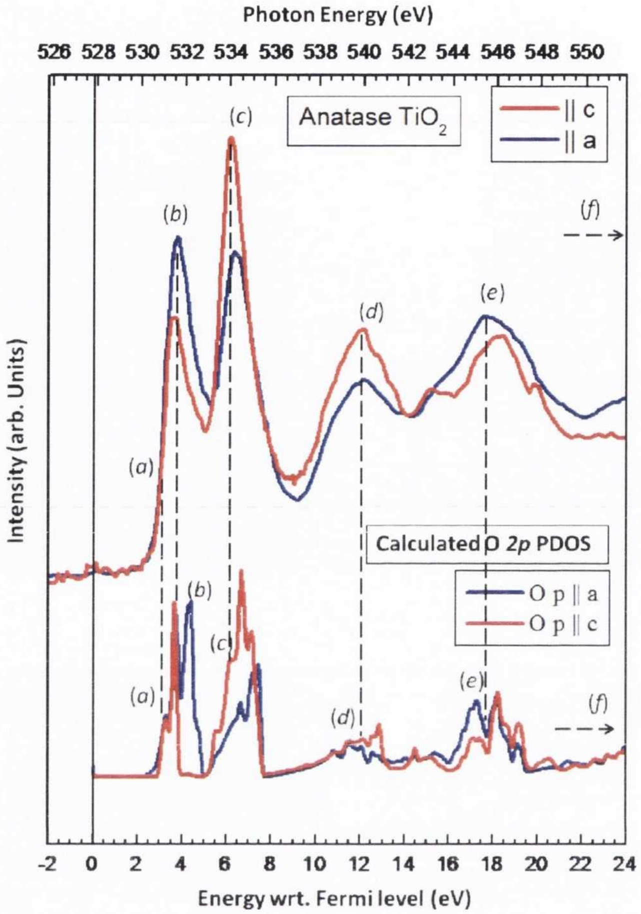

Figure 6.15: O K-edge XAS and calculated O $2p$ PDOS in the conduction band of anatase TiO_2 showing the resonant energies selected in the calculation and experiment

PDOS in the centre of the valence band, and the largely non-bonding O $2p$ PDOS at the top of the valence band respectively are clearly evident in the $E||a$, XES along c excitation/scattering geometry. The peak in the centre of the O K-edge RXES at an energy of $\sim$ 524 eV is suppressed for XES along a scattering geometries due to the smaller proportion of this π-bonded PDOS projected in the plane perpendicular to one of the crystalline a-axes compared to the plane perpendicular to the c-axis.

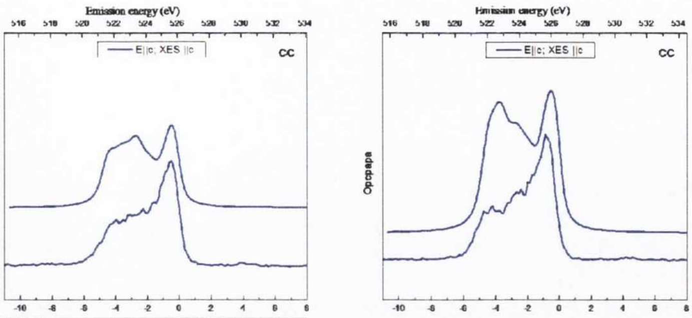

Excitation energy *a* (Threshold)

Excitation energy *b* (π^* peak)

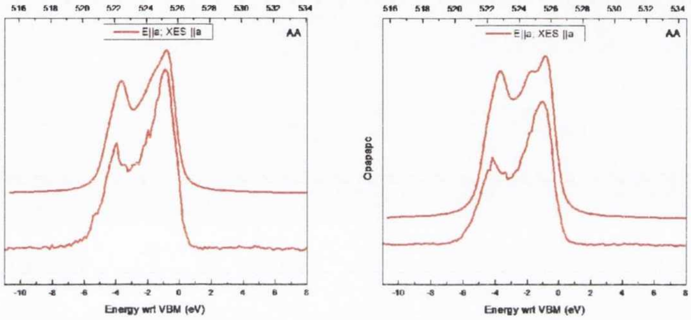

Figure 6.16: Simulated and experimental in-plane O *K*-edge RXES from anatase TiO_2 for excitation energies *a* and *b* in figure 6.15

6.6.3 Bulk single crystal anatase polarization-dependent RXES study

Figure 6.15 shows the resonant energies used in the experimental and simulated RXES, where, as indicated the NXES energy is outside the energy window of the figure. The features in the O *K*-edge XAS and the calculated projected O 2*p* PDOS corresponding to the resonant energies used are labeled $a-f$. Only the in-plane RXES for bulk anatase TiO_2 are shown. The figures containing the RXES are divided into two shaded halves, for two consecutive excitation energies. Within each shaded portion, the upper panels (blue trace) shows the E$||c$, XES along c excitation-scattering geometry and the lower panels show the E$||a$, XES along a geometry.

Figure 6.16 shows the in-plane RXES from anatase TiO_2 for excitation energies corresponding to the threshold of absorption and the π^* peak in the O *K*-edge XAS/calculated projected PDOS.

Figure 6.17 shows the in-plane RXES from bulk single crystal anatase TiO_2 for excitation energies corresponding to the σ^* peak, and the peak close to 540 eV that is most prominent in the E$||a$ excitation geometry.

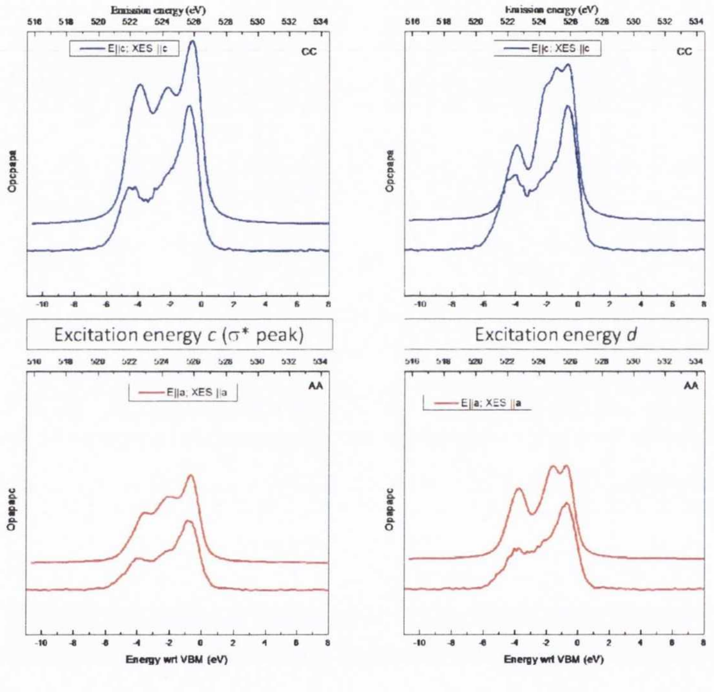

Figure 6.17: Simulated and experimental in-plane O K-edge RXES from anatase TiO_2 for excitation energies c and d in figure

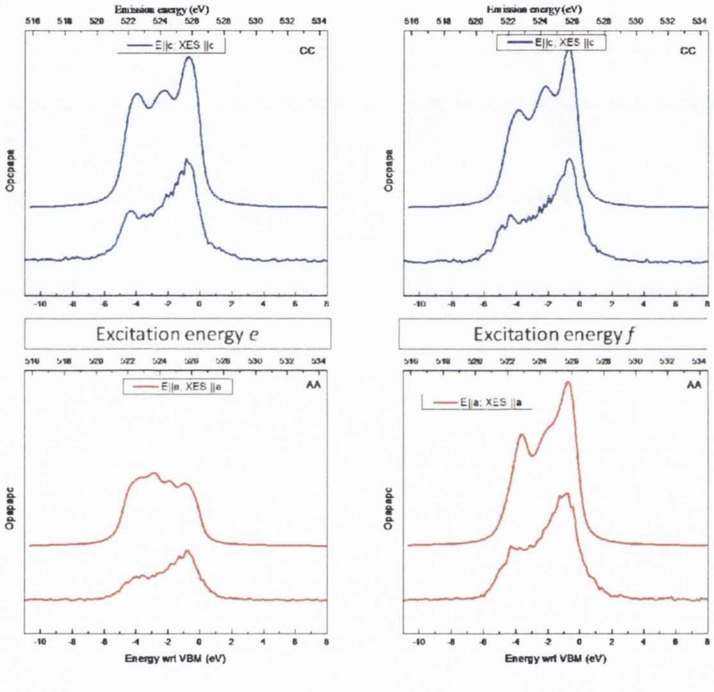

Figure 6.18: Simulated and experimental in-plane O K-edge RXES from anatase TiO_2 for excitation energies e and f in figure

Figure 6.18 shows the in-plane RXES for excitation energies corresponding to the peak at 545.5 eV that is most prominent in the E$||c$ excitation/scattering geometry, and the NXES at $\sim$ 555 eV.

The experimental RXES from the bulk single crystal anatase TiO_2 are scaled in intensity according to the relative intensities of the simulated RXES. There is a good correspondence between the simulated and experimental spectra, though the peak due to the π-bonded states in the middle of the valence band O $2p$ PDOS is not as well resolved as in the experimental spectra from the rutile single crystal. The simulated RXES for excitation energy e appears to retain an excess of k-selected character than what is appropriate for this excitation energy, as there is not a good correspondence between the simulated and experimental spectra at this excitation energy.

6.6.4 Anatase TiO_2 nanosheets O K edge spectra results and discussion

This section presents the O K-edge XAS and RXES from the anatase TiO_2 nanosheets, and compares the spectra from samples with 69% and 89% of (001) surface area. The excitation energies for the RXES are shown in the upper panel of figure 6.19, which contains the O K-edge XAS from the two samples, with the RXES shown in the lower panel.

As described previously, the anatase nanosheets were in the form of powder-like samples, and were pressed into In foil before mounting on a sample holder and being introduced to the analysis chamber. It is assumed that this means of sample preparation, by application of a compressive force, results in a predominantly flat orientation of the surfaces with largest areas in the sample. Approximating the nanosheets as having a "dinner-plate" form, the upper surface of the plate represents the surface with the largest proportion of the total surface area. As compression is applied, the "dinner-plates" will align with their largest surfaces perpendicular to the direction of the applied force. Thus the (001) surfaces are assumed to be predominantly aligned parallel to the plane of the In foil and sample holder, with the c axes by definition perpendicular to this plane.

The O K-edge RXES presented in figure 6.19, with the blue trace and red trace representing the 68% and 89% (001) samples respectively, were acquired at near-grazing angles of incidence ($\sim 20°$) / near-normal angles of emission, with a combined calculated instrumental resolution set to $\triangle E = 0.4$ eV. The resulting spectra show some mutual differences, especially in the shoulder-like feature at 523 eV which according to the calculated projected occupied O $2p$ PDOS in the valence band shown

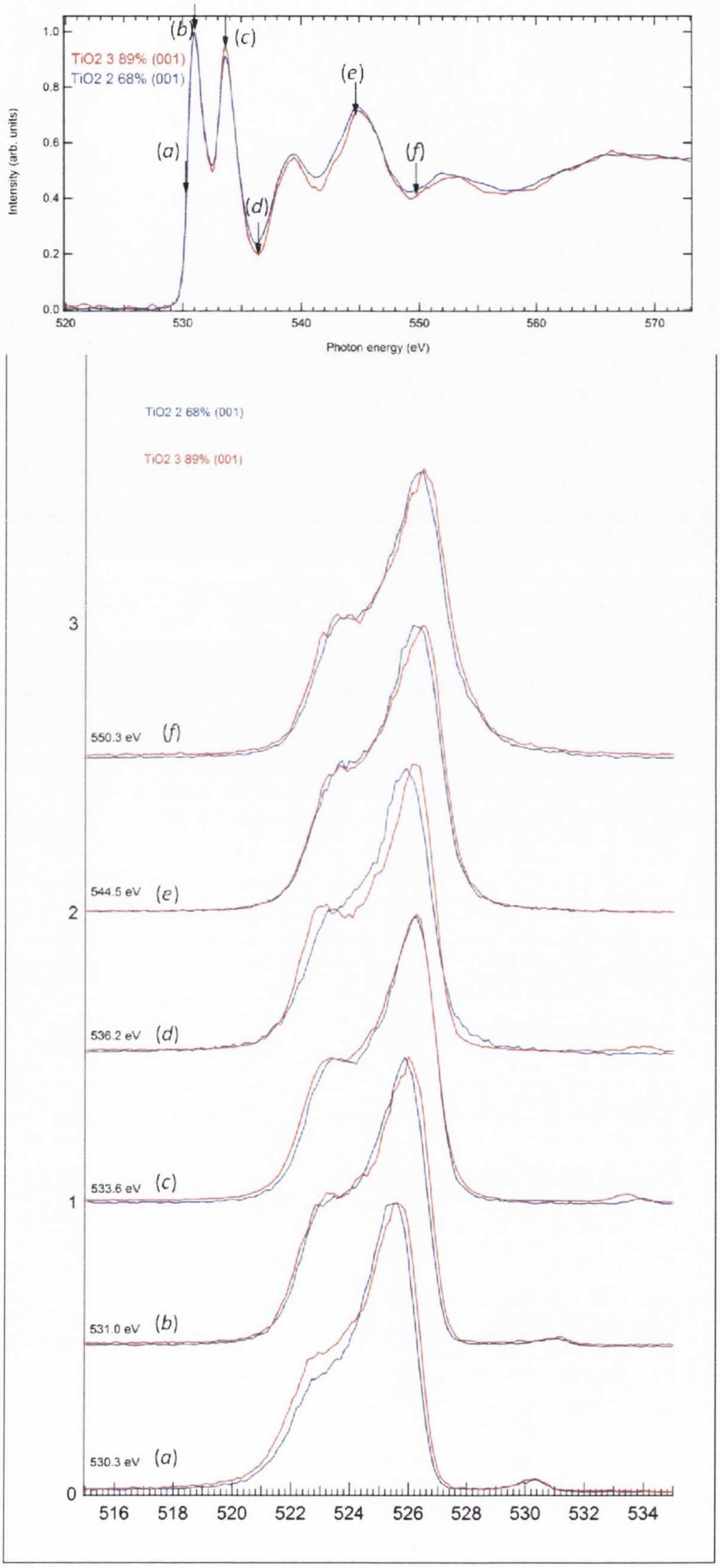

Figure 6.19: O K-edge XAS and RXES from samples of anatase TiO_2 nanosheets with 69% and 89% (001) surface area.

in figure 6.4 is associated with the π bonds formed between the O $2p_y$ and Ti $3d$ e_g $d_{x^2-y^2}$ orbitals. This PDOS has a strong projection in the plane perpendicular to the c axis which is the dominant contribution to the RXES in the E||c, XES along c scattering geometry. We note an increase in the spectral weight in this region for the sample with the 89% (001) surface area, which corresponds with the projected PDOS calculated for bulk anatase TiO_2.

6.7 Summary and Conclusions

TiO_2, the prototypical rutile, comprised the largest body of results gathered during the thesis, and in this chapter resonant absorption and emission spectroscopy at the O K-edge was presented and compared to the projected calculated O $2p$ and Ti $3d$ occupied and unoccupied calculated PDOS for both anatase and rutile TiO_2.

This is the first report of polarization-dependent XAS and RXES at the O K-edge in TiO_2, which due to its technological importance has an intensely studied electronic structure. We interpreted our results with reference to the predictions of the molecular-orbital bonding scheme for rutile and anatase TiO_2 and found that the non-bonding nature of the O $2p_y$-created PDOS at the top of the valence band, is reproduced in the calculated projected O $2p$ PDOS for both anatase and rutile. There is a more prominent PDOS due to M-O $2p_y$ π-bonding at the centre of the valence band in anatase TiO_2 compared to rutile due to the shorter M-O distance in the anatase crystal structure.

In a related investigation, anatase TiO_2 nanosheets produced with differing fractions of the most active (001) crystal surface were subject to O K-edge XAS and RXES during the course of the TiO_2 study. An increased spectral weight in the spectra from samples with 89% (001) surface area was observed, and related to the O $2p_y$ π-bonding, which gave a greater degree of emission from the PDOS projected in the plane perpendicular to the c-axis bserved in the near grazing scattering geometry.

Chapter 7

A Study of the Electronic Structure of Co-doped ZnO Thin Films by core-level and valence band soft x-ray spectroscopy

7.1 Introduction

This chapter reports on the results of x-ray spectroscopic studies of the electronic structure of a variety of Co-doped ZnO thin films. This study encompasses the O K -edge, Co and Zn L -edges , XES and XPS at the O K and Co L -edges; and valence band XPS of a number of cobalt doped ZnO films produced by two different growth techniques.

The foremost aim of the study is to acquire a thorough spectroscopic analysis of the electronic structure of Co doped ZnO by the element specific techniques of XAS and XES. A study of this type of both doped and undoped ZnO is needed, primarily motivated by the decade-long development of ZnO as a spintronic material, further to its various previously established useful properties as a transparent piezoelectric semiconducting material. We use the term spintronic material, to refer primarily to the dielectrics that show promise in providing a mechanism for manipulating electronic spin in previously charge-only applications. Under the spintronic materials umbrella, ZnO has from the beginning assumed a leading role where development has focused on the concept of magnetic transition metal substitutional doping at low concentrations, hence the widely used term of Dilute Magnetic Semiconductors (DMS) [153, 154]. For reasons that will be addressed in the introduction to this chapter, applying this label may not represent a satisfactory description of the exact nature of all the instances that have been reported as such. It should be clearly stated that the literature on this subject, and in particular on Co:ZnO is almost bewildering in the number of reports, both experimental and theoretical, that often contradict each other. A recent review by Pan *et al* lists several hundred references [155]. We cannot claim to have read even a small fraction of the literature on this subject which continues to excite both theoretical and experimental interest. Nevertheless, a short introduction and summary is attempted here.

The unsatisfactory implications of the term "dilute magnetic semiconductor" is essentially that it seems to prejudge the origins of the gross magnetic moment reported in lightly doped semiconducting hosts by the remote alignment of moments residing on the $3d$ dopant ions in the lattice. An explanation of the effect became more difficult as reports of ferromagnetic ordering in undoped oxides [156, 157], in oxides doped with non-magnetic species [158], and the variability in the size of the moment per dopant ion reported and its stability over time were added to the evidence.

The substitution of magnetic impurities in semiconducting hosts has been attempted for decades [153, 159], indicative of both the technological advantages of this combination of functionalities and the relative rarity of intrinsic magnetic semiconductors. Dilute magnetic semiconducting has been known in chalcogenides since the 1960's [153] and was discovered in Mn doped GaAs, with Curie temperatures far below 300 K [160, 161, 162]. However, the beginning of the intense period of interest in lightly doped, wide band-gap oxides that encompasses the fields of materials growth and characterization, experimental and theoretical magnetism and solid state electronic structure theory can be traced to Dietl's original prediction of a room temperature ferromagnetic moment in a ZnO lattice subject to a 5% substitution by Mn ions [163], and the subsequent reporting of such a moment experimentally in films of ZnO grown by pulsed laser deposition and subject to various concentrations of $3d$ transition metals by Ueda *et al* [164]. There are a number of figures of merit to choose from in assessing the potential applicability of this effect, but the most important is the Curie temperature of the ferromagnetic ordering transition. The magnitude of the magnetic moment in such films is also widely quoted as the moment in μ_B per $3d$ metal impurity present in the film, although this way of formulating the moment has been called into question for essentially the same reason that dilute magnetic semiconductors is not a universally acceptable term - the moment observed does not necessarily have its origins in the $3d$ dopants [165, 166, 167, 168].

Despite the uncertain fate of this category of materials, their development has revitalized research into magnetic ordering in more exotic settings and led surprising results such as so-called d^0 ferromagnetism [157, 156]. The renewed interest in a highly variable class of materials has in some senses posed a very apt problem for computational solid state physics to interpret. Indeed, since the initial prediction of ferromagnetic ordering in Mn doped ZnO, a wealth of electronic structure calculations have followed with some variety and contrast in where they assign the location of the impurity energy levels, see for example references cited in [169, 170] and [171].

This sub-field of magnetic materials can only benefit from careful probing of its characteristics, and soft x-ray absorption (XAS) and emission (XES), and x-ray photoelectron spectroscopy (XPS) provide an indispensable flank to the investigation of the electronic structure of these materials due to their particularly relevant strengths that we choose to recapitulate as follows:

- Element and momentum selectivity: the distinct, well defined energies of the core levels of different elements allow the contributions to the electronic structure from different elements to be probed individually. The $\triangle l = \pm 1$ selection rule derived from the dipole operator allows the O $2p$ and Co $3d$ density of states in the conduction and valence band to be probed individually.
- Local sensitivity: the highly localized nature of the core hole, in this case on a $1s$ level in oxygen, and $2p$ levels in cobalt or zinc means that the information gathered from its creation and decay provides access to the partial density of states projected onto the particular core level. Therefore a study of the electronic structure of a material using core level soft x-ray spectroscopy is highly sensitive to the environment of the probed atom, for instance the arrangement of its surrounding ions and its valence. The coordination of cobalt, for example, is largely evident in the features of the Co L XAS spectra by comparison with well characterized experimental and calculated spectra for tetrahedral and octahedral crystal fields, such as those published by de Groot [140].

The detailed electronic structure that we probe using soft x-ray spectroscopy includes the elementally specific resolved partial density of states in the valence and conduction bands, the position of additional densities of states due to doping or defects with their position with respect to the band gap and the degree of metal-ligand or dopant-ligand hybridization present in these dilute magnetic systems.

A particularly relevant x-ray spectroscopy pertinent to DMS materials is x-ray magnetic circular dichroism (XMCD). This can be applied to metal L-edges, metal K-edges and oxygen K-edges, and from the observed dichroism and application of sum rules (at L-edges only), the magnetic moment per dopant atom can be directly measured. No XMCD results are reported here as the data presented here are exclusively concerned with electronic structure. However, XMCD studies in the literature [172, 166, 173] of various differing samples have either shown evidence of clustering giving a spurious FM signal [172], or in the case of structurally perfect well substituted films with [173] or without additional carriers [174], only a paramagnetic interaction on the Co ions.

Unfortunately, the majority of x-ray spectroscopic methods, while not insensitive to defects such as oxygen vacancies, cannot directly probe these defects. A preponderance of evidence has suggested that defects in some manner mediate the FM observed, perhaps as suggested in a donor impurity model [175] or through other more complex theoretical investigations [169, 170] for example, while spectroscopic investigations have played a role whether by XAS [176], or XMCD [173] where Tietze *et al.* "by exclusion" have suggested oxygen vacancies as being a key ingredient for where the observed magnetic behaviour may originate. Others have also suggested this is the case based on spectroscopic evidence [176] and the variation with growth within differing pressures [177]. Likewise the literature on defects in ZnO is extensive with a recent review [178] citing 220 references and discussing some 30 different classes and subclasses of defects. Among these, native defects such as zinc vacancies and zinc interstitials are discussed, while the role of these defects in magnetic interactions in Co:ZnO has been extensively treated in theoretical literature on the subject (see *e.g.* Patterson [169] and references, or citations thereof).

Ultimately, it would be a highly anticipated development if the origins of the room temperature magnetic moments reported in the various semiconductor systems could be identified spectroscopically, and previous studies of this group using the same techniques and materials systems as this study have made influential moves in that direction [176]. The present study takes a circumspect approach to the magnetic properties of the films, and proceeds by giving as complete an account of the electronic structure of Co-doped ZnO as possible, the better to analyze which of the accounts of the origins of the magnetism in such semiconductors our data supports, or is consistent with.

In the remainder of this chapter, the *post hoc* design of the study in terms of the samples chosen for analysis and the approach taken for the comparative analysis of the spectra is explained in section 7.2. The growth and physical and magnetic characterization of the samples included in the study, which was carried out by others in the groups of Prof. J. M. D. Coey (School of Physics, TCD) and Prof. Y. K. Gun'ko (School of Chemistry, TCD), is also described in section 7.2. In section 7.3 the results of our study on Co doped ZnO are presented, where the spectra from the O *K*, Co *L* and Zn *L* edges are considered separately. Section 7.4 summarizes these results, and discusses the implications of our findings for the understanding of the electronic structure of this material.

7.2 Experimental Details

At the outset a variety of doped ZnO samples were available for inclusion in the proposed study due to the research effort already underway within both the School of Physics and the School of Chemistry aimed at producing ferromagnetic epitaxial films by pulsed laser deposition (PLD) and metal-organic chemical vapour deposition (MOCVD) in the Coey and Gun'ko groups. The samples available, provided to us by the respective groups, included those whose magnetic properties had already been reported in the literature [179, 46, 180, 181]. Mindful of the variety of sources of a magnetic moment, we note that to our knowledge the largest moment yet reported for a Co doped ZnO film was for one grown by MOCVD by the same group who deposited the films in the present study[181]. Alongside the comprehensive set of undoped and Co-doped ZnO films grown by PLD and MOCVD, there were a number of other materials systems available for study including Fe, Co, Mn and Cu-doped SnO_2 and Mn-doped GaN.

The decision to focus in the present chapter on the Co -doped ZnO samples is a reflection of both the number of Co:ZnO films available and the successful acquisition of a large number of XAS and XES spectra at the O *K*-edge and Co *L*-edge at a high resolution and the comparisons that can be drawn. From earlier work within the group [176] it seemed one of the most promising avenues of investigation. It is also important to acknowledge that within the subset of Co-doped ZnO films there were a number of spectroscopic angles of approach to pursue. For instance, the same dopant in a number of different concentrations could be studied with respect to its effect on the electronic structure and to construct at least empirical recipes for the growth of ferromagnetic films. To date, as far as we are aware a useful prescription for consistently producing magnetic films has not been discovered, and perhaps a material property with as many variable manifestations as dilute magnetic ferromagnetism provides an inappropriate basis for such an approach at the present. As the body of spectroscopic results from the films began to accumulate in the present study, and the number of diverse reports of magnetism in doped ZnO increased, some aspects of the phenomenon began to appear that influenced our continuing measurements and the impact these have had on our decision of the choice of samples selected from the variety available.

An important issue in the field that the present study was well placed to address, is the effect of varying the growth parameters on the observed electronic structure of the films. This question has some fundamental importance due to the contrasting observations of magnetic and nonmagnetic behaviour from films with the same constituent elements, in nominally the same proportions grown both by different techniques and by different parameters (substrate temperature, oxygen partial pressure *etc.*) even within the same growth technique. The literature suggests that non-equilibrium growth techniques such as PLD and MOCVD are more likely to produce a magnetic moment in a film than an equilibrium or quasi-equilibrium growth technique such as the chemical synthesis route of precipitating ZnO from decomposing zinc and cobalt acetates in acidic solutions [182]. The non-equilibrium techniques are also more likely to produce defects than the quasi-equilibrium techniques.

Having described the caveat that accompanies the term "dilute magnetic semiconductor" in the previous section, another note on the nomenclature we employed through our study is required, to qualify what is meant by referring to the samples investigated as "thin films". In this case it is used to describe the fact that the ZnO films are many orders of magnitude thinner than the substrates on which they are deposited, which are all Al_2O_3, notwithstanding the fact that they may be referred to by the alternative names of alumina or sapphire inadvertently elsewhere. It is assumed that the electronic structure of these samples is dominated by their bulk properties, and our spectroscopies, apart from XPS, are bulk spectroscopies.

Unfortunately, a more recent re-review of several hundred samples would tend to support the point that only a small percentage of the volume of many samples are magnetically active [165]. Much depends upon the distribution of the dopant homogeneously throughout the sample and this may not always be the case [183]. Particular species of Co, *e.g.* Co^0, may for instance aggregate near the surface [184], but even this is under dispute as there is a suggestion that Ar^+ sputtering preferentially results in the observation of metallic Co^0 at surfaces [185].

Then again, nanoparticulate Co-doped ZnO may behave differently to bulk [186], nanometre scale electron magnetic circular dichroism (EMCD) has shown evidence for Co-derived ferromagnetic behaviour [187] while nanoparticles have also shown Co surface segregation [188].

Our spectroscopies, representing sampling areas of $\sim 3000\ \mu m \times 200\ \mu m$ and sampling depths of as much as 200 nm in XES are in fact bulk spectroscopies and may measure the "average" bulk characteristics of a potentially inhomogeneous and defective material.

Film thickness was an important consideration of sample suitability due to the penetration depth of the x-ray photons, to ensure that the majority of the absorption and emission was taking place in the film rather than in the substrate. This was an essential consideration for the study of XAS and XES at the O K -edge, due to the fact that the substrate was also an oxide. The emitted intensity was calculated as a function of sample depth and angle of incidence and emission in the same manner as Jiménez-Mier *et al* [189]. XAS and XES at the O K edge was also carried out on a blank Al_2O_3 sample so that the possible spectroscopic contributions from the substrate could be approximated and detected if suspected artifacts were present in the spectra. The XES was also performed at as grazing an angle of incidence, $\leq 20°$ to the surface plane as the sample mount permitted, also with this consideration in mind.

Bulk ZnO is a direct band semiconductor with a bandgap of ~ 3.3 eV at 300 K. Its hexagonal crystal structure is commonly referred to as wurtzite, and it belongs to the hexagonal $P6_3mc$ space group. The arrangement of the Zn atoms in the lattice is in an approximately hexagonal close packed stacking of layers. The Zn ions are tetrahedrally coordinated by four ligand oxygens, and the bonding can thus be described in terms of hybridized orbitals formed between the Zn $3d$, $4s$ and O sp^3 hybridized orbitals. The tetrahedral crystal field of the oxygen ligands lift the degeneracy of the substituted Co ions such that the $3d$ t_{2g} orbitals are located lower in energy than the e_g levels, forming the uppermost (lowermost) states in the valence (conduction) band. The substrate material Al_2O_3 also has a hexagonal crystal structure and the films were deposited on either r $(1\bar{1}02)$ or c (0001) surface oriented substrates. As has already been mentioned samples with a variety of doping concentrations, deposition substrate temperatures, and growth atmospheres were produced. The nominal doping level of the films produced ranged between 1% and 25% (based on an assumption of one for one Co-Zn substitution).

It seems clear that a low concentration of substitutional Co in a ZnO lattice will not intrinsically result in ferromagnetic ordering, and various routes to an explanation for the effect in terms of the electronic structure of the material have been taken. These efforts include those of Coey *et al* who used a spin-split donor impurity band model to explain the presence of a magnetic moment in $3d$ doped ZnO, and also the variation between the moments measured for the various $3d$ dopants used [156]. The idea of a donor impurity band is a strong thread in the electronic structure calculations that seek pathways to magnetic ordering, and remains an influential proposition. In a system that has shown as much variation in experimental outcomes as ZnO [190, 155, 191], this model sits comfortably with the conclusion that it is defects in the films that mediate the magnetic moment in the films. Indeed, this is the starting point of the approach taken to the analysis of the spectroscopy presented in the present chapter. The forms of spectroscopy used are assessed with particular attention to the possibility of impurity and defect related states in the electronic structure. The various *point* defects in the Co doped ZnO lattice [178], which may leave their mark on the partial density of states, and have been successfully characterized by calculations available in the literature include zinc and oxygen vacancies, zinc and cobalt interstitials, and interstitial nitrogen and hydrogen and combinations of these individual defects and the substituted Co [170, 169, 171].

It is entirely acknowledged that the presence of unsubstituted interstitial Co or metallic clusters of Co and other $3d$ metals in a ZnO lattice could be the most likely explanation for some instances of the magnetic moments reported in thin films e.g. [183, 184], or indeed a proportion of the total moment measured from a given film [165, 184, 183]. Likewise, the phase separation of certain species of Co oxides within the ZnO lattice, or proximal aggregation of substituted Co ions (known as spinodal enrichment or spinodal decomposition) could also result in a gross magnetic moment being recorded [192]. The possibility of a magnetic response from films contaminated by inadvertent diffusion of dopants into the film or substrate from the metals (and glassware) they come in contact with during growth and processing has been reported [193] and underlined the attention that must be given to such sources of false positive magnetic moment results. On account of the unique opportunity for material composition analysis offered by the access to the synchrotron techniques and monochromated XPS with surface preparation, we devoted some time to investigating the presence C and N in the films. The results of these tests are not considered in the present analysis.

Though it is a matter of vital concern to the future direction of this form of magnetism, it was outside the scope of the present study, as defined, to form a link between the aspects of the electronic structure observed in the partial and total densities of states to the presence or absence of magnetism. Nor, necessarily, can such a link be obtained from our spectroscopies as XMCD is not undertaken here. Though we note the results of magnetic characterization on the deposited films, and pay close attention to variations in the electronic structure that may recur in samples that have produced similar results in magnetometry tests, the moment of the film is not measured concurrently with the spectroscopy, and perhaps the most that can be said about the magnetic behaviour of the films that we have spectroscopically studied is to refer to their characterization *at the time they were newly grown and measured.*

7.2.1 Sample Growth Techniques: PLD

A brief summary of the pulsed laser deposition growth of Co:ZnO samples grown by members of the group of J. M. D. Coey is given here. Pulsed laser deposition (PLD) is a non equilibrium growth technique suited to the production of DMS films primarily due to the range of stoichiometries accessible to it. The solid solubility of the dopant species in the host material can be surpassed by non equilibrium techniques, however with increasing concentrations of defects accompanying the higher doping levels.

The PLD system used to produce the films in the current investigation included a vacuum chamber with a base pressure of 5×10^{-6} mbar containing the laser target and within which the film deposition took place. Varying partial pressures of oxygen or other gaseous atmospheres are possible in the deposition chamber. The beam of a KrF excimer laser, with a wavelength of 248 nm is directed into the chamber through a window and focused on the surface of the target. The repetition rate of the laser and the energy per pulse is variable. Repetition rates of between 1 and 20 Hz were employed. The laser fluence at the target was varied between 1 and $5\,\mathrm{mJ/cm^2}$ similar to the method described by Fitzgerald for SnO_2 films grown by PLD [46].

The incident laser beam strikes a plasma from the target material. The substrate upon which the film is to be deposited is placed in close proximity to the target surface, in the system used for the present samples this distance is 3.5 cm. The stoichiometry of the deposited film closely resembles that of the targets, which were manufactured by sintering mixtures of high purity host and dopant oxide powders at 1250 K in air for 12 hours. In PLD a certain enhancement in the doping level of the deposited films is expected over the stoichiometry of the ceramic targets [179].

The thickness of the deposited films were monitored during deposition by monitoring the interference pattern created by the reflections from the film surface and substrate / film interface of a second laser source of 645 nm. Thickness measurements after deposition were calibrated using small angle x-ray scattering. The thickness of some PLD films was independently verified by a combination of AFM and ion beam milling, and films between 90 and 250 nm thick were included in the x-ray spectroscopic study. To minimize the proportion of the XES signal from the substrate, thinner films were excluded from the study.

Label	Name	Doping (PLD target)	Temp (°C)	Substrate	Magnetic
PLD1	182ZC501	5%	600	*r*	No
PLD2	224ZC501	5%	450	*r*	Yes
PLD3	274ZC501	5%	450	*r*	Yes
PLD4	1011Zn01	undoped	400	*c*	No

Table 7.1: Samples grown by PLD included in the present study

Label	Name	Doping	Temp (°C)	Substrate	Magnetic
CVD1	AN184Csap	2%	550	*c*	Yes
CVD2	AN185Rsap	5%	550	*r*	Yes
CVD3	AN215Csap	2%	550	*c*	No
CVD4	AN215Rsap	2%	550	*r*	No
CVD5	AN182Csap	undoped	550	*c*	No
CVD6	AN182Rsap	undoped	550	*r*	No

Table 7.2: Co-doped ZnO films deposited by MOCVD, that are included in the present study

The results reported in this chapter were primarily obtained from films grown by PLD on both *r* and *c* cut substrates and these are listed in Table 7.1.

7.2.2 Sample Growth techniques: MOCVD

A brief summary of the growth technique employed by members of the group of Y. K. Gun'ko is given here. The alternative growth method used to produce the samples included in the study was pulse-injection metal organic chemical vapour deposition (PI-MOCVD) [181]. Here, droplets of the deposition precursors contained in a solvent are introduced to an evaporation chamber. In the case of the Co:ZnO films the precursors are $Zn(tmhd)_2$ and $Co(tmhd)_2$. The evaporation chamber is maintained at a temperature sufficient to evaporate the injected solution but not to decompose the precursors, which are carried into an adjacent deposition chamber by a carrier gas composed of equal proportions of Ar and O_2. The resultant deposition occurs on the surface of either a *c* or *r*-cut Al_2O_3 substrate maintained at 550°C, and the films are slowly cooled afterward in an oxygen pressure of 1 atm. The thickness of the deposited thin films are monitored by white light reflectometry and range between 59 and 264 nm. The MOCVD-grown samples are listed in table 7.2.

7.2.3 Sample Characterization by XRD and Magnetometry

The crystalline quality of the PLD and MOCVD grown films and their surface morphology were characterized in a similar fashion within the respective groups by x-ray diffraction (XRD, Phillips *X*pert Pro, with a filtered Cu K_α source). The results of an ultra-sensitive XRD scan produced by a combination of a lengthy integration time and the enhanced detection sensitivity of a multidetector was able to detect the presence of Co clusters in one of the PLD grown Co-doped ZnO films, sample C in table 7.1 [183]. The shorter and less sensitive scans that were performed on most of the samples do not register the very weak metallic cobalt diffraction peak, and therefore the negative results for this peak in such scans cannot be taken as conclusive evidence of the absence of secondary phases.

The magnetization curves of the deposited films were measured using a Quantum Design SQUID magnetometer, where a variable DC magnetic field of up to 5 T was applied to the sample in a given orientation with respect to the film surface normal at film temperatures of 2 - 300K. As has already been alluded to in the introduction, the presence of a ferromagnetic signal does not directly discriminate between the various possible sources of such a moment and the results of vibrating sample magnetometry alone cannot be taken to indicate intrinsic ferromagnetism is present in a system. Strategic use of the SQUID does enhance the discrimination that can be applied to the possible sources of a magnetic moment as, for example, the moment of some of the Co doped ZnO films grown by PLD was found in this fashion to be highly anisotropic [194, 195], which is not a property expected from the moment of cobalt clusters, or other secondary phases.

7.3 Soft x-ray spectroscopy of Co:ZnO films

As outlined earlier the present section of the chapter presents the results of the x-ray spectroscopic measurements on an element by element basis, and, further, an XPS study of the valence band will also be presented. Due to the previously described dipole selection rules applying to the absorption and emission of a photon, the XAS (or NEXAFS) at the O *K* edge reflects the O 2*p* partial density of states in the conduction band. XES at the O *K* edge reflects the partial density of states of O 2*p* character in the valence band. At the transition metal *L* edge the metal 3*d* and 4*s* partial density of states are probed, in the conduction band by XAS and in the valence band by XES. The specific location in energy and contribution of the transition metal dopant to the electronic structure of the system can be explored by the hybridization of the dopant filled and unfilled states with the ligand oxygen $2p$ orbitals. In summary the degree of ligand and cation orbital hybridization, possible exchange mechanisms, on-site, and inter-site excitations can all be probed through resonant XES. XAS at the dopant L edge is a sensitive test of both valence and substitutional environment (see chapter 2). Extended x-ray absorption fine structure (EXAFS) at the dopant K-edge is a source of structural information but was not available to us under the auspices of the present study.

O K, Zn and Co L edge XAS from the PLD samples was recorded at beamline 7.0.1 of the Advanced Light Source. The procedure for recording XAS as either a sample drain current or a photon yield as the incident x-ray energy is stepped across an absorption threshold has been described in chapter 2. XAS on the PI-MOCVD grown samples was performed at both beamlines 8.0 and 7.0.1 of the Advanced Light Source in subsequent experiments.

Optically forbidden, or low-energy electronic excitations such as charge transfer and on-site d-d^* transitions are probed at the transition metal L-edge in the resonant inelastic x-ray scattering component (RIXS) of the XES spectra. RIXS spectra are sensitively dependent on both the splitting of the majority and minority carrier magnetic dopant d -levels and the fractional occupancy of these levels, where this occupancy is expected to play an important role in the magnetic behaviour of very dilute semiconductors. Comparison of RIXS spectra at the metal L-edge between several doping levels and host materials will be especially sensitive to the position and occupancy of this d -band.

Finally, the XPS system at NCESS was used for the core level and valence band XPS from the PLD grown films presented in this thesis. This system was previously described in chapter 2. Core level XPS was recorded from the films grown by PI-MOCVD as part of their characterization. The results of the PI-MOCVD XPS were published elsewhere and XPS was not repeated on these samples in the present study.

The samples were prepared for XPS by being cleaned sequentially with acetone and ethanol to remove dirt from the surface of the deposited film. The samples were mounted on a steel holder using carbon tape. Unless otherwise stated, the Co:ZnO films were not annealed or sputtered due to the consideration that the observed ferromagnetic behaviour and the electronic structure may be sensitive to such surface preparation. For instance, the annealing of ZnO in oxygen poor environments has been shown to increase the concentration of oxygen vacancies. As noted previously other studies have indicated that Ar^+ sputtering may lead to false positives in preparations of stoichiometric surfaces for photoemission [185], though others have claimed sputter-depth profiling reveal hidden metallic Co near surfaces [184]. It should be noted that no sputter depth profiling was undertaken at that time, i.e. only non-destructive XPS was considered as measurements of XES and XAS were to take place at a later date, as well as further XRD or other sample characterization measurements.

XPS survey spectra were recorded with good statistics to investigate the sample composition, and to define the binding energy regions where finer spectra were to be recorded for the core levels and the valence band. The core level spectra of the Co:ZnO samples were recorded at the Zn L, Co L, and O K edges. N K edge spectra were taken from some of the samples to investigate whether N doping may have taken place by contamination during the deposition process. The C K spectrum was recorded to allow the energy scale of the hemispherical analyzer to be calibrated with reference to the binding energy of the adventitious carbon present on the sample surfaces.

7.3.1 Core level spectroscopy at the O K - edge

7.3.1.1 O 1s XPS

The O K edge XPS spectra shown in figure 7.2 were recorded and compared to identify the differences between samples that have given a ferromagnetic response and those with different doping levels. Core level shifts observed as additional components in the O K peak could constitute evidence for oxygen related defects.

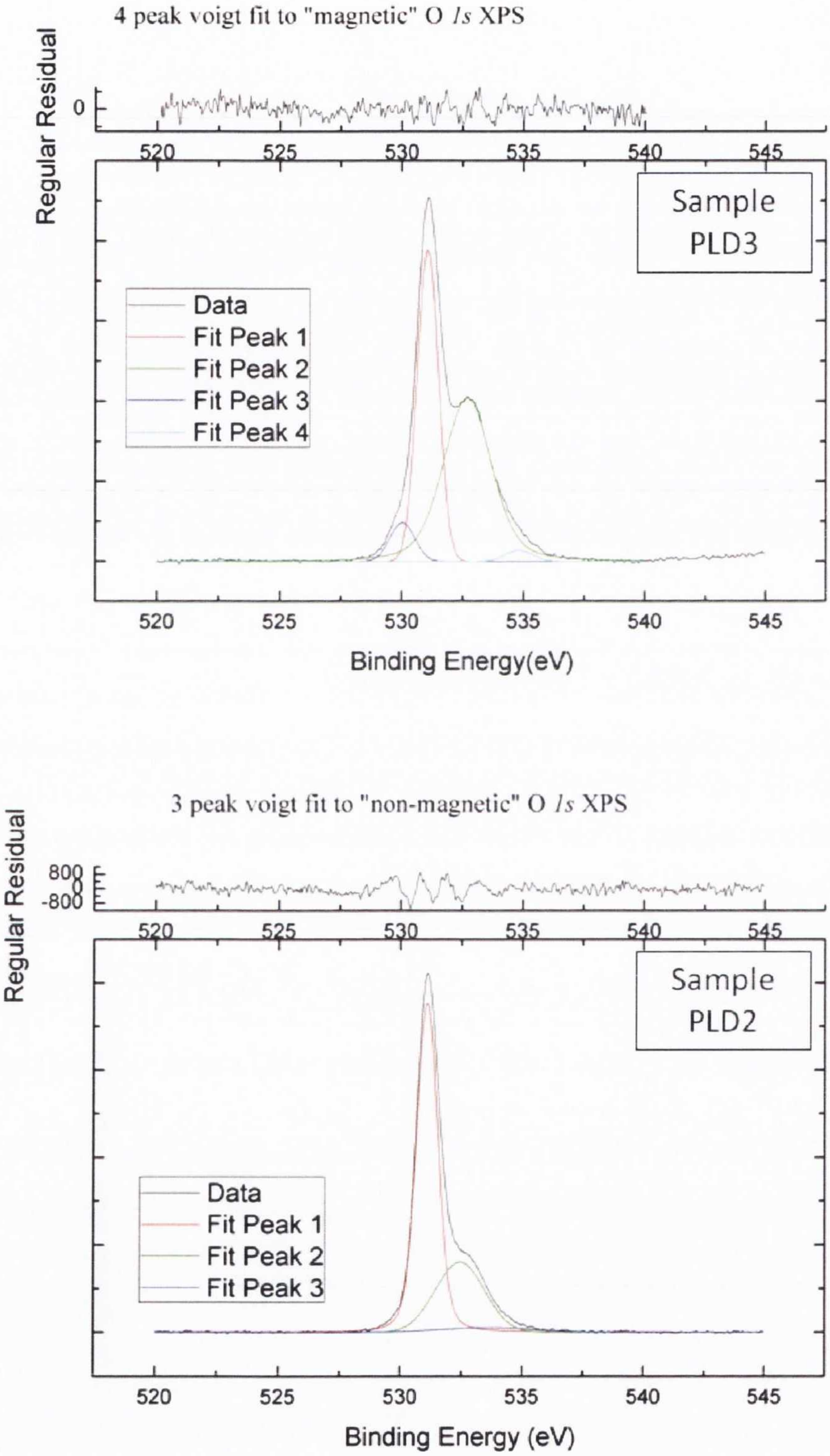

Figure 7.1: O 1s core level XPS from PLD deposited (magnetic) Co doped ZnO films showing fitted peaks and residuals of the fit. A Shirley background having previously been removed

The O 1s XPS shows two main components. In undoped ZnO, the O 1s binding energy is reported to be 530.35eV with $Zn(OH)_2$ at 531.88eV [196, 197] and adsorbed water at 532.83eV (obtained from a pressed sample of commercially pure ZnO powder) [198].

The curve from the non-magnetic sample is adequately fitted with 3 Voigt peaks. A fit composed of 4 and 5 Voigt peaks leads to lower residuals, but the additional peaks do not necessarily have a physical interpretation in the same sense as the 3 that gave the fit we accepted do. The O 1s peak at 531.10 eV, a peak at 532.46 ± 0.15 eV - consistent with an OH group, and a much smaller peak with a BE of 533.62 ± 1.28 eV - consistent with water from comparison with the Handbook of Monochromatic XPS Spectra [198]. The apparent shift in the O 1s binding energy we report and the value of 530.35eV reported elsewhere is liable to be caused by the charge-compensating flood gun we used on our samples. The fact that the samples are insulating necessitates the use of charge neutralization to make up for the loss of electrons that escape the sample surface. The current of thermal electrons also represents an alteration of the surface electrostatics that is difficult to reproduce between samples, and essentially alters the work function such as to create an offset in the O 1s binding energy we measure. The good quality of this sample is evident from the O 1s peak whose Gaussian width was 0.885 eV and Lorentzian width was 0.245 eV - consistent with the O 1s core hole lifetime.

The curve from the magnetic sample required at least 4 Voigt peaks due to the increased spectral weight at the low binding energy side. The O 1s peak has a binding energy of 531.07 eV and a Gaussian width of 1.03 eV. The Lorentzian width was best fitted as zero, giving an indication of disorder or a distribution of O 1s binding energies within the film, albeit over a narrow range. The OH peak was at 532.7 ± 0.1 eV - slightly displaced from what is obtained previously for $Zn(OH)_2$ or the nonmagnetic sample above. A stronger high-binding-energy peak at 534.82 ± 0.11 eV though this time not consistent with adsorbed water. Of particular note however is the O 1s "pre-peak" which has no equivalent reported in the literature and whose binding energy is at 530.03 ± 0.33eV and is a pure Gaussian fit with a width of 1.33eV. Thus somewhat a wider full width at half maximum than the main O 1s photoelectron peak.

7.3.2 O K -edge XAS

As mentioned previously in this section XAS at the O K edge provides a measure of the O 2p unoccupied PDOS. In undoped ZnO the O K-edge XAS has previously been reported by McGuinness *et al.* [10] , Guo *et al.* [199, 200], and Preston *et al.* [201]

among others, together with O K-edge XES. The main peak in the O K XAS located at 7 eV above the onset of absorption is formed by hybridization between O $2p$ and Zn $4s$ states and can be identified as the $2p_z$ component, along the crystalline c-axis. The two less intense peaks at higher energies are formed by hybridization between O $2p$ and Zn $4p$ states. In the energy region of greater than 20 eV above the onset of absorption the density of states is composed of oxygen hybridization with Zn $4d$ states.

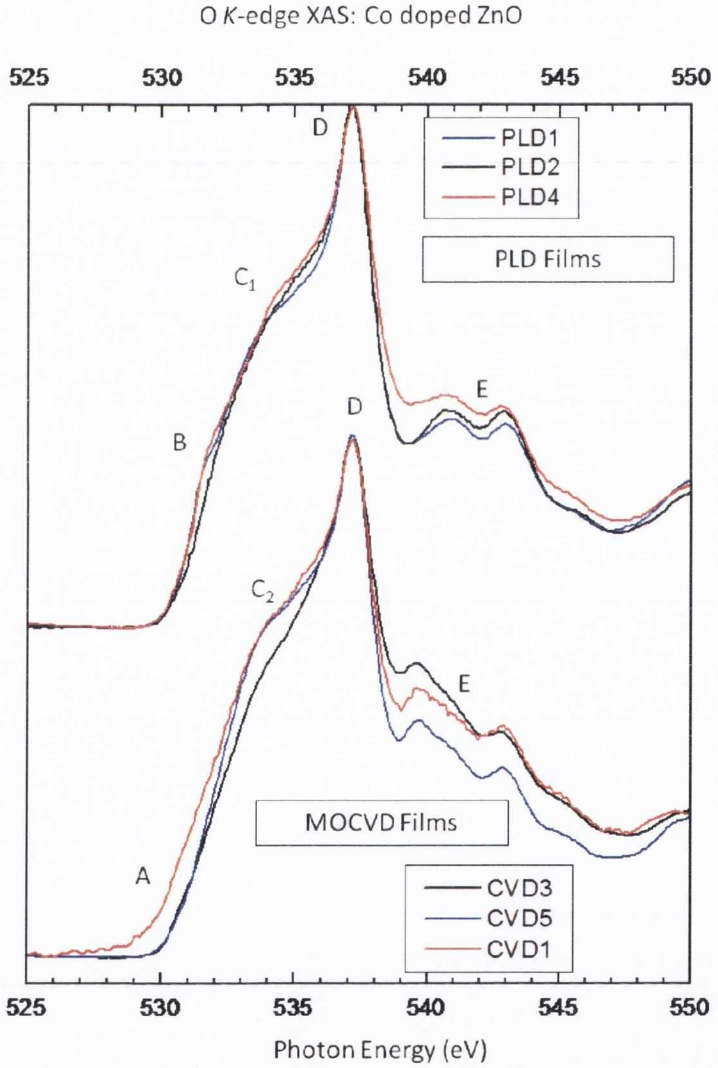

Figure 7.2: O K edge XAS from PLD and MOCVD deposited Co-doped and undoped ZnO epitaxial films

The O K edge XAS from the PLD and MOCVD grown samples are shown in figure 7.2. Comparing the O K XAS from an undoped ZnO film with those from doped films that have been reported as posessing a magnetic moment, and non-magnetic films allows the additional spectral weight arising from between the O $2p$ states and the Co $3d$ t_{2g} states. There is also a clear additional spectral weight or density of states at the bottom of the conduction band in some of the samples, both PLD and MOCVD, that recorded a ferromagnetic response during their characterization phase. The origins of the additional densities of states moving from undoped ZnO to doped magnetic and non magnetic can be interpreted with reference to electronic structure calculations and model spectra published elsewhere [199, 200, 202]. With respect to the features which are largely common to both the PLD and MOCVD grown samples, these are labeled C - E. Features C_1 and C_2 label the additional density of states present in the Co-doped films, and it is expected that they are due to Co $3d$-O sp^3 hybridization. The feature labeled D in both spectra reflect the main Zn $4s$-O sp^3 hybridized density of states. The features labeled E show a low degree of polarization variation is still present between the films. There are features further towards the bottom of the conduction band, and extending into the bandgap labeled A and B in the MOCVD and PLD grown films respectively. Additional feature B appears in the spectra from both the magnetic and non-magnetic samples, and the additional feature labeled A is only present in the magnetic MOCVD grown sample.

The onset of absorption at the O K edge does not seem to vary between the undoped and doped non-magnetic ZnO in the PLD grown samples reported here. This indicates that the additional spectral weight due to the Co hybrid orbitals does not lie within the bandgap.

The absorption threshold does appear to have shifted to lower energy for the magnetic MOCVD deposited film reported here. For certain samples, including those that were identified as ferromagnetic due to their observed magnetic hysteresis, the onset of absorption is red-shifted by $0.5 - 1.0$ eV. As noted in the O $1s$ XPS, an additional core level component at a lower binding energy may account for the origin of this spectral weight and the localized $1s$-$2p$ transition occurs at a lower photon energy. The character of the localized conduction band on this site may be quite different than in the undisturbed lattice. A complete calculation, incorporating the cause of the lowered $1s$ binding energy could, taking the final state rule into consideration, explain the observed feature. Thus this feature may be a fingerprint specific to the defect involved as suggested previously by Krishnamurthy *et al.* [176] , albeit from a different sample than that shown here.

Kumar *et al.*[203] and Chang *et al.* [204] report strong variations in the O K-edge XAS from Co:ZnO, similar to what is reported here. Other reports of the O K-edge XAS in Co:ZnO have noted no variation between samples with different doping levels, such as Fitzgerald *et al.* [179].

7.3.2.1 O K - edge RIXS

The occupied Oxygen partial density of states below the Fermi level were probed by XES at the O K edge performed at beamline 7.0.1 of the Advanced Light Source using the grazing incidence grating spectrometer and two dimensional detector described in a previous chapter.

The O K edge XES spectra from the PLD deposited films are shown in figure 7.3. The O K emission spectra were recorded using the 1200 lines/mm grating of the spectrometer and for the majority of the O K edge XES the resolution of the monochromator and the spectrometer were both set to 0.4 eV yielding a combined instrumental resolution of $\sim$ 0.6 eV.

For all the measured spectra, the angle of incidence between the x-ray beam and the surface of the Co:ZnO films was maintained as close to 20° as was practical for each film's position on the sample holder, the grazing angle of incidence determining that the majority of the emission originates from the deposited film rather than the substrate. It also implies a close to normal angle of emission due to the location of the emission spectrometer, with its optic axis at right angles to the direction of the incoming beam. Though the angle of incidence and emission was maintained approximately constant, there is still a variation in the O K-edge XAS spectral shape caused by a different orientation of the films' crystalline axes with the polarization of the incident x-rays, for the same angle of incidence. The films were grown on substrates with identical Al_2O_3 offcuts and have the same measured morphology [205]. The polarization dependence of the XAS and XES from ZnO has been well characterized [206, 201], and the XAS spectrum from the doped non-magnetic film in the upper panel of figure 7.3 clearly indicates an $\mathbf{E} \perp c$ orientation. The spectrum from the magnetic film is a combination of $\mathbf{E} \parallel c$ and $\mathbf{E} \perp c$ spectra. This seems to indicate that the c axis is within the plane of the film, and that by rotating our sample on the sample holder, we would have been able to achieve an identical crystalline orientation with respect to incident x-ray polarization. With hindsight, and as we proceeded to make explicitly polarization-dependent measurements on the rutile oxides, this would have been worth the time it would have taken during the experiment as the comparison of both the O K-edge XAS and XES would be more strongly conclusive if the effects of this polarization dependence could be removed from the consideration.

We have paid close attention in particular to the results of Preston *et al.* [201] , though they do not treat the polarization dependence of the O K-edge XES in the same detail as the XAS, we were able to analyze their published data to confirm the strong polarization dependence of the XES spectral weight. Bearing this in mind, observed variations in the O K-edge XES from different samples may just as likely reflect differences in crystal axes/polarization orientation as the electronic structure of the films.

Having said that, we also have a limited number of carefully selected XES spectra where the orientation of the crystalline axes with respect to the polarization of the incident x-ray is approximately identical, from which we have selected those shown in figure 7.4.

The emission signal is relatively stronger closer to normal exit angles, which is also a consideration where a high throughput is required, or a lower density of states in the conduction band is excited into.

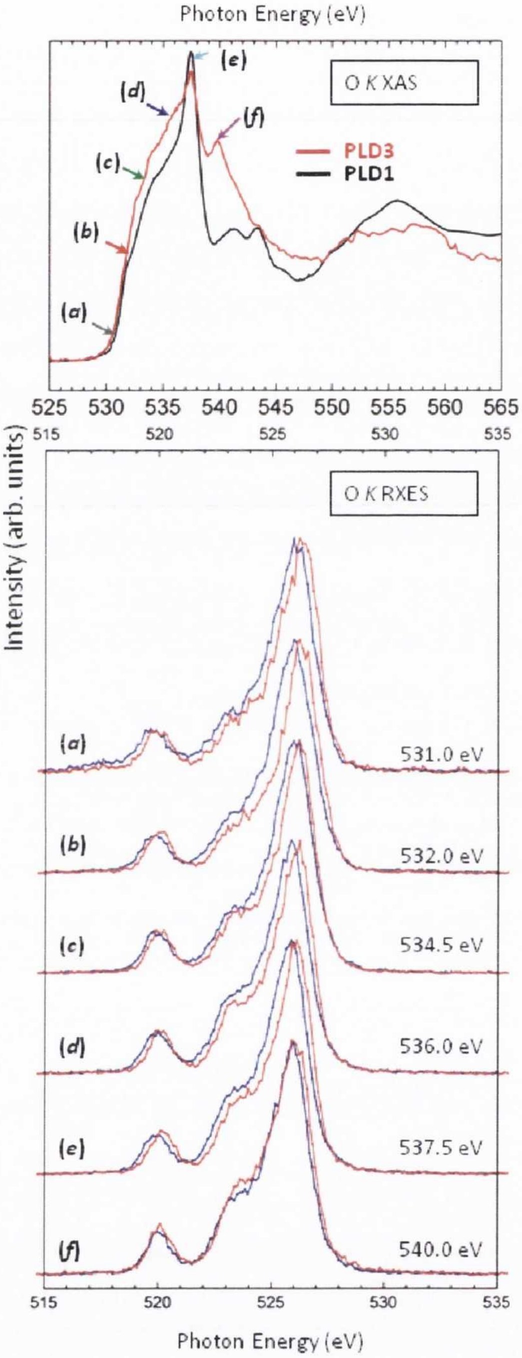

Figure 7.3: O K edge emission spectra for Co doped and undoped magnetic and non-magnetic ZnO films grown by PLD in the lower panel, with the relevant O K-edge XAS in the upper panel. The results are for a magnetic film (red trace in O K-edge XAS, and solid lines in XES) and a non-magnetic film (black trace in O K-edge XAS and dashed lines in XES)

The O K emission spectra of the undoped ZnO films are composed of three main

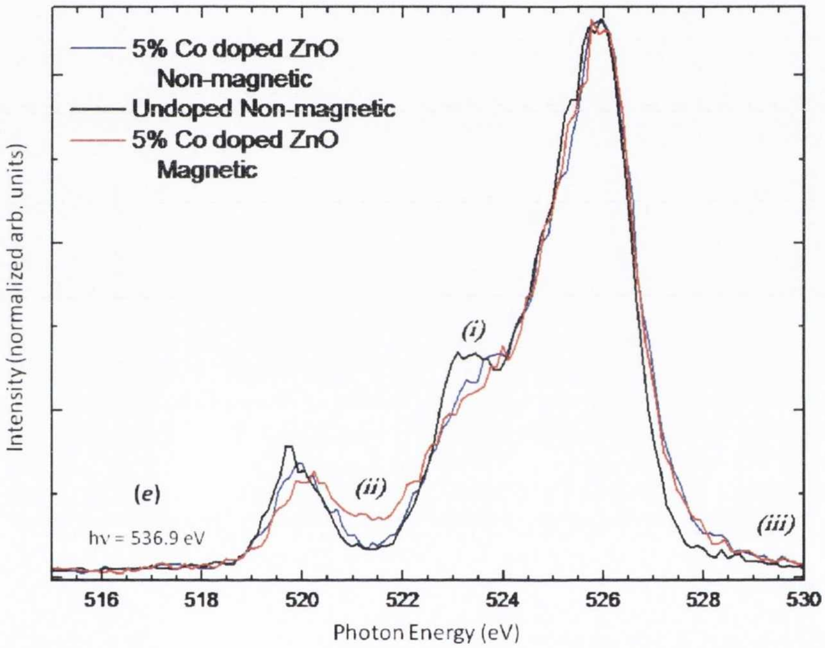

Figure 7.4: O *K* edge XES from PLD deposited magnetic (red trace) and non-magnetic Co doped (blue trace), and undoped ZnO (black trace) films, obtained for an excitation energy corresponding to the O $2p_z$-Zn $4s$ peak in the XAS (spectra normalized to the peak height at $\sim 526\,\text{eV}$)

components, which indicate the position in the valence band of the PDOS arising from admixing between O $2p$ and Zn $4p$, $4s$ and $3d$ orbitals. The most intense peak located at $\sim$ 526 eV is formed by the O $2p$ and a very small contribution of Zn $4p$ orbitals. The low energy shoulder attached to this peak in the emission spectrum, and located at $\sim$ 523 eV is attributed to the hybridized O $2p$ - Zn $4s$ states. This 523 eV feature varies in shape and increases strongly in intensity as the excitation energy increases towards the O $2p_z$ - Zn $4s$ peak in the absorption spectrum. The lowest in energy of the three features, located at $\sim$ 520 eV, is caused by the O $2p$-Zn $3d$ hybridized states, [54, 199, 201, 200].

The main difference in the XES spectra at the O K - edge between the doped magnetic and non-magnetic samples is located at the low energy side of the main peak, where some additional spectral weight appears around the shoulder associated with the Zn $4s$ hybridized states, marked (*i*) in figure 7.4 and the valley between this feature and the peak arising from the Zn $3d$-O $2p$ hybridized states marked (*ii*) in figure 7.4. The filling-in of the this valley between the Zn $3d$ and $4s$ hybridized states is a symptom of the more general broadening of the spectral features in the O K XES spectra of the doped samples. The possible influence of disorder in the lattice on the spectral weight, particularly in this region of the spectrum could arise from the lower O $1s$ binding energy, which would imply that an occupied $2p$-$1s$ transition with a lower emission energy, or range of energies. This result recalls the results of the O $1s$ XPS spectra, where the probability of a binding energy shift identified by a low binding-energy fitted peak was noted in that instance. This valley filling effect has also been noted in O K XES from Mn doped ZnO systems [207].

Also in figure 7.4, the comparison between the O K-edge XES of the Co doped films and undoped film shows a clear additional spectral weight in the Co-doped films at valence band maximum, i.e. above $\sim$ 527.5 eV. As these samples have identical orientation with respect to the polarization of the x-rays, we can neglect the strong polarization dependence of the XES in ZnO as a source of difference. The results of resonant photoemission (RPES) of the valence band of Co doped ZnO films by Wi *et al.* [208, 209] as well as those of Chiou [210, 211] and Lee [212], as well as our own valence band XPS results give good grounds to anticipate the presence of additional spectral weight in this region due to Co $3d$-Zn $2p$ hybridization. Comparison of our O K-edge XES results, particularly to the RPES difference spectrum of Wi [208] and Chiou [210] supports the main conclusion we make from our O K XES spectra regarding the position of the Co $3d$-O $2p$ hybridized PDOS at the top of the valence band. This also corresponds with Spaldin [213] and many others who give an occupied $3d$ PDOS that is pinned close to O $2p$ valence band maximum exclusively.

7.3.3 Spectroscopy at the Co L - edge

As with the previous section, we will first consider the results of the Co L-edge XPS, before continuing to the Co L-edge XAS and XES.

7.3.3.1 Co L-edge XPS of Co:ZnO

The valence of the Co present is the most immediate question about the films that the core level XPS aims to answer. The lineshape of the Co $2p_{3/2}$ and $2p_{1/2}$ peaks, shown in figure 7.5 and the magnitude of the spin orbit splitting provides evidence of the state of the Co ions within the sampled volume. As XPS is a surface sensitive technique, the core level spectra reflect the Co environment at and near the surface of the films. If the film composition of the PLD grown samples was known to be highly homogeneous, the Co valence indicated by the core level XPS could determine the local environment of the doped Co throughout the film. However, there is evidence of non-homogeneity of Co throughout the deposited films, and secondary Co-rich phases forming up to the inclusion of Co^0 within the films, which is well summarized in reference [214]. Both substituted Co^{2+} and Co^0 have been reported coexisting within the ZnO by Rode *et al.* [172], from evidence in the Co L-edge and K-edge XMCD. Dorneles *et al.* [183] estimated the magnetic moment arising from the amount of metallic Co they measure via XRD in a number of films and compared it to the measured moment from the entire film. In some but not all cases the entire moment was accounted for by the metallic Co.

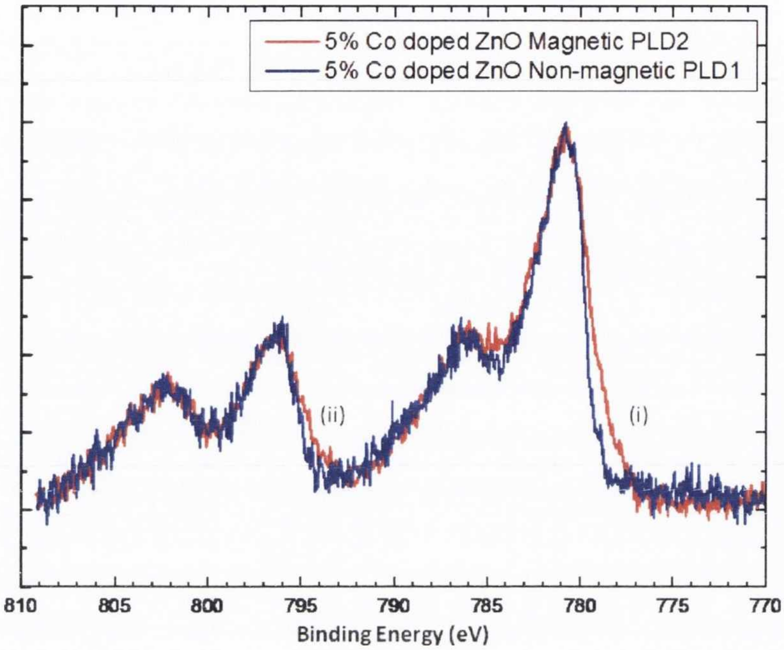

Figure 7.5: Co $2p$ core level XPS from Co doped ZnO films

Comparing the Co L XPS from films the same nominal concentration of Co in ZnO, but with different substrate temperatures during grown, provides a means to observe the rise of additional phases of Co that may be present at higher concentrations. In figure 7.5 the Co L-edge XPS from a magnetic and non-magnetic sample are shown. There is additional spectral weight on the low binding-energy side of both the Co $2p_{3/2}$ and $2p_{1/2}$ peaks in the magnetic sample that suggests a contribution from metallic Co to the spectrum. Comparing our spectra to others published in the literature, for instance the depth-profiling film composition study of Kaspar *et al.* [184] strongly suggests the feature we observe coincides with Co^0. A cross-comparison of Co L-edge XPS from a Co-doped ZnO film, and a polycrystalline Co film by Tuan *et al.* [215] lends further support to this. It must also be noted that electronic structure density of states calculations for Co^{2+} and oxygen vacancies (O_V) in close proximity in TiO_2 lattices introduces the possibility of an apparent shift in binding energy at the Co L-edge due to this combination of defects.

7.3.3.2 Co L -edge XAS of Co:ZnO

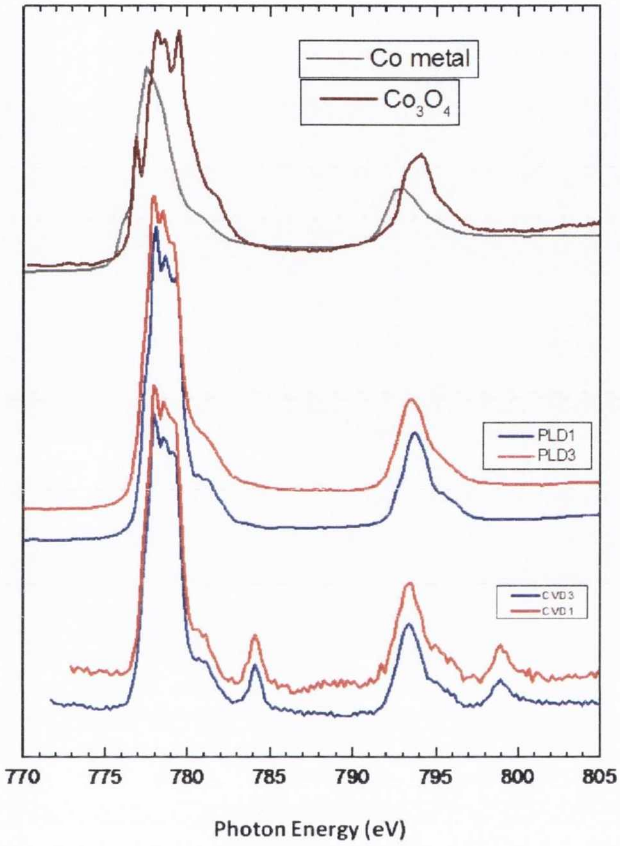

Figure 7.6: Co L edge XAS from PLD and MOCVD deposited Co doped ZnO samples. The results for both magnetic (red trace) and non magnetic (blue trace) are compared to the spectra measured from a pure Co metal foil and a CoO powder. The spectra are offset from each other for clarity

The Co L edge XAS spectra from PLD and MOCVD grown samples are shown in figure 7.6 . The spectra were acquired at beamline 7.0.1 at the ALS with a calculated monochromator resolution at 780 eV of 0.3 eV. The low and high energy spin-orbit split peaks are referred to as L_3 and L_2 respectively. The first of the two main peaks in the Co L - edge absorption spectrum is assigned to the L_3 Co $2p_{3/2}$ - $3d$ multiplet, while the higher energy peak is assigned to the L_2 $2p_{1/2}$ - $3d$ multiplet. While they should display similar multiplet features, the L_2 peak is more broadened. This loss of resolution is explained by the shorter lifetime for a hole on the $2p_{1/2}$ core level than the $2p_{3/2}$ due to the availability of additional radiationless Coster-Kronig decay channels for that core hole. The ratio of their intensities reflects the multiplicity of the occupied $2p$ levels, which are separated by the energy of the spin orbit interaction.

While core level XPS at the Co L edge show evidence of Co^{2+}valence state, it does not clearly distinguish between substitutional Co^{2+} in a tetrahedrally coordinated substitutional ZnO lattice or in octahedral CoO, for instance. XAS at the Co L edge allows the coordination environment of the Co dopant atoms to be determined with more certainty, as the multiplet structure in the absorption peaks distinctly depends on the charge states and crystal field splitting, thus by comparison with CoO [216] it is clearly not an octahedral site symmetry with a Co^{2+} valence. The difference in the Co L edge XAS spectrum between the Co doped ZnO films and Co metal tends to argue against extensive clustering of the Co within the tens of nanometres probed by the technique. In our figure we have compared the Co L-edge spectra from the films with those from metallic Co and octahedral CoO to illustrate the sensitivity of the Co L-edge in the fashion described. Alternatively, this may be further emphasized by comparison with simulated Co L - edge XAS spectra based on multiplet calculations contained in the literature [217, 218] in the mode of, for example, Wi *et al.* [209]. Kaspar *et al.* [184] have used XAS at the Co K-edge to identify the presence of a CoZn intermetallic phase in weakly magnetic films that had been annealed in a Zn vapour. In terms of the spin-orbit splitting energy, and the multiplet structure of the L_3 peak the results of the present Co L-edge XAS are broadly similar to those reported previously from Co-doped ZnO by Krishnamurthy *et al.* [219], Chiou *et al.* [210] , Rode *et al.* [220] and [172], Tietze *et al.* [173] and Kaspar *et al.* [196].

It must also be noted, considering the results of Rode [172], that the sensitivity of Co L-edge XAS to Co^0 is poor, and though we overlay the Co L-edge XAS from metallic Co foil for comparison, we do not use this comparison as evidence of the absence of metallic Co in the films measured.

The most significant difference between the Co L-edge XAS from the PLD and MOCVD deposited films is the presence of the narrow features at 783.4eV and 799.4eV in the spectra from both the magnetic and non-magnetic MOCVD-grown samples. This "6 eV satellite" so called due to the feature's position in energy with respect to the Co $2p$ XAS threshold has been reported in Co L-edge spectra before. We have also noted the feature in a Co-doped SnO_2 film, deposited by PLD and a report of such a feature was prepared by others arguing for its relevance to the magnetic ordering but, to our knowledge, this report was not published. Flipse and de Groot have observed a similar feature in CoO nanoparticles synthesized from the dissolution of a Co acetate precursor on a substrate. In this case the feature was attributed to the unsolved precursor forming a ligand bond with Co ions. Liu *et al.* [221] report a similar feature in CoO nanoparticles precipitated from an organic solvent solution, and proceeded to characterize the feature carefully by calculating a Co L-edge XAS spectrum within the single-impurity Anderson model for CoO nanocrystals bonded with an organic ligand. Most importantly, the authors note a size-dependence of the feature, where it is strongly present in the spectra of 3 nm diameter nanocrystallites, for 6 nm nanocrystallites it is barely visible.

7.3.3.3 Co L - edge RIXS of Co:ZnO

XES at the Co L edge of the Co doped ZnO films was carried out primarily at Beamline 7.0.1 of the Advanced Light Source. A series of spectra were also gathered at Beamline 8.0.1 of the ALS from the MOCVD deposited samples. The spectra for the PLD and MOCVD grown samples are shown in figures 7.7 and 7.8 respectively. A number of resonant excitation energies were chosen beginning at the threshold of the L_2 absorption edge and continuing over the peak. Fewer energies are selected for excitation at the L_2 edge as the emission resulting emission signal is a small fraction of the L_3 edge. Non-resonant spectra (NXES) were recorded at $\sim$ 30eV above threshold. Generally the resonant spectra were recorded with a combined instrumental resolution of 0.8eV at both beamlines, and this resolution was decreased to 1.0eV for the NXES.

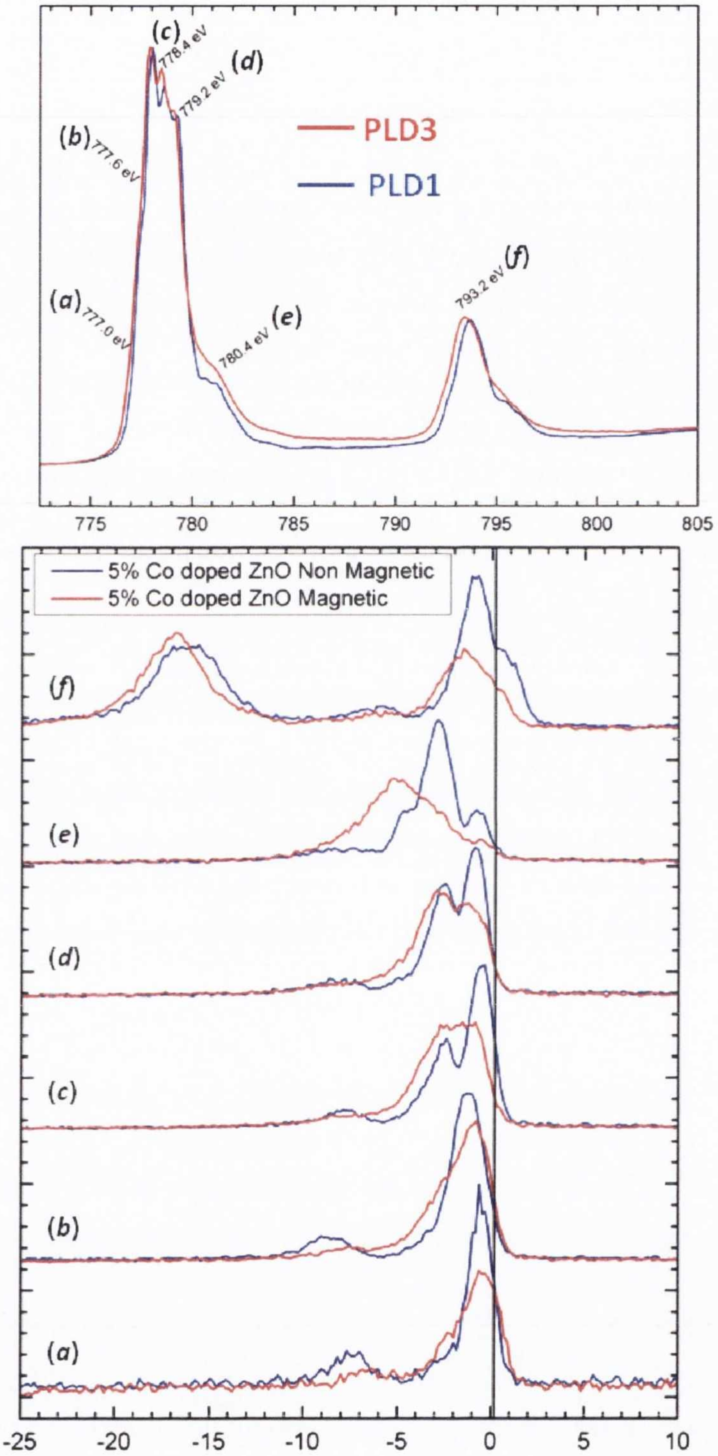

Figure 7.7: Co L edge RIXS from magnetic (red trace) and non-magnetic (blue trace) Co-doped ZnO films deposited by PLD. The RIXS is displayed with reference to an energy-loss scale. The samples shown are PLD1 and PLD3 as listed in table 7.1

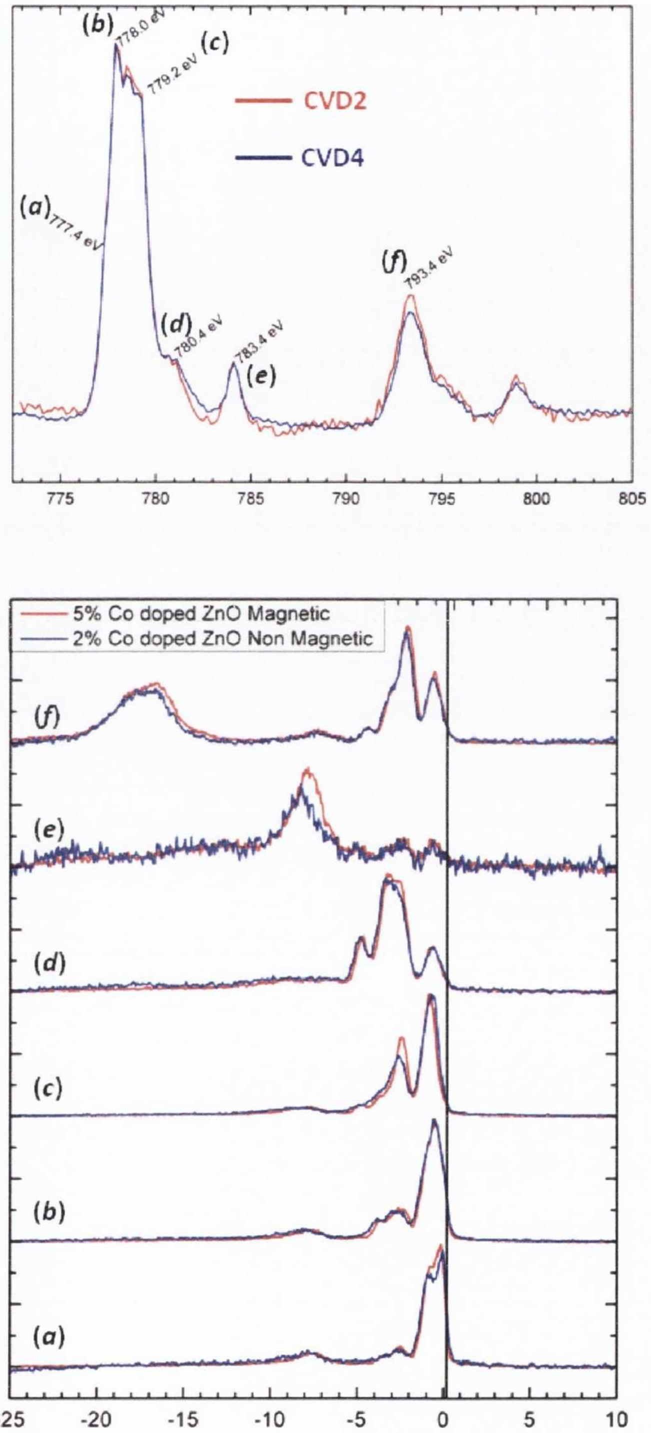

Figure 7.8: Co L edge RIXS from Co doped magnetic (red) and non-magnetic (blue) ZnO films deposited by MOCVD. The samples shown are CVD2 and CVD4 as listed in table 7.2. The RIXS spectra are referred to an energy-loss scale

In the Co L-edge RIXS of the PLD grown samples, the excitation energies, and the features on the Co L-edge XAS spectrum that they correspond to are labelled *a-f* in the top panel of figure 7.7, which correspond to five excitations from the threshold of absorption across the L_3 peak, and one at the L_2 peak. For the PLD-grown samples, the RIXS spectra presented are normalized to unit area, due to the huge difference in spectral weight between the features they contain which creates a misleading shape distortion when normalizing to peak height. As noted by Chang *et al.* [204], RIXS represents a probe of the local electronic structure of the Co impurities present in the films. In our case one of the magnetic films shows a very different environment compared to the non-magnetic film.

As noted in the caption for figures 7.7 and 7.8 we have presented our Co L-edge RIXS spectra on an energy loss scale, as the relative intensities of the inelastic loss features are at the heart of our discussion of the electronic structure of these films. The loss plot clearly indicates the position of the elastic feature, and the low energy d-d^*transitions down to $\sim$ 3 eV below this energy.

The lower-in-energy of the two transitions, located approximately within two-three electron volts of the elastic peak, are due to excitations within the transition metal d band to unoccupied d^* states within this band. Low energy d-d^* excitations are strongly favoured in L-edge RIXS spectra in transition metal oxides, and serve as a useful probe into these localized electronic states. Their energies are approximately the same as the weak d-d^* excitations seen in optical spectra [222] for Co^{2+} ions doped into ZnO. At larger Co concentrations these optical resonances broaden [223]. The Kramers-Heisenberg equation allows, in principle, for a very detailed study of such inelastic losses in $2p$-$3d$ RIXS given a beamline with sufficiently high resolution and an XES spectrometer of sufficient resolution of which, until recently only one was available at ADRESS in the Swiss Light Source. These transitions are found optically at transition energies of approximately $\sim$ 0.50eV, 0.86eV, 1.88eV and 2.04eV . These will differ somewhat in RIXS due to the $2p \rightarrow 3d$ matrix elements.

The energy loss feature corresponding to the highest energy d-d^* transition dominates over the lower energy transition in the magnetic film, compared to the non-magnetic film. Where the non-magnetic film (blue trace) shows the strongest spectral weight for the lowest energy d-d^* transition for all the excitation energies *a-e* across to the L_3 peak, at excitation energy *c*, the high energy d-d^* transition in the magnetic film is as prominent as the low energy excitation. The ratio of spectral weight between the two features then reverses, with the lower energy transition further suppressed. It is spectra c, d and e among the RIXS spectra that show the starkest contrast between the magnetic and non-magnetic film.

The feature located at ~ 8 eV below the elastic line, which is attributed to the transfer of an O $2p$ electron from the ligand to a Co $3d$ valence band state, is relatively more prominent in the non-magnetic sample, especially at the threshold excitation energy a. It is detectable in the RIXS from the magnetic film, but falls off rapidly, and contributes a tail to the low energy side of the emission features rather than forming a discernible peak as it does for the non-magnetic film. In general the width of the charge transfer peak gives an indication of the ligand-coordination of the Co cation[224]. The peak we observe in RIXS from tetrahedrally-coordinated Co in ZnO is narrower than that observed for the octahedrally coordinated Co in single crystal CoO [216]. The changes in the relative intensity of the charge transfer peak is clearly visible between the different Co:ZnO samples indicating some alteration in the first coordination sphere of the Co cation in different films.

Finally, for the excitation energy at the L_2 edge the ratio of the $L_3 : L_2$ intensity is reversed between the magnetic and non-magnetic film. For the non-magnetic sample the intensity of the L_2 emission line is larger than the L_3, while the L_3intensity is greater than the L_2 in the magnetic sample. The NXES spectrum from metallic cobalt shows a L_2/L_3 ratio $\ll 1$, as was compared to good effect to illustrate the difference in this ratio between different species of cobalt by Chang *et al.* [204].

An observation of the greatly reduced intensity of the low energy d-d^* transition feature at a loss energy of ~ 2 eV with respect to the d-d^* feature at a loss energy of ~ 3 eV in the magnetic film has not been reported in other Co L-edge RIXS studies we are aware of [224, 204]. Though the ratio of the intensity of the two d-d^*features in the magnetic film is striking, we ultimately tend to view the Co L-edge RIXS from the magnetic film as indicative of a much reduced L_3-edge emission in this sample rather than an absolute enhancement in the higher-energy transition feature. We have speculated on the possible link between this reduction in the L_3 emission intensity and the possibility of a significant contribution of emission from metallic Co in our spectra from this sample. To this end we compare the L_3 NXES emission from Co metal to the L_3 PDOS emission from the magnetic sample in figure 7.9, which lends further encouragement to this point of view.

The RIXS spectra from the MOCVD grown films is shown in figure 7.8. The top panel in figure 7.8 shows the excitation energies at which spectra were recorded. Compared to the PLD grown films, the RIXS spectra from the MOCVD grown samples show very little variation between the magnetic and non-magnetic films. What

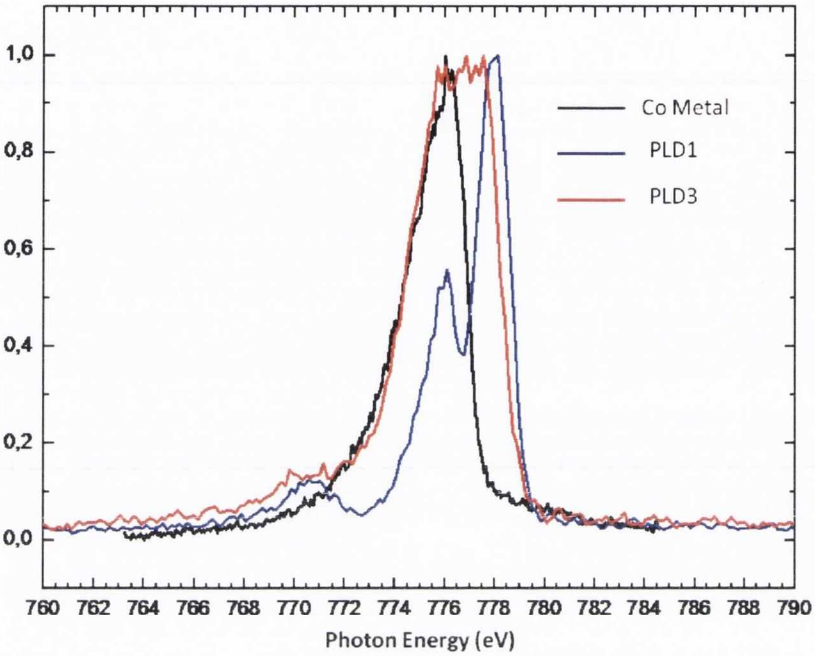

Figure 7.9: Comparison of the L_3 NXES from metallic Co to the L_3 PDOS emission from a magnetic PLD-grown Co-doped ZnO film

difference is present is located in spectrum *c*, taken on the L_3 peak and spectrum *e* taken at an energy corresponding to the "6 eV feature". In both of the MOCVD grown films the charge-transfer peak is not as prominent as the non-magnetic PLD grown film. It does make a strong contribution to spectrum *e*, particularly so for the magnetic film. Liu *et al.* report Co *L*-edge spectra from approximately the same energy as this feature in our MOCVD Co *L*-edge XAS spectrum, for two 5% Co-doped ZnO films and a 5% Co, 1% Al-doped ZnO [225]. They also report a variation in the strength of the charge transfer feature in their spectra, and interpret this variation as indicative of a greater delocalization of the O 2*p* electrons in the presence of a defect in the lattice, giving rise to a weaker charge transfer effect. Interpreting our results based on this scheme attributes a greater delocalization to the O 2*p* states in the non-magnetic of the two films.

7.3.4 VB XPS of Co:ZnO

The valence band spectra, shown in figure 7.10 outline the total density of states present in this region of the electronic structure composed by hybridized orbitals. The position of the additional density of states associated with the dopant species, and their effect on the over all density of states in the valence band will be clearly visible from the valence band spectra. The spectra recorded in this region, between a binding energy of 20 eV and the Fermi level will also allow the identification of any additional states that may be present within the band gap of the material. With respect to suggested models for magnetic ordering in dilutely doped ZnO, the presence of additional occupied states at the top of the valence band and extending into the band gap are necessary for the mediation of long range alignment of spins.

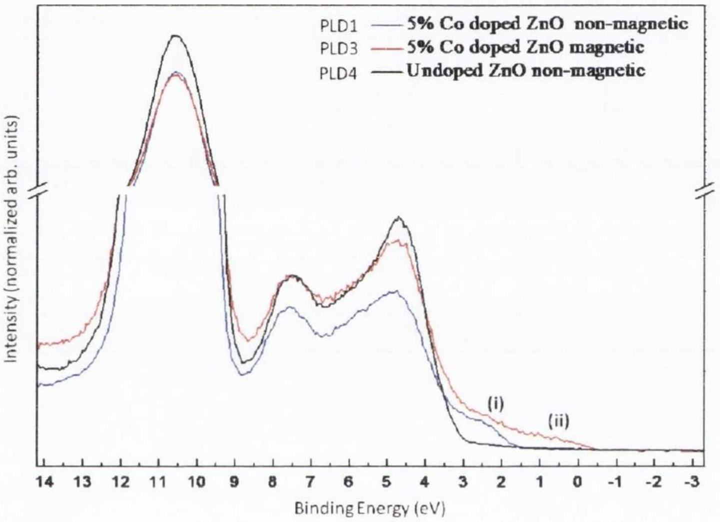

Figure 7.10: Valence band XPS of PLD deposited Co doped ZnO films. The undoped, doped non-magnetic and doped magnetic samples are PLD4, PLD1 and PLD3 respectively as detailed in table. 7.1 The Zn 3*d* peak is truncated in the spectrum by cutting away a section of the y axis

The valence band XPS from the undoped ZnO, and 5% Co doped magnetic and non-magnetic ZnO films have three features in common, similar to the XES spectra at the O K-edge. The filled Zn 3*d* states give rise to the peak at $\sim$ 11 eV binding energy. In the O K-edge XES spectra, this is the weakest feature, due to the weak hybridization of the Zn 3*d* and O 2*p* states. The peaks at 7 eV and 4.5 eV binding energy are due to the O 2*p*-Zn 4*s* and 4*p* hybridized states respectively. The valence band maximum for undoped ZnO is evident at a binding energy of 3 eV, and in both of the Co doped films we see an additional density of states extending into the bandgap, particularly the ledge-like feature that is approximately centred at 2 eV binding energy, labeled as feature (*i*) in figure 7.10. There is a further feature present in the VB XPS of the magnetic film labeled as feature (*ii*) in figure 7.10.

There are other good examples of the VB XPS feature we have labeled (*i*) our spectrum, *e.g.* Kaspar *et al.* [196]. As mentioned previously with regard to the additional spectral weight noted at in the bandgap in the O K-edge XES from Co-doped ZnO films grown by PLD, the studies by resonant photoemission of Chiou [210, 211], Wi [208, 209] and Lee [212] also indicate that this 2 eV binding-energy feature is the location of the Co $3d\, e_g$ states. It must be noted that it is not possible to categorically differentiate between the additional density of states due to the Co $3d$ levels reported in these and other films and the feature we distinguish as feature (*iii*) in the magnetic film.

Considering the evidence we have gathered, particularly from the O K-edge and Co L-edge XPS, and the O K-edge XES we have reported to this point, we assign the additional density of states, feature (*iii*) to the presence of defects in the magnetic films. Combining this observation with the O K-edge XAS from the magnetic Co-doped ZnO samples we report, as well as those from other reports of O K-edge XAS and FEFF simulations lends some support to the interpretation of the accumulation of spectral features as related to the presence of oxygen vacancies in the films. It is important that the co-doping of Al in cobalt-doped ZnO has been reported as giving rise to an improved structural quality of the films and the presence of less cobalt clustering, and the disappearance of ferromagnetism.

7.3.5 Core level spectroscopy at the Zn L -edge

XPS at the Zn L edge, which is not included in the results, was recorded to investigate the chemical environment of the Zn in the lattice and at the surface of the films. In a similar fashion to the previous discussion for metallic Co, the presence of metallic Zn in the films would be expected to detected by additional features in the Zn core level spectra. The spectra from the various samples were very similar at the Zn L edge, and were characteristic of Zn^{2+}.

The Zn L edge XAS of the undoped and doped samples, shown in figure 7.11 were recorded to assess what they could reveal about the Zn environment in the films with varied properties. Of particular importance in a number of electronic structure calculations of this material is the possible presence of interstitial Zn defects in the films. The similarity of the Zn L edge XAS between the undoped and doped films confirm that within the concentration limits of detectable by XAS, the Zn is located in a tetrahedrally coordinated environment.

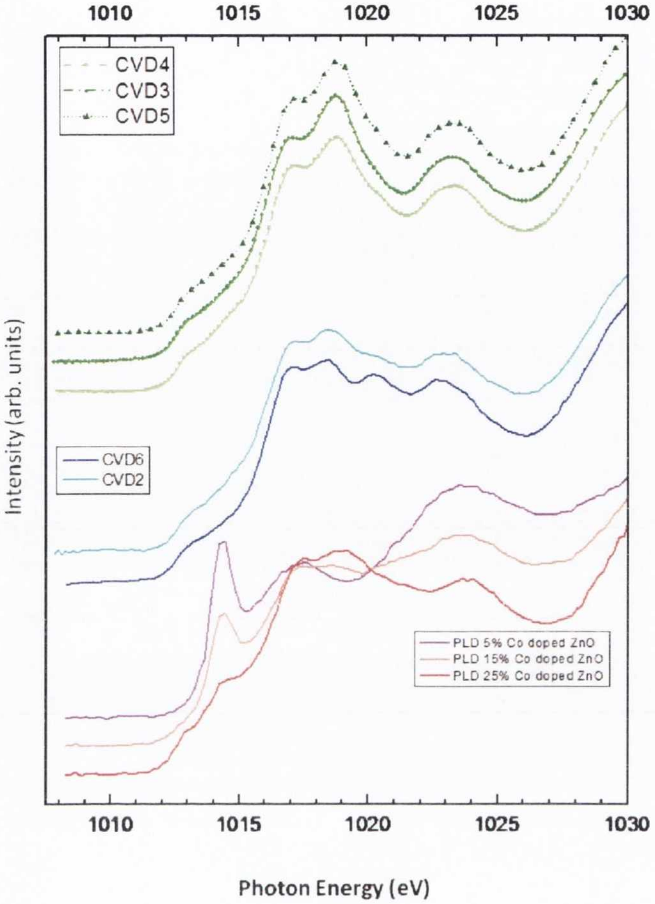

Figure 7.11: Zn L-edge XAS from PLD and MOCVD deposited Co doped ZnO films

In figure 7.11 we have compared the three different "types" of Zn L-edge spectra that we have measured. The spectra are presented in three groups of three spectra each. In the lowermost group of spectra, the samples measured have concentrations of Co of 25%, 15% and 5% respectively from lowermost to uppermost. They all show evidence of a different valence of Zn than the other six films included in the figure. This is evidenced by the sharp peak at 1014.5 eV, which is similar in origin to the white line reported at the L_3 edge in other metals with filled d levels, when the formation of an oxide for example in the case of CuO leads to unfilled d states that are more or less localized at the bottom of the conduction band, giving rise to the sharp absorption feature. These films had been rejected from the study as highly defective due to the surmised presence of water in the films from additional features that were present in the O K-edge RIXS spectra, not reported here. We are also aware of similar features reported in the Zn *L*-edge XAS spectra from Zn-aerosol complexes such as $Zn(NO_3)6H_2O$. In a previous report, the same feature was interpreted as positive evidence for an additional unoccupied hybridized density of states associated with the magnetism of the films via the previously mentioned bound polaron model [175, 226]. Even in the films that do not exhibit this feature that may be associated with H_2O and Zn, it is worth recalling that the O *K*-edge XPS recorded a spectrally very significant proportion of H_2O in the films.

The remaining spectra in figure 7.11 are all from the MOCVD grown samples. The difference between the blue and green traces in the middle and upper portion of the figure is the prominence of the Zn 4*s* feature located at 1018.5 eV. The MOCVD-grown samples measured entirely fall into one category or the other: those represented by spectra in the middle of the figure, with the reduction of spectral weight in this feature, and the spectra in the upper portion of the figure where this feature is prominent. Considering the anisotropy evidenced in reports of the O *K*-edge XAS [206], there are somewhat strong grounds to associate the origins of this variation as a polarization-dependent effect which a series of angle-dependent measurements would confirm.

7.4 Summary and Conclusions

The strong anisotropy in the O *K* -edge absorption of ZnO is clearly evident in our results and elsewhere in the literature [227, 201]. Therefore, caution is required when comparing the O *K* -edge absorption spectra from different samples and identifying unique features in one spectrum and attributing it to the presence of additional hybridized states in the system. We overcame this potential source of error by restricting our comparison of O *K* edge spectra to those acquired with the same orientation of the crystalline axes with respect to the x-ray polarization. In this fashion, we are able to make a firm conclusion that there is a consistent additional density of states located at the bottom of the conduction band in the Co doped films compared to the undoped films that are attributable to the O 2*p* - Co 3*d* e_g hybridized states.

In the O *K* - edge XAS spectra from both the PLD and MOCVD grown samples, there are examples of films with additional densities of states at the very onset of absorption that extend somewhat into the bandgap of the density of states. We note that the samples from which we observe this feature have previously been reported as magnetic. A previous calculation has attributed additional densities of states in this energy range to the presence of oxygen vacancies in the ZnO [204].

There is an also an additional density of states noted in the XPS at the O K edge in the two samples we measured which had been reported as possessing a magnetic moment, compared to the other doped and undoped films. We are aware of calculations that predict changes in the binding energy of the O 1s core level in the neighbourhood of interstitial and vacancy defects in ZnO [169]. In light of more recent RPES and partial XAS of this region it seems unwise to conclusively attribute these states to anything other than Co_3O_4.

Chapter 8

Conclusions and Further Work

From the experimental results, and particularly the results of the calculated electronic structures presented in this thesis we conclude that the adoption of the rutile structure strikes a balance between the ionic transfer of electrons to the ligand ions in MX_2 compounds, and covalent-bonding σ- and π-like interactions between the metal and ligand orbitals, that give rise to a natural linear dichroism. The spatial arrangement of the M-O σ and π states, combined with the other selection rules of the x-ray scattering process allow the weighted occupied O $2p$ partial density of states projections along individual crystal axes to be probed independently, in a k-selective, symmetry and geometry dependent manner.

The WIEN2K formulation of DFT yielded a realistic treatment of the electronic structure in such covalently bonded systems as were included in the study. It provided a projected partial density of states from which RXES spectra were simulated, allowing further interpretation of the experimental results.

In the work we presented, the valence band of SnO_2 received a very detailed treatment, with XPS and O K-edge XES and calculated electronic structure calculations. The experimental observation of the XES projected along the crystalline a and c axes took the form predicted by the spectra simulated from the calculated density of states. Further, this illustrates the power of RXES obtained in an orientation and polarization-dependent fashion, as a further insight into bonding.

We observed the natural linear dichroism in rutile RuO_2 in both the conduction and valence band via XAS and XES at the O K edge respectively. The O $2p$ PDOS in the conduction and valence band projected in the planes perpendicular to the a and c axes was probed independently. The effects of the anisotropic PDOS spatial projections were also evident via the structure observed "within" the elastic peak. The difference spectra produced showed the location in energy of the spectral weight due to the O $2p_y$ density of states perpendicular to the M_3O planes. Although the approach was not as conclusive as that applied in the case of SnO_2, the good agreement between the difference spectra in the E$||c$, XES along c geometry and the difference spectra for the corresponding simulated spectra indicates that the main parts of the σ versus π dependence is described correctly, certainly with respect to the NXES. Both the experimental RXES and difference spectra were well simulated by the calculated PDOS. RuO_2 is the only metallic oxide studied in the present thesis.

Resonant absorption and emission spectroscopy at the O K-edge was presented, and compared to the projected calculated O $2p$ and Ti $3d$ occupied and unoccupied PDOS for both anatase and rutile TiO_2. The non-bonding nature of the O $2p_y$-created PDOS at the top of the valence band, predicted by the molecular-orbital bonding scheme, is reproduced in the calculated projected O $2p$ PDOS for both anatase and rutile, with a somewhat more prominent PDOS due to M-O $2p_y$ π-bonding at the centre of the valence band in anatase TiO_2 compared to rutile.

Results of O K-edge XAS and RXES from samples of anatase TiO_2 nanosheets were presented and discussed with reference to the increased spectral weight related to the O $2p_y$ π-bonding that was observed in the samples with 89% (001) surface area, caused by the greater degree of emission from the PDOS projected in the plane perpendicular to the c-axis and consequently observed in the near grazing E$||c$, XES along c excitation and scattering geometry.

From our study of the O K- and Co L-edge RXES we note the strong anisotropy in the O K -edge absorption of ZnO, and note the consequent caution required when comparing the O K -edge absorption spectra from different samples and identifying unique features in one spectrum and attributing it to the presence of additional hybridized states in the system. We overcame this potential source of confusion by restricting our comparison of O K edge spectra to those acquired with the same orientation of the crystalline axes with respect to the polarization of the x-rays. In this fashion, we are able to make a firm conclusion that there is a consistent additional density of states located at the bottom of the conduction band in the Co doped films compared to the undoped films that are attributable to the O $2p$ - Co $3d$ e_g hybridized states. In the O K - edge XAS spectra from both the PLD and MOCVD grown samples, there are examples of films with additional densities of states at the very onset of absorption that extend somewhat into the bandgap of the density of states. We note that the samples from which we observe this feature have previously been reported as magnetic. We interpret our results in the light of calculations that have attributed additional densities of states in this energy range to the presence of oxygen vacancies and cobalt inclusions in the ZnO [204]. There is an also an additional density of states noted in the XPS at the O K edge in the two samples we measured which had been reported as possessing a magnetic moment, compared to the other doped and undoped films. We are aware of calculations that predict changes in the binding energy of the O 1s core level in the neighbourhood of interstitial and vacancy defects in ZnO [169]. However, we note that in light of more recent RPES and partial XAS of this region it seems unwise to conclusively attribute these states to anything other than Co_3O_4.

Though our polarization-dependent symmetry-selective study has gone some way to addressing the defecit in reported observation of the axes-projected O 2p PDOS in rutile oxides, the work continues with a larger set of materials such as IrO_2, CrO_2 and WO_2, which when combined with the results presented in this thesis will approach a systematic study of the projected O 2p PDOS with d-shell filling in rutile-type crystal structures.

Experimental and simulated RXES at the metal L-edge is also an interesting prospect, and will provide a more complete analysis of the bonding in rutile oxides.

Experimental and simulated RXES at the F K-edge in rutile type fluorides such as MnF_2 has already begun within our research group by Declan Cockburn and Dr. Cormac McGuinness, to investigate the effects of the electronegativity of the anion on the bonding in the rutile structure.

References

[1] S. Hufner, editor. *Very High Resolution Photoelectron Spectroscopy.* Springer Berlin, 2007.

[2] D.T. Attwood. *Soft x-rays and extreme ultraviolet radiation: principles and applications.* Cambridge University Press, 2000.

[3] J. Nordgren, G. Bray, S. Cramm, R. Nyholm, J.E. Rubensson, and N. Wassdahl. Soft x-ray emission spectroscopy using monochromatized synchrotron radiation (invited). *Review of Scientific instruments*, 60:1690, 1989.

[4] J. J. Jia, T. A. Callcott, J. Yurkas, A. W. Ellis, F. J. Himpsel, M. G. Samant, J. Stohr, D. L. Ederer, J. A. Carlisle, E. A. Hudson, L. J. Terminello, D. K. Shuh, and R. C. C. Perera. First experimental results from IBM/tenn/tulane/LLNL/LBL undulator beamline at the advanced light-source. *Rev. Sci. Instrum.*, 66(2):1394–1397–, 1995.

[5] F. Gel'mukhanov and H. Agren. Resonant x-ray raman scattering. *Phys. Rep.-Rev. Sec. Phys. Lett.*, 312(3-6):91–244–, 1999.

[6] J.A. Carlisle, E.L. Shirley, E.A. Hudson, L.J. Terminello, T.A. Callcott, JJ Jia, D.L. Ederer, R.C.C. Perera, and F.J. Himpsel. Probing the graphite band structure with resonant soft-x-ray fluorescence. *Physical Review Letters*, 74(7):1234–1237, 1995.

[7] P. I. Sorantin and K. Schwarz. Chemical bonding in rutile-type compounds. *Inorg. Chem.*, 31(4):567–576–, 1992.

[8] R Janes and E.A. Moore. *Metal-ligand Bonding.* Open University Press, 2004.

[9] RG Egdell, J Rebane, TJ Walker, and DSL Law. Competition between initial- and final-state effects in valence- and core-level x-ray photoemission of Sb-doped SnO_2. *Physical Review B*, 59(3):1792–1799, JAN 15 1999.

[10] C. McGuinness, C. B. Stagarescu, P. J. Ryan, J. E. Downes, D. F. Fu, K. E. Smith, and R. G. Egdell. Influence of shallow core-level hybridization on the electronic structure of post-transition-metal oxides studied using soft x-ray emission and absorption. *Phys. Rev. B*, 68(16):165104–, 2003.

[11] A. G. Thomas, W. R. Flavell, A. K. Mallick, A. R. Kumarasinghe, D. Tsoutsou, N. Khan, C. Chatwin, S. Rayner, G. C. Smith, R. L. Stockbauer, S. Warren, T. K. Johal, S. Patel, D. Holland, A. Taleb, and F. Wiame. Comparison of the electronic structure of anatase and rutile TiO_2 single-crystal surfaces using resonant photoemission and x-ray absorption spectroscopy. *Physical Review B*, 75(3), JAN 2007.

[12] J. Stöhr. *NEXAFS spectroscopy.* Springer, 1992.

[13] F. de Groot and A. Kotani. *Core level spectroscopy of solids.* CRC, 2008.

[14] J Stohr and H. C. Siegmann. *Magnetism from Fundamentals to Nanoscale.* Springer-Verlag, Berlin, 2006.

[15] M. O. Krause. Atomic radiative and radiationless yields for k and l shells. *Journal of Physical and Chemical Reference Data*, 8(2):307–327, 1979.

[16] Ulf von Barth and Günter Grossmann. Dynamical effects in x-ray spectra and the final-state rule. *Phys. Rev. B*, 25(8):5150–5179, Apr 1982.

[17] A. Kotani and S. Shin. Resonant inelastic x-ray scattering spectra for electrons in solids. *Reviews of Modern Physics*, 73(1):203–246, 2001.

[18] T. Schmitt. *Resonant soft X-ray emission spectroscopy of vanadium oxides and related compounds.* PhD thesis, Uppsala University, 2004.

[19] R. Denecke, P. Vaeterlein, M. Baessler, N. Wassdahl, S. Butorin, A. Nilsson, J.E. Rubensson, J. Nordgren, N. Maortensson, and R. Nyholm. Beamline I511 at MAX II, capabilities and performance. *Journal of Electron Spectroscopy and Related Phenomena*, 101:971–977, 1999.

[20] JJ Sakurai. *Advanced Quantum Mechanics.* Addison Weseley Publishing Company. Reading, Massachusetts, 1967.

[21] A. Corney. *Atomic and Laser Spectroscopy.* Clarendon Press, Oxford, 1977.

[22] J. A. R. Samson. *Techniques of Vacuum Ultraviolet Spectroscopy.* Wiley, 1967.

[23] T. Learmonth. *Soft x-ray spectroscopic studies of quasi-low dimensional and strongly correlated materials.* PhD thesis, Boston University, 2008.

[24] A. Kotani. Theory of resonant x-ray emission spectroscopy. *J. Synchrot. Radiat.*, 8:110–114–, 2001.

[25] J. H. Guo, N. Wassdahl, P. Skytt, S. M. Butorin, L. C. Duda, C. J. Englund, and J. Nordgren. End station for polarization and excitation-energy selective soft-x-ray fluorescence spectroscopy. *Rev. Sci. Instrum.*, 66(2):1561–1563–, 1995.

[26] T. Warwick, P. Heimann, D. Mossessian, W. McKinney, and H. Padmore. Performance of a high resolution, high flux density SGM undulator beamline at the als (invited). *Review of Scientific instruments*, 66:2037, 1995.

[27] J. K. Burdett. Electronic control of the geometry of rutile and related structures. *inorganic Chemistry*, 24(14):2244–2253, 1985.

[28] W. H. Baur and A. A. Khan. Rutile-type compounds 4. SiO_2, GeO_2 and a comparison with other rutile-type structures. *Acta Crystallographica Section B-Structural Crystallography and Crystal Chemistry*, B 27(NOV15):2133–&, 1971.

[29] A. A. Bolzan, C. Fong, B. J. Kennedy, and C. J. Howard. Structural studies of rutile-type metal dioxides. *Acta Crystallographica Section B-Structural Science*, 53(Part 3):373–380, JUN 1 1997.

[30] J. K. Burdett. Structural-electronic relationships in rutile. *Acta Crystallographica Section B-structural Science*, 51(Part 4):547–558, AUG 1 1995.

[31] R Restori, D Schwarzenbach, and J R Schneider. Charge-density in rutile, TiO_2. *Acta crystallographica section b-structural science*, 43(Part 3):251–257, JUN 1 1987.

[32] CE Boman. Refinement of crystal structure of ruthenium dioxide. *Acta Chemica Scandinavica*, 24(1):116, 1970.

[33] J Mimaki, T Tsuchiya, and T Yamanaka. The bond character of rutile type SiO_2, GeO_2 and SnO_2 investigated by molecular orbital calculation. *Zeitschrift Fur Kristallographie*, 215(7):419–423, 2000.

[34] P. Oppeneer P. M. Konig C. Fraune M. Rudiger U. Guntherodt G. Ambrosch-Draxl C. Kunes, J. Novak. Electronic structure of Cro_2 as deduced from its magneto-optical Kerr spectra. *Physical Review B*, 65:165105, 2002.

[35] J. Kohanoff and N. Gidopoulos. *Handbook of Molecular Physics and Quantum Chemistry*, chapter 26 "Density functional theory: basics, new trends and applications.". Wiley and Sons New York, NY, 2003.

[36] P. Hohenberg and W. Kohn. Inhomogeneous electron gas. *Phys. Rev.*, 136(3B):B864–B871, Nov 1964.

[37] S. Cottenier. *Density Functional Theory and the family of (L)APW-methods: a step-by-step introduction.* instituut voor Kern- en Stralingsfysica, K.U.Leuven, Belgium, 2002.

[38] K. Madsen G. K. H. Kvasnicka D. Luitz J. Blaha, P. Schwarz. *Wien2k An Augmented Plane Wave and Local Orbitals Program for calculating crystal properties.* Technische Universität Wien, 2010.

[39] F. Gelmukhanov and H. Agren. X-ray raman-scattering as a means for studies of near-edge and extended x-ray-absorption fine-structures. *Physica B*, 209(1-4):100–102–, 1995.

[40] M Batzill and U Diebold. The surface and materials science of tin oxide. *Progress in Surface Science*, 79(2-4):47–154, 2005.

[41] C Kilic and A Zunger. Origins of coexistence of conductivity and transparency in SnO_2. *Physical Review Letters*, 88(9), MAR 4 2002.

[42] Kate G. Godinho, Aron Walsh, and Graeme W. Watson. Energetic and electronic structure analysis of intrinsic defects in SnO_2. *Journal of Physical Chemistry C*, 113(1):439–448, JAN 8 2009.

[43] T J Godin and J P Lafemina. Surface atomic and electronic-structure of cassiterite SnO_2 (110). *Physical Review B*, 47(11):6518–6523, MAR 15 1993.

[44] R G Egdell, S Eriksen, and W R Flavell. Oxygen deficient SnO_2(110) and TiO_2(110) - a comparative-study by photoemission. *Solid State Communications*, 60(10):835–838, DEC 1986.

[45] J M Themlin, R Sporken, J Darville, R Caudano, J M Gilles, and R L Johnson. Resonant-photoemission study of SnO_2 - cationic origin of the defect band-gap states. *Physical Review B*, 42(18):11914–11925, DEC 15 1990.

[46] CB Fitzgerald, M. Venkatesan, LS Dorneles, R. Gunning, P. Stamenov, JMD Coey, PA Stampe, RJ Kennedy, EC Moreira, and US Sias. Magnetism in dilute magnetic oxide thin films based on Sno_2. *Physical Review B*, 74(11):115307, 2006.

[47] Hongxia Wang, Yu Yan, Kai Li, Xiaobo Du, Zhihuan Lan, and Hanmin Jin. Role of intrinsic defects in ferromagnetism of SnO_2 : First-principles calculations. *Physica Status Solidi B-Basic Solid State Physics*, 247(2):444–448, FEB 2010.

[48] B Thiel and R Helbig. Growth of SnO_2 single-crystals by a vapor-phase reaction method. *Journal of Crystal Growth*, 32(2):259–264, 1976.

[49] D Frohlich, R Kenklies, and R Helbig. Band-gap assignment in SnO_2 by 2-photon spectroscopy. *Physical Review Letters*, 41(25):1750–1751, 1978.

[50] FH Jones, R Dixon, JS Foord, RG Egdell, and JB Pethica. The surface structure of SnO_2(110) (4x1) revealed by scanning tunneling microscopy. *Surface Science*, 376(1-3):367–373, APR 10 1997.

[51] R Brydson, H Sauer, W Engel, and F Hofer. Electron energy-loss near-edge structures at the oxygen K-edges of titanium(iv) oxygen compounds. *Journal of Physics-condensed Matter*, 4(13):3429–3437, MAR 30 1992.

[52] L Kover, G Moretti, Z Kovacs, R Sanjines, I Csemy, G Margaritondo, J Palinkas, and H Adachi. High-resolution photoemission and auger parameter studies of electronic-structure of tin oxides. *Journal of Vacuum Science & Technology A-Vacuum Surfaces and Films*, 13(3, Part 2):1382–1388, MAY-JUN 1995.

[53] MO Figueiredo and JP Mirao. Soft x-ray absorption at the O K-edge in rutile-type natural oxides. *Nuclear instruments & Methods in Physics Research Section B-Beam interactions With Materials and Atoms*, 238(1-4):314–318, AUG 2005.

[54] C. Ryan P. J. Downes J. E. Fu D. F. Smith K. E. McGuinness, C. Stagarescu and R G Egdell. Influence of shallow core-level hybridization on the electric structure of post-transition-metal oxides studied using soft x-ray emission and absorption. *Physical Review B*, 68:165104–, 2003.

[55] J Robertson. Electronic-structure of SnO_2, GeO_2, PbO_2, TeO_2 and MgF_2. *Journal of Physics C-Solid State Physics*, 12(22):4767–4776, 1979.

[56] P M A Sherwood. Valence-band spectra of tin oxides interpreted by x-alpha calculations. *Physical Review B*, 41(14):10151–10154, MAY 15 1990.

[57] N I Medvedeva, V P Zhukov, M Y Khodos, and V A Gubanov. The electronic-structure and cohesive energy of HfO_2, ZrO_2, TiO_2, and SnO_2 crystals. *Physica Status Solidi B-Basic Research*, 160(2):517–527, AUG 1990.

[58] S Munnix and M Schmeits. Electronic-structure of tin dioxide surfaces. *Physical Review B*, 27(12):7624–7635, 1983.

[59] K Reimann and M Steube. Experimental determination of the electronic band structure of SnO_2. *Solid State Communications*, 105(10):649–652, MAR 1998.

[60] Qi-Jun Liu, Zheng-Tang Liu, and Li-Ping Feng. First-principles calculations of structural, electronic and optical properties of tetragonal SnO_2 and SnO. *Computational Materials Science*, 47(4):1016–1022, FEB 2010.

[61] B. A. Hamad. First-principle calculations of structural and electronic properties of rutile-phase dioxides (MO_2), M = Ti, V, Ru, Ir and Sn. *European Physical Journal B*, 70(2):163–169, JUL 2009.

[62] YM Mi, H Odaka, and S Iwata. Electronic structures and optical properties of ZnO, SnO_2 and In_2O_3. *Japanese Journal of Applied Physics Part 1-Regular Papers Short Notes & Review Papers*, 38(6A):3453–3458, JUN 1999.

[63] C Persson and S Mirbt. Improved electronic structure and optical properties of sp-hybridized semiconductors using LDA+U-SIC. *Brazilian Journal of Physics*, 36(2A):286–290, JUN 2006. 12th Brazilian Workshop on Semiconductor Physics (BWSP-12), Sao Jode dos Campos, BRAZIL, APR 04-08, 2005.

[64] C Persson and A Zunger. s-d coupling in zinc-blende semiconductors. *Physical Review B*, 68(7), AUG 15 2003.

[65] LS Roman, R Valaski, CD Canestraro, ECS Magalhaes, C Persson, R Ahuja, EF da Silva, I Pepe, and AF da Silva. Optical band-edge absorption of oxide compound SnO_2. *Applied Surface Science*, 252(15):5361–5364, MAY 30 2006.

[66] Carla D. Canestraro, Lucimara S. Roman, and Clas Persson. Polarization dependence of the optical response in SnO_2 and the effects from heavily F doping. *Thin Solid Films*, 517(23):6301–6304, OCT 1 2009.

[67] A. Ferreira da Silva, I. Pepe, C. Persson, J. Souza de Almeida, C. Moyses Araujo, R. Ahuja, B. Johansson, C. Y. An, and J. H. Guo. Optical properties of oxide compounds PbO, SnO_2 and TiO_2. *Physica Scripta*, T109:180–183, 2004.

[68] C Persson and AF da Silva. Strong polaronic effects on rutile TiO_2 electronic band edges. *Applied Physics Letters*, 86(23), JUN 6 2005.

[69] R. G. Egdell, J. Rebane, T. J. Walker, and D. S. L. Law. Competition between initial- and final-state effects in valence- and core-level x-ray photoemission of sb-doped sno2. *Phys. Rev. B*, 59(3):1792–1799–, 1999.

[70] R G Cox, P A Egdell, Jb Goodenough, A Hamnett, and Cc Naish. The metal-to-semiconductor transition in ternary ruthenium(iv) oxides - a study by electron-spectroscopy. *Journal of Physics C-Solid State Physics*, 16(32):6221–6239, 1983.

[71] K Schwarz. CrO_2 predicted as a half-metallic ferromagnet. *Journal of Physics F-Metal Physics*, 16(9):L211–L215, SEP 1986.

[72] Gerard Demazeau, Samir F. Matar, and Rainer Poettgen. Chemical bonding in metallic rutile-type oxides TO_2 (T = Ru, Rh, Pd, Pt). *Zeitschrift Fur Naturforschung Section B-a Journal of Chemical Sciences*, 62(7):949–954, JUL 2007.

[73] J. Emsley. *Nature's Building Blocks: an A to Z guide to the elements.* Oxford University Press, 2003.

[74] S Trasatti. Structure of the metal electrolyte solution interface - new data for theory. *Electrochimica Acta*, 36(11-12):1657–1658, 1991.

[75] A. K. Foor J. S. Green M. L. H. Grey C. P. Murrell A. J. Ashcroft, A. T. Cheetham. Selective oxidation of methane to synthesize gas using transition metal catalysts. *Nature*, 334:319–321, 1990.

[76] T Kawai and T Sakata. Photocatalytic decomposition of gaseous water over TiO_2 and TiO_2-RuO_2 surfaces. *Chemical Physics Letters*, 72(1):87–89, 1980.

[77] Y. S. Liang C. S. Hsieh D. S. Tsai D. S. Tiong K. K. Chen, R. S. Huang. Field emission from vertically aligned conductive IrO_2 nanorods. *Applied Physics Letters*, 84:1552–1554, 2004.

[78] D. S. Huang Y. S. Hsieh, C. S. Tsai. Preparation of ruthenium dioxide nanorods and their field emission characteristics. *Applied Physics Letters*, 85:3860, 2004.

[79] P. D. Pao C. W. Chiou J. W. Jan J. C. Krishna K. P. Kumar Pong F. Z. Tsai W. F. Chen M. H. Jang L. Y. Lee J. F. Chen R. S. Huang Y. S. Tsai D. S. Tsai, H. M. Babu. Comparison of electronic structures of RuO_2 and IrO_2 nanorods investigated by x-ray absorption and scanning photoelectron microscopy. *Applied Physics Letters*, 90:042108, 2007.

[80] M. D. Johannes, A. M. Stux, and K. E. Swider-Lyons. Electronic structure and properties of li-insertion materials: Li_2RuO_3 and RuO_2. *Physical Review B*, 77(7), FEB 2008.

[81] Lf Mattheiss. Electronic structure of RuO_2, OsO_2, and IrO_2. *Physical Review B*, 13(6):2433–2450, 1976.

[82] G. Georg C. A. Daniels, R. R. Margaritondo and F. Levy. Electronic states of rutile dioxides - Ruo_2, Iro_2, and $Ru_xIr_{1-x}O_2$. *Physical Review B*, 29(4):1813–1818, 1984.

[83] K. M. Glassford and J. R. Chelikowsky. Electronic and structural properties of RuO_2. *Physical Review B*, 47(4):1732–1741, JAN 15 1993.

[84] K M Glassford and J R Chelikowsky. Electron-transport properties in RuO_2 rutile. *Physical Review B*, 49(11):7107–7114, MAR 15 1994.

[85] BY Yavorsky, OV Krasovska, EE Krasovskii, AN Yaresko, and VN Antonov. Ab initio calculation of the fermi surface of RuO_2. *Physica B*, 225(3-4):243–250, JUL 1996.

[86] JS de Almeida and R Ahuja. Electronic and optical properties of RuO_2 and IrO_2. *Physical Review B*, 73(16), APR 2006.

[87] K Benyahia, Z Nabi, A Tadjer, and A Khalfi. Ab initio study of the structural and electronic properties of the complex structures of RuO_2. *Physica B-Condensed Matter*, 339(1):1–10, NOV 2003.

[88] E. E. Krasovska, O. V. Krasovskii and V. N. Antonov. Ab-initio calculation of the optical and photoelectron properties of RuO_2. *Physical Review B*, 52(16):11825–11829, OCT 15 1995.

[89] J. P. Perdew, K. Burke, and M. Ernzerhof. Generalized gradient approximation made simple. *Phys. Rev. Lett.*, 77(18):3865–3868–, 1996.

[90] S M Marcus. Measurement of magnetoresistance in transition metal oxide RuO_2. *Physics Letters A*, A 28(3):191, 1968.

[91] Je Graebner, Es Greiner, and Wd Ryden. Magnetothermal oscillations in RuO_2, OsO_2 and IrO_2. *Physical Review B*, 13(6):2426–2432, 1976.

[92] W D Ryden and A W Lawson. Magnetic susceptibility of IrO_2 and RuO_2. *Journal of Chemical Physics*, 52(12):6058, 1970.

[93] W D Ryden, A W Lawson, and C C Sartain. Temperature dependence of resistivity of RuO_2 and IrO_2. *Physics Letters A*, A 26(5):209, 1968.

[94] W D Ryden and A W Lawson. Electrical transport properties of IrO_2 and RuO_2. *Physical Review B*, 1(4):1494, 1970.

[95] B C Passenhe and D C McCollum. Heat capacity of ruo_2 and iro_2 between 0.54 degrees and 10 degrees k. *Journal of Chemical Physics*, 51(1):320, 1969.

[96] Goodenough Jb Tavener P J Telles D Cox, P A and R G Egdell. The electronic-structure of $Bi_{2-x}Gd_xRu_2O_7$ and RuO_2 - a study by electron-spectroscopy. *Journal of Solid State Chemistry*, 62(3):360–370, MAY 1986.

[97] Tenret-Noel C Pireaux J J Caudano R Verbist J J Riga, J and Y Gobillon. Electronic-structure of rutile oxides TiO_2, RuO_2 and IrO_2 studied by x-ray photoelectron-spectroscopy. *Physica Scripta*, 16(5-6):351–354, 1977.

[98] Z Hu, H von Lips, MS Golden, J Fink, G Kaindl, FMF de Groot, S Ebbinghaus, and A Reller. Multiplet effects in the Ru L_2,L_3 x-ray-absorption spectra of Ru(iv) and Ru(v) compounds. *Physical Review B*, 61(8):5262–5266, FEB 15 2000.

[99] H. M. Tsai, P. D. Babu, C. W. Pao, J. W. Chiou, J. C. Jan, K. P. K. Kumar, F. Z. Chien, W. F. Pong, M. H. Tsai, C. H. Chen, L. Y. Jang, J. F. Lee, R. S. Chen, Y. S. Huang, and D. S. Tsai. Comparison of electronic structures of RuO2 and IrO2 nanorods investigated by x-ray absorption and scanning photoelectron microscopy. *Appl. Phys. Lett.*, 90(4):042108–, 2007.

[100] Ak Goel, G Skorinko, and Fh Pollak. Optical-properties of single-crystal rutile RuO_2 and IrO_2 in the range 0.5 to 9.5 ev. *Physical Review B*, 24(12):7342–7350, 1981.

[101] D B Rogers, R D Shannon, A W Sleight, and J I Gillson. Crystal chemistry of metal dioxides with rutile-related structures. *inorganic Chemistry*, 8(4):841, 1969.

[102] Ys Huang, Hl Park, and Fh Pollak. Growth and characterization of RuO_2 single-crystals. *Materials Research Bulletin*, 17(10):1305–1312, 1982.

[103] CB Stagarescu, X Su, DE Eastman, KN Altmann, FJ Himpsel, and A Gupta. Orbital character of O-2p unoccupied states near the Fermi level in CrO_2. *Physical Review B*, 61(14):R9233–R9236, APR 1 2000.

[104] S. Eberhardt W. Eisebitt. Band structure information and resonant inelastic soft x-ray scattering in broad band solids. *Journal of Electron Spectroscopy and Related Phenomena*, 110&111:335–358, 2000.

[105] R Ruus, A Kikas, A Saar, A Ausmees, E Nommiste, J Aarik, A Aidla, T Uustare, and I Martinson. Ti 2p and O 1s x-ray absorption of TiO_2 polymorphs. *Solid State Communications*, 104(4):199–203, OCT 1997.

[106] X Rocquefelte, F Goubin, HJ Koo, MH Whangbo, and S Jobic. Investigation of the origin of the empirical relationship between refractive index and density on the basis of first principles calculations for the refractive indices of various TiO_2 phases. *Inorganic Chemistry*, 43(7):2246–2251, APR 5 2004.

[107] R Asahi, Y Taga, W Mannstadt, and AJ Freeman. Electronic and optical properties of anatase TiO_2. *Physical Review B*, 61(11):7459–7465, MAR 15 2000.

[108] U Diebold. The surface science of titanium dioxide. *Surface Science Reports*, 48(5-8):53–229, 2003.

[109] A Amtout and R Leonelli. Optical-properties of rutile near its fundamental-band gap. *Physical Review B*, 51(11):6842–6851, MAR 15 1995.

[110] Lionel (Editor) Vaysierres. *On Solar Hydrogen and Nanotechnology*. Wiley-Blackwell, 2010.

[111] H. Chen, J. F. Zhang, and H. K. Yuan. Electronic structure and magnetic properties of Cr-doped AlN. *Commun. Theor. Phys.*, 48(4):749–753–, 2007.

[112] KM Reddy, SV Manorama, and AR Reddy. Bandgap studies on anatase titanium dioxide nanoparticles. *Materials Chemistry and Physics*, 78(1):239–245, FEB 3 2003.

[113] Xiguang Han, Qin Kuang, Mingshang Jin, Zhaoxiong Xie, and Lansun Zheng. Synthesis of titania nanosheets with a high percentage of exposed (001) facets and related photocatalytic properties. *Journal of The American Chemical Society*, 131(9):3152+, MAR 11 2009.

[114] A Fujishima and K Honda. Electrochemical photolysis of water at a semiconductor electrode. *Nature*, 238(5358):37+, 1972.

[115] SUM Khan, M Al-Shahry, and WB Ingler. Efficient photochemical water splitting by a chemically modified n-TiO_2. *Science*, 297(5590):2243–2245, SEP 27 2002.

[116] M Gratzel. Dye-sensitized solar cells. *Journal of Photochemistry and Photobiology C-Photochemistry Reviews*, 4(2):145–153, OCT 31 2003.

[117] B. Eray S. Aydil Liu. Growth of oriented single-crystalline rutile TiO_2 nanorods on transparent conducting substrates for dye-sensitized solar cells. *Journal of the American Chemical Society*, 131:3985–3990, 2009.

[118] K Szacilowski, W Macyk, A Drzewiecka-Matuszek, M Brindell, and G Stochel. Bioinorganic photochemistry: Frontiers and mechanisms. *Chemical Reviews*, 105(6):2647–2694, JUN 2005.

[119] O Carp, CL Huisman, and A Reller. Photoinduced reactivity of titanium dioxide. *Progress in Solid State Chemistry*, 32(1-2):33–177, 2004.

[120] SA Chambers, S Thevuthasan, RFC Farrow, RF Marks, JU Thiele, L Folks, MG Samant, AJ Kellock, N Ruzycki, DL Ederer, and U Diebold. Epitaxial growth and properties of ferromagnetic Co-doped TiO_2 anatase. *Applied Physics Letters*, 79(21):3467–3469, NOV 19 2001.

[121] Seong Keun Kim, Gyu-Jin Choi, Sang Young Lee, Minha Seo, Sang Woon Lee, Jeon Hwan Han, Hyo-Shin Ahn, Seungwu Han, and Cheol Seong Hwang.

Al-doped Tio_2 films with ultralow leakage currents for next generation dram capacitors. *Advanced Materials*, 20(8):1429+, APR 21 2008.

[122] D. W. Kim, W. J. Cho, and T. W. Kim. Structural and magnetic properties of annealed ZnO-Co digital alloys. *J. Mater. Sci.*, 39(15):4917–4919–, 2004.

[123] K. A. Griffin, A. B. Pakhomov, C. M. Wang, S. M. Heald, and K. M. Krishnan. Intrinsic ferromagnetism in insulating cobalt doped anatase Tio2. *Phys. Rev. Lett.*, 94(15):157204–, 2005.

[124] John R. Jameson, Yoshiaki Fukuzumi, Zheng Wang, Peter Griffin, Koji Tsunoda, G. Ingmar Meijer, and Yoshio Nishi. Field-programmable rectification in rutile TiO_2 crystals. *Applied Physics Letters*, 91(11), SEP 10 2007.

[125] M Straumanis, W J James, and T Ejima. TiO_2 phase explored by lattice constant and density method. *Acta Crystallographica*, 14(5):493–&, 1961.

[126] H Miyaoka, G Mizutani, H Sano, M Omote, K Nakatsuji, and F Komori. Anomalous electro-migration of oxygen vacancies in reduced TiO_2. *Solid State Communications*, 123(9):399–404, 2002.

[127] E. Campus F. Walder L. Gratzel M. Bonhote, P. Gogniat. Nanocrystalline electrochromic displays. *Displays*, 20:137–144, 1999.

[128] G. Ryan M. Corr D. Rao S. N. Fitzmaurice D. Cummins, D. Boschloo. Ultrafast electrochromic windows based on redox-chromophore modified nanostructured semiconducting and conducting films. *Journal of Physical Chemistry B*, 104:11449–11459, 2000.

[129] Dmitri B. Strukov, Gregory S. Snider, Duncan R. Stewart, and R. Stanley Williams. The missing memristor found. *Nature*, 453(7191):80–83, MAY 1 2008.

[130] J. Joshua Yang, Matthew D. Pickett, Xuema Li, Douglas A. A. Ohlberg, Duncan R. Stewart, and R. Stanley Williams. Memristive switching mechanism for metal/oxide/metal nanodevices. *Nature Nanotechnology*, 3(7):429–433, JUL 2008.

[131] John Paul Strachan, J. Joshua Yang, Ruthm Muenstermann, Andreas Scholl, Gilberto Medeiros-Ribeiro, Duncan R. Stewart, and R. Stanley Williams. Structural and chemical characterization of TiO_2 memristive devices by spatially-resolved NEXAFS. *Nanotechnology*, 20(48), DEC 2 2009.

[132] L. S. Swamy, V. Dubrovinsky. Bulk modulus of anatase. *Journal of Physics and Chemistry of Solids*, 62:673–675, 2001.

[133] L. Jiang Olsen, J. S. Gerward. On the rutile/alpha-PbO_2-type phase boundary of TiO_2. *Journal of Physics and Chemistry of Solids*, 60:229–233, 1999.

[134] F M F Degroot, J Faber, J J M Michiels, M T Czyzyk, M Abbate, and J C Fuggle. Oxygen 1s x-ray-absorption of tetravalent titanium-oxides - a comparison with single-particle calculations. *Physical Review B*, 48(4):2074–2080, JUL 15 1993.

[135] C M Freeman, J M Newsam, S M Levine, and C R A Catlow. inorganic crystal-structure prediction using simplified potentials and experimental unit cells - application to the polymorphs of titanium-dioxide. *Journal of Materials Chemistry*, 3(5):531–535, MAY 1993.

[136] T. Miller G. J. Richardson J. W. Smith J. V. Burdett, J. K. Hughbanks. Structural electronic relationships in inorganic solids - powder neutron-diffraction studies of the rutile and anatase polymorphs of titanium-dioxide at 15- and 295- k. *Journal Of The American Chemical Society*, 109:3639, 1987.

[137] A. Ferreira da Silva, I. Pepe, C. Persson, J. Souza de Almeida, C. Moyses Araujo, R. Ahuja, B. Johansson, C. Y. An, and J. H. Guo. Optical properties of oxide compounds Pbo, Sno_2 and Tio_2. *Physica Scripta*, T109:180–183, 2004.

[138] K. S. Butz. T Ryu, S-B. Das. Nuclear quadrupole interaction at 44sc in the anatase and rutile modifications of TiO_2: Time-differential perturbed-angular-correlation measurements and ab initio calculations. *Physical Review B*, 77:094124, 2008.

[139] F. M. F. de Groot, M. Grioni, J. C. Fuggle, J. Ghijsen, G. A. Sawatzky, and H. Petersen. Oxygen 1s x-ray-absorption edges of transition-metal oxides. *Phys. Rev. B*, 40(8):5715–5723–, 1989.

[140] F. M. F. Degroot, J. C. Fuggle, B. T. Thole, and G. A. Sawatzky. 2p x-ray absorption of 3d transition-metal compounds - an atomic multiplet description including the crystal-field. *Phys. Rev. B*, 42(9):5459–5468–, 1990.

[141] K M Glassford and J R Chelikowsky. Optical-properties of titanium-dioxide in the rutile structure. *Physical Review B*, 45(7):3874–3877, FEB 15 1992.

[142] M Li, W Hebenstreit, U Diebold, MA Henderson, and DR Jennison. Oxygen-induced restructuring of rutile TiO_2(110): formation mechanism, atomic models, and influence on surface chemistry. *Faraday Discussions*, 114:245–258, 1999. Meeting on the Surface Science of Metal Oxides, AMBLESIDE, ENGLAND, SEP 01-03, 1999.

[143] B Silvi, N Fourati, R Nada, and C R A Catlow. Pseudopotential periodic hartree-fock study of rutile TiO_2. *Journal of Physics and Chemistry of Solids*, 52(8):1005–1009, 1991.

[144] I. Fleming, C. C. Fulton, G. Lucovsky, J. E. Rowe, M. D. Ulrich, and J. Luening. Local bonding analysis of the valence and conduction band features of TiO_2. *Journal of Applied Physics*, 102(3), AUG 1 2007.

[145] B Jiang, JM Zuo, N Jiang, M O'Keeffe, and JCH Spence. Charge density and chemical bonding in rutile, TiO_2. *Acta Crystallographica Section A*, 59(Part 4):341–350, JUL 2003.

[146] K. B. Joshi and B. K. Sharma. Electronic structure and momentum density distribution of titanium dioxide. *Journal of Alloys and Compounds*, 440(1-2):51–56, AUG 16 2007.

[147] C Heiliger, F Heyroth, F Syrowatka, HS Leipner, I Maznichenko, K Kokko, W Hergert, and I Mertig. Orientation-dependent electron-energy-loss spectroscopy of TiO_2: A comparison of theory and experiment. *Physical Review B*, 73(4), JAN 2006.

[148] JC Woicik, EJ Nelson, L Kronik, M Jain, JR Chelikowsky, D Heskett, LE Berman, and GS Herman. Hybridization and bond-orbital components in site-specific x-ray photoelectron spectra of rutile TiO_2. *Physical Review Letters*, 89(7), AUG 12 2002.

[149] G. Mattioli, F. Filippone, P. Alippi, and A. Amore Bonapasta. Ab initio study of the electronic states induced by oxygen vacancies in rutile and anatase TiO_2. *Physical Review B*, 78(24), DEC 2008.

[150] HC Choi, HJ Ahn, YM Jung, MK Lee, HJ Shin, SB Kim, and YE Sung. Characterization of the structures of size-selected TiO_2 nanoparticles using x-ray absorption spectroscopy. *Applied Spectroscopy*, 58(5):598–602, MAY 2004.

[151] Y Hwu, YD Yao, NF Cheng, CY Tung, and HM Lin. X-ray absorption of nanocrystal TiO_2. *Nanostructured Materials*, 9(1-8):355–358, 1997. 3rd international Conference on Nanostructured Materials, KONA, HI, JUL 08-12, 1996.

[152] Hua Gui Yang, Cheng Hua Sun, Shi Zhang Qiao, Jin Zou, Gang Liu, Sean Campbell Smith, Hui Ming Cheng, and Gao Qing Lu. Anatase TiO_2 single crystals with a large percentage of reactive facets. *Nature*, 453(7195):638–U4, MAY 29 2008.

[153] J. K. Furdyna. Diluted magnetic semiconductors. *J. Appl. Phys.*, 64(4):R29–R64–, 1988.

[154] F. Morko C. Liu, C. Yun. Ferromagnetism of zno and gan: a review. *Journal of Materials Science: Materials in Chemistry*, 16:555–597, 2005.

[155] F. Pan, C. Song, X. J. Liu, Y. C. Yang, and F. Zeng. Ferromagnetism and possible application in spintronics of transition-metal-doped ZnO films. *Mater. Sci. Eng. R-Rep.*, 62(1):1–35–, 2008.

[156] M. Venkatesan, C. B. Fitzgerald, and J. M. D. Coey. Unexpected magnetism in a dielectric oxide. *Nature*, 430(7000):630–630–, 2004.

[157] J. M. D. Coey, M. Venkatesan, P. Stamenov, C. B. Fitzgerald, and L. S. Dorneles. Magnetism in hafnium dioxide. *Phys. Rev. B*, 72(2):024450–, 2005.

[158] L. S. Dorneles, M. Venkatesan, M. Moliner, J. G. Lunney, and J. M. D. Coey. Magnetism in thin films of CaB_6 and SrB_6. *Appl. Phys. Lett.*, 85(26):6377–6379–, 2004.

[159] C. Liu, F. Yun, and H. Morkoc. Ferromagnetism of ZnO and GaN: A review. *J. Mater. Sci.-Mater. Electron.*, 16(9):555–597–, 2005.

[160] H. Ohno, A. Shen, F. Matsukura, A. Oiwa, A. Endo, S. Katsumoto, and Y. Iye. (Ga,Mn)As: A new diluted magnetic semiconductor based on GaAs. *Appl. Phys. Lett.*, 69(3):363–365–, 1996.

[161] H. Ohno. Making nonmagnetic semiconductors ferromagnetic. *Science*, 281(5379):951–956–, 1998.

[162] H. Ohno, F. Matsukura, A. Shen, Y. Sugawara, N. Akiba, and T. Kuroiwa. Ferromagnetic (ga, mn)as and its heterostructures. *Physica E*, 2(1-4):904–908–, 1998.

[163] T. Dietl, H. Ohno, F. Matsukura, J. Cibert, and D. Ferrand. Zener model description of ferromagnetism in zinc-blende magnetic semiconductors. *Science*, 287(5455):1019–1022–, 2000.

[164] K. Ueda, H. Tabata, and T. Kawai. Magnetic and electric properties of transition-metal-doped ZnO films. *Appl. Phys. Lett.*, 79(7):988–990–, 2001.

[165] J. M. D. Coey, J. T. Mlack, M. Venkatesan, and P. Stamenov. Magnetization process in dilute magnetic oxides. *IEEE Trans. Magn.*, 46(6):2501–2503–, 2010.

[166] A. Ney, T. Kammermeier, V. Ney, S. Ye, K. Ollefs, E. Manuel, S. Dhar, K. H. Ploog, E. Arenholz, F. Wilhelm, and A. Rogalev. Element specific magnetic properties of gd-doped gan: Very small polarization of ga and paramagnetism of gd. *Phys. Rev. B*, 77(23):233308–, 2008.

[167] J. Alaria, M. Venkatesan, and J. M. D. Coey. Magnetism of ZnO nanoparticles doped with 3d cations prepared by a solvothermal method. *J. Appl. Phys.*, 103(7):–, 2008.

[168] J. Alaria, H. Bieber, S. Colis, G. Schmerber, and A. Dinia. Absence of ferromagnetism in Al-doped $Zn_{0.9}Co_{0.10}O$ diluted magnetic semiconductors. *Appl. Phys. Lett.*, 88(11):–, 2006.

[169] C. H. Patterson. Comparison of hybrid density functional, hartree-fock, and gw calculations on nio. *Int. J. Quantum Chem.*, 106(15):3383–3386–, 2006.

[170] C. D. Pemmaraju, R. Hanafin, T. Archer, H. B. Braun, and S. Sanvito. Impurity-ion pair induced high-temperature ferromagnetism in Co-doped ZnO. *Phys. Rev. B*, 78(5):054428, Aug 2008.

[171] A. Chakrabarty and C. Patterson. Unpublished article. 2011.

[172] K. Rode, R. Mattana, A. Anane, V. Cros, E. Jacquet, J. P. Contour, F. Petroff, A. Fert, M. A. Arrio, P. Sainctavit, P. Bencok, F. Wilhelm, N. B. Brookes, and A. Rogalev. Magnetism of (Zn,Co)O thin films probed by x-ray absorption spectroscopies. *Appl. Phys. Lett.*, 92(1):012509–, 2008.

[173] T. Tietze, M. Gacic, G. Schutz, G. Jakob, S. Bruck, and E. Goering. Xmcd studies on Co and Li doped ZnO magnetic semiconductors. *New J. Phys.*, 10:055009–, 2008.

[174] A. Ney, K. Ollefs, S. Ye, T. Kammermeier, V. Ney, T. C. Kaspar, S. A. Chambers, F. Wilhelm, and A. Rogalev. Absence of intrinsic ferromagnetic interactions of isolated and paired Co dopant atoms in $Zn_{1-x}Co_xO$ with high structural perfection. *Phys. Rev. Lett.*, 100(15):–, 2008.

[175] J. M. D. Coey. High-temperature ferromagnetism in dilute magnetic oxides. *J. Appl. Phys.*, 97(10):10D313–, 2005.

[176] S. Krishnamurthy, C. McGuinness, LS Dorneles, M. Venkatesan, JMD Coey, JG Lunney, CH Patterson, KE Smith, T. Learmonth, P.A. Glans, et al. Soft-x-ray spectroscopic investigation of ferromagnetic Co-doped ZnO. *Journal of Applied Physics*, 99:08M111, 2006.

[177] X. C. Liu, E. W. Shi, Z. Z. Chen, B. Y. Chen, T. Zhang, L. X. Song, K. J. Zhou, M. Q. Cui, W. S. Yan, Z. Xie, B. He, and Q. W. Shi. Effect of oxygen partial pressure on the local structure and magnetic properties of Co-doped ZnO films. *J. Phys.-Condes. Matter*, 20(2):–, 2008.

[178] M. D. McCluskey and S. J. Jokela. Defects in ZnO. *J. Appl. Phys.*, 106(7):–, 2009.

[179] C. B. Fitzgerald, M. Venkatesan, J. G. Lunney, L. S. Dorneles, and J. M. D. Coey. Cobalt-doped ZnO - a room temperature dilute magnetic semiconductor. *Appl. Surf. Sci.*, 247(1-4):493–496–, 2005.

[180] P. Stamenov, M. Venkatesan, L. S. Dorneles, D. Maude, and J. M. D. Coey. Magnetoresistance of Co-doped ZnO thin films. *J. Appl. Phys.*, 99(8):08M124–, 2006.

[181] A. Zukova, A. Teiserskis, S. van Dijken, YK Gun ko, and V. Kazlauskiene. Giant moment and magnetic anisotropy in co-doped zno films grown by pulse-injection metal organic chemical vapor deposition. *Applied Physics Letters*, 89:232503, 2006.

[182] A. S. Risbud, N. A. Spaldin, Z. Q. Chen, S. Stemmer, and R. Seshadri. Magnetism in polycrystalline cobalt-substituted zinc oxide. *Phys. Rev. B*, 68(20):205202–, 2003.

[183] L. S. Dorneles, M. Venkatesan, R. Gunning, P. Stamenov, J. Alaria, M. Rooney, J. G. Lunney, and J. M. D. Coey. Magnetic and structural properties of Co-doped Zno thin films. *J. Magn. Magn. Mater.*, 310(2):2087–2088–, 2007.

[184] T. C. Kaspar, T. Droubay, S. M. Heald, M. H. Engelhard, P. Nachimuthu, and S. A. Chambers. Hidden ferromagnetic secondary phases in cobalt-doped ZnO epitaxial thin films. *Phys. Rev. B*, 77(20):–, 2008.

[185] M. A. White, T. C. Lovejoy, S. T. Ochsenbein, M. A. Olmstead, and D. R. Gamelin. Sputtering-induced Co^0 formation in x-ray photoelectron spectroscopy of nanocrystalline $Zn_{1-x}Co_xO$ spinodal enrichment models. *J. Appl. Phys.*, 107(10):–.

[186] J. M. D. Coey, K. Wongsaprom, J. Alaria, and M. Venkatesan. Charge-transfer ferromagnetism in oxide nanoparticles. *J. Phys. D-Appl. Phys.*, 41(13):–, 2008.

[187] Z. H. Zhang, X. F. Wang, J. B. Xu, S. Muller, C. Ronning, and Q. Li. Evidence of intrinsic ferromagnetism in individual dilute magnetic semiconducting nanostructures. *Nat. Nanotechnol.*, 4(8):523–527–, 2009.

[188] W. C. Hao, J. J. Li, H. Z. Xu, J. O. Wang, and T. M. Wang. Evidence of surface-preferential co distribution in ZnO nanocrystal and its effects on the ferromagnetic property. *ACS Appl. Mater. Interfaces*, 2(7):2053–2059–.

[189] J. Jiménez-Mier, J. van Ek, D. L. Ederer, T. A. Callcott, J. J. Jia, J. Carlisle, L. Terminello, A. Asfaw, and R. C. Perera. Dynamical behavior of x-ray absorption and scattering at the L edge of titanium compounds: Experiment and theory. *Phys. Rev. B*, 59(4):2649–2658, Jan 1999.

[190] S. Chambers. Is it really ferromagnetism? *Nature Materials*, 9:956, 2010.

[191] J. M. D. Coey and S. A. Chambers. Oxide dilute magnetic semiconductors-fact or fiction? *MRS Bull.*, 33(11):1053–1058–, 2008.

[192] T. Dietl, T. Andrearczyk, A. Lipinska, M. Kiecana, M. Tay, and Y. H. Wu. Origin of ferromagnetism in $Zn_{1-x}Co_xO$ from magnetization and spin-dependent magnetoresistance measurements. *Phys. Rev. B*, 76(15):155312–, 2007.

[193] D. W. Abraham, M. M. Frank, and S. Guha. Absence of magnetism in hafnium oxide films. *Appl. Phys. Lett.*, 87(25):252502–, 2005.

[194] M. Venkatesan, C. B. Fitzgerald, J. G. Lunney, and J. M. D. Coey. Anisotropic ferromagnetism in substituted zinc oxide. *Phys. Rev. Lett.*, 93(17):177206–, 2004.

[195] J. M. D. Coey, M. Venkatesan, C. B. Fitzgerald, L. S. Dorneles, P. Stamenov, and J. G. Lunney. Anisotropy of the magnetization of a dilute magnetic oxide. *J. Magn. Magn. Mater.*, 290:1405–1407–, 2005.

[196] T. C. Kaspar, T. Droubay, S. M. Heald, P. Nachimuthu, C. M. Wang, V. Shutthanandan, C. A. Johnson, D. R. Gamelin, and S. A. Chambers. Lack of ferromagnetism in n-type cobalt-doped ZnO epitaxial thin films. *New J. Phys.*, 10:–, 2008.

[197] Y. Z. Peng, T. Liew, W. D. Song, C. W. An, K. L. Teo, and T. C. Chong. Structural and optical properties of Co-doped ZnO thin films. *J. Supercond.*, 18(1):97–103–, 2005.

[198] B. V. Crist. *The elements and natives oxides handbook of monochromatic XPS spectra*, volume 2. Chichester, 2000.

[199] CL Dong, C. Persson, L. Vayssieres, A. Augustsson, T. Schmitt, M. Mattesini, R. Ahuja, CL Chang, and J.H. Guo. Electronic structure of nanostructured ZnO from x-ray absorption and emission spectroscopy and the local density approximation. *Physical Review B*, 70(19):195325, 2004.

[200] J. H. Guo, L. Vayssieres, C. Persson, R. Ahuja, B. Johansson, and J. Nordgren. Polarization-dependent soft-x-ray absorption of highly oriented ZnO microrod arrays. *J. Phys.-Condes. Matter*, 14(28):6969–6974–, 2002.

[201] A. R. H. Preston, B. J. Ruck, L. F. J. Piper, A. DeMasi, K. E. Smith, A. Schleife, F. Fuchs, F. Bechstedt, J. Chai, and S. M. Durbin. Band structure of ZnO from resonant x-ray emission spectroscopy. *Phys. Rev. B*, 78(15):155114, Oct 2008.

[202] JH Guo, A. Gupta, P. Sharma, KV Rao, MA Marcus, CL Dong, JMO Guillen, SM Butorin, M. Mattesini, PA Glans, et al. X-ray spectroscopic study of the charge state and local ordering of room-temperature ferromagnetic Mn-doped Zno. *Journal of Physics: Condensed Matter*, 19:172202, 2007.

[203] S. Kumar, Y. J. Kim, B. H. Koo, H. Choi, C. G. Lee, S. K. Sharma, M. Knobel, S. Gautam, and K. H. Chae. Ferromagnetism in chemically-synthesized Co-doped ZnO. *J. Korean Phys. Soc.*, 55(3):1060–1064–, 2009.

[204] GS Chang, EZ Kurmaev, DW Boukhvalov, LD Finkelstein, S. Colis, TM Pedersen, A. Moewes, and A. Dinia. Effect of Co and O defects on the magnetism in Co-doped ZnO: Experiment and theory. *Physical Review B*, 75(19):195215, 2007.

[205] K. Rode, J. M. D. Coey, and M. Venkatesan. *private communication*, pages –.

[206] J. H. Guo, L. Vayssieres, C. Persson, R. Ahuja, B. Johansson, and J. Nordgren. Polarization-dependent soft-x-ray absorption of a highly oriented zno microrod-array. *J. Phys.-Condes. Matter*, 17(1):235–240–, 2005.

[207] J. H. Guo, A. Gupta, P. Sharma, K. V. Rao, M. A. Marcus, C. L. Dong, J. M. O. Guillen, S. M. Butorin, M. Mattesini, P. A. Glans, K. E. Smith, C. L. Chang, and R. Ahuja. X-ray spectroscopic study of the charge state and local ordering of room-temperature ferromagnetic mn-doped zno. *J. Phys.-Condes. Matter*, 19(17):172202–, 2007.

[208] S. C. Wi, J. S. Kang, J. H. Kim, S. B. Cho, B. J. Kim, S. Yoon, B. J. Suh, S. W. Han, K. H. Kim, K. J. Kim, B. S. Kim, H. J. Song, H. J. Shin, J. H. Shim, and B. I. Min. Electronic structure of $Zn_{1-x}Co_xO$ using photoemission and x-ray absorption spectroscopy. *Appl. Phys. Lett.*, 84(21):4233–4235–, 2004.

[209] S. C. Wi, J. S. Kang, J. H. Kim, S. S. Lee, S. B. Cho, B. J. Kim, S. Yoon, B. J. Suh, S. W. Han, K. H. Kim, K. J. Kim, B. S. Kim, H. J. Song, H. J. Shin, J. H. Shim, and B. I. Min. Photoemission study of $Zn_{1-x}Co_xO$ as a possible dms. *Phys. Status Solidi B-Basic Res.*, 241(7):1529–1532–, 2004.

[210] J. W. Chiou, H. M. Tsai, C. W. Pao, K. P. K. Kumar, S. C. Ray, F. Z. Chien, W. F. Pong, M. H. Tsai, C. H. Chen, H. J. Lin, J. J. Wu, M. H. Yang, S. C. Liu, H. H. Chiang, and C. W. Chen. Comparison of the electronic structures of $Zn_{1-x}Co_xO$ and $Zn_{1-x}Mg_xO$ nanorods using x-ray absorption and scanning photoelectron microscopies. *Appl. Phys. Lett.*, 89(4):043121–, 2006.

[211] J. W. Chiou, H. M. Tsai, C. W. Pao, K. P. K. Kumar, J. H. Chen, D. C. Ling, F. Z. Chien, W. F. Pong, M. H. Tsai, J. J. Wu, M. H. Yang, S. C. Liu, I. H. Hong, C. H. Chen, H. J. Lin, and J. F. Lee. Role of valence-band Co 3d states on ferromagnetism in $Zn_{1-x}Co_xO$ nanorods. *Appl. Phys. Lett.*, 90(6):062103–, 2007.

[212] S. S. Lee, G. Kim, S. C. Wi, J. S. Kang, S. W. Han, Y. K. Lee, K. S. An, S. J. Kwon, M. H. Jung, and H. J. Shin. Investigation of the phase separations and the local electronic structures of $Zn_{1-x}T_xO$, (T= Mn, Fe, Co) magnetic semiconductors using synchrotron radiation. *J. Appl. Phys.*, 99(8):–, 2006.

[213] N. A. Spaldin. Search for ferromagnetism in transition-metal-doped piezoelectric Zno. *Phys. Rev. B*, 69(12):125201–, 2004.

[214] J. M. D. Coey, P. Stamenov, R. D. Gunning, M. Venkatesan, and K. Paul. Ferromagnetism in defect-ridden oxides and related materials. *New J. Phys.*, 12:–, 2010.

[215] A. C. Tuan, J. D. Bryan, A. B. Pakhomov, V. Shutthanandan, S. Thevuthasan, D. E. McCready, D. Gaspar, M. H. Engelhard, J. W. Rogers, K. Krishnan, D. R. Gamelin, and S. A. Chambers. Epitaxial growth and properties of cobalt-doped ZnO on alpha-al_2o_3 single-crystal substrates. *Phys. Rev. B*, 70(5):054424–, 2004.

[216] M. Magnuson, S. M. Butorin, J. H. Guo, and J. Nordgren. Electronic structure investigation of CoO by means of soft x- ray scattering. *Phys. Rev. B*, 65(20):art. no.–205106–, 2002.

[217] FMF Groot, M. Abbate, J. Elp, GA Sawatzky, YJ Ma, CT Chen, and F. Sette. Oxygen 1s and cobalt 2p X-ray absorption of cobalt oxides. *Journal of Physics: Condensed Matter*, 5:2277, 1993.

[218] G. Laan and IW Kirkman. The 2p absorption spectra of 3d transition metal compounds in tetrahedral and octahedral symmetry. *Journal of Physics: Condensed Matter*, 4:4189, 1992.

[219] S. Krishnamurthy, C. McGuinness, LS Dorneles, M. Venkatesan, JMD Coey, JG Lunney, CH Patterson, KE Smith, T. Learmonth, P.A. Glans, et al. Soft-x-ray spectroscopic investigation of ferromagnetic Co-doped ZnO. *Journal of Applied Physics*, 99:08M111, 2006.

[220] K. Rode, A. Anane, R. Mattana, J. P. Contour, O. Durand, and R. LeBourgeois. Magnetic semiconductors based on cobalt substituted ZnO. *J. Appl. Phys.*, 93(10):7676–7678–, 2003.

[221] H. Liu, J. Guo, Y. Yin, A. Augustsson, C. Dong, J. Nordgren, C. Chang, P. Alivisatos, G. Thornton, D.F. Ogletree, et al. Electronic structure of cobalt nanocrystals suspended in liquid. *Nano Lett*, 7(7):1919–1922, 2007.

[222] P. Koidl. Optical-absorption of Co^{2+} in ZnO. *Phys. Rev. B*, 15(5):2493–2499–, 1977.

[223] J. A. Sans, J. F. Sanchez-Royo, J. Pellicer-Porres, A. Segura, E. Guillotel, G. Martinez-Criado, J. Susini, A. Munoz-Paez, and V. Lopez-Flores. Optical, x-ray absorption and photoelectron spectroscopy investigation of the Co site configuration in $Zn_{1-x}Co_xO$ films prepared by pulsed laser deposition. *Superlattices Microstruct.*, 42(1-6):226–230–, 2007.

[224] K. J. Zhou, Y. Tezuka, M. Q. Cui, J. Zhao, X. C. Liu, Z. Z. Chen, and Z. Y. Wu. The mechanism of Al donor defects in (Zn, Co)O:Al: a view from resonant x-ray spectroscopies. *J. Phys.-Condes. Matter*, 21(49):–, 2009.

[225] X. C. Liu, E. W. Shi, Z. Z. Chen, T. Zhang, Y. Zhang, B. Y. Chen, W. Huang, X. Liu, L. X. Song, K. J. Zhou, and M. Q. Cui. Effect of donor localization on the magnetic properties of Zn-Co-O system. *Appl. Phys. Lett.*, 92(4):–, 2008.

[226] T.W. Huang J. Lee C.H. Liao, Y.F. Huang. X-ray absorption spectroscopy study of annealing effect on co-implanted ZnO epitaxial films. *IEEE Transactions On Magnetics*, 45:2431, 2009.

[227] J. W. Chiou, J. C. Jan, H. M. Tsai, C. W. Bao, W. F. Pong, M. H. Tsai, I. H. Hong, R. Klauser, J. F. Lee, J. J. Wu, and S. C. Liu. Electronic structure of ZnO nanorods studied by angle-dependent x-ray absorption spectroscopy and scanning photoelectron microscopy. *Appl. Phys. Lett.*, 84(18):3462–3464–, 2004.